



Ph.D. Thesis

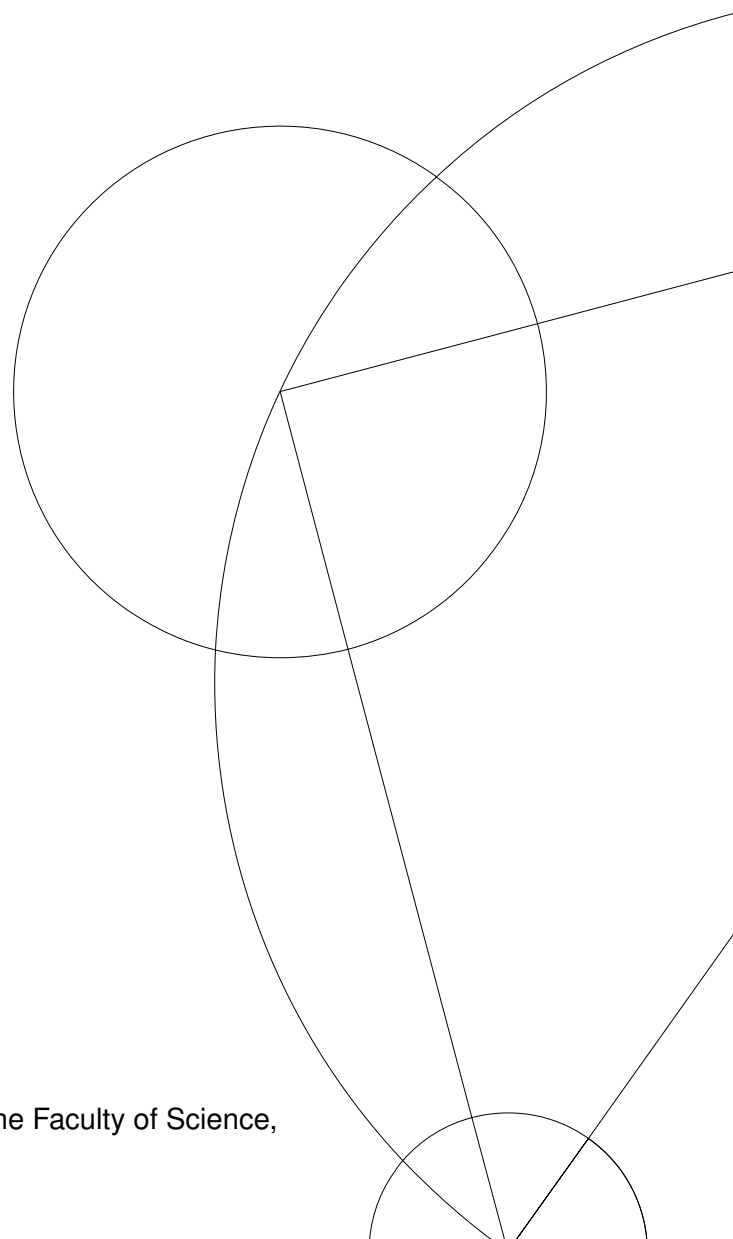
Daniel Steffensen

Nematicity, Superconductivity and Topological Effects in Multi-Orbital Systems

Advisor: Prof. Brian Møller Andersen

February 05, 2021

This thesis has been submitted to the PhD School of The Faculty of Science,
University of Copenhagen



Nematicity, Superconductivity and Topological Effects in Multi-Orbital Systems
Daniel Steffensen, M.Sc.

Ph.D. Thesis

X-Ray and Neutron Science
Niels Bohr Institute
University of Copenhagen

Academic advisor:

Prof. Brian Møller Andersen

Assessment committee:

Prof. Jens Paaske

Prof. Ilya Eremin

Prof. Andreas P. Schnyder

*“I’m a simple man without a lot of complicated twists and turns.
Look down my throat and you can see out my ass.”*

– Da Shi

Abstract

The study of phases of matter has consistently fascinated and puzzled the condensed matter community, and the discovery of high-temperature superconductors in 1986, and topological phases in 1980, are no exceptions. In particular the iron-based superconductors, one of the later additions to the ever-growing class of high-temperature superconductors, have in recent years attracted a considerable amount of attention, due to their intricate phase diagrams with a multitude of electronic phases in the vicinity of the superconducting state. Such phase diagrams call for an extensive investigation of the surrounding electronic phases, in the hope of elucidating their role in the resulting superconducting instability, and to broaden our understanding of correlated systems in general. A broad range of methods and theories have successfully been applied in the quest of understanding these materials. Nonetheless, the iron-chalcogenide FeSe appear to be the misfit in the family of iron-based superconductors, due to its lacking long-range magnetic order at ambient pressure, its highly anisotropic Fermi surface in the orthorhombic phase and its peculiar resulting gap structure.

Furthermore, recent theoretical and experimental findings suggest that FeSe also exhibits non-trivial topological phases. More specifically, FeSe doped with Te is argued to be an intrinsic manifestation of the celebrated Fu-Kane proposal, which is believed to harbor the coveted Majorana zero modes in the core of its superconducting vortices. The study of topological phases, and in particular the topological superconducting phases, has in recent years become one of the most active fields in condensed matter theory, and the indication that FeSe could be the rare case of an intrinsic topological superconductor, opens the door to investigate topological phases in similar materials. In fact, prime candidates are magnetic materials, that either coexist or are in proximity to a superconductor, since these can, under the right circumstances, demonstrate all the necessary ingredients to enter a topological superconducting phase.

In the first part of this thesis, we study in great detail some general symmetry tools and properties of multi-orbital systems. By keeping this discussion general, we can apply the tools on specific materials, like FeSe, but also on a broader class of systems, such as magnetic materials coexisting or in proximity to a superconductor. Motivated by the peculiar properties of FeSe, previous studies have found that nearest-neighbor Coulomb interactions in monolayer FeSe drive an intra-orbital nematic order with a d -wave form factor. With this in mind, and recent experiments on disorder-induced nematic order in iron-based superconductors, we perform a phenomenological, followed by a microscopic, study of impurities in systems close to a nematic instability. We find that a single impurity in the tetragonal phase locally induces nematic order, however, due to the specific featureless form of the single impurity, the induced nematic order spatially averages to zero. On the other hand, under the right conditions a critical density of impurities can modify the Stoner criterion, and thereby raise the nematic transition temperature. Inspired by the idea of nematic order generated from nearest-

neighbor interactions, we perform a thorough symmetry and mean-field study of such interactions, and find, in contrast to previous studies, the leading low temperature neamtic components to be of inter-orbital $d_{xz} - d_{xy}$ character. This specific form of the order parameter give rise to a hybridization gap, which can completely remove the Y pocket from the Fermi level in the 1-Fe unit cell, believed to be consistent with recent experiments. From this highly anisotropic band structure, we calculate the resulting superconducting gap within the theory of spin fluctuation mediated pairing, which also appears to agree with experiments. Lastly, we discuss the discrepancies found between our computed spin susceptibilities and the available neutron scattering experiments, as well as the necessary inclusion of orbital-dependent quasiparticle weights.

In the last part of this thesis, we proceed and study topological superconducting phases induced by magnetic textures in multi-orbital systems. Specifically, we demonstrate an alternative route to engineering Majorana zero modes, which are trapped in singular vortex defects in magnetic textures. The discussed magnetic textures are assumed to coexist or be in proximity to a nodal superconductor. Although this study is motivated by the iron-based superconductors, which can potentially have magnetism coexisting with superconductivity, we keep our discussion general, and it can thus be applied to a broad variety of hybrid structures and superconductors. Lastly, we perform a classification of topological superconductors induced by magnetic textures in the absence of singular defects. By taking into account the symmetries tied to the magnetic textures, and allow for general multiband spin-singlet superconductivity, we find a plethora of topological phases leading to flat, uni- or bi-directional, (quasi-)helical and chiral Majorana edge modes.

Resumé

Studiet af stoffers tilstandsformer har gennem tiden fascineret og forundret faststoffysikere, og opdagelsen af højtemperatur-superledere i 1986 og topologiske faser i 1980 er ingen undtagelse. Især de jernbaserede superledere, en af de nyere tilføjelser til den voksende klasse af højtemperatur-superledere, har de seneste par år tiltrukket stor opmærksomhed på grund af deres indviklede fasediagrammer med mange forskellige elektroniske faser tæt ved den superledende fase. Sådanne fasediagrammer giver anledning til vidtgående studier af de omkringliggende elektroniske faser i håbet om at opklare deres rolle i den resulterende superledende faseovergang og give os en bedre generel forståelse af korrelerede materialer. En bred vifte af metoder og teorier er blevet anvendt med succes i forsøget på at forstå disse materialer. Ikke desto mindre ser det ud til, at jernchalcogeniden FeSe ikke passer ind i familien af jernbaserede superledere, på grund af dens mangel på langtrækkende magnetisk orden ved atmosfæriske tryk, dens meget anisotrope Fermi-overflade i den orthorhombiske fase og dens besynderlige gabstruktur.

Derudover antyder nyere teoretiske og eksperimentelle studier, at FeSe også udviser ikke-trivielle topologiske faser. Det diskuteres om FeSe, dopet med Te, kan manifestere det berømte Fu-Kane-forslag, som forventes at give anledning til de eftertragtede Majorana-multilstande i centrene af superledende hvirvler. Studiet af topologiske faser, og især topologiske superledende faser, er de seneste par år blevet et af faststoffysikkens mest aktive felter, og antydningen af en topologisk superledende fase i FeSe giver anledning til at undersøge muligheden for topologiske faser i lignende materialer. Spidskandidaterne er de magnetiske materialer, som enten sameksisterer eller er tæt koblet til en superleder, da disse, under de rette omstændigheder, kan have alle de nødvendige karaktertræk til at træde ind i en topologisk superledende fase.

I første del af denne afhandling studerer vi generelle symmetriredskaber og -egenskaber af multi-orbitale systemer. Ved at holde vores diskussion generel, kan vi anvende disse redskaber på specifikke materialer, som FeSe, men også på bredere klasser af systemer, f.eks. magnetiske materialer, der enten sameksisterer eller er tæt koblet til en superleder. Med udgangspunkt i de besynderlige egenskaber fundet i FeSe, har tidligere studier vist, at nærmeste-nabo-Coulomb-vekselvirkninger i monolag FeSe driver en intraorbital nematisk orden med en d -bølge-formfaktor. Med dette i mente, samt nyere eksperimenter på urenheds-induceret nematisk orden i jernbaserede superledere, udfører vi et fænomenologisk, efterfulgt af et mikroskopisk, studie af urenheder i systemer tæt på en nematisk faseovergang. Vi konkluderer, at en enkelt urenhed i den orthorhombiske fase inducerer lokal nematisk orden, men at den inducerede fase er lig nul, hvis man tager et gennemsnit over hele systemet. Derudover konkluderer vi, at en kritisk tæthed af urenheder under de rette omstændigheder kan hæve den kritiske nematiske temperatur. Inspireret af ideen om nematisk orden genereret fra nærmeste-nabo-vekselvirkninger, udfører vi et grundigt symmetri- og middelfelt-studie af sådanne vekselvirkninger

og konkluderer, i kontrast til tidligere studier, at den ledende lav-temperatur-ordensparameter har interorbital $d_{xz} - d_{xy}$ karakter. Denne ordensparameters specifikke form giver anledning til et hybridiseringsgab, der kan fjerne Y-lommen fra Fermi-niveauet i 1-Fe-enhedscellen, hvilket lader til at stemme overens med tidligere eksperimenter. Fra denne meget anisotrope båndstruktur udregner vi det resulterende superledendegab, som også lader til at stemme overens med eksperimenter. Til sidst diskuterer vi uoverensstemmelser mellem vores beregnede spin-susceptibiliteter og de tilgængelige resultater fra neutronsprengningseksperimenter samt den nødvendige inklusion af orbital-afhængige kvasipartikel-vægte.

I den sidste del af denne afhandling begiver vi os videre og studerer topologisk superledning induceret af magnetiske teksturer i multi-orbitale systemer. Vi demonstrerer en alternativ vej til at opnå Majorana-nultilstande, ved at fange disse i singulære hvirvler i magnetiske teksturer. De diskuterede magnetiske teksturer antages at sameksistere eller at være tæt koblet til en "nodal" superleder. På trods af at dette studie er motiveret af de jernbaserede superledere, som potentielt kan have magnetisk sameksistens med superledning, holder vi vores diskussion generel, og den kan derfor anvendes på en bred klasse af hybrid-strukturer og superledere. Til sidst klassificerer vi topologiske faser induceret af magnetiske teksturer uden singulære hvirvler. Ved at tage højde for de symmetrier forbundet med de magnetiske teksturer og ved at tillade en generel multibånd spin-singlet superledning, finder vi en overflod af topologiske faser, hvilket fører til flade, uni- og bi-retningsbestemte, (kvasi-)spirale og kirale Majoranakanttilstande.

Acknowledgements

During my time as a Ph.D. student in the Condensed Matter Theory (CMT) group at the Niels Bohr Institute, University of Copenhagen, I would first and foremost like to thank the Carlsberg Foundation for financial support. Secondly, I would like to express my sincere gratitude to my principal Ph.D. advisor Prof. Brian Møller Andersen, for his never-ending support, patience and critical questioning. Through tough, but also good times, his guidance helped me in my research and to arrive at the finalized version of this thesis. – *Tak ska' du ha'!*

A special thanks to the Institute of Theoretical Physics at the Chinese Academy of Sciences in Beijing for hosting me during my three months abroad. My time in Beijing was both challenging, exciting and fun, and would not have been the same without Yun-Peng Huang, Junang Wang, Dr. Tilen Cadez, and Prof. Panagiotis Kotetes. A great *xiè xiè* goes out to you and your brokers! Also thanks to Prof. Hongqi Xu at Peking University, and Prof. Xinqi Li at Tianjin University for inviting and hosting us.

I would also like to thank Prof. Peter J. Hirschfeld, Prof. Indranil Paul, Dr. Kristofer Björnsson, Dr. Morten H. Chistensen, Dr. Andreas Kreisel, Dr. Astrid T. Rømer, Dr. Daniel D. Scherer, Clara N. Breiø, Raffael Gawatz and Hano O. M. Sura for challenging, rewarding and enlightening discussions. Over the course of the last three years, the CMT group has been a pleasant work environment with great facilities and people. I have been especially fond of the CMT Bouldering Club, which helped clear my head after a full day of physics. Thanks to all of you for creating a pleasant daily rut. An additional special thanks to Prof. Panagiotis Kotetes, for always lending a helping hand, and for the (sometimes constructive) criticism. I still owe you a tub of gin, if not a couple of tubs. – *Tak P(olemarch)*.

Thanks to my dear friends and family for supporting me in all these years, and for always being there for me. It means more than you know, and for that, I am grateful. Especially thanks to Stine Rusmann for being my lovely everyday rock, and to Anna Rusmann for helping me write the abstract in danish, which turned out to be way harder than expected!

Lastly, I am greatly indebted to caffeine from pour-over coffee and Thugger's pitchy tunes. Thanks for keeping me (in)sane in the writing process of this thesis.



Daniel Steffensen
Snekkersten, February 2021

Contents

Introduction	1
I Nematic and Superconducting Phases of Multi-Orbital Systems	7
1 A Symmetry Perspective on Multi-Orbital Systems	9
1.1 Non-Spatial Symmetries	10
1.2 Spatial Symmetries	12
Appendices for Chapter 1	23
1.A MF Decoupling and Wave-Vector Representation of the Prototypical Hamiltonian . . .	23
1.B Symmetries of Anomalous Terms	25
2 Disorder-Induced Electronic Nematicity	31
2.1 Introduction	31
2.2 Phenomenological Landau Approach	33
2.3 Microscopic Model and Self-Consistent Calculations	35
2.4 Summary	38
Appendices for Chapter 2	41
2.A Landau Theory: Phenomenological Analysis	41
2.B Interaction in the Nematic Channel and Mean-Field Theory Decoupling	43
2.C Landau Theory: Microscopic Analysis	44
2.D Self-Consistent Calculation of the Nematic Order Parameter	45
2.E Disorder-Modified Stoner Criterion and the Resulting $T_{\text{nem}}^{\text{imp}}$	45
3 Inter-Orbital Nematicity in FeSe	49
3.1 Introduction	49
3.2 Model and Method	51
3.3 Results	53
3.4 Discussion and Conclusions	61
Appendices for Chapter 3	65
3.A Details on Bond-Order Fields and Self-Consistent Calculations	65
3.B Irreducible Representation of Bond-Order Fields	68
3.C Susceptibility and Pairing from a Partially Incoherent Electronic Structure	74

II	Topological Phases of Multi-Orbital Systems	81
4	Majorana Zero Modes in Magnetic Texture Vortices	85
4.1	Introduction	85
4.2	Microscopic Continuum Model	86
4.3	Topological Invariants and Numerical Results	88
4.4	Summary and Conclusions	92
	Appendices for Chapter 5	95
4.A	Derivations for the w_3 and \mathcal{C}_2 Topological Invariants	95
4.B	Additional Numerical Investigations for BDI, D, and DIII Class Models	96
5	Topological Superconductivity Induced by Magnetic Textures	101
5.1	Introduction	101
5.2	Summary of our Topological Classification Results	105
5.3	Modeling Considerations	108
5.4	1D Topological Superconductors	110
5.5	2D Topological Superconductors	123
5.6	Conclusions and Outlook	146
	Appendices for Chapter 6	153
5.A	Summarizing Tables of Topological Invariants	153
5.B	Sublattice Formulation in 1D	154
5.C	Space Group Symmetry-Protected Degeneracies	155
5.D	Details on Topological Invariants	157
5.E	Functions for the representation of the BdG Hamiltonian in 2D	162
	Conclusions and Outlook	165
	Bibliography	169

“More is different”

– Phillip W. Anderson

Introduction

We set the scene for this thesis, with the celebrated quote made in 1972 by the late Phillip W. Anderson [1]. This quote not only challenges the reductionist approach to science, it also manifests one of the cornerstones of condensed matter physics. Namely that the synergy of a great number of degrees of freedom spontaneously can lead to a less symmetrical state, compared to that of its individual constituents. A well-established example of this, is the crystalline ordering of atoms, where the continuous translations and rotations of the initial collection of atoms are reduced to the discrete symmetries of the formed crystal lattice. Fittingly, such types of phase transitions are referred to as spontaneous symmetry breaking [2], since the system displays a spontaneously-generated symmetry breaking ground state, although the equations of motion are perfectly symmetrical. Other, perhaps more exotic, examples of spontaneous phase transitions are nematic [3], ferromagnetic [4] and superconducting [5] phases, which are respectively breaking rotational, continuous spin rotational, and local $U(1)$ symmetry. Although these phases appear more abstract, compared to that of crystalline order, the underlying principle is the same, namely symmetries. The essence of spontaneous symmetry breaking is in fact to identify which of the underlying symmetries that get broken, but also to predict and recognize the symmetries and physical ramifications of the newly established ground state.

Another important, yet relatively new, facet of condensed matter physics is the study of topological phases of matter, where physics now join forces with the mathematical concept of topology, to predict new and exotic states in many-body systems. In general terms, topology in mathematics is concerned with properties of geometrical objects, that do not change under continuous deformations [6]. Geometrical objects that are classified as topologically equivalent carry the same topological index, i.e. an integer which does not change upon smooth deformations of the object. The stereotypical example of such an index, is the genus g , e.g. a sphere has $g = 0$, while a torus has $g = 1$, making it impossible to smoothly deform a ball into a doughnut, in contrast to a mug and a doughnut which are topologically equivalent. In the same way, can classes of Hamiltonians be characterized by a robust topological invariant with respect to band structure singularities, or vortices of complex fields [7, 8]. Note that Hamiltonians falling into the same topological class, need not to describe the same physical systems, as long as they are all adiabatically interconnected. One of the consequence of a system exhibiting a non-trivial topological invariant, is the manifestation of topologically-protected fractionalized excitations at interfaces where the topological invariant changes abruptly, e.g. the soliton mass of the Dirac particle in the Jackiw-Rebbi model [9], at the ends of a polyacetylene chain in the Su-Schrieffer-Heeger model [10], at the edges of a two-dimensional quantum Hall system [11], in vortices of a chiral $p + ip$ superconductor [7, 8, 12], at the ends of a one-dimensional spinless p -wave superconductor [13] and at the edges of a two-dimensional system displaying the spin quantum Hall effect [14–18].

The novelty and importance of topological phases were in 2016 acknowledged by the Nobel Com-

mittee, by granting the Nobel prize in physics to David J. Thouless, F. Duncan M. Haldane and J. Michael Kosterlitz, for their founding work on the subject [19–23]. Despite the fact that the first topological phase was experimentally observed in the integer quantum Hall effect in 1980 by von Klitzing *et al.* [11], it was only much later, around the time of the theoretical and experimental discovery of time-reversal invariant topological insulators [14–18], that the field caught the attention of the broader physics community. This led the way for a more systematic approach in classifying topological systems, based on three discrete non-spatial symmetries [24–26]. This classification further laid the foundation for a multitude of classification schemes, that now also include topological defects [27], point group symmetries [28, 29], gapless phases [30, 31] and nonsymmorphic space group symmetries [32]. Further effort was put into developing an alternative classification scheme relying on the crystalline structure of the system, rather than the symmetries of the Hamiltonian, since the former often is directly accessible in experiments. This resulted in the theory of topological quantum chemistry [33], and was recently extended to include also magnetic materials [34]. Similarly, a classification of Bogoliubov-de Gennes (BdG) Hamiltonians, based on symmetry indicators, was also developed [35, 36]. From all these classification schemes, it is evident that symmetries also here play an indispensable role in finding and predicting new topological phases of matter, similar to the case of spontaneously generated phases discussed above. Note, however, the distinction that here the symmetries are used as tools to identify topological phases, and are not broken when entering a topological non-trivial phase.

Motivated by the important role that symmetries play in predicting novel phases of matter, we set out to study a general class of Hamiltonians, which can potentially demonstrate both spontaneous symmetry breaking behavior, topological phase transitions and an intricate interplay between the two. Let us here define the general structure of the prototypical Hamiltonian to be studied throughout this thesis, and connect it to relevant physical systems later in this chapter. To this end, we introduce the typical many-body Hamiltonian describing condensed matter systems [37]

$$H = H_{\text{el}} + H_{\text{ion}} + H_{\text{el-ion}}. \quad (1)$$

The terms describe the dynamics of the electrons, ions and interactions between electrons and ions, respectively. We will restrict our study to concern only the electronic degrees of freedom, H_{el} , and assume the ions to have reached their equilibrium position, thus only serving as an underlying periodic potential. The Hamiltonian of interest can therefore be approximated to take the form

$$H \sim \int d\mathbf{r} \psi_{\sigma}^{\dagger}(\mathbf{r}) T(\mathbf{r}) \psi_{\sigma}(\mathbf{r}) + \frac{1}{2} \int d\mathbf{r} \int d\mathbf{r}' \psi_{\sigma}^{\dagger}(\mathbf{r}) \psi_{\sigma'}^{\dagger}(\mathbf{r}') V(\mathbf{r} - \mathbf{r}') \psi_{\sigma'}(\mathbf{r}') \psi_{\sigma}(\mathbf{r}), \quad (2)$$

where $V(\mathbf{r} - \mathbf{r}')$ is the Coulomb interaction potential, $T(\mathbf{r})$ is the matrix element of the single particle operator containing the underlying periodic potential and $\psi_{\sigma}(\mathbf{r})$ annihilates an electron at position \mathbf{r} with spin-projection σ . Note that throughout this thesis, summation over repeated spin and/or orbital indices is implied. There are in general two ways of treating the influence of the underlying crystalline potential, either in the nearly free electron approximation or the tight-binding approximation. For the latter approach, one utilizes the orthonormality of the localized Wannier functions $\langle \mathbf{R}\mu | \mathbf{r} \rangle$, where μ labels the Wannier orbital and \mathbf{R} denotes the lattice centers of the given Bravais lattice. By adopting this approach, we can expand the fermionic field operators in the Wannier functions, in the following

way $\psi_\sigma(\mathbf{r}) = \sum_{\mathbf{R}} \langle \mathbf{R} \mu | \mathbf{r} \rangle c_{\mathbf{R} \mu \sigma}$, and arrive at the Hamiltonian

$$H = - \sum_{\mathbf{R}, \mathbf{R}'} c_{\mathbf{R} \tilde{\mu}}^\dagger (t_{\mathbf{R}, \mathbf{R}'}^{\tilde{\mu} \tilde{\nu}} + \mu_0 \delta_{\mathbf{R}, \mathbf{R}'} \delta_{\tilde{\mu}, \tilde{\nu}}) c_{\mathbf{R}' \tilde{\nu}} + \frac{1}{2} \sum_{\mathbf{R}, \mathbf{R}'} c_{\mathbf{R} \tilde{\mu}_2}^\dagger c_{\mathbf{R}' \tilde{\mu}_4}^\dagger [V_{\mathbf{R}, \mathbf{R}'}]_{\tilde{\mu}_4 \tilde{\mu}_3}^{\tilde{\mu}_2 \tilde{\mu}_1} c_{\mathbf{R}' \tilde{\mu}_3} c_{\mathbf{R} \tilde{\mu}_1}, \quad (3)$$

where we adopted the compact notation $\tilde{\mu}_1 = \{\mu_1, \sigma_1\}$ for spin σ_1 and orbital μ_1 . By strictly relying on the tight-binding approximation, the above Hamiltonian appears to be suitable for describing electrons tightly bound to the ion cores of the Bravais lattice, as for example seen in crystals composed of transition metals. In such materials, the interaction strength is usually approximated by on-site interactions only, and we thus see that the Hamiltonian within this approximation is nothing but the multi-orbital generalization of the notorious Hubbard model [38]. Despite its simple form, the Hubbard model has proven to display a multitude of fascinating phenomena in condensed matter physics, such as anti-ferromagnetic order through superexchange [39], Mott insulating phases [40] and unconventional high-temperature superconductivity. As a consequence, the Hubbard model laid much of the foundation for the study of correlated materials, and is believed to be the underlying model describing the phase diagram of the cuprate high-temperature superconductors, originally discovered in 1986 by Bednorz and Müller [41]. The importance of the multi-orbital generalization of the Hubbard model later became apparent by the discovery of unconventional superconductivity in Sr_2RuO_4 [42], iron-based superconductors (FeSCs) [43] and recently in nickelates [44]. These are all transition metal materials believed to exhibit normal state Fermi surfaces with substantial multi-orbital content, rendering the multi-orbital Hubbard model, if nothing else, an adequate starting point in describing these materials.

Of particular interest in this thesis are the FeSCs, which are known to host complex phase diagrams with nematicity [45–63], magnetism [64–77], superconductivity [78, 79] and macroscopic coexistence of magnetism and superconductivity [66, 80–85]. The discovery of this new class of materials in 2006 [43] brought a great deal of excitement to the community, since the FeSCs appeared to be the perfect platform for testing our knowledge of correlated materials, and the various theories developed in the context of superconductivity in cuprates. For example, both cuprates and FeSCs have phase diagrams with the superconducting phase emerging in proximity to a magnetic phase, which advocates for the electron pairing to be mediated by spin fluctuations. Now, more than a decade later, a broad consensus regarding the gap structure in FeSCs has been established, nonetheless, the iron-chalcogenide FeSe does not immediately fit into this picture. First off, in FeSe superconductivity condenses from a nematic, rather than a magnetic, phase, in contrast to the usual FeSCs. This challenges the spin fluctuation mediated pairing paradigm, but also poses the questions of the microscopic origin of the nematic order. Furthermore, although nematic phase transitions are seen throughout the family of FeSCs, in FeSe it seems to drastically alter the Fermi surface (FS) [61–63], and thereby the resulting gap structure [86]. Lastly, and perhaps more importantly, FeSe can under the right manipulations, such as intercalation, single layer deposition on substrates, and pressure, produce some of the highest critical temperatures in the FeSC family. The latter property strongly calls for a deeper understanding of this material, its electronic phases, and the underlying principles governing correlated materials.

In addition, growing evidence point to the FeSCs, more specifically $\text{FeTe}_{0.55}\text{Se}_{0.45}$, as being the sought-after case of an intrinsic topological superconductor [87–91]. It is argued that Te-doping of FeSe allows for a topological band inversion to take place along the ΓZ direction in the 3D Brillouin zone (BZ), ultimately resulting in helical Dirac surface states. Upon reaching the critical temperature

T_c , these surface bands are then believed to be “self-proximitized” and gapped out by bulk superconductivity. If the latter is indeed the case, $\text{FeTe}_{0.55}\text{Se}_{0.45}$ might just be an intrinsic manifestation of the Fu-Kane proposal [12], which has been theoretically proven to host the coveted Majorana zero modes (MZMs) in vortices of the superconducting order parameter. In recent years, the MZMs, and topological superconductors in general, have been under intensive investigation. The reason for this, is that the MZMs are predicted to be spatially localized, topologically protected, charge neutral and governed by exotic exchange statistics. Combined, all these properties render MZMs key components in fault-tolerant quantum computations [92–94]. Moreover, the prospect of intrinsic topological superconductivity in $\text{FeTe}_{0.55}\text{Se}_{0.45}$ has paved the way for numerous proposals for achieving topological phases in FeSCs [95–100], but it has also motivated a search for topological phases in similar materials beyond the FeSCs, such as noncentrosymmetric superconductors [101] and magnetic materials. Cases similar to the later has been extensively studied in the past [102–125], since, in certain scenarios, magnetic textures can display all the necessary ingredients for a topological non-trivial phase. Once again the FeSCs appear as prime candidates, since they can display microscopic coexistence of magnetism and superconductivity [66, 80–85].

From the above, it appears that multi-orbital systems offer a versatile platform for studying symmetry breaking phase transitions, e.g. nematic and superconducting order in FeSe, but also to study new topological phases generated from the interplay between the spontaneously generated order parameters, e.g. topological superconductivity induced by magnetic textures. In this respect, our starting point for this thesis is the many-body Hamiltonian in eqn. (3), however, for the purpose of studying the various effects addressed above, we perform a general mean-field (MF) decoupling in the particle-hole and particle-particle channels (for further details see app. 1.A) and arrive at the following Hamiltonian

$$\begin{aligned}
H^{\text{MF}} = & - \sum_{\mathbf{R}, \mathbf{R}'} c_{\mathbf{R}\bar{\mu}}^\dagger (t_{\mathbf{R}, \mathbf{R}'}^{\bar{\mu}\bar{\nu}} + \mu_0 \delta_{\mathbf{R}, \mathbf{R}'} \delta_{\bar{\mu}, \bar{\nu}}) c_{\mathbf{R}'\bar{\nu}} + \sum_{\mathbf{R}, \mathbf{R}'} c_{\mathbf{R}\bar{\mu}}^\dagger ([N_{\mathbf{R}}]^{\bar{\mu}\bar{\nu}} \delta_{\mathbf{R}, \mathbf{R}'} + [N_{\mathbf{R}, \mathbf{R}'}]_{\bar{\nu}}^{\bar{\mu}}) c_{\mathbf{R}'\bar{\nu}} \\
& + \frac{1}{2} \sum_{\mathbf{R}, \mathbf{R}'} (c_{\mathbf{R}\bar{\mu}}^\dagger [\Delta_{\mathbf{R}, \mathbf{R}'}]_{\bar{\nu}}^{\bar{\mu}} c_{\mathbf{R}'\bar{\nu}}^\dagger + \text{h.c.}) + \text{const.}
\end{aligned} \tag{4}$$

where we introduced the direct and exchange fields $[N_{\mathbf{R}}]^{\bar{\mu}\bar{\nu}}$ and $[N_{\mathbf{R}, \mathbf{R}'}]_{\bar{\nu}}^{\bar{\mu}}$, respectively, and the superconducting order parameter $[\Delta_{\mathbf{R}, \mathbf{R}'}]_{\bar{\nu}}^{\bar{\mu}}$. In general, these fields can be non-zero, depending on the specifics of the system, and potentially lead to a less symmetrical system, i.e. a spontaneous symmetry breaking. We argue that the above Hamiltonian is the most general form of the class of Hamiltonians we wish to study, since the density fields, depending on the interaction potential, can give rise to magnetic order, band renormalizing terms, electronic nematic order and so much more, making it the perfect starting point for this thesis. We will thus henceforth refer to H^{MF} as the prototypical Hamiltonian, as we will study various cases of it in the upcoming chapters. In particular, we focus our study on nematic order in FeSe, and topological superconductivity in multi-orbital systems induced by magnetic textures.

Thesis Outline

This thesis mainly revolves around the nematic and topological superconducting phases of the prototypical Hamiltonian in eqn. (4), and is bisected accordingly into the following parts

I Nematic and Superconducting Phases of Multi-Orbital Systems

This part of the thesis commences with an introductory chapter, chap. 1, on all the relevant symmetry tools and types of symmetries, i.e. non-spatial symmetries and (non)symmorphic space groups, relevant throughout this work. In chap. 2 we proceed and make use of these tools, by studying the effects of disorder in systems close to an electronic nematic instability. Previous studies have shown that nearest-neighbor (NN) Coulomb interactions can generate intra-orbital nematic order in mono-layer FeSe [126, 127]. This specific type of nematic order is directly applicable to the phenomenological theory parts of chap. 2. Lastly, in chap. 3 we perform a thorough case study of nematic order generated by NN interactions in bulk FeSe, and its consequences on the spin susceptibility and superconducting order parameter. We find two consecutive phase transitions, with the low-temperature order being of an inter-orbital nematic type. From this newly established nematic phase, we calculate the spin susceptibility and leading gap structure by including additional self-energy effects, and try to reconcile these with experimental findings.

II Topological Phases of Multi-Orbital Systems

This part of the thesis relies on the topological symmetry classification scheme, based on a generalization of the three non-spatial symmetries discussed in chap. 1. In chap. 4 we make use of this classification scheme, by employing it on systems with singular vortices in magnetic textures which either coexisting or in proximity to a nodal superconductors. We study a paradigmatic continuum model, calculate the associated topological invariants, and confirm our findings through numerical calculations. Furthermore, in chap. 5 we perform an extensive topological symmetry classification of topological superconductivity induced by magnetic textures, in the absence of singular defects. We find the underlying symmetry of the magnetic texture and superconducting gap to play an essential role in the classification. In the last chapter, titled **Conclusions and Outlook**, we finally present our conclusions and suggestions for future directions.

Note lastly that this thesis by no means is a monograph, and is thus primarily based on my manuscripts and published papers, as indicated by the infoboxes in the upcoming chapters. The manuscripts and papers have unavoidably been subjected to minor modifications and changes, in order to fit the format and overall narrative of this thesis.

Part I

Nematic and Superconducting Phases of Multi-Orbital Systems

1

A Symmetry Perspective on Multi-Orbital Systems



Info: This chapter is in part based on the my master’s thesis [“[Topological Magnetic Superconductors](#),” [University of Copenhagen \(2017\)](#)] and various books and lecture notes on symmetries in condensed matter physics [129–141].

As it was already pointed out in the introductory chapter of this thesis, the concept of symmetries plays a fundamental role in not only condensed matter physics, but physics in general. Throughout time it has cemented its importance by revealing fundamental concepts in physics, such as conservation laws [142], identification of fundamental particles in relativistic quantum mechanics [143] and spin statistics in quantum mechanics [144], just to name a few. In addition to these, symmetries also serve as useful tools for reducing the complexity of a given calculation, allow us to study symmetry-equivalent systems phenomenologically, to identify symmetry-allowed terms in a given Hamiltonian, and so much more. We will therefore in this chapter introduce the here-relevant symmetries and symmetry-related tools, employed throughout the upcoming chapters. Note that this chapter is mainly based on textbooks, and can thus be skipped by the seasoned reader.

We set out to study the symmetries of the prototypical Hamiltonian presented in eqn. (4), and we will therefore focus our discussion on Hamiltonians bilinear in fermionic operators. Instead of disclosing only the symmetry aspects of eqn. (4), we extend our study to the more generalized version of the Hamiltonian, namely

$$H = H_{\text{norm}} + H_{\text{anom}} = \sum_{i,j} c_i^\dagger \mathcal{H}_{ij} c_j + \frac{1}{2} \sum_{i,j} \left(c_i^\dagger \mathcal{A}_{ij} c_j^\dagger + \text{h.c.} \right), \quad (1.1)$$

where \mathcal{H}_{ij} are matrix elements of the single-particle Hamiltonian \mathcal{H} , while \mathcal{A}_{ij} describes the anomalous terms arising in e.g. the mean-field theory of superconductors. The above form of H , besides being more general, also greatly simplifies the notation in the upcoming sections and can at any time be mapped to eqn. (4) by identifying the indices i, j with the appropriate electronic degrees of freedom, e.g. $i = \{\mathbf{R}\mu\sigma\}$. In general, a Hamiltonian is said to display the symmetry O , if the commutation relation $[H, O] = 0$ is satisfied. Here O refers to a general symmetry operator, i.e. either a linear and unitary, or antilinear and antiunitary operator acting on the Hilbert space [129, 130]. We denote the former by U , while the latter can be represented as $A = U_A K$, where U_A is the unitary part of A , while K is the action of complex conjugation. In the upcoming sections, we will focus on symmetry properties of the normal state Hamiltonian H_{norm} , while app. 1.B is devoted to the anomalous terms \mathcal{A}_{ij} entering in H_{anom} . These terms have to be treated more carefully, since they are not simply matrix elements of some single-particle operator $\mathcal{A}_{ij} \neq \langle i | \mathcal{A} | j \rangle$, where $\{|i\rangle\}$ is the set of single-particle basis states generated from the vacuum $c_i^\dagger |0\rangle$. Furthermore, in app. 1.B we also employ the BdG formalism, and introduce a convenient spinor to facilitate a more transparent symmetry study of a Hamiltonian containing both \mathcal{H}_{ij} and \mathcal{A}_{ij} , which will come in handy in part II of this thesis. Lastly, before proceeding, we want to emphasize that on the single-particle level, it is well-known that \mathcal{H} can be represented as a matrix, denoted here by $D[\mathcal{H}]$, with the matrix elements $D[\mathcal{H}]^{ij} = \langle i | \mathcal{H} | j \rangle$.

The remainder of this chapter is organized as follows. In sec. 1.1 we discuss the so-called non-spatial symmetries, which play a fundamental role in the topological symmetry classification scheme. Then, in sec. 1.2 we introduce and discuss the more familiar set of spatial symmetries, and some of their group-related properties.

1.1 Non-Spatial Symmetries

The set of non-spatial symmetries, as the name indicates, are symmetry operations that leave the real space lattice vector \mathbf{R} invariant, specifically

$$O\mathbf{R} = \mathbf{R}, \quad \text{thus} \quad O \in \text{Non-spatial symmetry.} \quad (1.2)$$

As a consequence of the above, these symmetries are often treated on a more fundamental level, since they do not rely on the formation of an underlying periodic lattice potential, and can generally also be present in completely disordered systems. In fact, non-spatial symmetries are the fundamental elements of the topological symmetry classification [24–26], which we will employ in part II of this thesis. Related to the topological properties, these symmetries also reveal general properties and symmetry-protected degeneracies of the energy spectrum, that can be utilized to simplify various calculations. In the upcoming we will discuss three essential physical realizations of non-spatial symmetries, namely time reversal T , charge conjugation C and chiral symmetry S .

Time Reversal Symmetry

The action of time reversal T , also referred to as the reversal of motion [129, 130, 136], inverts the sign of the time coordinate $t \rightarrow -t$. In Newtonian mechanics this obviously leaves the equations of motion invariant in the absence of dissipative forces, allowing for simultaneous solutions with opposite time coordinates [145]. In quantum mechanics, however, the dynamics are described by the

Schrödinger equation, a linear differential equation in time, implying that the action of $t \rightarrow -t$ alone does not suffice. Nonetheless, by considering the canonical commutation relation between position and momentum, combined with the action of time reversal on t and \mathbf{r} , it is straightforward to show that T must be anti-unitary in the quantum mechanical description, since

$$T[\mathbf{r}, \mathbf{p}]T^{-1} = -[\mathbf{r}, \mathbf{p}] = T\mathbf{i}T^{-1}, \quad \text{thus} \quad T = U_T K. \quad (1.3)$$

After having established the anti-unitarity of T , we can now proceed and see how T affects the normal part of the Hamiltonian in eqn. (1.1). In order to do so, we first need to consider how the fermionic operators c_i transform under time reversal. Since the reversal of time is only expected to alter the electronic degrees of freedom, i.e. momentum, spin etc., we expect the following general transformation [25, 26, 146, 147]

$$Tc_iT^{-1} = \sum_j \langle i|U_T^\dagger|j\rangle c_j, \quad \text{and} \quad Tc_i^\dagger T^{-1} = \sum_j c_j^\dagger \langle j|U_T|i\rangle. \quad (1.4)$$

By implementing the above, we find that H_{norm} is time-reversal invariant if the following is satisfied

$$\begin{aligned} H_{\text{norm}} = TH_{\text{norm}}T^{-1} &= \sum_{l,i} \sum_{j,k} c_l^\dagger \langle l|U_T|i\rangle \langle i|\mathcal{H}|j\rangle^* \langle j|U_T^\dagger|k\rangle c_k, \\ &\Rightarrow D[\mathcal{H}] = D[U_T]D^\dagger[\mathcal{H}]D^\dagger[U_T]. \end{aligned} \quad (1.5)$$

Thus, on the single-particle level time reversal is nothing but a transposition of $D[\mathcal{H}]$, followed by a unitary transformation. The fact that T commutes with the Hamiltonian, hints at the possibility of symmetry-protected degeneracies. However, since T is anti-unitary, the conventional representation theory does not hold, and one needs to adopt the so-called co-representation [34, 129, 130, 148–150]. Leaving aside the symmetry-protected degeneracies for sec. 1.2, we can still conclude this paragraph with the general relation between time-reversal-related eigenstates of \mathcal{H} , namely that these have the same eigenenergies

$$\mathcal{H}|\alpha\rangle = E_\alpha |\alpha\rangle, \quad \mathcal{H}T|\alpha\rangle = T\mathcal{H}|\alpha\rangle = E_\alpha T|\alpha\rangle. \quad (1.6)$$

Charge Conjugation Symmetry

Another important non-spatial symmetry is charge conjugation, also referred to as particle-hole symmetry in condensed matter physics. The role of this symmetry is to interchange particles with their corresponding anti-particles, thus manifesting itself by swapping creation and annihilation operators, in the following way [26, 146, 147]

$$Cc_iC^{-1} = \sum_j c_j^\dagger \langle j|U_C|i\rangle, \quad \text{and} \quad Cc_i^\dagger C^{-1} = \sum_j \langle i|U_C^\dagger|j\rangle c_j. \quad (1.7)$$

While the above bear similarities with the transformation of the fermionic operators under T , the crucial distinct is that C is unitary $C = U_C$, which can be shown by applying C to the canonical commutation relation between position and momentum. Ultimately, this leads to the following relation for C -symmetric systems

$$\begin{aligned} H_{\text{norm}} = CH_{\text{norm}}C^{-1} &= - \sum_{l,i} \sum_{j,k} c_k^\dagger \langle k|U_C|j\rangle \langle j|\mathcal{H}|i\rangle^* \langle i|U_C^\dagger|l\rangle c_l + \sum_i \langle i|\mathcal{H}|i\rangle, \\ &\Rightarrow D[\mathcal{H}] = -D[U_C]D^\dagger[\mathcal{H}]D^\dagger[U_C]. \end{aligned} \quad (1.8)$$

Surprisingly, in the single-particle representation we conclude that C effectively acts as an anti-unitary operator $C \rightarrow D[U_C]K$, as a consequence of fermionic statistics. Furthermore, we conclude that the single-particle Hamiltonian $D[\mathcal{H}]$ is charge-conjugation symmetric, if $D[\mathcal{H}]$ anti-commutes with $D[U_C]K$. The latter puts the constraint on the energy spectrum, that every energy comes in pairs $\pm E_\alpha$, since the charge conjugation related eigenstates $\{|\alpha\rangle, C|\alpha\rangle\}$ of \mathcal{H} have the following eigenequations

$$\mathcal{H}|\alpha\rangle = E_\alpha |\alpha\rangle, \quad \mathcal{H}C|\alpha\rangle = -C\mathcal{H}|\alpha\rangle = -E_\alpha C|\alpha\rangle. \quad (1.9)$$

Chiral Symmetry

If both T and C are symmetries of the Hamiltonian H_{norm} , then their product $S = CT$ must also be a symmetry $[H_{\text{norm}}, S] = C[H_{\text{norm}}, T] + [H_{\text{norm}}, C]T = 0$. Note that this commutation relation can alternatively be written in terms of anticommutators $[H_{\text{norm}}, S] = \{H_{\text{norm}}, C\}T - C\{H_{\text{norm}}, T\}$, implying that if both T and C is broken, then the system can in fact still exhibit the symmetry S . In the topological symmetry classification community S is termed the chiral symmetry, while in molecular electronics it is often referred to as the sub-lattice symmetry, since it naturally appears in alternant/bipartite molecules [151–153], e.g. in the Su-Schrieffer-Heeger model [10]. By straightforwardly inferring the results for T and C , we get that the fermionic operators are transformed by S in the following way

$$Sc_i S^{-1} = \sum_{j,l} \langle i|U_T^\dagger|l\rangle \langle l|U_C^\dagger|j\rangle^* c_j^\dagger, \quad \text{and} \quad Sc_i^\dagger S^{-1} = \sum_{j,l} c_j \langle j|U_C|l\rangle^* \langle l|U_T|i\rangle, \quad (1.10)$$

which leads to the following criteria for H_{norm} to display the symmetry S

$$\begin{aligned} H_{\text{norm}} = SH_{\text{norm}}S^{-1} &= - \sum_{l,i} \sum_{j,k} c_k^\dagger \langle k|U_S|j\rangle \langle j|\mathcal{H}|i\rangle \langle i|U_S^\dagger|l\rangle c_l + \sum_i \langle i|\mathcal{H}|i\rangle, \\ &\Rightarrow \quad D[\mathcal{H}] = -D[U_S]D[\mathcal{H}]D^\dagger[U_S]. \end{aligned} \quad (1.11)$$

Hence, in the single-particle representation S simply acts a unitary operator $D[U_S] = D[U_C]D^*[U_T]$, and is only a symmetry of H_{norm} , if it anticommutes with the single-particle Hamiltonian \mathcal{H} . Similar to the charge conjugation symmetry, S also leads to an energy spectrum where for every eigenenergy E_α there is a state with energy $-E_\alpha$, as seen from the simple relations

$$\mathcal{H}|\alpha\rangle = E_\alpha |\alpha\rangle, \quad \mathcal{H}S|\alpha\rangle = -S\mathcal{H}|\alpha\rangle = -E_\alpha S|\alpha\rangle. \quad (1.12)$$

Although this energy relation shares similarities with the one for C -symmetric systems in eqn. (1.9), we note the major distinction that S is unitary in the single-particle representation, while C is anti-unitary. This distinction allows us to pick a basis for which S is diagonal and \mathcal{H} is off-diagonal, as a consequence of the anti-commutation relation $\{\mathcal{H}, S\} = 0$. This off-diagonal structure of \mathcal{H} can then be utilized for calculating the so-called topological winding number [26], see chap. 4 and 5, but also to predict chiral symmetry-protected zero-energy states [151, 153–155].

1.2 Spatial Symmetries

Now we turn our attention to the probably more familiar class of symmetries, namely the spatial symmetries. Such symmetries, in contrast to their non-spatial counterparts discussed in sec. 1.1, will

in general transforms the real space lattice vector \mathbf{R} in the following way

$$O\mathbf{R} = g\mathbf{R} + \mathbf{t}, \quad \text{thus} \quad O \in \text{Spatial symmetry.} \quad (1.13)$$

We see that the operation of O consecutively transforms the real space lattice vector under the action of g , an unitary or antiunitary operator, followed by a translation of \mathbf{t} . In order to emphasize this combination of g and \mathbf{t} , it is often appropriate to adopt the more transparent Seitz notation $O = \{g | \mathbf{t}\}$.

In order to explore the consequences of spatial symmetries, we must first pin down how these transform the Hamiltonian in question, specifically we need to consider the operation of O on the fermionic operators. In the case of a unitary spatial operator $O = U$, we get the following transformations

$$Uc_iU^{-1} = \sum_j \langle i|U^\dagger|j\rangle c_j, \quad \text{and} \quad Uc_i^\dagger U^{-1} = \sum_j c_j^\dagger \langle j|U|i\rangle, \quad (1.14)$$

which readily leads to

$$H_{\text{norm}} = UH_{\text{norm}}U^{-1} = \sum_{l,i} \sum_{j,k} c_l^\dagger \langle l|U|i\rangle \langle i|\mathcal{H}|j\rangle \langle j|U^\dagger|k\rangle c_k, \quad \Rightarrow \quad D[\mathcal{H}] = D[U]D[\mathcal{H}]D^\dagger[U]. \quad (1.15)$$

As expected, the action of U on the single-particle level, is nothing but an unitary transformation of \mathcal{H} . Now, applying the same logic for a spatial antiunitary operator $O = A = U_A K$, we arrive at the familiar relation

$$\begin{aligned} H_{\text{norm}} &= AH_{\text{norm}}A^{-1} = \sum_{l,i} \sum_{j,k} c_l^\dagger \langle l|U_A|i\rangle \langle i|\mathcal{H}|j\rangle^* \langle j|U_A^\dagger|k\rangle c_k, \\ &\Rightarrow \quad D[\mathcal{H}] = D[U_A]D^\dagger[\mathcal{H}]D[U_A], \end{aligned} \quad (1.16)$$

akin to the action of time-reversal on $D[\mathcal{H}]$, cf. eqn. (1.5), with the distinction that T leaves the real space lattice vector invariant, while A is a spatial symmetry. In fact, the similarities between T and the antiunitary spatial symmetry operator A stem from the fact that in physical systems, specifically magnetic materials, A generally consist of a spatial unitary operator U combined with T , i.e. $A = UT = UU_T K \equiv U_A K$.

In general, the Hamiltonian H_{norm} will not only be left invariant under a single spatial symmetry O , but a whole set, denoted here $\mathcal{O} = \{O_0, O_1, \dots, O_{N-1}\}$, with each individual symmetry operation being either unitary or antiunitary, depending on the system in question. In addition, these N symmetry operations must be interrelated, since $[H, O_m] = [H, O_n] = [H, O_m O_n] = O_m [H, O_n] + [H, O_m] O_n = 0$, i.e. if $O_m, O_n \in \mathcal{O}$ then their product must also be contained in the set, $O_m O_n \in \mathcal{O}$. Consequently, all this hints at the fact that spatial symmetries form finite groups. Now, for us to gain deeper insight into the consequences of spatial symmetries, we will in the following discuss essential properties of finite groups and representation theory, which we will use extensively throughout this thesis. Note that the following by no means serves as a stand-alone introduction to finite groups, and should be complemented by various books and lecture notes on the topic, e.g. refs. [129–135, 137–139].

Properties of Finite Groups and Representation Theory

A collection of elements $\mathcal{O} = \{O_0, O_1, \dots, O_{N-1}\}$ is said to form a group of order N , when the following four postulates are satisfied

- The group is stable, i.e. the product of any two elements of the group $O_m O_n = O_p$ is itself contained in the group, $\{O_m, O_n, O_p\} \in \mathcal{O}$.
- The associative law is true, $O_m(O_n O_p) = (O_m O_n)O_p$ for $\{O_m, O_n, O_p\} \in \mathcal{O}$.
- The set \mathcal{O} has an identity element E , often defined as the first element of the group $O_0 \equiv E$, which commutes with any other element of the group, $[E, O] = 0$ for all $O \in \mathcal{O}$.
- For every element $O \in \mathcal{O}$, there exists an inverse element O^{-1} such that $O^{-1}O = OO^{-1} = E$.

Following the above definitions, various properties and aspects of finite groups can be derived. While a complete and in-depth study of group theory is beyond the scope of this thesis, we still define and derive some key aspects which we will use in the upcoming chapters. Once more, we refer the interested reader to various books and lecture notes on the topic, see for example refs. [129–135, 137–139].

The stable group postulate allows us to define a multiplication table for the group, i.e. a table relating the products of elements to other elements of the group. Not only does this table allow one to replace the consecutive operation of two elements with a single element, thus simplifying the operation, it also reveals whether the elements of the group commute, $[O_m, O_n] = 0$ for $O_m, O_n \in \mathcal{O}$. A group where all elements commute is called Abelian. In table 1.1 we show a simple example of a multiplication table for the group $\{E, U_1\}$, which is clearly Abelian due to the group postulate that $[E, O] = 0$ for all $O \in \mathcal{O}$. More importantly, the multiplication table can also be used to identify whether there exists a correspondence between elements of two distinct groups \mathcal{O} and \mathcal{O}' . Specifically, if \mathcal{O} and \mathcal{O}' have the same multiplication table, then the two are said to be isomorphic, and the groups are thus equivalent in a symmetry perspective.

The same principles apply in defining a representation of the group \mathcal{O} . For simplicity, we assume in the following that all elements of \mathcal{O} are unitary $O = U$. In the end of this sections, we take into account the consequences of antiunitary elements in \mathcal{O} . Per definition, a faithful representation of an abstract group \mathcal{O} is a substitution group, with an isomorphic correspondence between the two groups. Specifically we must have the following correspondence

$$U_m \mapsto D[U_m], \quad U_n \mapsto D[U_n], \quad \text{and} \quad D[U_n]D[U_m] = D[U_n U_m], \quad (1.17)$$

where $D[U_m]$ is some matrix representation of the group element U_m . One could, for example, identify the matrix elements of the representation as $D[U_m]^{ij} = \langle i|U_m|j\rangle$, for which we immediately observe from eqns. (1.14–1.16), that the matrix representation of the group elements plays an indispensable role in the classification of the prototypical Hamiltonian in eqn. (1.1). However, matrix representations are not uniquely defined, since one can either combine two representations into one $D[U_m] \oplus D'[U_m]$, or simply rewrite the matrix in a different basis $\tilde{U}D[U_m]\tilde{U}^{-1}$. To overcome this ambiguity, it is customary to consider instead the irreducible representations (IRs) $D^\Gamma[U_m]$, which are matrices that cannot be brought on a block diagonal form by any basis transformations. In other words, IRs are matrix representations with the lowest possible dimensionality. Still, this does not take care of the ambiguity with regards to the basis dependence of the representations. To sort out this issue, it is natural to introduce a basis independent quantity, namely the character of the IRs. Now, the character $X^\Gamma[U_m]$ is nothing but the trace of the IRs, and is uniquely defined as

$$X^\Gamma[U_m] = \sum_i D^\Gamma[U_m]^{ii} = \text{tr}D^\Gamma[U_m]. \quad (1.18)$$

Multiplication table			Character table			
\cdot	E	U_1		E	U_1	Basis func.
E	E	U_1	Γ_1	1	1	$f^{\Gamma_1}(\mathbf{r})$
U_1	U_1	E	Γ_2	1	-1	$f^{\Gamma_2}(\mathbf{r})$

Table 1.1: Example of multiplication and character table for the group $\{E, U_1\}$. The multiplication table shows how two elements are combined into a single element, while the character table lists the characters for the two IRs labeled by Γ_1 and Γ_2 . The group is Abelian, and, as a consequence, all the IRs are one-dimensional, thus the character coincides with the IRs $X^{\Gamma_i}[O_m] = D^{\Gamma_i}[O_m]$. Note that in the last column of the character table we list the basis functions $f^{\Gamma_i}(\mathbf{r})$, that can be used either to generate the IRs of the group, if these are not known, or to project out IRs of some arbitrary function.

The actual task of determining the IRs, and their belonging characters for a given group \mathcal{O} , can be a demanding chore. Conveniently, the characters for all the relevant groups considered in this thesis, have already been tabulated in the literature and online, see e.g. [134, 156–159, 159, 160]. Had this not been the case, one would have to derive the characters of the group by employing various versions of the so-called “Wonderful Orthogonality Theorem”

$$\frac{1}{N} \sum_m D^\Gamma[U_m]^{ij} D^{\Gamma'}[U_m^{-1}]^{j'i'} = \delta_{i,i'} \delta_{j,j'} \delta_{\Gamma,\Gamma'} / \ell_\Gamma, \quad (1.19)$$

where ℓ_Γ is the dimensionality of the IR $D^\Gamma[U_m]$. For a step-by-step guide in generating all the characters for a finite group, see chap. 3.8 in ref. [134]. Alternatively, see chap. 2.4 in ref. [128] for an example of this guide used in practice.

In table 1.1 we show an example of how the characters usually are tabulated in the literature. In addition to the characters of the group, the tables generally also display the basis functions $f_i^\Gamma(\mathbf{r})$, see last column in table 1.1, which act as basis vectors of the IRs $D^\Gamma[U]$ for all $U \in \mathcal{O}$. For convenience, let us in the following denote these basis functions as states, in the following way $f_i^\Gamma(\mathbf{r}) \sim |\Gamma, i\rangle$, where the index $i = 1 \dots \ell_\Gamma$ labels the number of basis vectors for the given IR. Had the IR for example been a 2×2 matrix ($\ell_\Gamma = 2$), then $i = 1, 2$, whereas for 1D IRs $i = 1$ and is often not written explicitly, similar to those listed in table 1.1. With these basis vectors at hand, we can readily generate all the IRs $D^\Gamma[U_m]$, through the following

$$U_m |\Gamma, j\rangle = \sum_{\Gamma'} \sum_i |\Gamma', i\rangle \langle \Gamma', i | U_m | \Gamma, j \rangle = \sum_i D^\Gamma[U_m]^{ij} |\Gamma, i\rangle. \quad (1.20)$$

Note that the basis states $|\Gamma, i\rangle$ should in general not be confused with the single particle basis states $|i\rangle$. We thus see from the above, that one can easily acquire the characters and the IRs, simply by considering the already tabulated character table of the group in question.

Now, to make use of the IRs and basis vectors, we point out yet another powerful application in the language of point group theory, namely that the basis vectors $|\Gamma, i\rangle$ can be used to project out IRs of an arbitrary function F . To facilitate this, let us in the following consider the general function

F , which can be written as a linear combination of basis vectors

$$F = \sum_{\Gamma} \sum_i a_{\Gamma,i} |\Gamma, i\rangle, \quad (1.21)$$

with $a_{\Gamma,i}$ being expansion coefficients. We define the operator P_i^{Γ} , which projects out the basis vector $|\Gamma, i\rangle$, and can be proven to take the form [134]

$$P_i^{\Gamma} = \frac{\ell_{\Gamma}}{N} \sum_m (D^{\Gamma}[U_m]^{ii})^* U_m. \quad (1.22)$$

Now, by acting with P_i^{Γ} on F , we straightforwardly get

$$P_i^{\Gamma} F = \frac{\ell_{\Gamma}}{N} \sum_m \sum_{\Gamma',j} \sum_l a_{\Gamma',j} |\Gamma', l\rangle (D^{\Gamma}[U_m]^{ii})^* D^{\Gamma'}[U_m]^{lj} = a_{\Gamma,i} |\Gamma, i\rangle, \quad (1.23)$$

where we made use of eqn. (1.20) and the ‘‘Wonderful Orthogonality Theorem’’. If the basis vectors are properly normalized, one can extract the expansion coefficients through the simple relation $\langle \Gamma, i | P_i^{\Gamma} F = a_{\Gamma,i}$. To exemplify this projection procedure, let us once more turn our attention towards the group $\{E, U_1\}$ with the characters shown in table 1.1. Let us further assume that we wish to extract the basis functions entering in some general function $F(\mathbf{r}) = af^{\Gamma_1}(\mathbf{r}) + bf^{\Gamma_2}(\mathbf{r})$. By applying the projection operator, we readily find

$$\begin{aligned} P_1^{\Gamma_1} F(\mathbf{r}) &= \frac{\ell_{\Gamma_1}}{N} \sum_m (D^{\Gamma_1}[U_m]^{11})^* U_m F(\mathbf{r}) = \frac{E + U_1}{2} [af^{\Gamma_1}(\mathbf{r}) + bf^{\Gamma_2}(\mathbf{r})] = af^{\Gamma_1}(\mathbf{r}), \\ P_1^{\Gamma_2} F(\mathbf{r}) &= \frac{\ell_{\Gamma_2}}{N} \sum_m (D^{\Gamma_2}[U_m]^{11})^* U_m F(\mathbf{r}) = \frac{E - U_1}{2} [af^{\Gamma_1}(\mathbf{r}) + bf^{\Gamma_2}(\mathbf{r})] = bf^{\Gamma_2}(\mathbf{r}). \end{aligned} \quad (1.24)$$

This projection procedure will come in handy, when one wants to identify symmetry breaking terms entering in, for example, the prototypical Hamiltonian in eqn. (4).

The last important property that want to address about the basis vectors, is their relation to the single particle eigenstates $\mathcal{H}|\alpha\rangle = E_{\alpha}|\alpha\rangle$. The commutation relation $[\mathcal{H}, U] = 0$ for all $U \in \mathcal{O}$ tells us that we can find simultaneous eigenstates of U and \mathcal{H} , as seen from the simple relations

$$\mathcal{H}|\alpha\rangle = E_{\alpha}|\alpha\rangle, \quad \mathcal{H}U_m|\alpha\rangle = U_m\mathcal{H}|\alpha\rangle = E_{\alpha}U_m|\alpha\rangle. \quad (1.25)$$

The above only holds true if $U_m|\alpha\rangle \propto |\alpha\rangle$, i.e. $|\alpha\rangle$ is an eigenstate of U_m , or if we have an energy degeneracy where U_m only acts within this degenerate subspace. With this in mind, and by close inspection of eqn. (1.20), we find the former to hold true for basis vectors belonging to one-dimensional IRs, while basis vectors for multi-dimensional IRs fulfill the latter, as can be seen from the action of U_m on the basis vectors

$$\begin{aligned} \text{One-dimensional IR:} \quad U_m|\Gamma, i\rangle &= \sum_j D^{\Gamma}[U_m]^{ji} |\Gamma, j\rangle \equiv X^{\Gamma}[U_m]|\Gamma, i\rangle, \\ \text{Multi-dimensional IR:} \quad U_m|\Gamma, i\rangle &= \sum_j D^{\Gamma}[U_m]^{ji} |\Gamma, j\rangle. \end{aligned} \quad (1.26)$$

Thus, any eigenstate can simply be labeled by the IR and the belonging component $i = 1 \dots \ell_{\Gamma}$, i.e. $|\alpha\rangle \equiv |\Gamma, i\rangle$. Recall that i labels the ℓ_{Γ} basis vectors belonging to a ℓ_{Γ} -dimensional IR. This further

indicates that ℓ_Γ -dimensional IRs generally will lead to ℓ_Γ -fold symmetry-protected degeneracies in the energy spectrum. Moreover, the above informs us that we can block diagonalize a Hamiltonian into blocks labeled by the IRs of the group, which proves useful when considering the IRs of the translation subgroup of space groups, but also in classifying topological systems in the presence of symmetries, see chap. 5.

To conclude this rather technical section, we want lastly to address the consequences when antiunitary elements A_m are present in the group \mathcal{O} . Such groups are called magnetic groups, and contain equal parts unitary and antiunitary elements $\mathcal{O} = \{U_0, U_1, \dots, U_{N/2}, A_{N/2+1}, \dots, A_N\} \equiv \mathcal{M}$, since the unitary elements $\mathcal{U} = \{U_0, U_1, \dots, U_{N/2}\}$ form a self-conjugate subgroup of index 2. In fact, any magnetic group \mathcal{M} can be rewritten in terms of the right coset $M = \mathcal{U} + \mathcal{U}A$, where A is some antiunitary element in \mathcal{M} [149]. Now, since \mathcal{U} is a unitary subgroup of \mathcal{M} , we can simply adopt the unitary IR $D^\Gamma[U_m]$, as discussed in the above paragraphs, for the elements in \mathcal{U} . However, the presence of the antiunitary element A , tells us that we need to extend this representation to also include the basis states $A|\Gamma, i\rangle$. For this extended basis, we find the following transformation rules

$$\begin{aligned} U_m|\Gamma, j\rangle &= \sum_i |\Gamma, i\rangle \langle \Gamma, i|U_m|\Gamma, j\rangle = \sum_i D^\Gamma[U_m]^{ij}|\Gamma, i\rangle, \\ U_mA|\Gamma, j\rangle &= \sum_i A|\Gamma, i\rangle \langle \Gamma, i|A^{-1}U_mA|\Gamma, j\rangle = \sum_i (D^\Gamma[A^{-1}U_mA]^{ij})^* A|\Gamma, i\rangle. \end{aligned} \quad (1.27)$$

Note that $D^\Gamma[A^{-1}U_mA]$ is in fact an unitary IR since $A^{-1}U_mA \in \mathcal{U}$. Applying the same principle to antiunitary elements $B_m \in \mathcal{U}A$, we end up with the following unitary representation of the magnetic group \mathcal{M} in the extended basis $\{|\Gamma, i\rangle, A|\Gamma, i\rangle\}$

$$\mathcal{D}[U_m]^{ij} = \begin{pmatrix} D^\Gamma[U_m]^{ij} & 0 \\ 0 & (D^\Gamma[A^{-1}U_mA]^{ij})^* \end{pmatrix}, \quad \mathcal{D}[B_m]^{ij} = \begin{pmatrix} 0 & D^\Gamma[B_mA]^{ij} \\ (D^\Gamma[A^{-1}B_m]^{ij})^* & 0 \end{pmatrix}, \quad (1.28)$$

with $A^{-1}B_m, B_mA \in \mathcal{U}$. We have thus accomplished to construct a representation \mathcal{D} for all elements in \mathcal{M} , consisting solely of unitary IRs $D^\Gamma[U]$ for $U \in \mathcal{U}$. Although \mathcal{D} appears as yet another representation, we find that it does not conserve the conventional multiplication rule, see eqn. (1.17), and we find instead

$$\begin{aligned} \mathcal{D}[U_m]\mathcal{D}[U_n] &= \mathcal{D}[U_mU_n], & \mathcal{D}[U_m]\mathcal{D}[B_n] &= \mathcal{D}[U_mB_n], \\ \mathcal{D}[B_m](\mathcal{D}[U_n])^* &= \mathcal{D}[B_mU_n], & \mathcal{D}[B_m](\mathcal{D}[B_n])^* &= \mathcal{D}[B_mB_n]. \end{aligned} \quad (1.29)$$

A representation with the above multiplication is referred to as a co-representation [34, 129, 130, 148–150], and is in general reducible, similar to its conventional counterpart D . We therefore seek to determine the irreducible co-representations, i.e. matrices in the extended basis $\{|\Gamma, i\rangle, A|\Gamma, i\rangle\}$ with the lowest possible dimensionality. In order to do so, we first and foremost need to identify which of the following three cases \mathcal{D} belongs to

$$\frac{2}{N} \sum_{B \in \mathcal{AU}} X^\Gamma[B^2] = \begin{cases} 1 & \text{Case (a): } \mathcal{D} \text{ is reducible} \\ -1 & \text{Case (b): } \mathcal{D} \text{ is irreducible} \\ 0 & \text{Case (c): } \mathcal{D} \text{ is irreducible} \end{cases} \quad (1.30)$$

where $B^2 \in \mathcal{U}$ and Γ labels the unitary IR $D^\Gamma[U]$ for $U \in \mathcal{U}$. The above is sometimes called the modified Forbenius-Schur indicator, or the Dimmock and Wheeler test, based on their founding studies [148, 161], although the specific form of the above was derived by C. J. Bradley and B. L. Davies [149]. For the well-known case where $A = T$, we retrieve the usual Herring rule [162], which leads to the well-known Kramers degeneracy for particles with half-integer spin.

By not being concerned with the explicit matrix structure of the irreducible co-representations,¹ we can conclude how the three distinct cases in eqn. (1.30) modifies the energy spectrum, compared to that of the conventional IR D^Γ . In case (a), \mathcal{D} is reducible, and thus retrieves the same matrix dimensions as D^Γ , i.e. no extra degeneracies in the spectrum. In contrast, for case (b), \mathcal{D} is irreducible, meaning that the irreducible co-representation must be a $2\ell_\Gamma \times 2\ell_\Gamma$ matrix, where ℓ_Γ is the matrix dimension of D^Γ . This ultimately leads to a $2\ell_\Gamma$ -fold protected degeneracy in the energy spectrum, in contrast to a ℓ_Γ -fold degeneracy for the usual IR. Lastly, for case (c), \mathcal{D} is also irreducible, thus leading to a $2\ell_\Gamma$ -fold degeneracy in the energy spectrum, similar to case (b). The difference here, however, is the fact that the irreducible co-representation now combines two IRs D^Γ and $D^{\Gamma'}$ into a single irreducible co-representation, for further details see ref. [149]. Nonetheless, as we stated above, we are not concerned with the explicit form of the irreducible co-representations, only how these can affect the energy spectrum, thus, case (c) effectively lead to the same conclusion as in (b).

From the above, it is evident that antiunitary elements in \mathcal{O} , generally call for an extended representation, the so-called co-representation, which can ultimately lead to additional degeneracies in the energy spectrum. In this regard, the modified Forbenius-Schur indicator in eqn. 1.30 should be consulted anytime the group is of the magnetic kind. In fact, in chap. 5 we will encounter several antiunitary symmetry elements, as a consequence of the various magnetic textures studied in that chapter, which lead to symmetry-protected degeneracies in the magnetic BZ. Before closing this section, let us exemplify the above by considering a system left invariant under the symmetry elements of the magnetic group $\{E, U_1\} \otimes \{E, T\}$, i.e. the group of table. 1.1 in the presence of time-reversal symmetry. By applying the Herring rule we find

$$\frac{2}{N} \sum_{B \in \mathcal{AU}} X^\Gamma[B^2] = \text{sgn}(T^2) \quad \text{for } \Gamma_1 \text{ and } \Gamma_2, \quad (1.31)$$

thus leading to a Kramers degeneracy for particles with half-integer spin ($T^2 = -1$). Strictly speaking, when considering a system of particles with half-integer spin, one needs to invoke the so-called double groups $\tilde{\mathcal{O}}$. These groups arise because of the 4π -rotation periodicity of half-integer spin particles, and consequently leads to a doubling of the number of group elements, compared to the single group \mathcal{O} , i.e. $\tilde{\mathcal{O}} = \mathcal{O} + C_1\mathcal{O}$ where C_1 is a 2π rotation. This means that one needs to label the eigenstates of the system with respect to the IRs of the double group $\tilde{\mathcal{O}}$. Nonetheless, observables g do exhibit a 2π -periodicity, $C_1 g C_1^{-1} = g$, and we can thus simply label these by the IRs of the normal group \mathcal{O} . For a further discussion on this, see for example chap. 1, sec. 2.2 in ref. [141].

Space Groups of Crystals

After having established the here-relevant properties and tools for finite groups, we can now go ahead and apply these to physical systems. With an eye to apply this theory on Hamiltonians describing

¹We refer the interested reader to ref. [149] for examples on how to construct the explicit matrix form of the irreducible co-representations.

electrons subjected to a crystalline lattice potential, we need to study the specific symmetry groups that leave the given crystal lattice invariant. Such groups are referred to as space groups \mathcal{G} , and consist in general of both pure point group symmetries $\{G_i | \mathbf{0}\}$, pure lattice translations $\{E | \mathbf{R}\}$, and the so-called compound symmetries $\{G'_i | \mathbf{t}_i\}$ where \mathbf{t}_i is a non-primitive lattice vector. Point group symmetries are operations leaving at least a single point fixed, such as $2\pi/n$ rotations C_n , reflections σ , inversion I , improper rotations S_n and rotoinversions IC_n , while the compound symmetries $\{G'_i | \mathbf{t}_i\}$ combine reflections (rotations) with non-primitive lattice translations, and is referred to as glide plane (screw axis) symmetries. Space groups are notoriously difficult to work with, since the order of the group N , i.e. the number of symmetry elements, is tremendously large $N = \mathcal{N}(N_G + N_{G'})$, where $\mathcal{N} \sim 10^{23}$ is the number of primitive unit cells of the crystal, and N_G ($N_{G'}$) is the number of pure point group (compound) symmetries $\{G_i | \mathbf{0}\}$ ($\{G'_i | \mathbf{t}_i\}$).

To work around this issue, we first note that the pure translations $\{E | \mathbf{R}\}$ constitute a self-conjugate subgroup of \mathcal{G} , the so-called translation group \mathcal{T} . Now, since \mathcal{T} is a subgroup, we can rewrite the space group in terms of the cosets

$$\mathcal{G} = \mathcal{T}\{G | \mathbf{0}\} + \mathcal{T}\{G' | \mathbf{t}\}, \quad (1.32)$$

with $\{G | \mathbf{0}\} = \{G_1 | \mathbf{0}\}, \{G_2 | \mathbf{0}\} \dots \{G_{N_G} | \mathbf{0}\}$ and $\{G' | \mathbf{t}\} = \{G'_1 | \mathbf{t}_1\}, \{G'_2 | \mathbf{t}_2\} \dots \{G'_{N_{G'}} | \mathbf{t}_{N_{G'}}\}$. Furthermore, we note that since \mathcal{T} is self-conjugate, the above cosets themselves form a group of order $N_G + N_{G'}$, the so-called factor group \mathcal{G}/\mathcal{T} . This factor group, in return, is isomorphic to the point group $G + G'$, i.e. the group of pure point group and compound symmetries without translations. Thus, there exists a one-to-one correspondence between the elements of \mathcal{G}/\mathcal{T} and $G + G'$, and we have effectively reduced the number of elements from $\mathcal{N}(N_G + N_{G'})$ to $N_G + N_{G'}$. For example, the nonsymmorphic space group for FeSe is $P4/nmm$, for which the factor group $(P4/nmm)/\mathcal{T}$ is isomorphic to the point group D_{4h} .

Space groups can be further divided into symmorphic and nonsymmorphic groups. In order to illustrate the distinction between the two, we first need to introduce the multiplication rule for the space group elements $\{g_i | \mathbf{l}_i\}\{g_j | \mathbf{l}_j\} = \{g_i g_j | \mathbf{l}_i + g_i \mathbf{l}_j\}$ and their inverse elements $\{g_i | \mathbf{l}_i\}^{-1} = \{g_i^{-1} | -g_i^{-1} \mathbf{l}_i\}$. Through these, we can emphasize the fact that any space group element is defined with respect to some coordinate system, which we can always translate to some other point in space, specifically

$$\{E | \mathbf{l}\} \{G'_i | \mathbf{t}_i\} \{E | -\mathbf{l}\} = \{G'_i | \mathbf{t}_i + \mathbf{l} - G'_i \mathbf{l}\}. \quad (1.33)$$

From the above, we see that for some compound symmetries $\{G'_i | \mathbf{t}_i\}$ we can potentially remove the translational part by choosing an appropriate real space coordinate system, and render the compound symmetry a simple point group element. For the above example, this would be the case for $\mathbf{t}_i = G'_i \mathbf{l} - \mathbf{l}$. In fact, for some space groups we can pick a coordinate system for which all compound symmetries become point group symmetries $\{G' | \mathbf{t}\} \rightarrow \{G' | \mathbf{0}\}$, such groups are the symmorphic space groups. On the other hand, groups containing at least a single compound symmetry, no matter the coordinate system, are the nonsymmorphic space groups. The convenient property of symmorphic space groups, although not apparent here, is that the coset representatives in eqn. (1.32) can be chosen to be solely point group symmetries, with the trade-off that the space group IRs, roughly speaking, are simple products of \mathcal{T} IRs and $G + G'$ IRs [134].

Nature itself displays a total of 230 distinct non-magnetic space groups, whereof 73 are symmorphic and the remaining 157 are nonsymmorphic. In part I of this thesis, we exclusively encounter

symmorphic non-magnetic space groups, which makes the IRs of the space groups particular simple, since we can consider the IRs of the translation group \mathcal{T} and the point group $G + G'$ separately, as mentioned above. For nonsymmorphic symmetries, on the other hand, one needs to be more careful, since certain points in the BZ do not conserve the multiplication rule, see eqn. 1.17. To work around this issue, one need to employ the so-called Herring method [163], not to be confused with the Herring rule [162]. However, as already mentioned, we are only concerned with symmorphic space groups in the first part of this thesis, and we thus refer the interested reader to various books on the subject, and the very detailed example in ref. [164] in the context of FeSe.

By extending the space groups to also include magnetic symmetries, i.e. antiunitary symmetries, we get a total of 1,651 magnetic space groups \mathcal{M} , and 36 magnetic Bravais lattices. We will in fact encounter such nonsymmorphic magnetic space groups in chap. 5, when we perform the topological symmetry classification of magnetic textures. Nonetheless, since we are only concerned with the topological classification in that chapter, we shall not be concerned with the explicit IRs of \mathcal{M} . In fact, as we shall see, for 2D systems the nonsymmorphic symmetries are in general broken on all edges of the system, and can thus not lead to any symmetry-protected topological edge states [32].

IRs of the Translation Group and Bloch's Theorem

The fact that the translation group \mathcal{T} is a subgroup of a given space group \mathcal{G} , informs us that we can label the eigenstates $|\alpha\rangle$ of the Hamiltonian with respect to the IRs of \mathcal{T} , which in return allows us to diagonalize the Hamiltonian into blocks labeled by the corresponding IRs. Exactly this block diagonalization with respect to the IRs of \mathcal{T} reduces the matrix representation of the single-particle Hamiltonian $D[\mathcal{H}]$ from a $\ell\mathcal{N} \times \ell\mathcal{N}$ matrix, to \mathcal{N} individual $\ell \times \ell$ matrices, where \mathcal{N} is the number of primitive unit cells, and ℓ is the number of the remaining degrees of freedom, i.e. the number of spin projections, orbitals etc.

In order to find the IRs of \mathcal{T} , we first and foremost note that \mathcal{T} is Abelian, i.e. all elements of the group commute

$$\{E | \mathbf{R}\}\{E | \mathbf{R}'\} = \{E | \mathbf{R}'\}\{E | \mathbf{R}\} = \{E | \mathbf{R} + \mathbf{R}'\}, \quad (1.34)$$

which tells us that the IRs of \mathcal{T} are all one-dimensional. From eqn.(1.26), we know that one-dimensional IRs coincide with their character, $D^\Gamma[U_m] \equiv X^\Gamma[U_m]$, and, more importantly, we also see that the problem of determining the IRs of \mathcal{T} , basically boils down to the following eigenproblem $\{E | \mathbf{R}\}|\Gamma\rangle = X^\Gamma[\{E | \mathbf{R}\}]|\Gamma\rangle$. We thus simply need to determine the eigenvalues of all the operators contained in \mathcal{T} . In order to do so, we further note that any Bravais lattice vector can be written as a linear combination of the primitive lattice vectors \mathbf{a}_i , in the following way $\mathbf{R} = n_1\mathbf{a}_1 + n_2\mathbf{a}_2 + n_3\mathbf{a}_3$, where n_i are integers. The latter lets us rewrite $\{E | \mathbf{R}\} = \{E | n_1\mathbf{a}_1\}\{E | n_2\mathbf{a}_2\}\{E | n_3\mathbf{a}_3\}$. Now, by considering each component separately, and assuming periodic boundary conditions, i.e. $\mathbf{R} + \mathcal{N}_i\mathbf{a}_i \equiv \mathbf{R}$, where \mathcal{N}_i is the number of unit cells in the i th direction, we note the following relations

$$\{E | \mathbf{a}_i\}^{\mathcal{N}_i}|\mathbf{R}\rangle = |\mathbf{R} + \mathcal{N}_i\mathbf{a}_i\rangle \equiv |\mathbf{R}\rangle, \quad \Rightarrow \quad X^{n_i}[\{E | \mathbf{a}_i\}] = e^{i2\pi n_i/\mathcal{N}_i}, \quad (1.35)$$

thus the IRs are labeled by the integer $n_i = 0, 1 \dots \mathcal{N}_i - 1$, and is directly related to all translations along \mathbf{a}_i . In the field of condensed matter physics, it is common to instead label the IRs with the wave vector $\mathbf{k}_i = 2\pi n_i \hat{\mathbf{a}}_i / \mathcal{N}_i |\mathbf{a}_i|$, which results in $X^{\mathbf{k}_i}[\{E | \mathbf{a}_i\}] = \exp(i\mathbf{k}_i \cdot \mathbf{a}_i)$. By including

translations in all three directions, we end up with the following IRs/characters labeled by the wave vector $\mathbf{k} = \mathbf{k}_1 + \mathbf{k}_2 + \mathbf{k}_3$

$$X^{\mathbf{k}}[\{E | \mathbf{a}_i\}] = e^{i\mathbf{k} \cdot \mathbf{a}_i}, \quad \{E | \mathbf{a}_i\} |\mathbf{k}\rangle = X^{\mathbf{k}}[\{E | \mathbf{a}_i\}] |\mathbf{k}\rangle = e^{i\mathbf{k} \cdot \mathbf{a}_i} |\mathbf{k}\rangle, \quad (1.36)$$

where we introduced the basis functions $|\Gamma, i\rangle = |\mathbf{k}\rangle$, and observe Bloch's theorem in the latter equation.

As discussed above, it advantageous to rewrite the Hamiltonian H_{norm} in terms of the basis functions $|\mathbf{k}\rangle$. To see this, we will momentarily return to the full set of electronic degrees of freedom, namely $i = \{\mathbf{R}\tilde{\mu}\}$, and perform the basis transformation of the fermionic operators

$$c_{\mathbf{R}\tilde{\mu}} = \sum_{\mathbf{k}} \langle \mathbf{R} | \mathbf{k} \rangle c_{\mathbf{k}\tilde{\mu}}, \quad \text{and} \quad c_{\mathbf{R}\tilde{\mu}}^\dagger = \sum_{\mathbf{k}} c_{\mathbf{k}\tilde{\mu}}^\dagger \langle \mathbf{k} | \mathbf{R} \rangle. \quad (1.37)$$

By directly inserting the above in H_{norm} , we arrive at

$$H_{\text{norm}} = \sum_{\mathbf{R}, \mathbf{R}'} \sum_{\mathbf{k}, \mathbf{k}'} c_{\mathbf{k}\tilde{\mu}}^\dagger \langle \mathbf{k} | \mathbf{R} \rangle \langle \mathbf{R} \tilde{\mu} | \mathcal{H} | \mathbf{R}' \tilde{\nu} \rangle \langle \mathbf{R}' | \mathbf{k}' \rangle c_{\mathbf{k}'\tilde{\nu}} = \sum_{\mathbf{k}} c_{\mathbf{k}\tilde{\mu}}^\dagger \langle \tilde{\mu} | \mathcal{H}_{\mathbf{k}} | \tilde{\nu} \rangle c_{\mathbf{k}\tilde{\nu}}, \quad (1.38)$$

where we in the latter equality utilized the fact that \mathcal{H} commutes with the elements of \mathcal{T} , and is therefore diagonal $\langle \mathbf{k}' | \mathcal{H} | \mathbf{k} \rangle = \mathcal{H}_{\mathbf{k}} \delta_{\mathbf{k}, \mathbf{k}'}$. Alternatively, this can be seen by identifying the matrix elements as plane waves $\langle \mathbf{R} | \mathbf{k} \rangle = \exp(i\mathbf{k} \cdot \mathbf{R}) / \sqrt{\mathcal{N}}$ [136, 165], and perform the sums explicitly

$$\sum_{\mathbf{R}, \mathbf{R}'} \langle \mathbf{k} | \mathbf{R} \rangle \langle \mathbf{R} \tilde{\mu} | \mathcal{H} | \mathbf{R}' \tilde{\nu} \rangle \langle \mathbf{R}' | \mathbf{k}' \rangle = \frac{1}{\mathcal{N}} \sum_{\mathbf{R}, \mathbf{R}'} e^{-i\mathbf{k} \cdot \mathbf{R}} \langle \mathbf{R} \tilde{\mu} | \mathcal{H} | \mathbf{R}' \tilde{\nu} \rangle e^{i\mathbf{k}' \cdot \mathbf{R}'} \equiv \langle \tilde{\mu} | \mathcal{H}_{\mathbf{k}, -\mathbf{k}'} | \tilde{\nu} \rangle / \mathcal{N}, \quad (1.39)$$

where it is well-known that for translational invariant systems $\langle \tilde{\mu} | \mathcal{H}_{\mathbf{k}, -\mathbf{k}'} | \tilde{\nu} \rangle = \mathcal{N} \langle \tilde{\mu} | \mathcal{H}_{\mathbf{k}} | \tilde{\nu} \rangle \delta_{\mathbf{k}, -\mathbf{k}'}$ [165]. We have thus accomplished to reduce a $\ell\mathcal{N} \times \ell\mathcal{N}$ matrix $D[\mathcal{H}]$, into \mathcal{N} individual $\ell \times \ell$ matrices $D[\mathcal{H}_{\mathbf{k}}]$. Note that here, D is the representation in combined spin and orbital space.

Running through the various symmetry transformation detailed in the previous sections of this chapter, we see that $D[\mathcal{H}_{\mathbf{k}}]$ has to satisfy the following relations in order to display the non-spatial symmetries

$$\begin{aligned} T : \quad & D[\mathcal{H}_{\mathbf{k}}] = D[U_T] D^\dagger[\mathcal{H}_{-\mathbf{k}}] D^\dagger[U_T], \\ C : \quad & D[\mathcal{H}_{\mathbf{k}}] = -D[U_C] D^\dagger[\mathcal{H}_{-\mathbf{k}}] D^\dagger[U_C], \\ S : \quad & D[\mathcal{H}_{\mathbf{k}}] = -D[U_S] D[\mathcal{H}_{\mathbf{k}}] D^\dagger[U_S], \end{aligned} \quad (1.40)$$

and similarly for the spatial symmetries

$$\begin{aligned} U : \quad & D[\mathcal{H}_{\mathbf{k}}] = D[U] D[\mathcal{H}_{U^{-1}\mathbf{k}}] D^\dagger[U], \\ A : \quad & D[\mathcal{H}_{\mathbf{k}}] = D[U_A] D^\dagger[\mathcal{H}_{-U_A^{-1}\mathbf{k}}] D^\dagger[U_A], \end{aligned} \quad (1.41)$$

where we in the last two relations only focused on point group symmetry elements. From the above transformations, it is clear that symmetries in general take \mathbf{k} and map it to some other wave vector \mathbf{k}' , such a collection of wave vectors are referred to as the star of \mathbf{k} . In contrast, some symmetries map \mathbf{k} onto itself modulo reciprocal lattice vectors, at specific points in the BZ. A collection of such symmetries is called the group of the wave vector \mathbf{k} . Special for the group of the wave vector \mathbf{k} , as we shall see in chap. 5, is that we can further block diagonalize $D[\mathcal{H}_{\mathbf{k}}]$ with respect to these symmetries.

At this point we end our general discussion about symmetries in multi-orbital systems, since we have acquired all the necessary tools for the upcoming chapters, which are primarily based on manuscripts and published papers.

Appendices for Chapter 1

1.A Mean-Field Decoupling and Wave-Vector Representation of the Prototypical Hamiltonian

The many-body Hamiltonian describing multi-orbital systems in condensed matter systems, see eqn. (3), generally takes the form

$$\begin{aligned} H &= H_{\text{kin}} + H_{\text{int}} \\ &= - \sum_{\mathbf{R}, \mathbf{R}'} c_{\mathbf{R}\tilde{\mu}}^\dagger (t_{\mathbf{R}, \mathbf{R}'}^{\tilde{\mu}\tilde{\nu}} + \mu_0 \delta_{\mathbf{R}, \mathbf{R}'} \delta_{\tilde{\mu}, \tilde{\nu}}) c_{\mathbf{R}'\tilde{\nu}} + \frac{1}{2} \sum_{\mathbf{R}, \mathbf{R}'} c_{\mathbf{R}\tilde{\mu}_2}^\dagger c_{\mathbf{R}'\tilde{\mu}_4}^\dagger [V_{\mathbf{R}, \mathbf{R}'}]_{\tilde{\mu}_4 \tilde{\mu}_3}^{\tilde{\mu}_2 \tilde{\mu}_1} c_{\mathbf{R}'\tilde{\mu}_3} c_{\mathbf{R}\tilde{\mu}_1}, \end{aligned} \quad (1.42)$$

where we adopted the shorthand notation $\tilde{\mu}_i = \{\mu_i, \sigma_i\}$. The multi-orbital interaction potential $[V_{\mathbf{R}, \mathbf{R}'}]_{\tilde{\mu}_4 \tilde{\mu}_3}^{\tilde{\mu}_2 \tilde{\mu}_1}$ is related to the usual Coulomb interaction potential $V(\mathbf{r} - \mathbf{r}')$, in the following way

$$[V_{\mathbf{R}, \mathbf{R}'}]_{\tilde{\mu}_4 \tilde{\mu}_3}^{\tilde{\mu}_2 \tilde{\mu}_1} = \int d\mathbf{r} \int d\mathbf{r}' \langle \mathbf{r} | \mathbf{R}\mu_2 \rangle \langle \mathbf{r}' | \mathbf{R}'\mu_4 \rangle V(\mathbf{r} - \mathbf{r}') \langle \mathbf{R}'\mu_3 | \mathbf{r}' \rangle \langle \mathbf{R}\mu_1 | \mathbf{r} \rangle, \quad (1.43)$$

where $\langle \mathbf{R}\mu_i | \mathbf{r} \rangle$ are the Wannier functions. On the mean-field level, the operators entering in the interaction can be approximated by their respective fields

$$\begin{aligned} c_{\mathbf{R}\tilde{\mu}}^\dagger c_{\mathbf{R}'\tilde{\nu}} &\sim \langle c_{\mathbf{R}\tilde{\mu}}^\dagger c_{\mathbf{R}'\tilde{\nu}} \rangle + (c_{\mathbf{R}\tilde{\mu}}^\dagger c_{\mathbf{R}'\tilde{\nu}} - \langle c_{\mathbf{R}\tilde{\mu}}^\dagger c_{\mathbf{R}'\tilde{\nu}} \rangle), \\ c_{\mathbf{R}\tilde{\mu}}^\dagger c_{\mathbf{R}'\tilde{\nu}}^\dagger &\sim \langle c_{\mathbf{R}\tilde{\mu}}^\dagger c_{\mathbf{R}'\tilde{\nu}}^\dagger \rangle + \underbrace{(c_{\mathbf{R}\tilde{\mu}}^\dagger c_{\mathbf{R}'\tilde{\nu}}^\dagger - \langle c_{\mathbf{R}\tilde{\mu}}^\dagger c_{\mathbf{R}'\tilde{\nu}}^\dagger \rangle)}_{\text{small fluctuation}}. \end{aligned} \quad (1.44)$$

By inserting the above in the interacting part of the Hamiltonian, H_{int} , and only keep up to linear order in the small fluctuations, we arrive at the mean-field decoupled Hamiltonian seen in eqn. (4)

$$\begin{aligned} H^{\text{MF}} &= - \sum_{\mathbf{R}, \mathbf{R}'} c_{\mathbf{R}\tilde{\mu}}^\dagger (t_{\mathbf{R}, \mathbf{R}'}^{\tilde{\mu}\tilde{\nu}} + \mu_0 \delta_{\mathbf{R}, \mathbf{R}'} \delta_{\tilde{\mu}, \tilde{\nu}}) c_{\mathbf{R}'\tilde{\nu}} + \sum_{\mathbf{R}, \mathbf{R}'} c_{\mathbf{R}\tilde{\mu}}^\dagger ([N_{\mathbf{R}}]^{\tilde{\mu}\tilde{\nu}} \delta_{\mathbf{R}, \mathbf{R}'} - [N_{\mathbf{R}, \mathbf{R}'}]_{\tilde{\nu}}^{\tilde{\mu}}) c_{\mathbf{R}'\tilde{\nu}} \\ &\quad + \frac{1}{2} \sum_{\mathbf{R}, \mathbf{R}'} (c_{\mathbf{R}\tilde{\mu}}^\dagger [\Delta_{\mathbf{R}, \mathbf{R}'}]_{\tilde{\nu}}^{\tilde{\mu}} c_{\mathbf{R}'\tilde{\nu}}^\dagger + \text{h.c.}) + \text{const.}, \end{aligned} \quad (1.45)$$

where we introduced the direct, exchange and superconducting fields

$$\begin{aligned} [N_{\mathbf{R}}]^{\tilde{\mu}\tilde{\nu}} &= \sum_{\mathbf{R}'} [V_{\mathbf{R}, \mathbf{R}'}]_{\tilde{\mu}'\tilde{\nu}'}^{\tilde{\mu}\tilde{\nu}} \langle c_{\mathbf{R}'\tilde{\mu}'}^\dagger c_{\mathbf{R}'\tilde{\nu}'} \rangle, & [N_{\mathbf{R}, \mathbf{R}'}]_{\tilde{\nu}}^{\tilde{\mu}} &= [V_{\mathbf{R}, \mathbf{R}'}]_{\tilde{\mu}'\tilde{\nu}'}^{\tilde{\mu}\tilde{\nu}'} \langle c_{\mathbf{R}'\tilde{\mu}'}^\dagger c_{\mathbf{R}\tilde{\nu}'} \rangle, \\ \text{and} & & [\Delta_{\mathbf{R}, \mathbf{R}'}]_{\tilde{\nu}}^{\tilde{\mu}} &= [V_{\mathbf{R}, \mathbf{R}'}]_{\tilde{\nu}\tilde{\nu}'}^{\tilde{\mu}\tilde{\mu}'} \langle c_{\mathbf{R}'\tilde{\nu}'} c_{\mathbf{R}\tilde{\mu}'} \rangle, \end{aligned} \quad (1.46)$$

respectively. Once more, we emphasize that summation over repeated spin and orbital indices is implied.

The kinetic part of the Hamiltonian, H_{kin} , is assumed to be left invariant under the symmetry elements of the (magnetic) space group $(\mathcal{M}) \mathcal{G}$. Within this group, we find the self-conjugate translation subgroup \mathcal{T} , which contains all Bravais lattice translations $\{E | \mathbf{R}\}$. Because of this, as we explicitly saw in sec. 1.2, it is often convenient to block diagonalize the Hamiltonian with respect to the IRs of \mathcal{T} . As it turns out, see eqn. 1.39, this is nothing but a simple Fourier transform of the Hamiltonian, which, for the prototypical Hamiltonian, reads

$$H^{\text{MF}} = \frac{1}{\mathcal{N}} \sum_{\mathbf{k}, \mathbf{q}} c_{\mathbf{k}+\mathbf{q}\bar{\mu}}^\dagger \left(\xi_{\mathbf{k}+\mathbf{q}, -\mathbf{k}+\mathbf{q}}^{\bar{\mu}\bar{\nu}} + [N_{\mathbf{Q}}]^{\bar{\mu}\bar{\nu}} - [N_{\mathbf{k}+\mathbf{q}, -\mathbf{k}+\mathbf{q}}]_{\bar{\nu}}^{\bar{\mu}} \right) c_{\mathbf{k}-\mathbf{q}\bar{\nu}} + \frac{1}{2\mathcal{N}} \sum_{\mathbf{k}, \mathbf{q}} \left(c_{\mathbf{k}+\mathbf{q}\bar{\mu}}^\dagger [\Delta_{\mathbf{k}+\mathbf{q}, -\mathbf{k}+\mathbf{q}}]_{\bar{\nu}}^{\bar{\mu}} c_{-\mathbf{k}+\mathbf{q}\bar{\nu}}^\dagger + \text{h.c.} \right) + \text{const.}, \quad (1.47)$$

where $\mathbf{Q} = 2\mathbf{q}$. In the above, we used the following definitions of the Fourier transforms

$$f_{\mathbf{Q}} = \sum_{\mathbf{R}} f_{\mathbf{R}} e^{-i\mathbf{Q}\cdot\mathbf{R}} \quad \Leftrightarrow \quad f_{\mathbf{R}} = \frac{1}{\mathcal{N}} \sum_{\mathbf{Q}} f_{\mathbf{Q}} e^{i\mathbf{Q}\cdot\mathbf{R}}, \quad (1.48)$$

$$f_{\mathbf{k}+\mathbf{q}, -\mathbf{k}+\mathbf{q}} = \sum_{\mathbf{R}, \mathbf{R}'} e^{-i(\mathbf{k}+\mathbf{q})\cdot\mathbf{R}} f_{\mathbf{R}, \mathbf{R}'} e^{-i(-\mathbf{k}+\mathbf{q})\cdot\mathbf{R}'} \quad \Leftrightarrow \quad f_{\mathbf{R}, \mathbf{R}'} = \frac{1}{\mathcal{N}^2} \sum_{\mathbf{k}, \mathbf{q}} e^{i(\mathbf{k}+\mathbf{q})\cdot\mathbf{R}} f_{\mathbf{k}+\mathbf{q}, -\mathbf{k}+\mathbf{q}} e^{i(-\mathbf{k}+\mathbf{q})\cdot\mathbf{R}'}$$

More specifically, we define the Hamiltonian terms in wave vector space as follows

$$\begin{aligned} \xi_{\mathbf{k}+\mathbf{q}, -\mathbf{k}+\mathbf{q}}^{\bar{\mu}\bar{\nu}} &= - \sum_{\mathbf{R}, \mathbf{R}'} e^{-i(\mathbf{k}+\mathbf{q})\cdot\mathbf{R}} \left(t_{\mathbf{R}, \mathbf{R}'}^{\bar{\mu}\bar{\nu}} + \mu_0 \delta_{\mathbf{R}, \mathbf{R}'} \delta_{\bar{\mu}, \bar{\nu}} \right) e^{-i(-\mathbf{k}+\mathbf{q})\cdot\mathbf{R}'}, \\ [N_{\mathbf{Q}}]^{\bar{\mu}\bar{\nu}} &= \sum_{\mathbf{R}} [N_{\mathbf{R}}]^{\bar{\mu}\bar{\nu}} e^{-i\mathbf{Q}\cdot\mathbf{R}}, \\ [N_{\mathbf{k}+\mathbf{q}, -\mathbf{k}+\mathbf{q}}]_{\bar{\nu}}^{\bar{\mu}} &= \sum_{\mathbf{R}, \mathbf{R}'} e^{-i(\mathbf{k}+\mathbf{q})\cdot\mathbf{R}} [N_{\mathbf{R}, \mathbf{R}'}]_{\bar{\nu}}^{\bar{\mu}} e^{-i(-\mathbf{k}+\mathbf{q})\cdot\mathbf{R}'}, \\ [\Delta_{\mathbf{k}+\mathbf{q}, -\mathbf{k}+\mathbf{q}}]_{\bar{\nu}}^{\bar{\mu}} &= \sum_{\mathbf{R}, \mathbf{R}'} e^{-i(\mathbf{k}+\mathbf{q})\cdot\mathbf{R}} [\Delta_{\mathbf{R}, \mathbf{R}'}]_{\bar{\nu}}^{\bar{\mu}} e^{-i(-\mathbf{k}+\mathbf{q})\cdot\mathbf{R}'}. \end{aligned} \quad (1.49)$$

By explicitly evaluating the above transformations, and assuming translational-invariant interaction potentials, i.e. $[V_{\mathbf{R}, \mathbf{R}'}]_{\bar{\nu}}^{\bar{\mu}} \equiv [V_{\mathbf{R}-\mathbf{R}'}]_{\bar{\nu}}^{\bar{\mu}}$, we get

$$\begin{aligned} [N_{\mathbf{Q}}]^{\bar{\mu}\bar{\nu}} &= [V_{\mathbf{Q}}]_{\bar{\nu}\bar{\nu}'}^{\bar{\mu}\bar{\nu}} \sum_{\mathbf{k}} \langle c_{\mathbf{k}'-\mathbf{q}\bar{\mu}'}^\dagger c_{\mathbf{k}'+\mathbf{q}\bar{\nu}'} \rangle, & [N_{\mathbf{k}+\mathbf{q}, -\mathbf{k}+\mathbf{q}}]_{\bar{\nu}}^{\bar{\mu}} &= \sum_{\mathbf{k}'} [V_{\mathbf{k}-\mathbf{k}'}]_{\bar{\nu}\bar{\nu}'}^{\bar{\mu}\bar{\nu}'} \langle c_{\mathbf{k}'-\mathbf{q}\bar{\mu}'}^\dagger c_{\mathbf{k}'+\mathbf{q}\bar{\nu}'} \rangle, \\ \text{and} & & [\Delta_{\mathbf{k}+\mathbf{q}, -\mathbf{k}+\mathbf{q}}]_{\bar{\nu}}^{\bar{\mu}} &= \sum_{\mathbf{k}'} [V_{\mathbf{k}-\mathbf{k}'}]_{\bar{\nu}\bar{\nu}'}^{\bar{\mu}\bar{\nu}'} \langle c_{-\mathbf{k}'+\mathbf{q}\bar{\nu}'} c_{\mathbf{k}'+\mathbf{q}\bar{\mu}'} \rangle. \end{aligned} \quad (1.50)$$

From eqn. (1.48), we see that \mathbf{k} is the wave vector related to the relative position $\mathbf{R} - \mathbf{R}'$, whereas $\mathbf{Q} = 2\mathbf{q}$ is related to the absolute coordinates \mathbf{R} and $(\mathbf{R} + \mathbf{R}')/2$, for $f_{\mathbf{Q}}$ and $f_{\mathbf{k}+\mathbf{q}, -\mathbf{k}+\mathbf{q}}$, respectively. However, a translational invariant system can only depend on the relative coordinate $\mathbf{R} - \mathbf{R}'$, meaning that all fields will have $\mathbf{Q} = \mathbf{0}$, and the Hamiltonian will be diagonal in \mathbf{k} . In fact, the latter was the sole motivation behind rewriting the Hamiltonian in terms of the IRs of \mathcal{T} .

Now, by explicitly assuming H_{kin} to be left invariant under the space group symmetries, we must have that $t_{\mathbf{R}, \mathbf{R}'}^{\bar{\mu}\bar{\nu}} \equiv t_{\mathbf{R}-\mathbf{R}'}^{\bar{\mu}\bar{\nu}}$, ultimately leading to a \mathbf{Q} independent dispersion $\xi_{\mathbf{k}}^{\bar{\mu}\bar{\nu}}$. On the other hand, as

discussed in the introductory chapter of this thesis, the fields introduced in the mean-field decoupling will in general belong to some subgroup of the space group, and can lead to a spontaneous symmetry breaking. There is therefore no restriction saying that $\mathbf{Q} = \mathbf{0}$ for these fields, and they can therefore potentially give rise to new Bravais lattices, as for example seen for spin, charge and pair density waves. Usually, such phase transitions can be identified by peaks away from $\mathbf{Q} = \mathbf{0}$ in the relevant susceptibilities. Note, furthermore, that disorder generally also leads to a Hamiltonian with $\mathbf{Q} \neq \mathbf{0}$, as for example seen in chap. 2.

Despite the above, we will in the following assume the system to be translational invariant with respect to the space group \mathcal{G} , for which the following relation holds $f_{\mathbf{k}, -\mathbf{k}'} = \mathcal{N} f_{\mathbf{k}} \delta_{\mathbf{k}, -\mathbf{k}'}$, resulting in

$$\begin{aligned} \xi_{\mathbf{k}+\mathbf{q}, -\mathbf{k}+\mathbf{q}}^{\tilde{\mu}\tilde{\nu}} &= \mathcal{N} \delta_{\mathbf{q}, \mathbf{0}} \xi_{\mathbf{k}}^{\tilde{\mu}\tilde{\nu}}, & [N_{\mathbf{q}}]^{\tilde{\mu}\tilde{\nu}} &= \mathcal{N} \delta_{\mathbf{q}, \mathbf{0}} [N]^{\tilde{\mu}\tilde{\nu}}, \\ [N_{\mathbf{k}+\mathbf{q}, -\mathbf{k}+\mathbf{q}}]^{\tilde{\mu}}_{\tilde{\nu}} &= \mathcal{N} \delta_{\mathbf{q}, \mathbf{0}} [N_{\mathbf{k}}]^{\tilde{\mu}}_{\tilde{\nu}}, & [\Delta_{\mathbf{k}+\mathbf{q}, -\mathbf{k}+\mathbf{q}}]^{\tilde{\mu}}_{\tilde{\nu}} &= \mathcal{N} \delta_{\mathbf{q}, \mathbf{0}} [\Delta_{\mathbf{k}}]^{\tilde{\mu}}_{\tilde{\nu}}, \end{aligned} \quad (1.51)$$

where $[N_{\mathbf{R}}]^{\tilde{\mu}\tilde{\nu}} \equiv [N]^{\tilde{\mu}\tilde{\nu}}$, i.e. the field has the same value at all lattice sites. We thus only need to perform the Fourier transforms with respect to the relative coordinate $\boldsymbol{\delta} = \mathbf{R} - \mathbf{R}'$

$$\begin{aligned} \xi_{\mathbf{k}}^{\tilde{\mu}\tilde{\nu}} &= - \sum_{\boldsymbol{\delta}} \left(t_{\boldsymbol{\delta}}^{\tilde{\mu}\tilde{\nu}} + \mu_0 \delta_{\boldsymbol{\delta}, \mathbf{0}} \delta_{\tilde{\mu}, \tilde{\nu}} \right) e^{-i\mathbf{k} \cdot \boldsymbol{\delta}}, \\ [N_{\mathbf{k}}]^{\tilde{\mu}}_{\tilde{\nu}} &= \sum_{\boldsymbol{\delta}} [N_{\boldsymbol{\delta}}]^{\tilde{\mu}}_{\tilde{\nu}} e^{-i\mathbf{k} \cdot \boldsymbol{\delta}} = \frac{1}{\mathcal{N}} \sum_{\mathbf{k}'} [V_{\mathbf{k}-\mathbf{k}'}]^{\tilde{\mu}}_{\tilde{\nu}} \langle c_{\mathbf{k}'\tilde{\mu}'}^{\dagger} c_{\mathbf{k}'\tilde{\nu}'} \rangle, \\ [\Delta_{\mathbf{k}}]^{\tilde{\mu}}_{\tilde{\nu}} &= \sum_{\boldsymbol{\delta}} [\Delta_{\boldsymbol{\delta}}]^{\tilde{\mu}}_{\tilde{\nu}} e^{-i\mathbf{k} \cdot \boldsymbol{\delta}} = \frac{1}{\mathcal{N}} \sum_{\mathbf{k}} [V_{\mathbf{k}-\mathbf{k}'}]^{\tilde{\mu}}_{\tilde{\nu}'} \langle c_{-\mathbf{k}'\tilde{\nu}'} c_{\mathbf{k}'\tilde{\mu}'} \rangle, \end{aligned} \quad (1.52)$$

and arrive at the following simple looking Hamiltonian

$$H^{\text{MF}} = \sum_{\mathbf{k}} c_{\mathbf{k}\tilde{\mu}}^{\dagger} \left(\xi_{\mathbf{k}}^{\tilde{\mu}\tilde{\nu}} + [N]^{\tilde{\mu}\tilde{\nu}} - [N_{\mathbf{k}}]^{\tilde{\mu}}_{\tilde{\nu}} \right) c_{\mathbf{k}\tilde{\nu}} + \frac{1}{2} \sum_{\mathbf{k}} \left(c_{\mathbf{k}\tilde{\mu}}^{\dagger} [\Delta_{\mathbf{k}}]^{\tilde{\mu}}_{\tilde{\nu}} c_{-\mathbf{k}\tilde{\nu}}^{\dagger} + \text{h.c.} \right) + \text{const.} \quad (1.53)$$

1.B Symmetries of Anomalous Terms

Throughout chap. 1 we studied the fundamental symmetry aspects of the normal state single-particle Hamiltonian \mathcal{H} . However, the prototypical Hamiltonian H in eqn. (1.1) carries also the anomalous terms \mathcal{A}_{ij} ($\mathcal{A}_{ij}^{\dagger}$), which are bilinear in fermionic creation (annihilation) operators. This must mean that these terms transform differently compared to \mathcal{H} . Below, we explicitly carry out the symmetry transformations for the anomalous terms \mathcal{A}_{ij} , and their hermitian counterparts, for non-spatial and spatial symmetries. Lastly, we also infer the well-established BdG formalism for H , and write up the corresponding representation $D_{\text{BdG}}^{\text{X}}[U]$ for the unitary operator U . Conclusively we find that the BdG representation conserves the multiplication rule, i.e. $D_{\text{BdG}}^{\text{X}}[U_m] D_{\text{BdG}}^{\text{X}}[U_n] = D_{\text{BdG}}^{\text{X}}[U_m U_n]$, thus all the derivations made for the single-particle representation $D[U_m]$ applies.

Non-Spatial Symmetries of Anomalous Terms

We have already determined how the fermionic operators transform under the three non-spatial symmetries; time reversal T , charge conjugation C and chiral symmetry S , see sec. 1.1, and we therefore

straightforwardly obtain the relations, that need to be satisfied for the respective symmetries to be present

$$\begin{aligned} T \left(\sum_{i,j} c_i^\dagger \mathcal{A}_{ij} c_j^\dagger + \text{h.c.} \right) T^{-1} &= \sum_{l,i} \sum_{j,k} c_l^\dagger \langle l|U_T|i\rangle \mathcal{A}_{ij}^* \langle j|U_T^\dagger|k\rangle^* c_k^\dagger + \text{h.c.} \\ &\Rightarrow \mathcal{A}_{ij} = \sum_{l,k} \langle i|U_T|l\rangle \mathcal{A}_{lk}^* \langle k|U_T^\dagger|j\rangle^*, \end{aligned} \quad (1.54)$$

$$\begin{aligned} C \left(\sum_{i,j} c_i^\dagger \mathcal{A}_{ij} c_j^\dagger + \text{h.c.} \right) C^{-1} &= \sum_{l,i} \sum_{j,k} c_l \langle l|U_C|i\rangle^* \mathcal{A}_{ij} \langle j|U_C^\dagger|k\rangle c_k + \text{h.c.} \\ &\Rightarrow \mathcal{A}_{ij} = - \sum_{l,k} \langle i|U_C|l\rangle \mathcal{A}_{lk}^* \langle k|U_C^\dagger|j\rangle^*, \end{aligned} \quad (1.55)$$

$$\begin{aligned} S \left(\sum_{i,j} c_i^\dagger \mathcal{A}_{ij} c_j^\dagger + \text{h.c.} \right) S^{-1} &= \sum_{l,i} \sum_{j,k} c_l \langle l|U_S|i\rangle^* \mathcal{A}_{ij}^* \langle j|U_S^\dagger|k\rangle c_k + \text{h.c.} \\ &\Rightarrow \mathcal{A}_{ij} = - \sum_{l,k} \langle i|U_S|l\rangle \mathcal{A}_{lk} \langle k|U_S^\dagger|j\rangle^*. \end{aligned} \quad (1.56)$$

Spatial Symmetries of Anomalous Terms

We now proceed with the transformation of \mathcal{A}_{ij} under the influence of spatial symmetries. As for the non-spatial symmetries, we already know how the fermionic operators transform under $O = U, A$, see eqn. (1.14), and we thus readily find

$$\begin{aligned} O \left(\sum_{i,j} c_i^\dagger \mathcal{A}_{ij} c_j^\dagger + \text{h.c.} \right) O^{-1} &= \sum_{i,l} \sum_{j,k} c_l^\dagger \langle l|U|i\rangle \mathcal{A}_{ij} \langle j|U^\dagger|k\rangle^* c_k^\dagger + \text{h.c.} \\ &\Rightarrow \mathcal{A}_{ij} = \sum_{l,k} \langle i|U|l\rangle \mathcal{A}_{lk} \langle k|U^\dagger|j\rangle^*, \end{aligned} \quad (1.57)$$

$$\begin{aligned} O \left(\sum_{i,j} c_i^\dagger \mathcal{A}_{ij} c_j^\dagger + \text{h.c.} \right) O^{-1} &= \sum_{i,l} \sum_{j,k} c_l^\dagger \langle l|U_A|i\rangle \mathcal{A}_{ij}^* \langle j|U_A^\dagger|k\rangle^* c_k^\dagger + \text{h.c.} \\ &\Rightarrow \mathcal{A}_{ij} = \sum_{l,k} \langle i|U_A|l\rangle \mathcal{A}_{lk}^* \langle k|U_A^\dagger|j\rangle^*, \end{aligned} \quad (1.58)$$

which needs to be satisfied in order for the system to exhibit the given symmetry.

Bogoliubov-de Gennes Representation

Convenient for single-particle Hamiltonians is that these can simply be represented as matrices $D[h]^{ij} = \langle i|h|j\rangle$. Note that we here, in contrast to the main text, adopt h as the single particle Hamiltonian. The BdG formalism takes this idea one step further, and combines h_{ij} and \mathcal{A}_{ij} into a single matrix, by considering the fermionic operators as basis vectors. In doing so, we effectively

double the number of degrees of freedom, and arrive at the Hamiltonian

$$\begin{aligned} H &= \sum_{i,j} c_i^\dagger h_{ij} c_j + \frac{1}{2} \sum_{i,j} \left(c_i^\dagger \mathcal{A}_{ij} c_j^\dagger + \text{h.c.} \right) + \text{const.} \\ &= \frac{1}{2} \sum_{i,j} \begin{pmatrix} c_i^\dagger & c_i \end{pmatrix} \begin{pmatrix} h_{ij} & \mathcal{A}_{ij} \\ -\mathcal{A}_{ij}^* & -h_{ij}^* \end{pmatrix} \begin{pmatrix} c_j \\ c_j^\dagger \end{pmatrix} + \frac{1}{2} \sum_i \mathcal{H}_{ii} + \text{const.} \end{aligned} \quad (1.59)$$

By applying our knowledge on charge conjugation symmetric single-particle Hamiltonians, see eqn. (1.8), and co-representations, see eqn. (1.28), we see that the BdG formalism is nothing but a basis extension from $\{|i\rangle\}$ to $\{|i\rangle, C|i\rangle\}$. Specifically

$$\begin{aligned} h|j\rangle &= \sum_i |i\rangle \langle i|h|j\rangle = \sum_i D[h]^{ij} |i\rangle \\ hC|j\rangle &= \sum_i C|i\rangle \langle i|C^{-1}hC|j\rangle = \sum_i D[C^{-1}hC]^{ij} C|i\rangle = -\sum_i D^*[h]^{ij} C|i\rangle. \end{aligned} \quad (1.60)$$

The latter only holds true if $[H_{\text{norm}}, C] = 0$. Adopting this notation furthermore implies

$$\begin{aligned} \mathcal{A}C|j\rangle &= \sum_i |i\rangle \langle i|\mathcal{A}C|j\rangle = \sum_i D[\mathcal{A}C]^{ij} |i\rangle \equiv \sum_i \mathcal{A}_{ij} |i\rangle, \\ \mathcal{A}|j\rangle &= \sum_i C|i\rangle \langle i|C^{-1}\mathcal{A}|j\rangle = \sum_i D[C^{-1}\mathcal{A}]^{ij} C|i\rangle \equiv -\sum_i \mathcal{A}_{ij}^* C|i\rangle = -\sum_i D^*[\mathcal{A}C]^{ij} C|i\rangle, \end{aligned} \quad (1.61)$$

revealing that we can readily adopt the anomalous terms as matrices. The latter equality above tells us, that all anomalous terms are odd under quantum number exchange, i.e. $D^\top[\mathcal{A}C] = -D[\mathcal{A}C]$, assuming \mathcal{A} is hermitian. By expressing the full Hamiltonian, here denoted by \mathcal{H} , in the extended BdG basis, we find the following matrix representation

$$D_{\text{BdG}}[\mathcal{H}]^{ij} = \begin{pmatrix} D[h]^{ij} & D[\mathcal{A}C]^{ij} \\ -D^*[\mathcal{A}C]^{ij} & -D^*[h]^{ij} \end{pmatrix}. \quad (1.62)$$

By performing the same steps for some unitary operator U_m , we get that any unitary operator conserves the multiplication rule, see eqn. (1.17), and takes the the form

$$\sum_l D_{\text{BdG}}^X[U_m]^{il} D_{\text{BdG}}^X[U_n]^{lj} = D_{\text{BdG}}^X[U_m U_n]^{ij}, \quad D_{\text{BdG}}^X[U_m]^{ij} = \begin{pmatrix} D[U_m]^{ij} & 0 \\ 0 & \chi D^*[U_m]^{ij} \end{pmatrix}. \quad (1.63)$$

This representation is thus isomorphic to $D[U_m]$, and all the rules defined in sec. 1.2 for finite groups apply. Here $\chi = \pm 1$, and is defined for every unitary symmetry, through the relation [35, 36]

$$\chi D[\mathcal{A}C] = D[U]D[\mathcal{A}C]D^\top[U]. \quad (1.64)$$

Ultimately we find the following relations, that need to be fulfilled for the respective symmetry to be present in the BdG Hamiltonian

$$\begin{aligned} T : & \quad D_{\text{BdG}}[\mathcal{H}] = D_{\text{BdG}}[U_T] D_{\text{BdG}}^\top[\mathcal{H}] D_{\text{BdG}}^\dagger[U_T], \\ C : & \quad D_{\text{BdG}}[\mathcal{H}] = -D_{\text{BdG}}[U_C] D_{\text{BdG}}^\top[\mathcal{H}] D_{\text{BdG}}^\dagger[U_C], \\ S : & \quad D_{\text{BdG}}[\mathcal{H}] = -D_{\text{BdG}}[U_S] D_{\text{BdG}}[\mathcal{H}] D_{\text{BdG}}^\dagger[U_S], \end{aligned} \quad (1.65)$$

for the non-spatial symmetries, and

$$\begin{aligned} U : \quad D_{\text{BdG}}[\mathcal{H}] &= D_{\text{BdG}}^{\times}[U]D_{\text{BdG}}[\mathcal{H}](D_{\text{BdG}}^{\times}[U])^{\dagger}, \\ A : \quad D_{\text{BdG}}[\mathcal{H}] &= D_{\text{BdG}}^{\times}[U_A]D_{\text{BdG}}^{\top}[\mathcal{H}](D_{\text{BdG}}^{\times}[U_A])^{\dagger}, \end{aligned} \quad (1.66)$$

for the spatial symmetries, i.e. relations similar to those for the single-particle Hamiltonian discussed in the main text. Note, however, that for the BdG representation, $D_{\text{BdG}}[U_C]$ takes the form

$$D_{\text{BdG}}[U_C]^{ij} = \begin{pmatrix} 0 & D^*[U_C]^{ij} \\ D[U_C]^{ij} & 0 \end{pmatrix}. \quad (1.67)$$

Now, let us momentarily reintroduce the relevant electronic degrees of freedom $i = \{\mathbf{R}\mu\sigma\}$. For a given orbital μ and lattice site \mathbf{R} , it is sometimes custom to order the basis in the following way

$$\{|\mathbf{R}\mu \uparrow\rangle, |\mathbf{R}\mu \downarrow\rangle, C|\mathbf{R}\mu \uparrow\rangle, C|\mathbf{R}\mu \downarrow\rangle\}. \quad (1.68)$$

However, as we see in the main text chap. 4 and 5, it proves convenient to adopt instead the following rotated basis

$$\{|\mathbf{R}\mu \uparrow\rangle, |\mathbf{R}\mu \downarrow\rangle, C|\mathbf{R}\mu \downarrow\rangle, -C|\mathbf{R}\mu \uparrow\rangle\}. \quad (1.69)$$

By introducing the Pauli spin matrices $\boldsymbol{\sigma}$ accompanied by the respective identity matrix $\mathbf{1}_{\sigma}$, we note that the BdG matrix representation of the Hamiltonian, and a given unitary operator U_m , take the following forms in this new basis

$$\begin{aligned} D_{\text{BdG}}[\mathcal{H}] &= \begin{pmatrix} D[h] & D[\mathcal{A}C](-i\sigma_y) \\ i\sigma_y D^{\dagger}[\mathcal{A}C] & -\sigma_y D^{\top}[h]\sigma_y \end{pmatrix}, & D_{\text{BdG}}^{\times}[U_m] &= \begin{pmatrix} D[U_m] & 0 \\ 0 & \sigma_y \chi D^*[U_m]\sigma_y \end{pmatrix}, \\ D_{\text{BdG}}[U_C] &= \begin{pmatrix} 0 & D^*[U_C](-i\sigma_y) \\ D[U_C](i\sigma_y) & 0 \end{pmatrix}, \end{aligned} \quad (1.70)$$

where D now represents matrices in the combined \mathbf{R} , μ and σ space. Next, going through the same arguments but in the wave vector representation, we readily find

$$D_{\text{BdG}}[\mathcal{H}_{\mathbf{k}}] = \begin{pmatrix} D[h_{\mathbf{k}}] & D[\mathcal{A}_{\mathbf{k}}C](-i\sigma_y) \\ i\sigma_y D^{\dagger}[\mathcal{A}_{\mathbf{k}}C] & -\sigma_y D^{\top}[h_{-\mathbf{k}}]\sigma_y \end{pmatrix}, \quad D_{\text{BdG}}^{\times}[U_{m;\mathbf{k}}] = \begin{pmatrix} D[U_{m;\mathbf{k}}] & 0 \\ 0 & \sigma_y \chi D^*[U_{m;-\mathbf{k}}]\sigma_y \end{pmatrix}. \quad (1.71)$$

Furthermore, for the wave vector representation of the BdG Hamiltonian, we find the following relations that need to be satisfied for the system to display the respective symmetries

$$\begin{aligned} T : \quad D_{\text{BdG}}[\mathcal{H}_{\mathbf{k}}] &= D_{\text{BdG}}[U_T]D_{\text{BdG}}^{\top}[\mathcal{H}_{-\mathbf{k}}]D_{\text{BdG}}^{\dagger}[U_T], \\ C : \quad D_{\text{BdG}}[\mathcal{H}_{\mathbf{k}}] &= -D_{\text{BdG}}[U_C]D_{\text{BdG}}^{\top}[\mathcal{H}_{-\mathbf{k}}]D_{\text{BdG}}^{\dagger}[U_C], \\ S : \quad D_{\text{BdG}}[\mathcal{H}_{\mathbf{k}}] &= -D_{\text{BdG}}[U_S]D_{\text{BdG}}[\mathcal{H}_{\mathbf{k}}]D_{\text{BdG}}^{\dagger}[U_S], \end{aligned} \quad (1.72)$$

$$\begin{aligned} U : \quad D_{\text{BdG}}[\mathcal{H}] &= D_{\text{BdG}}^{\times}[U]D_{\text{BdG}}[\mathcal{H}_{\mathbf{k}}](D_{\text{BdG}}^{\times}[U])^{\dagger}, \\ A : \quad D_{\text{BdG}}[\mathcal{H}] &= D_{\text{BdG}}^{\times}[U_A]D_{\text{BdG}}^{\top}[\mathcal{H}_{-\mathbf{k}}](D_{\text{BdG}}^{\times}[U_A])^{\dagger}. \end{aligned} \quad (1.73)$$

2

Disorder-Induced Electronic Nematicity



Info: This chapter has been published by me, Panagiotis Kotetes, Indranil Paul and Brian M. Andersen in [*Phys. Rev. B* **100**, 064521 (2019)].

2.1 Introduction

The study of electronic nematic quantum phases [3] is becoming increasingly important in condensed matter systems due to a growing class of recently discovered materials exhibiting nematic behavior, i.e. spontaneous generation of spatial anisotropy. Nematicity has been experimentally identified in a number of correlated quantum materials [3], including quantum Hall states in higher Landau levels of 2D electron gases [167, 168], bilayer strontium ruthenates [169], cuprate high-temperature superconductors [170], doped Bi_2Se_3 superconductors [171–173], FeSCs [45–59] and, possibly, twisted bilayer graphene [174]. Thus, nematicity begins to be established as a universal electronic state of matter, which motivates further theoretical studies of its distinct properties.

Nematic phases are particularly prevalent in Fe-based superconductors, where experimental evidence for electronic nematicity comes from a wide range of techniques, including transport measurements [45–52], angle-resolved photoemission spectroscopy [53], scanning tunneling spectroscopy [54], neutron scattering [55], light spectroscopy [56, 57, 175], Andreev-point-contact measurements [58] and torque magnetometry [59]. In this case, the emergence of nematicity refers to the spontaneous breaking of fourfold (C_4) rotational symmetry. Notably, the identification of the driving mechanism of nematicity in these systems is complicated, due to the coupling of spin, orbital, and lattice degrees of freedom at temperatures T below the tetragonal-to-orthorhombic structural phase transition occurring

	E	$2C_4$	C_2	$2C'_2$	$2C''_2$	I	$2S_4$	σ_h	$2\sigma_v$	$2\sigma_d$	Basis functions
A_{1g}	+1	+1	+1	+1	+1	+1	+1	+1	+1	+1	$x^2 + y^2, z^2, f_{\mathbf{k}}^s$
A_{2g}	+1	+1	+1	-1	-1	+1	+1	+1	-1	-1	L_z
B_{1g}	+1	-1	+1	+1	-1	+1	-1	+1	+1	-1	$x^2 - y^2, f_{\mathbf{k}}^d$
B_{2g}	+1	-1	+1	-1	+1	+1	-1	+1	-1	+1	xy
E_g	+2	0	-2	0	0	+2	0	-2	0	0	$(L_x, L_y), (xz, yz)$
A_{1u}	+1	+1	+1	+1	+1	-1	-1	-1	-1	-1	
A_{2u}	+1	+1	+1	-1	-1	-1	-1	-1	+1	+1	z
B_{1u}	+1	-1	+1	+1	-1	-1	+1	-1	-1	+1	xyz
B_{2u}	+1	-1	+1	-1	+1	-1	+1	-1	+1	-1	$z(x^2 - y^2)$
E_u	+2	0	-2	0	0	-2	0	+2	0	0	$(x, y), (f_{\mathbf{k}}^{px}, f_{\mathbf{k}}^{py})$

Table 2.1: Character table for the point group D_{4h} , where we also included the basis functions $f_{\mathbf{k}} = \cos k_x + \cos k_y$, $f_{\mathbf{k}}^d = \cos k_x - \cos k_y$ and $(f_{\mathbf{k}}^{px}, f_{\mathbf{k}}^{py}) = i\sqrt{2}(\sin k_x, \sin k_y)$.

at $T = T_{\text{nem}}$ [60]. Particularly, the origin of nematicity in FeSe remains controversial at present [61].

The growing ubiquity of nematic correlated electronic systems, that are scarcely free from impurities, calls for resolving the influence of disorder on the emergence of nematicity. In fact, the strong relevance of disorder to the nematic ordering is also supported from a notable number of experiments detecting local C_4 -symmetry breaking around impurities [54, 176–181]. While some of these results may be attributable to, for instance, residual sample strain which explicitly breaks the C_4 symmetry locally [181–183], or the presence of stripe-ordered antiferromagnetism [176], the possible pinning of nematic fluctuations due to the presence of disorder appears as a promising and, at the moment, poorly-explored alternative [184–188]. Disorder has also been proposed to play an important role in generating split structural (nematic) and magnetic transitions in some FeSCs [189]. Even more, there are strong indications for disorder-pinned static local nematicity in the bulk tetragonal phase, i.e. above T_{nem} [59, 190–195]. For example, two recent NMR experiments on FeSe [192, 193], found a clear splitting and broadening of the NMR lineshape above T_{nem} . The presence of short-range nematic order above the bulk T_{nem} in FeSe has also been inferred from ARPES and optical-pump conductivity measurements [196, 197]. Finally, two very recent pair distribution function (PDF) measurements of FeSe found clear evidence of pronounced local orthorhombicity at the length scale of a few nm well above T_{nem} [198, 199], thus providing additional evidence for disorder-induced local nematicity in these systems.

Here, we perform a detailed theoretical study of the role of disorder in systems with D_{4h} point-group symmetry, see table. 2.1, which additionally feature strong fluctuations or ordering in the nematic channel. The emergence of nematicity is reflected in a non-zero field $N(\mathbf{r})$, which transforms according to the B_{1g} IR of D_{4h} . We mainly focus on T above the respective T_{nem} , at which, the spontaneous thermodynamic C_4 -symmetry breaking takes place. By employing both phenomenological and microscopic approaches, we address the following three questions: 1) Under what circumstances can disorder generate nematicity locally? 2) What is the spatial profile of the resulting nematic-defect structure? 3) How do finite disorder concentrations influence the nematic transition?

Our main results can be summarized as follows. For $T > T_{\text{nem}}$, *i)* an impurity potential of arbitrary strength with a spatial profile which respects the C_4 symmetry, generates a local nematic field $N(\mathbf{r})$ with a spatial profile belonging to the B_{1g} IR. By transferring to a polar coordinate system $(x, y) \rightarrow (r, \phi)$, this yields the spatial profile $N(r, \phi) \propto \cos(2\phi)$. *ii)* This further implies, that, an impurity potential with a C_4 -symmetric profile does not induce net nematicity, i.e., $\int d\mathbf{r} N(\mathbf{r}) = 0$, but local probes may still detect evidence of C_4 symmetry breaking. *iii)* However, we show that such a potential can still drive a nematic transition already at $T > T_{\text{nem}}$, since it modifies the Stoner criterion for the nematic instability. *iv)* A C_4 -symmetry-breaking impurity potential can induce nonzero net nematicity and, thus, stabilize long-range nematic order. For $T < T_{\text{nem}}$, an impurity potential with a spatial profile which respects C_4 symmetry modifies the bulk nematicity (N_B) locally, and results in an inhomogeneous nematic field $N(\mathbf{r}) = N_B + \delta N(\mathbf{r})$, with a $\delta N(r, \phi)$ which is generally not proportional to $\cos(2\phi)$.

2.2 Phenomenological Landau Approach

We first examine the implications of disorder within a continuum Landau approach, that allows exposing generic features of the induced nematic field, i.e. independent of the origin of the electronic nematicity. In fact, our Landau results also apply to situations where the nematic field originates from the spontaneous mixing of superconducting order parameters belonging to the A_{1g} and B_{1g} IRs [200, 201]. However, there, one has to further include the possible influence of disorder on the pairing.

The free energy density $\mathcal{F}(\mathbf{r})$ is a functional of $N(\mathbf{r})$ and the disorder potential $V(\mathbf{r})$. Its invariance under D_{4h} point group operations and time reversal T , leads to

$$\mathcal{F}[N(\mathbf{r}), V(\mathbf{r})] = \alpha(T - T_{\text{nem}}) \frac{[N(\mathbf{r})]^2}{2} + \beta \frac{[N(\mathbf{r})]^4}{4} + c \frac{[\nabla N(\mathbf{r})]^2}{2} + g N(\mathbf{r}) (\partial_x^2 - \partial_y^2) V(\mathbf{r}), \quad (2.1)$$

with $\alpha, \beta, c > 0$. Here, we restricted to the *lowest-order* possible coupling between $V(\mathbf{r})$ and $N(\mathbf{r})$. Later on, we consider effects of higher-order terms. For further details on the Landau approach, we refer to app. 2.A. From eqn. (2.1), one observes that the nematic field couples to the second derivatives of the disorder potential and, thus, to a particular linear combination of the electric field gradients. The nematic field is proportional to the quadrupolar electronic charge density defined as $Q_{x^2-y^2}(\mathbf{r}) = (x^2 - y^2)\rho(\mathbf{r})$, which transforms according to the B_{1g} IR of D_{4h} , i.e. similar to $N(\mathbf{r})$. In the above, $\rho(\mathbf{r})$ denotes the electric charge density, which belongs to the trivial A_{1g} IR of D_{4h} . The appearance of a nonzero $N(\mathbf{r})$, solely due to the presence of disorder, is a consequence of the broken translational invariance, and can be viewed as a result of linear response, since the electric field gradient $(\partial_x^2 - \partial_y^2) V(\mathbf{r})$ acts as a quadrupolar source field, which leads to a nonzero and *necessarily* inhomogeneous $Q_{x^2-y^2}(\mathbf{r})$ and thus $N(\mathbf{r})$.

For the remainder, we consider $T > T_{\text{nem}}$ (unless explicitly stated), which implies that the system resides in the C_4 -symmetric phase in the absence of disorder. In this case, we can drop the quartic nematic term, since $N(\mathbf{r})$ is generally small. Thus, for $T > T_{\text{nem}}$, the Euler-Lagrange equation of motion for eqn. (2.1) reads

$$[\alpha(T - T_{\text{nem}}) - c\nabla^2]N(\mathbf{r}) = -g(\partial_x^2 - \partial_y^2)V(\mathbf{r}). \quad (2.2)$$

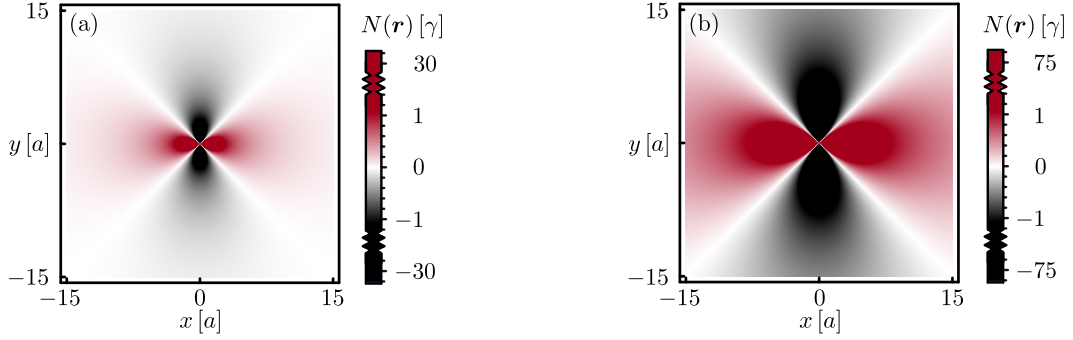


Figure 2.1: (a) Nematic order parameter $N(\mathbf{r})$ at $T \gg T_{\text{nem}}$, where $\xi_{\text{nem}} \sim 5a$. (b) Same as in (a), but with $T \gtrsim T_{\text{nem}}$ resulting in a larger nematic coherence length $\xi_{\text{nem}} \sim 15a$. The figures were obtained using eqn. (2.3) with a convenient impurity profile of the form $V(\mathbf{r}) = V/|\mathbf{r}|$, without loss of generality. We introduced $\gamma = -\pi gV/(2\xi_{\text{nem}})$ and used $c = 1$.

The above equation of motion provides the proportionality relation between the electric field gradient and the resulting nematic field, i.e.

$$N(\mathbf{r}) = \frac{g}{c} \int \frac{d\mathbf{q}}{(2\pi)^2} \frac{(q_x^2 - q_y^2)V(\mathbf{q})}{\mathbf{q}^2 + \xi_{\text{nem}}^{-2}} e^{i\mathbf{q}\cdot\mathbf{r}}, \quad (2.3)$$

where we introduced the nematic coherence length in the tetragonal phase $\xi_{\text{nem}}^{-1} = \sqrt{\alpha(T - T_{\text{nem}})/c}$.

For a C_4 -symmetric impurity potential we integrate the angular part of the right-hand side in eqn. (2.3), and find the earlier-announced spatial profile $N(r, \phi) \propto \cos(2\phi)$. This profile decays away from the impurity within a range given by ξ_{nem} , and this length scale diverges as $T \rightarrow T_{\text{nem}}$. Both results are depicted in fig. 2.1. The angular dependence transforms exactly according to the B_{1g} IR of D_{4h} . This constraint on the spatial profile of $N(\mathbf{r})$ is a direct consequence of the featureless A_{1g} nature of the disorder potential $V(\mathbf{r})$ itself. Thus, the net electronic nematicity and quadrupolar charge are zero, since

$$\int d\mathbf{r} N(\mathbf{r}) = N(\mathbf{q} = \mathbf{0}) \propto \int_0^{2\pi} d\phi N(r, \phi) = 0. \quad (2.4)$$

Nonetheless, probes like NMR and PDF pick up a signal from atoms in the lobes of the induced $N(\mathbf{r})$, and do therefore detect clear evidence for local nematicity and orthorhombicity even though global effects are absent.

Equation 2.4 also reveals that the linear coupling of the nematic field to the electric field gradient cannot stabilize a net thermodynamic nematicity which emerges when $N(\mathbf{q} = \mathbf{0}) \neq 0$. Therefore, the quadrupolar coupling can neither preempt nor smear out the bulk nematic phase transition. A nonzero $N(\mathbf{q} = \mathbf{0})$ can, however, be induced when the spatial profile of the disorder potential explicitly breaks C_4 symmetry. This can be seen by including higher-order couplings in the Landau free energy (see also app 2.A)

$$\delta\mathcal{F}(\mathbf{r}) = -\left(g'V(\mathbf{r}) + g''[V(\mathbf{r})]^2\right) \frac{[N(\mathbf{r})]^2}{2}. \quad (2.5)$$

The above terms provide couplings between $V(\mathbf{q} \neq \mathbf{0})$ and $N(\mathbf{q} = \mathbf{0})$, as well as the $N(\mathbf{q} \neq \mathbf{0})$ nematic-field components. These couplings are essential to describe a disorder-driven preemptive nematic transition above T_{nem} , as well as the emergence of net nematicity when the potential breaks C_4 symmetry. To demonstrate both aspects, we derive the modified equation of motion for the $N(\mathbf{q} = \mathbf{0})$ component after adding the contribution of eqn. (2.5) to the free energy of eqn. (2.1). We find the following equation of motion

$$\alpha(T - T_{\text{nem}})N(\mathbf{q} = \mathbf{0}) = g' \int d\mathbf{p} V(\mathbf{p})N(-\mathbf{p}) + g'' \int d\mathbf{p} \int d\mathbf{p}' V(\mathbf{p}')V(\mathbf{p} - \mathbf{p}')N(-\mathbf{p}). \quad (2.6)$$

Thus, a nonzero $N(\mathbf{q} = \mathbf{0})$ can only emerge when components with $\mathbf{q} \neq \mathbf{0}$ are already nonzero. By assuming that the potential is weak, the $N(\mathbf{q} \neq \mathbf{0})$ components remain given by the Fourier transform of eqn. (2.2). Therefore, we obtain the following equation up to second order in $V(\mathbf{r})$

$$\left[\alpha(T - T_{\text{nem}}) - g'' \int d\mathbf{p} |V(\mathbf{p})|^2 \right] N(\mathbf{q} = \mathbf{0}) = \frac{gg'}{c} \int d\mathbf{p} \frac{(p_x^2 - p_y^2) |V(\mathbf{p})|^2}{p^2 + \xi_{\text{nem}}^{-2}}. \quad (2.7)$$

Equation (2.7) implies that a C_4 -symmetric configuration of impurities cannot source a homogeneous component for the nematic field, since the right-hand side is zero. As we prove in app 2.A, this holds even after including all the symmetry-allowed higher-order Landau terms. In fact, this result is also recovered in the case of a large number of randomly-distributed and uncorrelated impurities, in which situation, translational and rotational symmetries are preserved on average. Thus, a C_4 -symmetric disorder potential solely modifies the nematic Stoner criterion, i.e.

$$T_{\text{nem}}^{\text{imp}} = T_{\text{nem}} + \frac{g''}{\alpha} \int d\mathbf{p} |V(\mathbf{p})|^2. \quad (2.8)$$

Depending on the microscopic details which control the sign of the coupling constant g'' , the nematic transition temperature can be enhanced. Note, however, that such an enhancement tends to zero in the thermodynamic limit, unless a critical density of impurities n_{imp} is present. This is because the g'' coefficient is inversely proportional to the system size. Interestingly, a detailed transport study with controlled disorder by electron irradiation found cases where the critical nematic transition temperature increased slightly with disorder [202].

Before proceeding, we point out that the first term of eqn. (2.5) also allows to describe the induced net nematicity when the disorder potential breaks C_4 symmetry. To exemplify this, we consider a dimer impurity potential $V(\mathbf{r}) = V[\delta(\mathbf{r} - \hat{\mathbf{x}}) + \delta(\mathbf{r} + \hat{\mathbf{x}})]$, which yields $V(\mathbf{p}) = V(f_{\mathbf{p}}^s + f_{\mathbf{p}}^d)$, where the basis functions $f_{\mathbf{k}}^{\gamma}$ are defined in table 2.1. The breaking of C_4 symmetry is ensured by the combined presence of the A_{1g} and B_{1g} IRs. In general, a nonzero $N(\mathbf{q} = \mathbf{0})$ arises whenever $|V(\mathbf{q})|^2$ contains at least one B_{1g} term.

2.3 Microscopic Model and Self-Consistent Calculations

To support the above Landau findings, we employ a microscopic tight-binding model of electrons coupled to disorder. This analysis not only verifies the above Landau results, but more importantly, allows to uncover further microscopic details which control the emergence of nematicity. In the absence of disorder, the electrons are described by the dispersion $\xi_{\mathbf{k}} = -2t f_{\mathbf{k}}^s - \mu_0$. The spin degree of freedom is neglected throughout this work, since it merely introduces a factor of 2 in all thermodynamic

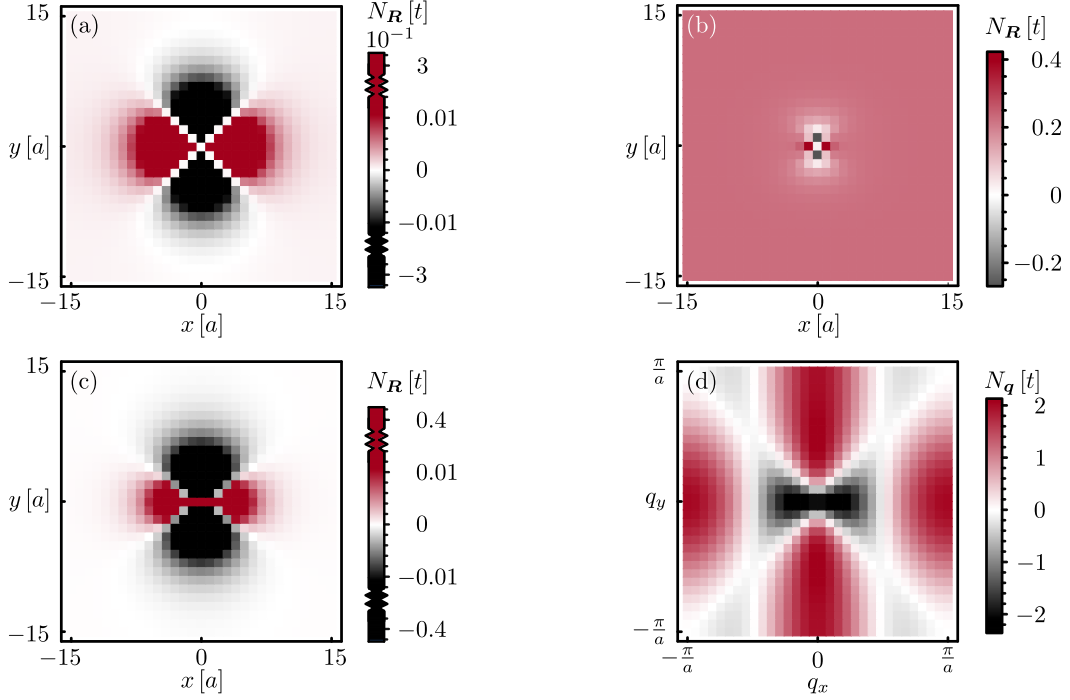


Figure 2.2: Numerically-obtained nematic order parameter using the microscopic model in eqn. (2.10): (a) displays the local nematic order pinned by a single impurity at $\mathbf{R} = \mathbf{0}$ for $T = 0.8t$. For the given set of parameters, the Stoner criterion is fulfilled for $T \sim 0.78t$. (b) Same as in (a), but in the bulk nematic phase ($T = 0.76t$). (c) Induced nematic order in the presence of a dimer impurity potential, $V_{\mathbf{R}} = V(\delta_{\mathbf{R},\hat{x}} + \delta_{\mathbf{R},-\hat{x}})$, and (d) its discrete Fourier transform ($T = 0.8t$). From panel (d), one clearly sees that the breaking of C_4 symmetry indeed induces $N_{\mathbf{q}=\mathbf{0}} \neq 0$. All the figures were obtained using $V = 5t$, $\mathcal{N}_x = \mathcal{N}_y = 31$, $V_{\text{nem}} = 4t$, $k_B = 1$ and $\langle n \rangle = 0.53$.

averages. We assume that the electrons feel an attractive effective interaction in the Pomeranchuk nematic channel as in ref. [203], which, after mean-field decoupling, yields the nematic order parameter (for details see app. 2.B)

$$N_{\mathbf{R}} = -\frac{V_{\text{nem}}}{2} \sum_{\delta} f_{\delta}^d \langle c_{\mathbf{R}+\delta}^{\dagger} c_{\mathbf{R}} + c_{\mathbf{R}}^{\dagger} c_{\mathbf{R}+\delta} \rangle, \quad (2.9)$$

i.e. the lattice analog of $N(\mathbf{r})$. This introduces a local or global C_4 -breaking to the electron-hopping matrix elements. The d -wave form factor in real-space is nonzero for $\delta = \pm\hat{x}, \pm\hat{y}$, and reads $f_{\pm\hat{x}}^d = -f_{\pm\hat{y}}^d = 1/2$. Note that \hat{x} (\hat{y}) corresponds to the unit vector in the x (y) direction. Disorder is considered in the form of point-like identical impurities. The total mean-field Hamiltonian becomes

$$H^{\text{MF}} = -\sum_{\mathbf{R},\delta} c_{\mathbf{R}}^{\dagger} (2t f_{\delta}^s + \mu_0 \delta_{\delta,\mathbf{0}}) c_{\mathbf{R}+\delta} + \frac{1}{2} \sum_{\mathbf{R},\delta} N_{\mathbf{R}} f_{\delta}^d (c_{\mathbf{R}+\delta}^{\dagger} c_{\mathbf{R}} + \text{h.c.}) + \sum_{\mathbf{R}} c_{\mathbf{R}}^{\dagger} V_{\mathbf{R}} c_{\mathbf{R}}, \quad (2.10)$$

where we also made use of the s -wave form factor in the real space representation $f_{\pm\hat{x}}^s = f_{\pm\hat{y}}^s = 1/2$.

For a single delta-function impurity potential $V_{\mathbf{R}} = V\delta_{\mathbf{R},\mathbf{0}}$, we evaluate the nematic order parameter in eqn. (2.9) self-consistently for a fixed electron density $\langle n \rangle$ (see app. 2.D). The resulting nematic

order is displayed in fig. 2.2(a), and possesses the same spatial profile as those shown in fig. 2.1. In the case of a dimer impurity potential $V_{\mathbf{R}} = V(\delta_{\mathbf{R},\hat{x}} + \delta_{\mathbf{R},-\hat{x}})$, which explicitly breaks C_4 symmetry, we obtain the profile shown in fig. 2.2(c). Its Fourier transform, see fig. 2.2(d), exhibits $N_{\mathbf{q}=\mathbf{0}} \neq 0$, which originates from the right-hand side of eqn. (2.7). We stress that, the fact that the induced clover pattern in fig. 2.2(a) is directly sourced by the electric field gradient, makes it distinct from other microscopic studies of impurity-induced local order [204–206]. There, the impurity potential induces a spontaneous symmetry breaking locally, by means of a local fulfillment of the Stoner criterion, i.e. analogously to eqn. (2.8).

We proceed by studying the effects of a single impurity for $T < T_{\text{nem}}$, where the system resides in the bulk phase with a value N_{B} for the nematic order parameter. In this case, the order parameter assumes the form $N(\mathbf{r}) = N_{\text{B}} + \delta N(\mathbf{r})$, where $\delta N(\mathbf{r})$ incorporates the spatial variation of the nematic order parameter near the impurity. For a weak impurity potential, we expand the equation of motion stemming from eqn. (2.1) up to linear order in $\delta N(\mathbf{r})$ (see app. 2.A). We find that $\delta N(\mathbf{r})$ possesses the spatial profile of eqn. (2.3), with the difference that the coherence length is now given by $\xi_{\text{nem}}^{-1} = \sqrt{2\alpha(T_{\text{nem}} - T)/c}$ due to an additional contribution of the quartic term which has to be taken into account for $T < T_{\text{nem}}$. From a microscopic calculation, we obtain the spatial profile for the nematic order parameter which is shown in fig. 2.2(b), exhibiting an anisotropic local structure which is slightly elongated along the y direction. To lowest order in $V(\mathbf{r})$, this asymmetry found via the microscopic model can be reproduced in the Landau theory by including the first term of eqn. (2.5). The presence of this term yields $\delta N(\mathbf{r}) \propto f(r) \cos(2\phi) + h(r)N_{\text{B}}$, where $f(r)$ and $h(r)$ are decaying functions of the radial coordinate, transforming according to the A_{1g} IR. Note that additional higher order terms, e.g. $\propto V(\mathbf{r})(\partial_x^2 + \partial_y^2)[N(\mathbf{r})]^2$, can further contribute to this anisotropy by modifying $h(r)$. In general, we find that depending on the sign of the impurity potential, point-like disorder at $T < T_{\text{nem}}$ may either locally enhance or decrease the nematic order.

Finally, we verify the possibility of disorder-enhanced T_{nem} within the microscopic model. We assume random and dilute disorder of density n_{imp} , that on average preserves the C_4 symmetry. Within the 1st order Born approximation [165], the quasiparticle lifetime is

$$\frac{1}{\tau_{\mathbf{k}}} = 2\pi n_{\text{imp}} V^2 \frac{1}{\mathcal{N}} \sum_{\mathbf{p}} \delta_{\xi_{\mathbf{p}}, \xi_{\mathbf{k}}}. \quad (2.11)$$

By use of eqn. (2.11), we can evaluate the microscopic coefficients which enter the modified Stoner criterion of eqn. (2.8), brought about by the impurities. Starting from eqn. (2.9), we find that the self-consistency equation for the $\mathbf{q} = \mathbf{0}$ component of the nematic mean-field order parameter, corresponding to net nematicity $N \equiv \sum_{\mathbf{R}} N_{\mathbf{R}}/\mathcal{N} = N_{\mathbf{q}=\mathbf{0}}/\mathcal{N}$, reads

$$N = -V_{\text{nem}} \frac{1}{\mathcal{N}} \sum_{\mathbf{k}} f_{\mathbf{k}}^d \int_{-\infty}^{+\infty} \frac{d\xi}{2\pi} \frac{n_F(\xi + \xi_{\mathbf{k}} + N f_{\mathbf{k}}^d)}{\xi^2 + 1/(2\tau_{\mathbf{k}})^2} \frac{1}{\tau_{\mathbf{k}}}, \quad (2.12)$$

with $n_F(\xi)$ the Fermi-Dirac distribution function. Linearizing the right-hand side with respect to N , yields the modified Stoner criterion

$$\frac{1}{V_{\text{nem}}} = -\frac{1}{\mathcal{N}} \sum_{\mathbf{k}} (f_{\mathbf{k}}^d)^2 \int_{-\infty}^{+\infty} \frac{d\xi}{2\pi} \frac{n'_F(\xi + \xi_{\mathbf{k}})}{\xi^2 + 1/(2\tau_{\mathbf{k}})^2} \frac{1}{\tau_{\mathbf{k}}}. \quad (2.13)$$

In the absence of disorder, i.e. $\tau_{\mathbf{k}} \rightarrow \infty$, the integration yields the derivative of the Fermi-Dirac distribution $n'_F(\xi_{\mathbf{k}})$. However, for finite $\tau_{\mathbf{k}}$, each \mathbf{k} state is broadened, and the density of states for the

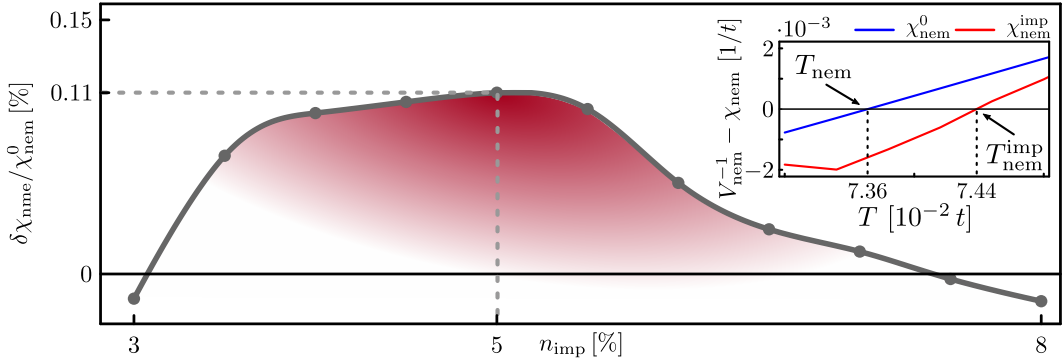


Figure 2.3: Relative disorder-induced modification of the nematic susceptibility $\delta\chi_{\text{nem}}/\chi_{\text{nem}}^0 = (\chi_{\text{nem}}^{\text{imp}} - \chi_{\text{nem}}^0)/\chi_{\text{nem}}^0$ versus the disorder concentration n_{imp} . Here, χ_{nem}^0 is the right-hand side of eqn. (2.13) in the absence of disorder $\tau_{\mathbf{k}} \rightarrow \infty$. The inset shows that the T_{nem} increases by approximately 1% for $n_{\text{imp}} \approx 5\%$, due to the disorder-modified Stoner criterion. Parameters: $V_{\text{nem}} = 1.584t$, $\langle n \rangle = 0.53$, $\mathcal{N}_x = \mathcal{N}_y = 201$, $T = 0.075t$ and $V = 5t$.

\mathbf{k} points mainly contributing to the nematic instability may be enhanced. To explore this effect, we numerically calculate the nematic susceptibility $\chi_{\text{nem}}^{\text{imp}}$ in the presence of disorder, which is identified with the right-hand side of eqn. (2.13). Figure 2.3 shows how this quantity changes versus the disorder concentration n_{imp} , relative to the disorder-free case. For an impurity density of $n_{\text{imp}} \approx 5\%$, we obtain the maximal relative enhancement of $\chi_{\text{nem}}^{\text{imp}}$ leading to a corresponding small enhancement of T_{nem} . It is tempting to assign the similar small enhancement of the nematic transition temperature measured experimentally in ref. [202] to the effect demonstrated in fig. 2.3.

The origin of the enhancement effect shown in fig. 2.3 is the presence of a nearby van Hove singularity whose spectral weight can be utilized to boost $\chi_{\text{nem}}^{\text{imp}}$ in the presence of finite $\tau_{\mathbf{k}}$. Without favorable density of states conditions, disorder generally suppresses the nematic susceptibility and hence also T_{nem} . Such a suppression tendency has been previously found in ref. [207] and is also demonstrated in our app. 2.E. Further, we remark that even in the disorder-free case, the presence of a van Hove singularity is pivotal for the stabilization of an electron nematic phase of the Pomeranchuk type. For more details see refs. [208, 209].

2.4 Summary

In summary, we have elucidated the coupling of nematicity to disorder from both a phenomenological Landau approach and microscopic calculations. Importantly, disorder is always locally relevant for inducing nematicity since the electric field gradient $(\partial_x^2 - \partial_y^2)V(\mathbf{r})$ directly acts as a quadrupolar source field for nematicity. This explains the detection of local nematicity/orthorhombicity in experimental probes sensitive to different atomic environments within materials. At the global scale, however, disorder does not generally generate long-range nematicity at $T > T_{\text{nem}}$ where the system remains tetragonal. Finite disorder concentrations may, however, under favorable circumstances enhance nematic order.

Appendices for Chapter 2

2.A Landau Theory: Phenomenological Analysis

Equation 2.1 of the main text is obtained by demanding that the free energy density is a real functional transforming according to the trivial IR of the ensuing point group. Here, we assume a system with tetragonal and inversion symmetries present, which is described by the D_{4h} point group symmetry. The free energy density transforms according to the A_{1g} IR of D_{4h} and is here also assumed invariant under time reversal.

Equation of Motion

The equation describing the nematic field is found via the Euler-Lagrange equation of motion

$$\frac{\partial \mathcal{F}}{\partial N} = \partial_x \frac{\partial \mathcal{F}}{\partial (\partial_x N)} + \partial_y \frac{\partial \mathcal{F}}{\partial (\partial_y N)} \quad (2.14)$$

and reads

$$[\alpha(T - T_{\text{nem}}) - c\nabla^2]N(\mathbf{r}) + \beta[N(\mathbf{r})]^3 = -g(\partial_x^2 - \partial_y^2)V(\mathbf{r}). \quad (2.15)$$

From the above, one notes that if the potential $V(\mathbf{r})$ is homogeneous, i.e. $V(\mathbf{r}) = V$, the equation of motion includes only derivatives of $N(\mathbf{r})$ and no other spatially-dependent functions or source terms. Thus, for an infinite (bulk) system $N(\mathbf{r}) = N$. When $T > T_{\text{nem}}$, the appearance of nematicity is disfavored and, thus, $N = 0$ in the bulk. In contrast, the presence of an inhomogeneous potential functions as a source of nematicity and allows for non-zero inhomogeneous solutions of $N(\mathbf{r})$.

Case Study: Single Impurity for $T > T_{\text{nem}}$

Above T_{nem} , we drop the cubic term in the equation of motion in eqn. (2.15) above, and obtain eqn. (2.2) of the main text. For a potential satisfying $V(\mathbf{q}) = V(|\mathbf{q}|)$, we set $q_x = q \cos \theta$, $q_y = q \sin \theta$, $x = r \cos \phi$ and $y = r \sin \phi$, and find

$$N(r, \phi) = -\cos(2\phi) \frac{g}{c} \int_0^\infty \frac{dq}{2\pi} \frac{q^3 V(q)}{q^2 + \xi_{\text{nem}}^{-2}} J_2(qr), \quad (2.16)$$

with $J_2(z)$ the respective Bessel function of the first kind. One notes the distinctive angular dependence of the spatial profile of the induced nematic order, which is fixed by the B_{1g} IR of $N(\mathbf{r})$, the A_{1g} IR

of $V(\mathbf{r})$, and the fourfold-symmetric impurity profile. We resolve the radial dependence in the case $V(\mathbf{r}) = V/r$, and find

$$N(r, \phi) = \frac{\gamma}{c} [I_2(r/\xi_{\text{nem}}) - L_{-2}(r/\xi_{\text{nem}})] \cos(2\phi), \quad (2.17)$$

where we introduced the modified Bessel and Struve functions, and defined $\gamma = -\pi gV/(2\xi_{\text{nem}})$. Notably, the decaying function in the brackets yields approximately 1/2 for $r = \xi_{\text{nem}}$.

Non-Induction of Net Nematicity by a C_4 -Symmetric Potential

In this section we explore whether there exists a term in the Landau expansion which can induce a nonzero $N(\mathbf{q} = \mathbf{0})$ for an impurity-potential profile which preserves C_4 symmetry. Consider the most general term

$$\int d\mathbf{r} [N(\mathbf{r})]^n [V(\mathbf{r})]^m (\partial_x^2 - \partial_y^2)^\ell V(\mathbf{r}) \quad (2.18)$$

where, if ℓ is odd, then $n = \ell + 2\mathbb{N}$. We fix the spatial profile of $V(\mathbf{r})$ to be C_4 -symmetric. The above general term can be mapped to two distinct types of couplings

$$\int d\mathbf{r} [N(\mathbf{r})]^{2n}, \quad \text{and} \quad \int d\mathbf{r} [N(\mathbf{r})]^{2n+1} (\partial_x^2 - \partial_y^2) V(\mathbf{r}). \quad (2.19)$$

The respective equations of motion read

$$N(\mathbf{r}) \propto [N(\mathbf{r})]^{2n-1} \quad \text{and} \quad N(\mathbf{r}) \propto [N(\mathbf{r})]^{2n} (\partial_x^2 - \partial_y^2) V(\mathbf{r}). \quad (2.20)$$

We Fourier transform the first equation and find

$$N(\mathbf{q} = \mathbf{0}) \propto \int d\mathbf{p}_1 \dots \int d\mathbf{p}_{2n-1} N(\mathbf{p}_1) \dots N(\mathbf{p}_{2n-1}) \delta\left(\sum_s^{2n-1} \mathbf{p}_s\right). \quad (2.21)$$

Assuming that the components appearing on the right-hand side are given by

$$\bar{N}(\mathbf{q}) = \frac{g}{c} \frac{(q_x^2 - q_y^2)V(\mathbf{q})}{\mathbf{q}^2 + \xi_{\text{nem}}^{-2}} \equiv \cos(2\theta) \frac{g}{c} \frac{q^2 V(q)}{q^2 + \xi_{\text{nem}}^{-2}}, \quad (2.22)$$

where we set $q_x = q \cos \theta$ and $q_y = q \sin \theta$, we find that the angular part of the integral is proportional to

$$\int_0^{2\pi} d\theta_1 \dots \int_0^{2\pi} d\theta_{2n-2} \cos(2\theta_1) \dots \cos(2\theta_{2n-2}) \left[\sum_{s=1}^{2n-2} p_s^2 \cos(2\theta_s) + \sum_{s \neq \ell}^{2n-2} p_s p_\ell \cos(\theta_s + \theta_\ell) \right] = 0, \quad (2.23)$$

where we set $\cos \theta_s = p_{s,x}/p_s$ and $\sin \theta_s = p_{s,y}/p_s$, with $p_s = |\mathbf{p}_s|$. A similar treatment for the remaining equation also yields zero. This result naturally confirms, that a C_4 -symmetric spatial profile for the impurity potential cannot lead to net nematicity.

Case Study: Single Impurity for $T < T_{\text{nem}}$

In order to explain the elongated clover-like spatial profile induced by the impurity in the bulk nematic phase ($T < T_{\text{nem}}$), we need to include higher order terms in the free energy described by eqn. (2.15). To demonstrate how this elongation comes about, it is sufficient to solely retain the first term of eqn. (2.5) presented in the main text. The modified equation of motion has the form

$$[\alpha(T - T_{\text{nem}}) - c\nabla^2]N(\mathbf{r}) + \beta[N(\mathbf{r})]^3 = -g(\partial_x^2 - \partial_y^2)V(\mathbf{r}) + g'N(\mathbf{r})V(\mathbf{r}). \quad (2.24)$$

We separate the nematic field into two parts, i.e. $N(\mathbf{r}) = N_{\text{B}} + \delta N(\mathbf{r})$. Here, N_{B} denotes the value of the bulk nematic order parameter and is given by $\beta N_{\text{B}}^2 = \alpha(T_{\text{nem}} - T)$ for $T < T_{\text{nem}}$, while $\delta N(\mathbf{r})$ denotes the contribution stemming from the presence of the impurity. For $|\delta N(\mathbf{r})| \ll |N_{\text{B}}|$ we linearize the above equation of motion and obtain

$$[2\alpha(T_{\text{nem}} - T)/c - \nabla^2]\delta N(\mathbf{r}) = -\frac{g}{c}(\partial_x^2 - \partial_y^2)V(\mathbf{r}) + \frac{g'}{c}N_{\text{B}}V(\mathbf{r}). \quad (2.25)$$

In the above, we retained the terms which lead to a $\delta N(\mathbf{r})$ which is linear in terms of the strength of the impurity potential. Within this assumption, we dropped the term $\delta N(\mathbf{r})V(\mathbf{r})$ which leads to higher-order contributions with respect to the strength of the impurity potential. In the same line of arguments as the ones leading to eqn. (2.16), we obtain a constant angular profile superimposed on the usual $\cos(2\phi)$ -form

$$\delta N(r, \phi) = -\cos(2\phi)\frac{g}{c}\int_0^\infty \frac{dq}{2\pi} \frac{q^3 V(q)}{q^2 + \xi_{\text{nem}}^{-2}} J_2(qr) + N_{\text{B}}\frac{g'}{c}\int_0^\infty \frac{dq}{2\pi} \frac{qV(q)}{q^2 + \xi_{\text{nem}}^{-2}} J_0(qr), \quad (2.26)$$

with the coherence length being given now by $\xi_{\text{nem}}^{-2} = 2\alpha(T_{\text{nem}} - T)$ due to the contribution of the quartic term of the free energy. In connection to eqn. (2.17), we find that for $V(\mathbf{r}) = V/r$

$$\begin{aligned} \delta N(r, \phi) &= \frac{\gamma}{c} \left[I_2 \left(\frac{r}{\xi_{\text{nem}}} \right) - L_{-2} \left(\frac{r}{\xi_{\text{nem}}} \right) \right] \cos(2\phi) - \frac{\gamma'}{c} \left[I_0 \left(\frac{r}{\xi_{\text{nem}}} \right) - L_0 \left(\frac{r}{\xi_{\text{nem}}} \right) \right] N_{\text{B}} \\ &\equiv f(r) \cos(2\phi) + h(r)N_{\text{B}} \end{aligned} \quad (2.27)$$

with $\gamma' = -\pi g' V \xi_{\text{nem}}/2$. From the above, one can read off the decaying functions $f(r)$ and $h(r)$ discussed in the main text. This spatial profile does indeed lead to a profile on the same form as the anisotropic induced order in fig. 2.2(b). Furthermore, note that it is the presence of the nonzero bulk nematic order parameter N_{B} , that induces the anisotropy.

2.B Interaction in the Nematic Channel and Mean-Field Theory Decoupling

We assume the presence of the interaction

$$H_{\text{int}} = -\frac{V_{\text{nem}}}{2} \sum_{\mathbf{R}} \mathcal{O}_{\mathbf{R}}^2, \quad (2.28)$$

which contributes to the desired nematic channel. In the above, we have introduced

$$\mathcal{O}_{\mathbf{R}} = \frac{1}{2} \sum_{\delta} f_{\delta}^d \left(c_{\mathbf{R}+\delta}^{\dagger} c_{\mathbf{R}} + c_{\mathbf{R}}^{\dagger} c_{\mathbf{R}+\delta} \right), \quad (2.29)$$

where we have defined the real space lattice version of the d -wave form factor $f_{\pm\hat{x}}^d = -f_{\pm\hat{y}}^d = 1/2$. Note that the lattice constant has been set to unity. We perform a mean-field decoupling of the interaction in the direct channel by introducing the nematic order parameter $N_{\mathbf{R}} = -V_{\text{nem}}\langle\mathcal{O}_{\mathbf{R}}\rangle$. The latter steps led to eqn. (2.9) of the main text. In wavevector space we have $N_{2\mathbf{q}} = \sum_{\mathbf{R}} N_{\mathbf{R}} e^{-i2\mathbf{q}\cdot\mathbf{R}}$ and the complete mean-field Hamiltonian reads

$$H = \frac{1}{\mathcal{N}} \sum_{\mathbf{k}, \mathbf{q}} c_{\mathbf{k}+\mathbf{q}}^\dagger \left(\xi_{\mathbf{k}} \mathcal{N} \delta_{\mathbf{q}, \mathbf{0}} + V_{2\mathbf{q}} + N_{2\mathbf{q}} \frac{f_{\mathbf{k}+\mathbf{q}}^d + f_{-\mathbf{k}+\mathbf{q}}^d}{2} \right) c_{\mathbf{k}-\mathbf{q}} \quad (2.30)$$

with \mathcal{N} being the number of lattice sites, while the nematic form factor in wavevector space takes the form $f_{\mathbf{k}}^d = \cos k_x - \cos k_y$. The mean-field Hamiltonian has to be supplemented with the self-consistency equation for the nematic order parameter, which reads

$$N_{2\mathbf{q}} = -V_{\text{nem}} \sum_{\mathbf{k}} \frac{f_{\mathbf{k}-\mathbf{q}}^d + f_{-\mathbf{k}-\mathbf{q}}^d}{2} \langle c_{\mathbf{k}-\mathbf{q}}^\dagger c_{\mathbf{k}+\mathbf{q}} \rangle \equiv -V_{\text{nem}} T \sum_{\mathbf{k}, k_n} \frac{f_{-\mathbf{k}-\mathbf{q}}^d + f_{\mathbf{k}-\mathbf{q}}^d}{2} G_{\mathbf{k}+\mathbf{q}, k_n; \mathbf{k}-\mathbf{q}, k_n} \quad (2.31)$$

where we introduced the full single-particle fermionic Matsubara Green function

$$G_{\mathbf{k}+\mathbf{q}, k_n; \mathbf{k}-\mathbf{q}, k_n} = -\langle c_{\mathbf{k}+\mathbf{q}, k_n} c_{\mathbf{k}-\mathbf{q}, k_n}^\dagger \rangle. \quad (2.32)$$

In the above, $k_n = (2n+1)\pi T$ ($k_B = 1$) and the Matsubara Green function for the free electrons has the form $G_{\mathbf{k}, k_n}^0 = 1/(ik_n - \xi_{\mathbf{k}})$. The above construction allows us to employ Dyson's equation in order to perform an expansion of the right-hand side of the self-consistency equation with respect to the nematic order parameter and/or the impurity potential.

2.C Landau Theory: Microscopic Analysis

Given the above, here we show how the electro-nematic coefficient g relates to the microscopic parameters for the disorder-free microscopic model under consideration. We employ a perturbative expansion by means of the Dyson equation for the full Matsubara Green function which reads

$$G_{\mathbf{k}+\mathbf{q}, k_n; \mathbf{k}-\mathbf{q}, k_n} = G_{\mathbf{k}, k_n}^0 \delta_{\mathbf{q}, \mathbf{0}} + G_{\mathbf{k}+\mathbf{q}, k_n}^0 \sum_{\mathbf{p}} U_{\mathbf{k}+\mathbf{q}; \mathbf{p}} G_{\mathbf{p}, k_n; \mathbf{k}-\mathbf{q}, k_n}, \quad (2.33)$$

where we introduced

$$U_{\mathbf{k}+\mathbf{q}; \mathbf{p}} = \frac{1}{\mathcal{N}} \left(V_{\mathbf{k}+\mathbf{q}-\mathbf{p}} + N_{\mathbf{k}+\mathbf{q}-\mathbf{p}} \frac{f_{\mathbf{k}+\mathbf{q}}^d + f_{-\mathbf{p}}^d}{2} \right). \quad (2.34)$$

We obtain the lowest order contribution of U by replacing the full Green function on the right-hand side in eqn. (2.33) by the bare one. We find

$$g_{2\mathbf{q}} = -\frac{T}{\mathcal{N}} \sum_{\mathbf{k}, k_n} \frac{f_{-\mathbf{k}-\mathbf{q}}^d + f_{\mathbf{k}-\mathbf{q}}^d}{2} G_{\mathbf{k}+\mathbf{q}, k_n}^0 G_{\mathbf{k}-\mathbf{q}, k_n}^0. \quad (2.35)$$

To facilitate the calculations, we consider the continuum limit of our model and assume spinless single-band electrons with a parabolic dispersion $\xi(\mathbf{k}) = E_F [(k/k_F)^2 - 1]$ with $\mathbf{k} = (k_x, k_y)$, $k = |\mathbf{k}|$ and set $f^d(\mathbf{k}) = (k_x^2 - k_y^2)/k_F^2$. The quantity of interest, after taking into account the symmetries of $\xi(\mathbf{k})$, $f^d(\mathbf{k})$ and restricting up to second order terms in \mathbf{q} , reads

$$g(2\mathbf{q}) \approx -\int \frac{d\mathbf{k}}{(2\pi)^2} \left[n'_F[\xi(k)] + [f^d(\mathbf{k})]^2 \frac{1}{3} E_F^2 n'''_F[\xi(k)] \right] f(\mathbf{q}) \equiv g(q_x^2 - q_y^2). \quad (2.36)$$

2.D Self-Consistent Calculation of the Nematic Order Parameter

By means of the microscopic Hamiltonian in eqn. (2.10) of the main text, we calculate the nematic order parameter self-consistently until we reach an accuracy of 10^{-6} , while keeping the electron density fixed. The expectation values entering in the order parameter and the electron density are calculated by expressing the fermionic field operators in the diagonal basis of the Hamiltonian $c_{\mathbf{R}} = \sum_{\alpha} \gamma_{\alpha} |\mathbf{R}|\alpha\rangle$ with the defining equation $\mathcal{H}\gamma_{\alpha}^{\dagger}|0\rangle = E_{\alpha}|\alpha\rangle$. Here \mathcal{H} is the single-particle Hamiltonian, see eqn. (1.1). This leads to the following simplified expressions for the order parameter, and electron density, respectively

$$N_{\mathbf{R}} = -V_{\text{nem}} \sum_{\delta} \sum_{\alpha} f_{\delta}^d \text{Re}[\langle \alpha | \mathbf{R} + \delta \rangle \langle \mathbf{R} | \alpha \rangle] n_F(E_{\alpha}), \quad \text{and} \quad \langle n \rangle = \frac{1}{\mathcal{N}} \sum_{\alpha} n_F(E_{\alpha}). \quad (2.37)$$

2.E Disorder-Modified Stoner Criterion and the Resulting $T_{\text{nem}}^{\text{imp}}$

In the presence of dilute and uncorrelated identical impurities, the disorder may enhance T_{nem} . This was shown in the main text by investigating the modified nematic Stoner criterion. In fig. 2.4, we provide additional results for other electron-density values. The electron density is calculated via

$$\langle n \rangle = \frac{1}{\mathcal{N}} \sum_{\mathbf{k}} \int_{-\infty}^{\infty} \frac{d\xi}{2\pi} \frac{1}{\tau_{\mathbf{k}}} \frac{n_F(\xi)}{(\xi - \xi_{\mathbf{k}})^2 + 1/(2\tau_{\mathbf{k}})^2}, \quad (2.38)$$

which recovers its usual form $\langle n \rangle = \sum_{\mathbf{k}} n_F(\xi_{\mathbf{k}})/\mathcal{N}$ in the disorder-free case, i.e. $\tau_{\mathbf{k}} \rightarrow \infty$. For these calculations finite size effects are diminishing for $\mathcal{N} \sim 40 \times 10^3$.

In fig. 2.4 we demonstrate two typical situations, in which, T_{nem} becomes either enhanced or reduced. This is reflected in the behavior of the quantity $\delta\chi_{\text{nem}}/\chi_{\text{nem}}^0 \equiv (\chi_{\text{nem}}^{\text{imp}} - \chi_{\text{nem}}^0)/\chi_{\text{nem}}^0$ which is depicted. We first focus on n_{imp} in the vicinity of 5%, i.e. the optimal value discussed in the main text.

For the value $\langle n \rangle = 0.51$ of the electron density, the Fermi energy is tuned very near the van Hove singularity (see figs. 2.4(a,b)), which constitutes the sweet spot for the development of the nematic order parameter in the absence of disorder, since there, χ_{nem}^0 obtains its maximum value. From fig. 2.4(c) we find that introducing disorder worsens the tendency of the system to develop a nematic order parameter as reflected in the negative values of $\delta\chi_{\text{nem}}/\chi_{\text{nem}}^0$. The addition of disorder broadens the spectral function, and the density of states unavoidably becomes lowered, since contributions from low density of states \mathbf{k} points are taken into account. In contrast, in the case $\langle n \rangle = 0.53$ discussed in the main text, and also shown here, the broadening allows the density of states to increase by picking up contributions from the van Hove singularity, while at the same time avoiding significant contributions from other low density of states \mathbf{k} points. Increasing the electron density to $\langle n \rangle = 0.55$ shifts the Fermi level further away from the van Hove singularity and thus reduces its favorable impact on the density of states. As a result, the nematic susceptibility drops and $\delta\chi_{\text{nem}}/\chi_{\text{nem}}^0$ is negative.

The balance between the contributions to the density of states originating from the van Hove singularity and the low density of states \mathbf{k} points is controlled by the concentration of impurities. Varying n_{imp} leads to a modification of the relative strength of the two competing contributions and allows the sign changes of $\delta\chi_{\text{nem}}/\chi_{\text{nem}}^0$ which are shown in fig. 2.4(c) for $\langle n \rangle = 0.55$.

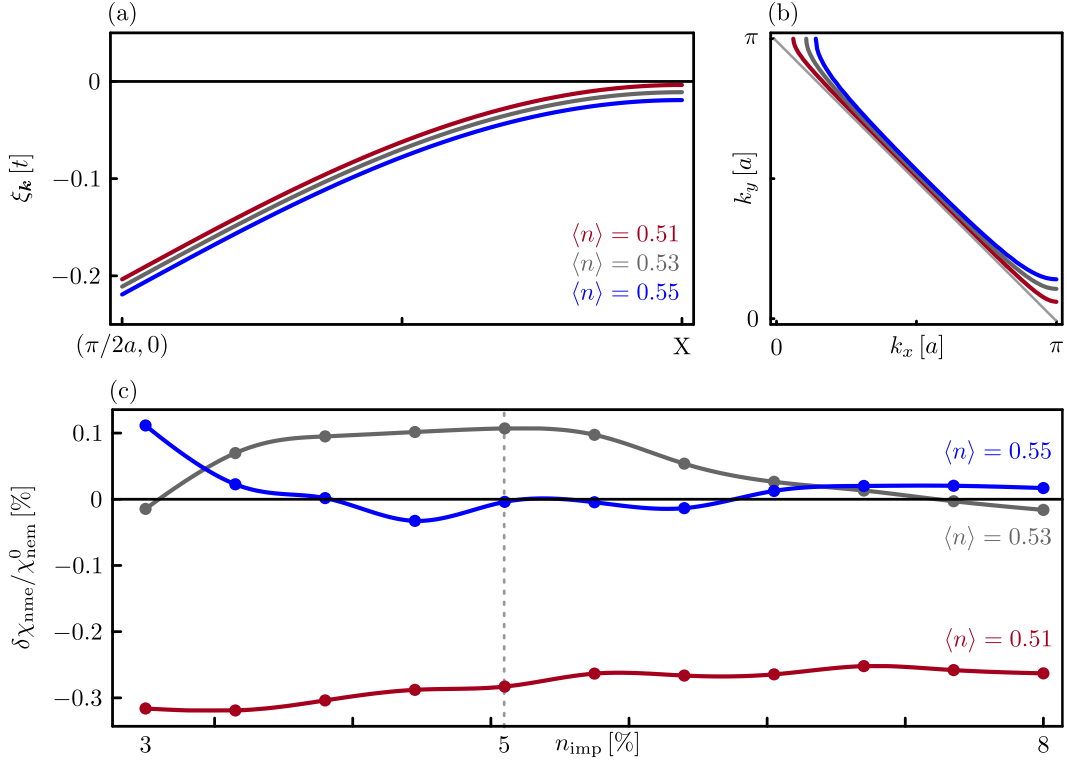


Figure 2.4: (a) Energy dispersion along the ΓX line, (b) Fermi line in (k_x, k_y) space and (c) $\delta\chi_{\text{nem}}/\chi_{\text{nem}}^0$ as a function of n_{imp} , all shown for different electron fillings $\langle n \rangle = 0.51, 0.53, 0.55$. Panel (c) reveals that disorder always has a negative impact on the nematic susceptibility when the Fermi level is tuned very near the van Hove singularity, as inferred for $\langle n \rangle = 0.51$. When the Fermi level is tuned sufficiently away from the van Hove singularity, the resulting nematic susceptibility can be either enhanced or reduced depending on the relative strength of the contributions to the density of states stemming from the van Hove singularity and the low density of states \mathbf{k} points. This ratio is controlled by the concentration of impurities n_{imp} .

3

Inter-Orbital Nematicity and the Origin of a Single Electron Fermi Pocket in FeSe



Info: This chapter has been submitted for publication, and can be found as an [arXiv preprint \[arXiv:2012.07020 \[cond-mat.supr-con\]\]](#) by me, Andreas Kreisel, Peter J. Hirschfeld and Brian M. Andersen. Note that calculations on the spin susceptibility and pairing gap were performed by Andreas Kreisel.

3.1 Introduction

The research of electronic properties of iron-based superconductors has proven to be a rich field that challenges our understanding of correlated multi-band systems. In this respect, particularly the superconducting iron-chalcogenides, FeSe and doped FeTe, have attracted considerable attention due to their unusual low-energy electronic states [61–63]. FeSe enters an orthorhombic phase near $T_{\text{nem}} \sim 90$ K without concomitant static magnetic order at lower temperatures, unlike most of the iron-pnictide superconductors. There is strong evidence that the rotational symmetry breaking at T_{nem} is driven by the electronic degrees of freedom, and thus constitutes a rare example of electronic nematicity [60]. In particular, the spectrum of low-energy spin excitations, thought to drive electron pairing, is extremely anisotropic in untwinned crystals [211]. The superconducting phase sets in around $T_c \sim 9$ K and is therefore generated from an instability of the nematic normal state. Thus, it is not surprising that the superconducting properties also break rotational symmetry, as is indeed observed experimentally [86]. However, the origins of the extreme normal state nematicity, as well as

the reasons for the absence of magnetism at ambient pressure, are still being debated [61–63].

The very high level of rotational anisotropy is evident, e.g., from theoretical modelling of experimental data measured at low temperatures in FeSe [63]. Quite generally, the anisotropy inherent to standard electronic bands in the orthorhombic state, is not enough to explain the much more extreme anisotropy observed experimentally [86, 211–215]. Thus, various interaction-driven feedback effects that enhance the symmetry breaking have been proposed [86, 216–218]. In this respect, several works have argued for orbital-dependent quasiparticle weights Z_μ and shown how this effect may reconcile several experimental probes with simple models [86, 214, 216, 219–222]. The existence of orbital-dependent Z -factors has been explored extensively within dynamical mean-field theory (DMFT) and related methods, and arise naturally in multi-orbital systems with different degrees of orbital contributions to the Fermi level electronic states [219, 223–227]. For the specific case of FeSe, it was shown that Z_{xy} must be strongly reduced from 1, but additionally that a large quasiparticle weight anisotropy of $Z_{xz}/Z_{yz} \sim 0.2 - 0.3$ was necessary in order to obtain agreement with experiments [86, 214, 228] within this approach. The origin of this rather small ratio remains unsettled, but may be related to strong feedback effects on the electronic states close to a stripe magnetic quantum critical point. One of the important implications of these extracted values for the orbital weights Z_μ was that the electron pocket at Y should be nearly completely incoherent, and thus difficult to observe with spectroscopic probes; indeed, no conclusive observation of this pocket has been reported by either angular-resolved photoemission spectroscopy (ARPES) [229–231] or scanning tunneling microscopy (STM) [214].

Subsequently, however, laser ARPES studies reported significant d_{yz} content on the Γ hole pocket, as well as a strong d_{xz} component apparently inconsistent with the extreme scenario of orbital dependent Z -factors [232]. Furthermore, very recent synchrotron ARPES measurements on detwinned FeSe have proposed that the Y pocket may be lifted entirely from the Fermi surface (FS) rather than unobservable due to incoherence [233, 234]. The explanation of the unusual spectroscopic observations of this pocket is therefore important not only to obtain the correct low-energy electronic band structure relevant for (detwinned) nematic FeSe, but also to ultimately understand the origin of the strong electronic nematicity in FeSe.

Obviously, any theoretical approach for explaining the large electronic anisotropy of FeSe relies on having a reasonable starting point for inclusion of interactions in the band structure. It was initially proposed, based on comparison to ARPES data available at the time, that FeSe features nematicity in the d_{xz} and d_{yz} intra-orbital channels with form factors transforming as the IRs A_{1g} and B_{1g} of the given point group [196, 235–241]. More recently, however, several works have advocated for the relevance of (intra-orbital) nematicity involving also the d_{xy} orbitals [126, 242–246]. Until recently, first principles approaches were unable to stabilize a nematic ground state without concomitant stripe magnetism. However a recent density functional theory DFT+U exploration of the energy landscape found a lowest energy nematic state transforming according to the E_u IR of the D_{4h} point group, containing significant inter-orbital nematic components [247]. This form of nematicity, which breaks also inversion symmetry, was shown to produce FSs containing only a single electron pocket [247]. Whether this approach has material-specific predictive power is still an open question¹, however, and in any case it remains important to identify the cause of nematic ordering using more transparent model-based methods.

¹Applying a similar approach to LiFeAs, for example, produces a dramatically distorted low-energy band structure with missing d_{xy} band at the Fermi level. R. Valenti, private communication.

These recent developments raise a number of important questions related to the low-energy band structure and the associated superconducting gap structure of FeSe. For example, what underlying physical interactions naturally produce nematic order that generate single-electron-pocket bands [246, 247], and what are the consequences of this low-energy band structure for our broader understanding of this material?

Here, motivated by several earlier theoretical studies of the effects of longer-range Coulomb interactions on band structure renormalizations of iron-based superconductors [126, 127, 248, 249], we explore the nematic phase spontaneously generated by such interactions. Reference [126] originally investigated these effects for FeSe, and additionally found a dominant intra-orbital d -wave bond nematic order arising from nearest neighbor Coulomb repulsion. These results are, however, inconsistent with the current ARPES description of the FeSe FS and deserve to be re-examined. To this end, we have begun with the canonical DFT calculation of the FeSe band structure in the tetragonal phase [250], and introduced nematic order driven by longer-range Coulomb interactions systematically. We find that such interactions, in addition to the generation of small electron and hole pockets, also generates *inter-orbital* nematicity between d_{xz} and d_{xy} states (or equivalently between d_{yz} and d_{xy} states), and in a large region of parameter space at low temperatures. This form of nematic order is distinct from those discussed previously in the literature [126, 245–247]. The inter-orbital nematic order components hybridize the low-energy bands near Y (or equivalently near X), and thereby allow, depending on their amplitudes, for the lifting of one of the electron pockets. We explore this scenario of longer range Coulomb interactions for nematicity and FS anisotropy, and demonstrate how it naturally generates FSs containing only a single electron pocket. We next discuss the comparison of the spin excitations obtained using this renormalized band structure with the highly anisotropic spectrum reported in the experimental literature [211]. Finally, we compute the resulting momentum-dependent superconducting gap structure, and discuss implications for other experimental probes of FeSe.

3.2 Model and Method

In order to explore how the electronic structure of FeSe is affected by longer-range Coulomb interactions, specifically nearest-neighbor (NN) density interactions, we employ the following many-body Hamiltonian

$$\begin{aligned}
 H &= H_{\text{kin}} + H_{\text{soc}} + H_{\text{int}} \\
 &= - \sum_{\mathbf{R}, \mathbf{R}'} c_{\mathbf{R}\mu\sigma}^\dagger (t_{\mathbf{R}-\mathbf{R}'}^{\mu\nu} + \mu_0 \delta_{\mathbf{R}, \mathbf{R}'} \delta_{\mu, \nu}) c_{\mathbf{R}'\nu\sigma} + \lambda_{\text{SOC}} \sum_{\mathbf{R}} c_{\mathbf{R}\mu\sigma}^\dagger \mathbf{L}^{\mu\nu} \cdot \mathbf{S}^{\sigma\sigma'} c_{\mathbf{R}\nu\sigma'} + \frac{V}{2} \sum_{\langle \mathbf{R}, \mathbf{R}' \rangle} n_{\mathbf{R}} n_{\mathbf{R}'},
 \end{aligned} \tag{3.1}$$

where $\langle \mathbf{R}, \mathbf{R}' \rangle$ indicates the set of NN sites. Here, the operator $c_{\mathbf{R}\mu\sigma}$ annihilates an electron in orbital d_μ with spin projection σ at lattice site \mathbf{R} , and $n_{\mathbf{R}} = c_{\mathbf{R}\mu\sigma}^\dagger c_{\mathbf{R}\mu\sigma}$ represents the density operator at lattice site \mathbf{R} . The kinetic part of the Hamiltonian H_{kin} contains the hopping matrix elements and the chemical potential μ_0 , H_{soc} includes the atomic spin-orbit coupling (SOC) with strength λ_{SOC} , and H_{int} describes the repulsive NN density interaction. For all results presented in this chapter, we adjust μ_0 to keep a fixed electron density of $\langle n \rangle = 6.0$. Note that for simplicity we completely discard the usual onsite Hubbard Coulomb repulsion H_U in the model. As it is well-known, such interactions can lead to important band renormalization, magnetism, and nematicity [60, 63, 251–253], none of which

	E	$2S_4$	C_2	$2C'_2$	$2\sigma_d$	Basis functions
A_1	+1	+1	+1	+1	+1	$x^2 + y^2, f_{\mathbf{k}}^s = \cos k_x + \cos k_y$
A_2	+1	+1	+1	-1	-1	L_z
B_1	+1	-1	+1	+1	-1	$x^2 - y^2, f_{\mathbf{k}}^d = \cos k_x - \cos k_y$
B_2	+1	-1	+1	-1	+1	z, xy
E	+2	0	-2	0	0	$(x, y), (xz, yz), (f_{\mathbf{k}}^{p_x}, f_{\mathbf{k}}^{p_y}) = i\sqrt{2}(\sin k_x, \sin k_y)$

Table 3.1: Character table for the point group D_{2d} , where we also included the relevant form factors $f_{\mathbf{k}}^\gamma$. Note that D_{2d} is a subgroup of D_{4h} .

lift the Y electron pocket. Here, we assume that H_U merely renormalizes the DFT band structure, though we do not include such effects explicitly. Thus we explore the nematic instability generated solely from H_{int} containing only NN Coulomb repulsion.

The symmetry properties of FeSe, and thereby H , are governed by the non-symmorphic space group $P4/nmm$, which consists of pure lattice translations $\{E | \mathbf{R}\}$, eight pure point group elements $\{g | (0, 0)\}$ for $g \in D_{2d}$, and eight compound symmetries $\{gI | (a/2, a/2)\}$ with I denoting inversion and a being the lattice constant, which we will set to unity $a \equiv 1$. For both analytical tractability and numerical simplicity we perform our study in the 1-Fe unit cell, for which the cosets of $(P4/nmm)/\mathcal{T}$ are pure point group elements of D_{2d} . This allows us to consider the IRs of \mathcal{T} and D_{2d} separately. Although one thereby lacks certain symmetry elements of the original system, it is still possible to capture the violation of rotational symmetry and the emergence of nematic order. In particular, we need to focus only on the generators of the D_{2d} group $g = \{S_4, C_2, C'_2, \sigma_d\}$, and the associated five IRs $\Gamma = \{A_1, A_2, B_1, B_2, E\}$, see table. 3.1. Here, the generator S_4 refers to the combined operation of $C_4\sigma_{xy}$.

We incorporate the effects of NN Coulomb interactions by performing a Hartree-Fock mean-field decoupling of H_{int} , and introduce the following homogeneous bond-order fields in wave-vector space [126, 127] for a given spin projection σ

$$N_{\mathbf{k}\sigma}^{\mu\nu} = -\frac{2}{\mathcal{N}} \sum_{\mathbf{k}'} f_{\mathbf{k}-\mathbf{k}'}^s \langle c_{\mathbf{k}'\nu\sigma}^\dagger c_{\mathbf{k}\mu\sigma} \rangle, \quad (3.2)$$

with \mathcal{N} being the number of lattice sites, and $f_{\mathbf{k}}^s$ being the form factor of the interaction, which transforms as the IR A_1 , see table. 3.1. Note that in the decoupling of H_{int} , the Hartree terms contribute only to a constant energy shift, which can be readily absorbed in the chemical potential $\mu_0 \rightarrow \mu_0 - 4V \sum_{\mathbf{k}'} \langle n_{\mathbf{k}'} \rangle / \mathcal{N}$.

Upon reaching the nematic transition temperature T_{nem} , the system will spontaneously violate S_4 symmetry, and we therefore seek to split the bond order fields into S_4 symmetry-preserving and symmetry-breaking terms, in order to identify the origin of nematicity driven by NN interactions. The symmetry-preserving terms, denoted by $N_{\mathbf{k}\sigma, \text{br}}^{\mu\nu}$, will in general lead to band renormalizing (br) terms, and is obtained by projecting out the A IR of the subgroup $S_4 = \{E, S_4, S_4^2, S_4^3\}$, see eqn. (1.22)

$$N_{\mathbf{k}\sigma, \text{br}}^{\mu\nu} = \frac{1}{4} \sum_{\ell=0}^3 D_{\text{orb}}[S_4^\ell]^{\mu\mu'} N_{S_4^{-\ell}\mathbf{k}\sigma}^{\mu'\nu'} D_{\text{orb}}^\dagger[S_4^\ell]^{\nu'\nu}, \quad (3.3)$$

where $D_{\text{orb}}[S_4^\ell]$ is the representation of S_4^ℓ in orbital space. As a consequence of SOC, one should in general also perform the S_4 averaging in spin space. However, by exploiting that the fields $N_{\mathbf{k}\sigma}^{\mu\nu}$ are diagonal in spin space and the fact that the action of S_4 is equivalent to a $\pi/2$ -rotation about the spin z -axis, we find that S_4 leaves the spin projection σ of $N_{\mathbf{k}\sigma}^{\mu\nu}$ invariant. Momentum dependent band renormalizing terms, such as $N_{\mathbf{k}\sigma,\text{br}}^{\mu\nu}$, have been previously put forward as potential candidates for explaining the band structure renormalizations of iron-pnictides and iron-chalcogenides [126, 127, 252].

Here, the main focus is on the S_4 symmetry breaking (sb) terms leading to nematic order, which are simply the remainder of the total field $N_{\mathbf{k}\sigma,\text{sb}}^{\mu\nu} = N_{\mathbf{k}\sigma}^{\mu\nu} - N_{\mathbf{k}\sigma,\text{br}}^{\mu\nu}$. In order to extract the form factors entering in the symmetry-preserving and symmetry-breaking fields, we perform the following projection onto the normalized lattice versions of the basis functions $f_{\mathbf{k}}^\gamma$ belonging to the group D_{2d}

$$N_{\mathbf{k}\sigma,\text{br/sb}}^{\mu\nu} = \sum_{\gamma} f_{\mathbf{k}}^{\gamma} N_{\gamma\sigma,\text{br/sb}}^{\mu\nu}. \quad (3.4)$$

As a consequence of the NN interaction, the sum over γ is restricted to include only the lowest order lattice harmonics, i.e. only linear combinations of $\cos(k_{x,y})$ and $\sin(k_{x,y})$ enter in $f_{\mathbf{k}}^\gamma$, while a longer-ranged interaction in general allows for higher order terms. Thus, we arrive at the following MF decoupled interaction

$$H_{\text{int}}^{\text{MF}} = V \sum_{\mathbf{k}} \sum_{\gamma,i} c_{\mathbf{k}\mu\sigma}^\dagger f_{\mathbf{k}}^{\gamma i} \left(N_{\gamma i\sigma,\text{br}}^{\mu\nu} + \beta N_{\gamma i\sigma,\text{sb}}^{\mu\nu} \right) c_{\mathbf{k}\nu\sigma}. \quad (3.5)$$

Note that we here introduced the enhancement factor β , since the interaction strength V in the symmetry-preserving and symmetry-breaking channels in general will be different, since the fields belong to different IRs of the point group, and can potentially lead to distinct couplings in a renormalization group procedure. Thus we allow $\beta \neq 0$ throughout, similar to earlier works [126, 127].

Lastly, in app. 3.A we elaborate further on the construction of $N_{\gamma\sigma,\text{br/sb}}^{\mu\nu}$, display their explicit matrix structure, and list the basis functions $f_{\mathbf{k}}^\gamma$ used in the upcoming sections.

3.3 Results

Equipped with the above model Hamiltonian and symmetry considerations, we are now able to calculate the bond order fields $N_{\gamma\sigma,\text{br/sb}}^{\mu\nu}$ self-consistently for a fixed electron filling $\langle n \rangle = 6.0$, (for details see app. 3.A). In our calculations we adopt the kinetic Hamiltonian for FeSe given in ref. [250], after including SOC in the spin z -direction of bare strength $\lambda_{\text{SOC}} = 30$ meV. However, the exact value of λ_{SOC} is not qualitatively important for the emergence of inter-orbital nematic components and the concomitant disappearance of one of the electron pockets, as found further below. However, SOC is important, within the current model, for the FS to contain only a single hole pocket at Γ . Due to weak inter-layer coupling in the c direction, we restrict our study to the quasi-2D lattice of a single layer of Fe and Se atoms. The resulting orbitally-resolved FS and band structure in the absence of NN interactions are displayed in fig. 3.1(a) and 3.1(c), respectively.

The effects of NN interactions, captured by the terms entering in eqn. (3.5), give rise to the two aforementioned effects, namely band renormalization and S_4 symmetry breaking. Let us momentarily discuss the former, $N_{\gamma\sigma,\text{br}}^{\mu\nu}$, by focusing on the low-energy t_{2g} orbitals. For this case, the fields lead to the following two effects: *i*) collective down-shift of the hole pockets at Γ and M, and *ii*) up-shift of the Dirac points at X and Y. The down-shift of the hole pockets is readily attributed to the

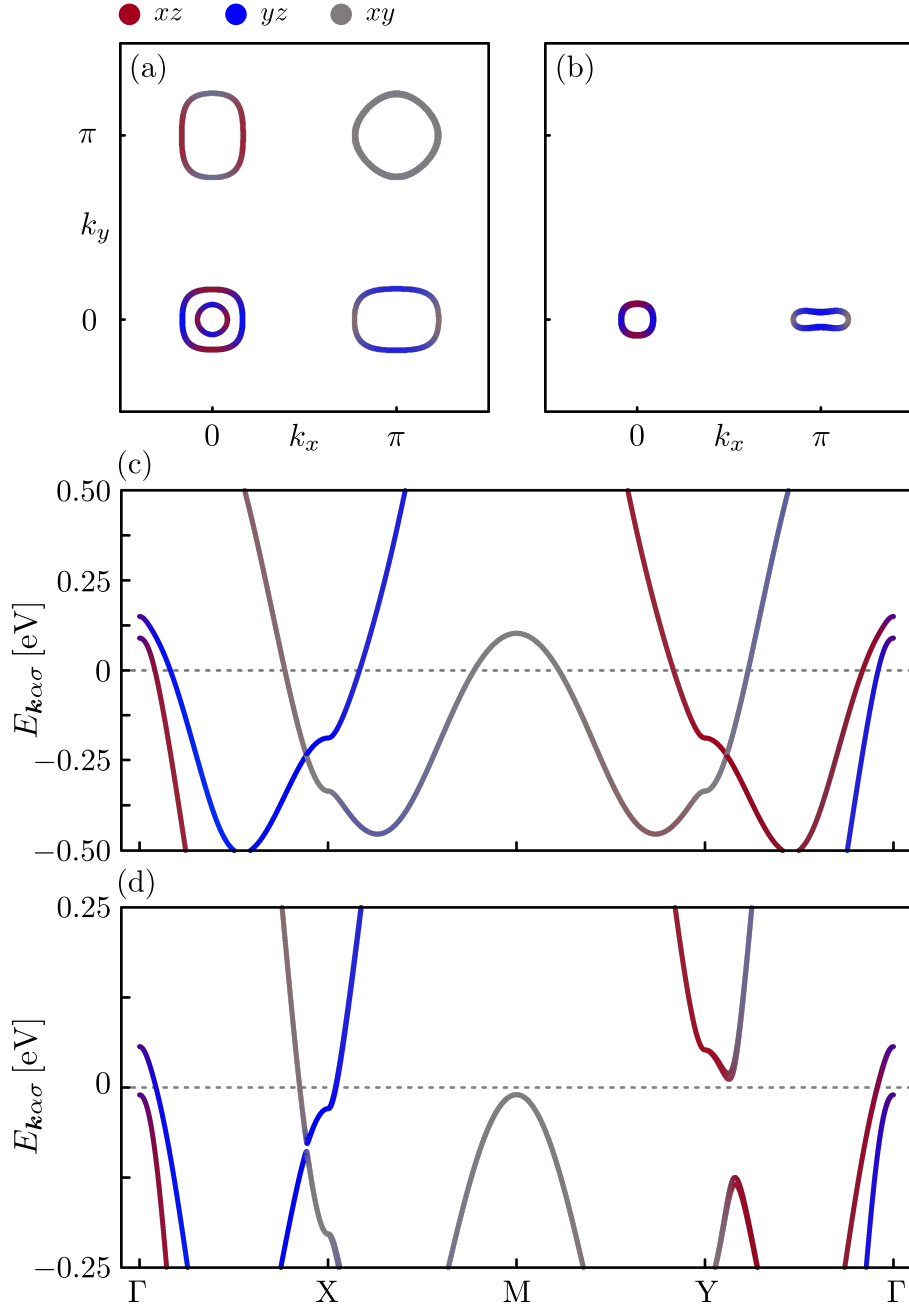


Figure 3.1: Orbitally resolved FSs and band structures in the absence (a),(c) and presence (b),(d) of NN interaction effects. The latter were obtained with $V = 0.45$ eV and $\beta = 2.8$. The band was adopted from ref. [250], with $k_z = 0$ and SOC coupling in the spin z -direction, $\lambda_{\text{SOC}} = 30$ meV. In (d) we clearly see the band shifts and gap openings discussed in the main text, resulting in the highly anisotropic FS displayed in panel (b). All figures were obtained with $k_B T = 1$ meV and $k_B \equiv 1$.

self-consistent fields in fig. 3.2(a), which couple to the form factor $f_{\mathbf{k}}^s = \cos k_x + \cos k_y$. Specifically the fields $N_{s\sigma,br}^{xz\,xz} = N_{s\sigma,br}^{yz\,yz} = -0.22$ lead to a down-shift of d_{xz}, d_{yz} -dominated bands at Γ , while $N_{s\sigma,br}^{xy\,xy} = 0.24$ ensures the down-shift of d_{xy} -dominated bands at M. The latter occurs since the form factor has a relative sign on the two pockets $f_{\Gamma}^s = -f_M^s$. Additionally we note that the effects of the s -wave fields on the electron pockets are minimal since $f_X^s = f_Y^s = 0$.

By contrast to the above, the fields presented in fig. 3.2(b) are dominant at the X and Y points due to the d -wave form factor $f_{\mathbf{k}}^d = \cos k_x - \cos k_y$. In fact, the field $N_{d\sigma,br}^{xz\,xz} = 0.09$ ($N_{d\sigma,br}^{yz\,yz} = -0.09$) shifts $d_{xz}(d_{yz})$ -dominated bands at Y (X), pushing the Dirac points up closer to the Fermi level. Similar to the s -wave fields, also here the symmetry of the form factor, $f_X^d = -f_Y^d$, compensates the relative sign between the two fields $N_{d\sigma,br}^{xz\,xz}/N_{d\sigma,br}^{yz\,yz} = -1$. Furthermore, we point out that the electron pockets acquire a peanut-like shape for appropriate values of V , since the fields $N_{d\sigma,br}^{\mu\nu}$ do not affect the d_{xy} orbitals. Lastly note that the down- (up-) shift of the hole pockets (Dirac points) leads to smaller Γ and M (X and Y) pockets. In fact, it was previously shown that $N_{\mathbf{k}\sigma,br}^{\mu\nu}$ can completely remove the M pocket in FeSe, while for LiFeAs it was the Γ pockets which were pushed away from the Fermi level [252].

Turning our attention to the symmetry breaking fields, $N_{\gamma\sigma,sb}^{\mu\nu}$, we find that only fields that are coupled to the d -wave form factor play an essential role, see fig. 3.2(c) and 3.2(d). By applying the same logic as for the band renormalizing terms, we observe that the field $N_{d\sigma,sb}^{xz\,xz}$ ($N_{d\sigma,sb}^{yz\,yz}$) leads to an up- (down-) shift of $d_{xz}(d_{yz})$ -dominated bands at Y (X). While this effect appears similar to the one encountered for $N_{d\sigma,br}^{\mu\nu}$, we stress that here the Dirac points are shifted in opposite directions due to the violation of S_4 -symmetry. This reduction in symmetry also allows for anisotropic inter-orbital $d_{xz} - d_{xy}$ and $d_{yz} - d_{xy}$ hybridization terms, namely $\beta N_{d\sigma,sb}^{xz\,xy} \approx 0.10$ and a vanishing coupling $\beta N_{d\sigma,sb}^{yz\,xy}$. It is in fact these particular couplings which lead to the distinct hybridization gaps at X and Y evident from fig. 3.1(d), and they will, in synergy with all the effects discussed above, result in the highly anisotropic FS shown in fig. 3.1(b), featuring only a single electron pocket at the X point. Thus, as a function of temperature, a Lifshitz transition necessarily takes place such that a shrinking Y-pocket eventually disappears at a certain temperature below T_{nem} . A detailed discussion of the experimental evidence for such a temperature-induced Lifshitz transition can be found in ref. [246].

To gain deeper insight into the emergent nematic order, we now proceed and study more carefully the IRs of $N_{\mathbf{k}\sigma,br/sb}^{\mu\nu}$. By construction, the S_4 symmetry preserving fields can only consist of terms transforming as A_1 and A_2 , and, in fact, we find through our self-consistent calculations that only A_1 terms are non-zero in $N_{\mathbf{k}\sigma,br}^{\mu\nu}$, see app. 3.B for further details.

In contrast, $N_{\mathbf{k}\sigma,sb}^{\mu\nu}$ can contain terms transforming as the remaining three IRs of the group, i.e. B_1 , B_2 and E , allowing for the nematic order to arise in any of these three channels. As we explicitly show in app. 3.B, we find non-zero S_4 symmetry breaking terms belonging to two distinct IRs, namely B_1 and E . This implies that the system undergoes two consecutive phase transitions upon lowering of the temperature. In order to quantify this, we focus on the t_{2g} orbitals, and define the following leading order parameters

$$\begin{aligned} N_{B_1} &= (N_{d\sigma,sb}^{xz\,xz} + N_{d\bar{\sigma},sb}^{xz\,xz} + N_{d\sigma,sb}^{yz\,yz} + N_{d\bar{\sigma},sb}^{yz\,yz})/4, \\ N_E &= \left([N_{d\sigma,sb}^{xz\,xy} + N_{d\bar{\sigma},sb}^{xz\,xy}]/2, [N_{d\sigma,sb}^{yz\,xy} + N_{d\bar{\sigma},sb}^{yz\,xy}]/2 \right) \\ &\equiv (N_{E_x}, N_{E_y}), \end{aligned} \quad (3.6)$$

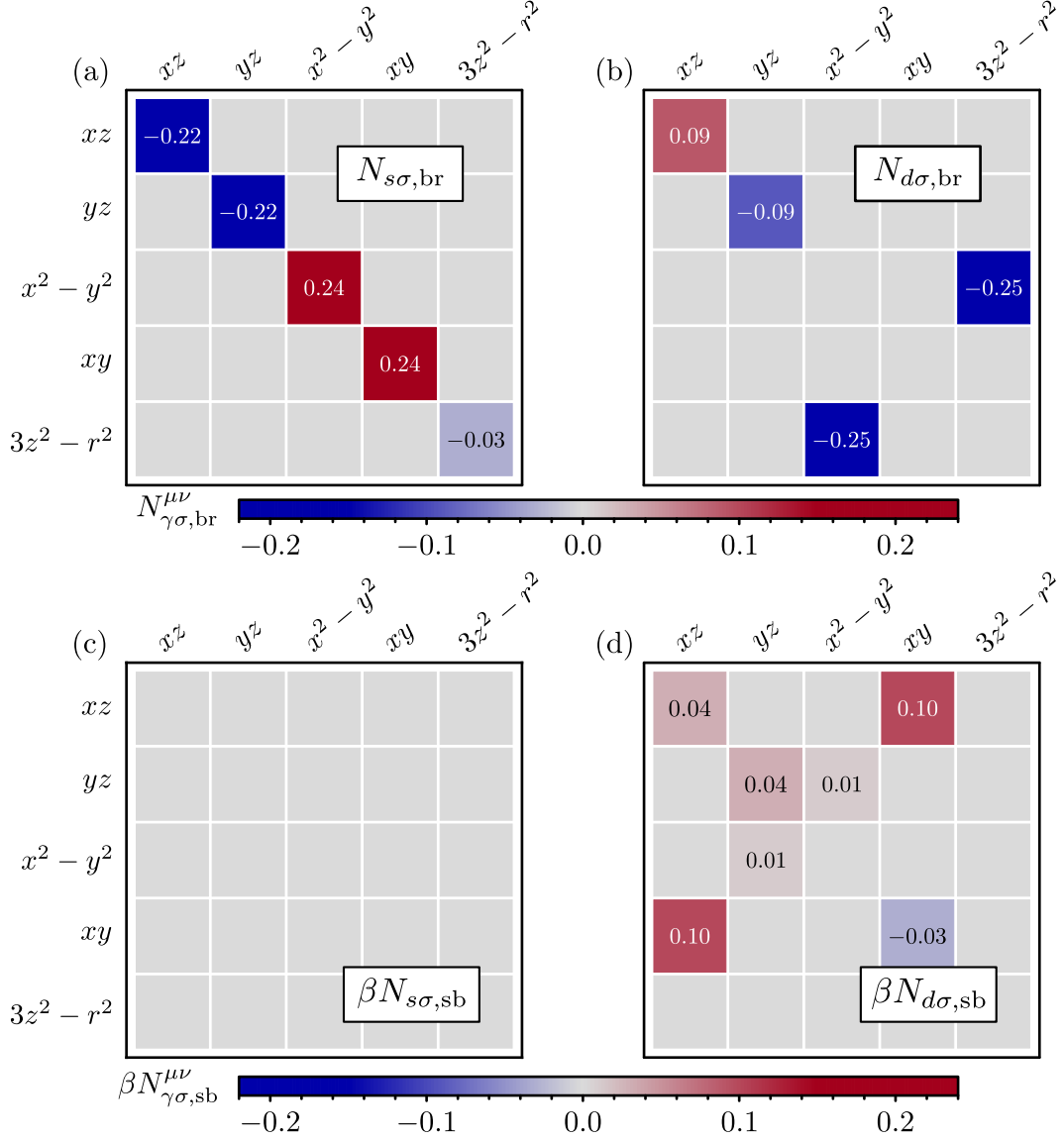


Figure 3.2: Band renormalizing (br) and S_4 symmetry breaking (sb) bond-order fields $N_{\gamma\sigma, \text{br/sb}}^{\mu\nu}$, calculated self-consistently for the parameters and temperature used in fig. 3.1(b) and (d), and fixed electron filling $\langle n \rangle = 6.0$, see app. 3.A for further details. The fields in (a),(c) couple to the form factor $f_{\mathbf{k}}^s = \cos k_x + \cos k_y$, while the ones displayed in (b),(d) couple to $f_{\mathbf{k}}^d = \cos k_x - \cos k_y$. The values of all matrix elements have for clarity been rounded to the second decimal place. For brevity we only display $\gamma = \{s, d\}$, but additional plots of the remaining fields can be found in app. 3.A.

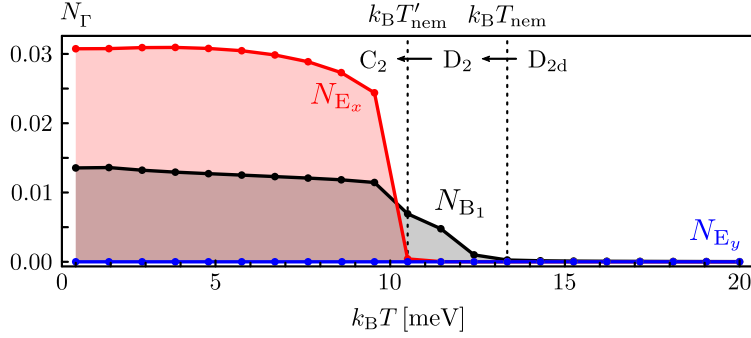


Figure 3.3: Leading order parameters N_{B_1} and N_E versus temperature. The system becomes nematic at T_{nem} , and displays a second phase transition at T'_{nem} . For the latter, N_{E_x} becomes non-zero, allowing for hybridization terms at Y. In this figure, we used the same parameters as in figs. 3.1 and 3.2.

where $\bar{\sigma}$ is the opposite spin projection of σ . For details see app. 3.B. In fig. 3.3 we show the values of these order parameters for various temperatures, and indeed find that N_{B_1} becomes non-zero at T_{nem} , while only the single component N_{E_x} condenses at lower temperatures T'_{nem} . An intra-orbital nematic order thus arises at T_{nem} , lowering the point group symmetry from D_{2d} to D_2 , and leads to the up- (down-) shift of d_{xz} (d_{yz})-dominated bands at Y (X) discussed in the previous paragraph. The second transition at T'_{nem} further reduces the point group to C_2 and allows for anisotropic inter-orbital $d_{xz} - d_{xy}$ or $d_{yz} - d_{xy}$ hybridization terms, i.e. the effects ultimately leading to the highly anisotropic FS, shown in fig. 3.1(b).

We stress that the effects of the e_g orbitals and remaining fields $N_{\gamma\sigma, \text{br/sb}}^{\mu\nu}$ not displayed in fig. 3.2, are all incorporated in our calculations, but do not lead to qualitative changes of the low-energy band structure and FS, and are therefore not explicitly mentioned in the above discussion. For a complete overview of all fields $N_{\gamma\sigma, \text{br/sb}}^{\mu\nu}$, see app. 3.A. Furthermore, we note that the final nematic band structure, as seen e.g. in fig. 3.1(d), obviously depends on the starting point, i.e. the tetragonal DFT band structure. Thus, the final quantitative energy scales, i.e. the hybridization gap at Y and the required amplitudes of V and β for generating a FS similar to that shown in fig. 3.1(b), depend on the initial bare band structure. Lastly, we note that the purely intra-orbital nematic order generated from NN Coulomb repulsion found earlier [126, 127], can be reproduced here when applying the same band structure as in ref. [126]. We have not located the exact band property that leads to the additional inter-orbital nematic fields from the DFT bulk FeSe band model used in the current study [250], but note that the solution presented in fig. 3.1 is quite generic at low temperatures and exists for a wide parameter range.

The low-energy electronic structure established above has important consequences for spin excitations that should be compared with experiments. In this respect, a series of inelastic neutron scattering experiments [211, 254, 255] have established a remarkable set of magnetic phenomena in FeSe. At low temperatures in the nematic phase, but high energies ~ 100 meV, strong (π, π) (Néel) fluctuations dominate the spectrum, with weaker but still prominent $(\pi, 0)$ and $(0, \pi)$ (stripe-like) fluctuations. As the energy is lowered to a few tens of meV, a spin gap develops in the (π, π) spectrum, but $(\pi, 0)$ spin fluctuations strengthen. Notably, the only measurement of *detwinned* FeSe crystal finds that at low

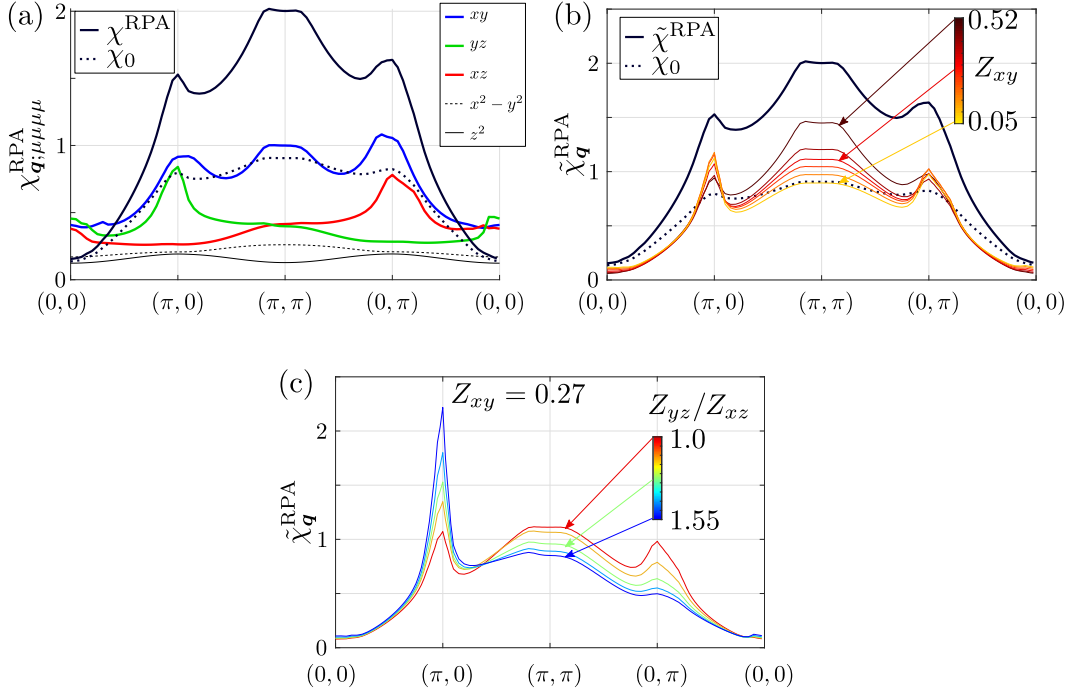


Figure 3.4: (a) Spin susceptibility as calculated from our model including the nematic order induced by nearest-neighbor Coulomb interactions, but using a fully coherent electronic structure, $Z_\mu = 1$, $U = 0.805$ eV, $J/U = 1/6$. (b) Spin susceptibility as obtained from a weakly correlated system by assuming orbitally selective quasiparticle weights [220] (dark red curve) ($U = 3.1$ eV) and successively decreasing the quasiparticle weight for the d_{xy} orbital to almost negligible quasiparticle contribution (yellow, $U = 3.65$ eV). (c) Moderate correlation with a small $Z_{xy} = 0.27$, but additionally splitting the quasiparticle weights between the d_{xz} and d_{yz} orbitals yields a strongly anisotropic susceptibility with no visible peak at $(0, \pi)$ starting from $Z_{yz}/Z_{xz} \approx 1.3$ (U decreased slightly to not cross the magnetic instability).

energies the intensity of the $(0, \pi)$ fluctuations essentially vanishes [211]. This extraordinary result should emerge from a proper theory of low energy spin and orbital degrees of freedom. We show now that, counter-intuitively, the current proposal for low-energy nematic electronic structure is not sufficient to explain the above-mentioned magnetic properties, and requires the additional physics of orbital selective correlations.

In fig. 3.4(a), we first illustrate the bare magnetic susceptibility $\text{Re } \chi_{0\mathbf{q},\omega=0}$, together with the enhanced susceptibility obtained in the random phase approximation χ^{RPA} of a fully coherent electronic structure. The spectrum is clearly dominated by intense (π, π) fluctuations arising from scattering between the d_{xy} states, which are not observed in experiment. Furthermore, $(\pi, 0)$ and $(0, \pi)$ states are nearly degenerate, in contradiction to the results of ref. [211]. Note that these issues are also common to conventional spin-fluctuation theories of FeSe including a Y pocket [228, 256], or other novel schemes to lift the Y pocket [246] via nematic order. In ref. [228], it was proposed that they could be resolved by assuming orbitally selective incoherence of d_{xy} , d_{xz} , and d_{yz} states, such as should take place according to previous theory [227] and as observed in some experiments [225]. With a phenomenological insertion of orbitally dependent quasiparticle weights Z_μ , with μ an orbital index, ref. [228] could fit inelastic neutron data on FeSe using very strong suppression of d_{xy} weights and somewhat smaller suppression of d_{xz} and d_{yz} weights, assuming also a large ratio of at least 1.7 for the ratio Z_{yz}/Z_{xz} .

By calculating the real part of the susceptibility at zero frequency, $\tilde{\chi}_{\mathbf{q}}^{\text{RPA}}$, we explore how orbital incoherence influences the peak structure in momentum space. As found in earlier investigations [228, 257] and explicitly checked also in this work, a strong peak in $\tilde{\chi}_{\mathbf{q}}^{\text{RPA}}$ is accompanied by spin fluctuations at low energies reflected in $\text{Im}\tilde{\chi}_{\mathbf{q},\omega}^{\text{RPA}}$, the quantity measured directly by inelastic neutron scattering experiments.

In fig. 3.4(b), we present the results for weak correlations, and the evolution of the susceptibility as correlations are enhanced by a substantial suppression of the d_{xy} quasiparticle weight (see app. 3.C for a brief discussion of the ansatz made by ref. [228]). As anticipated from the contribution of the orbitally resolved susceptibility of the d_{xy} orbital (see fig. 3.4(a)), with reduction of Z_{xy} comes the suppression of the Néel peak and concomitant moderate enhancement of the $(\pi, 0)$ stripe peak. On the other hand the $(\pi, 0)/(0, \pi)$ anisotropy is still much weaker than that reported in ref. [211]. In fig. 3.4(c), we therefore show the effect of additionally increasing the Z_{yz}/Z_{xz} anisotropy. It is easy to see that much larger $(\pi, 0)/(0, \pi)$ anisotropies are obtained in this case, but also that substantially smaller quasiparticle weight ratios, of order ~ 1.3 , are required compared to ref. [228], due to the effect of inter-orbital nematic order introduced here.

On the other hand, these various hypothetical renormalizations do not lead to substantial changes in the gap structure obtained for FeSe within the corresponding spin fluctuation pairing theory. This is simply because in a multiband system even at $\omega = 0$ contributions to $\chi_{\mathbf{q}}$ arise from states tens or even hundreds of meV from the Fermi level [257]. By contrast, FS states determine the anisotropy of the effective pairing interaction completely. This effect can be seen easily in fig. 3.5, where we plot the leading eigenvector of the linearized gap equation (see app. 3.C) for the same three cases described in fig. 3.4. The overall structure of the gaps and the density of states are seen to be virtually identical.

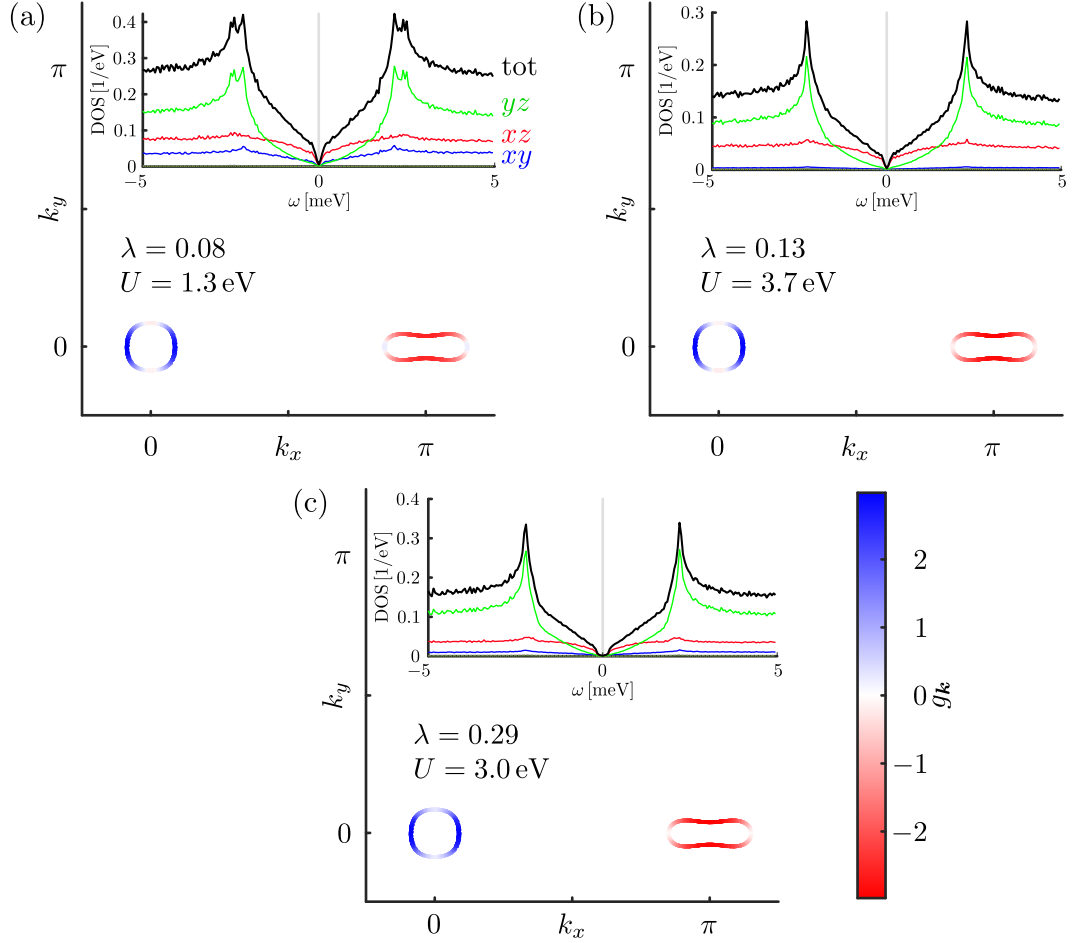


Figure 3.5: (a) Superconducting gap symmetry function $g_{\mathbf{k}}$ as calculated from a fully coherent electronic structure showing the strongly anisotropic gap on the two pockets. The expected spectrum shows nodal features and the eigenvalue λ is sizeable but small. (b) $g_{\mathbf{k}}$ calculated from a electronic structure with very incoherent d_{xy} orbital; almost no effect is visible except that the eigenvalue can be larger since the relative contribution of the $(\pi, 0)$ scattering is higher. (c) Same quantity, but calculated including a moderately correlated d_{xy} orbital and a nematic splitting of the quasiparticle weights in the d_{yz} and d_{xz} orbitals, yielding an order parameter with a tiny true gap, in contrast to nodes in (a) and (b).

3.4 Discussion and Conclusions

In this work we have pursued a scenario where nematicity originates entirely from NN Coulomb repulsion, even though it is well-known that onsite interactions alone may also drive a nematic instability as a precursor to stripe magnetism [60]. Interestingly, orbitally resolved studies within the spin-nematic onsite interaction-only scenario, do find sizable inter-orbital nematic susceptibilities [258]. Such studies, however, have only been performed in the tetragonal paramagnetic phase, and it remains to be seen whether spontaneous breaking in the inter-orbital channel, similar to the current proposal, can also arise from higher order processes solely from onsite interactions. However, the absence of magnetism in FeSe and the overall agreement of the here-presented results to the experimental facts, raises the question of whether indeed NN-repulsion is the generator of nematicity for FeSe. From cRPA [259] and DMFT [260] calculations it is known that interactions are generally larger in FeSe than any of the other iron-based superconducting systems, presumably because a lack of intervening spacer layers reduces the screening. Onsite interactions U , J are known to lead to band renormalizations, in particular FS pocket shrinkage [248, 249] and orbital-dependent band narrowing. It is tempting to speculate that this, in turn, effectively enhances the importance of the unusually large V in FeSe, thereby boosting instabilities driven by this channel.

Recently, another theoretical study investigated the possibility of nematic order lifting one of the electron pockets (above the Fermi level) in FeSe [246]. In agreement with the present work, a Lifshitz transition necessarily takes place as a function of temperature, and a superconducting gap structure consistent with experiments follows directly from the resulting FS with the missing Y-pocket. A main difference between ref. [246] and the current approach is the nature of the nematic order; whereas Rhodes *et al.* [246] begin with a phenomenological $\mathbf{k} \cdot \mathbf{p}$ expansion around Γ , X and Y, and explore the role of a large intra-orbital B_{1g} d_{xy} -nematic order parameter imposed by “hand” on the band structure, together with additional onsite Hartree shifts to this orbital, we have started from a nearest-neighbor Coulomb interaction, and shown that (self-consistently generated) inter-orbital $d_{xy} - d_{xz/yz}$ nematic components lift the Y-pocket. Thus, while a B_{1g} intra-orbital d_{xy} nematic component is also present in our approach as seen from fig. 3.2(d), the most important nematic components for generating a FS containing no electron Y-pocket are the distinct inter-orbital components.

As mentioned in sec. 3.3, the nematic lowest-temperature phase advocated in this work, resides in the C_2 (monoclinic) group, containing only a C_2 rotation around the x -axis as the remaining symmetry operation. This constitutes a clear prediction within the current scenario; the electronic sector should exhibit a double transition as the temperature is lowered. We are not aware of such evidence, e.g. from specific heat data [261–263], which may be because of the very small electronic entropy change at the second transition, or simply because the two transitions are accidentally close (in temperature) (see app. 3.B for more details) in FeSe. In addition, if the nematic order couples strongly enough to the atomic lattice, such symmetry lowering could be tested by experiments sensitive to the overall crystal point group. In this regard, however, we note that recent experimental and theoretical studies have advocated for a more complex static crystal microstructure in FeSe than previously thought. Locally, FeSe appears to accommodate a myriad of inhomogeneous nanoscale lattice distortions, where only the spatially averaged structure complies with the standard tetragonal (orthorhombic) crystal symmetries at high (low) temperatures [198, 199, 247, 264]. This may in fact be the result of two nematic channels very close in energy. Lastly, it is tempting to speculate that the inter-orbital nematic order discussed

here, may be relevant for the recent experimental studies of structural transitions in $\text{Bi}_{1-x}\text{Sr}_x\text{Ni}_2\text{As}_2$, which exhibit transitions from a high-temperature tetragonal phase to a triclinic low-temperature phase [265].

Recent theoretical works explored the possibility of pinned local nematic order [166, 184, 185], and chap. 2. In particular, we explored in chap. 2 the local disorder-induced nematicity from nonmagnetic impurities in the tetragonal phase at $T > T_{\text{nem}}$. Several experimental works have reported evidence for such local nematic order above T_{nem} [198, 199]. Our results in chap. 2 were obtained by applying a one-band model and relied on interactions leading to a single-component B_{1g} nematic order, and hence the question arises how local pinned nematic order gets affected by the presence of the substantial inter-orbital components found in this work? We have answered this question by performing a real-space calculation similar to that of chap. 2, but generalized to the multi-orbital case. For the intra-orbital B_1 order parameter N_{B_1} studied here, we observe that it enters the Landau free energy expansion in the exact same manner as the order parameter studied in chap. 2. Therefore the local impurity-induced order exhibits a clover-shape pinned by nonmagnetic impurities. However, for the lower temperature phase, the spatially dependent local nematic impurity-induced order is distinct from that consider in chap. 2, since the order parameter N_E couples differently to the nonmagnetic impurity. It remains an interesting future study to investigate the detailed experimental consequences of these various local nematic orders.

In summary, we have discovered an inter-orbital nematic order generated from nearest-neighbor Coulomb repulsion for electronic models relevant for FeSe in particular, and perhaps the iron-based systems more broadly. A natural property of this kind of nematic order is the generation of highly anisotropic FSs, featuring in some cases, only a single hole and electron pocket. We have shown how, for FeSe, this explains photoemission data and the experimentally extracted very anisotropic superconducting gap structure. However, a consistent picture of the neutron scattering data, cannot be straightforwardly obtained within this nematic scenario, without invoking additional self-energy effects, which in the simplest case, involves sizable corrections in the form of reduced orbitally dependent quasiparticle weights.

Appendices for Chapter 3

3.A Details on Bond-Order Fields and Self-Consistent Calculations

The explicit forms of $N_{\mathbf{k}\sigma,\text{br}}^{\mu\nu}$ and $N_{\mathbf{k}\sigma,\text{sb}}^{\mu\nu}$ are found through the averaging in eqn. (3.3), and the difference $N_{\mathbf{k}\sigma,\text{sb}}^{\mu\nu} = N_{\mathbf{k}\sigma}^{\mu\nu} - N_{\mathbf{k}\sigma,\text{br}}^{\mu\nu}$, respectively. Yet this procedure can be further simplified, by relying on the projection of the fields onto the normalized lattice versions of the basis functions $f_{\mathbf{k}}^{\gamma}$

$$N_{\mathbf{k}\sigma}^{\mu\nu} = \sum_{\gamma} f_{\mathbf{k}}^{\gamma} N_{\gamma\sigma}^{\mu\nu}. \quad (3.7)$$

This projection disentangles the wave-vector and orbital dependence, and thereby greatly simplifies eqn. (3.3). For NN interactions in 2D systems, which are left invariant under the elements of D_{2d} , the set of basis functions entering in eqn. (3.7) are

$$\begin{aligned} f_{\mathbf{k}}^s &= \cos k_x + \cos k_y, & f_{\mathbf{k}}^d &= \cos k_x - \cos k_y, \\ f_{\mathbf{k}}^{p_x} &= \sqrt{2}i \sin k_x, & f_{\mathbf{k}}^{p_y} &= \sqrt{2}i \sin k_y, \end{aligned} \quad (3.8)$$

with $a_x = a_y = a \equiv 1$. For NN interactions in three dimensions, the above equations are accompanied by $f_{\mathbf{k}_z}^s = \sqrt{2} \cos(k_z c)$ and $f_{\mathbf{k}_z}^d = \sqrt{2}i \sin(k_z c)$, with $a_z \equiv c \neq a$. Each basis function transforms according to one of the IRs Γ of the point group. Specifically, $f_{\mathbf{k}}^s$ ($f_{\mathbf{k}}^d$) transforms as A_1 (B_1), while $(f_{\mathbf{k}}^{p_x}, f_{\mathbf{k}}^{p_y})$ transform jointly as the 2D IR E.

Next step in determining $N_{\mathbf{k}\sigma,\text{br/sb}}^{\mu\nu}$, is to represent S_4 in spin space and in the relevant orbital basis $\{d_{xz}, d_{yz}, d_{x^2-y^2}, d_{xy}, d_{3z^2-r^2}\}$. The former is needed since the SOC in eqn. (3.1) breaks spin-rotation symmetry. Additionally, we also need to determine how S_4^{-1} acts on the wave-vector \mathbf{k} . Straightforwardly, we find

$$D[S_4] = D_{\text{orb}}[S_4] \otimes D_{\text{spin}}[S_4] = \begin{pmatrix} 0 & 1 & 0 & 0 & 0 \\ -1 & 0 & 0 & 0 & 0 \\ 0 & 0 & -1 & 0 & 0 \\ 0 & 0 & 0 & -1 & 0 \\ 0 & 0 & 0 & 0 & 1 \end{pmatrix} \otimes \frac{\mathbb{1}_{\sigma} - i\sigma_z}{\sqrt{2}}, \quad S_4^{-1}\mathbf{k} = (k_y, -k_x, -k_z), \quad (3.9)$$

where $D_{\text{orb}}[S_4]$ and $D_{\text{spin}}[S_4]$ are matrix representations in orbital and spin space, respectively, while $D[S_4]$ is the representation in the combined space. Any symmetry operation acting in spin space can be expressed in terms of the Pauli matrices $\sigma_{x,y,z}$ accompanied by the identity matrix $\mathbb{1}_{\sigma}$. Note, however, that the fields $N_{\mathbf{k}\sigma}^{\mu\nu}$ are diagonal in spin space, and are therefore not affected by $D_{\text{spin}}[S_4]$. One can therefore solely consider the action of $D_{\text{orb}}[S_4]$, as discussed in connection to eqn. (3.3). In

general, when considering a given symmetry element g of the point group D_{2d} , one needs to apply the full representation $D[g]$.

By executing the above on a 2D system, we end up with the following band renormalizing (br) terms

$$N_{s\sigma,br} = \begin{pmatrix} \frac{1}{2}(N_{s\sigma}^{11} + N_{s\sigma}^{22}) & \frac{1}{2}(N_{s\sigma}^{12} - N_{s\sigma}^{21}) & 0 & 0 & 0 \\ \frac{1}{2}(N_{s\sigma}^{21} - N_{s\sigma}^{12}) & \frac{1}{2}(N_{s\sigma}^{11} + N_{s\sigma}^{22}) & 0 & 0 & 0 \\ 0 & 0 & N_{s\sigma}^{33} & N_{s\sigma}^{34} & 0 \\ 0 & 0 & N_{s\sigma}^{43} & N_{s\sigma}^{44} & 0 \\ 0 & 0 & 0 & 0 & N_{s\sigma}^{55} \end{pmatrix}, \quad (3.10a)$$

$$N_{d\sigma,br} = \begin{pmatrix} \frac{1}{2}(N_{d\sigma}^{11} - N_{d\sigma}^{22}) & \frac{1}{2}(N_{d\sigma}^{12} + N_{d\sigma}^{21}) & 0 & 0 & 0 \\ \frac{1}{2}(N_{d\sigma}^{12} + N_{d\sigma}^{21}) & -\frac{1}{2}(N_{d\sigma}^{11} - N_{d\sigma}^{22}) & 0 & 0 & 0 \\ 0 & 0 & 0 & 0 & N_{d\sigma}^{35} \\ 0 & 0 & 0 & 0 & N_{d\sigma}^{45} \\ 0 & 0 & N_{d\sigma}^{53} & N_{d\sigma}^{54} & 0 \end{pmatrix}, \quad (3.10b)$$

$$N_{p_x\sigma,br} = \begin{pmatrix} 0 & 0 & \frac{1}{2}(N_{p_x\sigma}^{13} + N_{p_y\sigma}^{23}) & \frac{1}{2}(N_{p_x\sigma}^{14} + N_{p_y\sigma}^{24}) & \frac{1}{2}(N_{p_x\sigma}^{15} - N_{p_y\sigma}^{25}) \\ 0 & 0 & \frac{1}{2}(N_{p_x\sigma}^{23} - N_{p_y\sigma}^{13}) & \frac{1}{2}(N_{p_x\sigma}^{24} - N_{p_y\sigma}^{14}) & \frac{1}{2}(N_{p_x\sigma}^{25} + N_{p_y\sigma}^{15}) \\ \frac{1}{2}(N_{p_x\sigma}^{31} + N_{p_y\sigma}^{32}) & \frac{1}{2}(N_{p_x\sigma}^{32} - N_{p_y\sigma}^{31}) & 0 & 0 & 0 \\ \frac{1}{2}(N_{p_x\sigma}^{41} + N_{p_y\sigma}^{42}) & \frac{1}{2}(N_{p_x\sigma}^{42} - N_{p_y\sigma}^{41}) & 0 & 0 & 0 \\ \frac{1}{2}(N_{p_x\sigma}^{51} - N_{p_y\sigma}^{52}) & \frac{1}{2}(N_{p_x\sigma}^{52} + N_{p_y\sigma}^{51}) & 0 & 0 & 0 \end{pmatrix}, \quad (3.10c)$$

$$N_{p_y\sigma,br} = \begin{pmatrix} 0 & 0 & -\frac{1}{2}(N_{p_x\sigma}^{23} - N_{p_y\sigma}^{13}) & -\frac{1}{2}(N_{p_x\sigma}^{24} - N_{p_y\sigma}^{14}) & \frac{1}{2}(N_{p_x\sigma}^{25} + N_{p_y\sigma}^{15}) \\ 0 & 0 & \frac{1}{2}(N_{p_x\sigma}^{13} + N_{p_y\sigma}^{23}) & \frac{1}{2}(N_{p_x\sigma}^{14} + N_{p_y\sigma}^{24}) & -\frac{1}{2}(N_{p_x\sigma}^{15} - N_{p_y\sigma}^{25}) \\ -\frac{1}{2}(N_{p_x\sigma}^{32} - N_{p_y\sigma}^{31}) & \frac{1}{2}(N_{p_x\sigma}^{31} + N_{p_y\sigma}^{32}) & 0 & 0 & 0 \\ -\frac{1}{2}(N_{p_x\sigma}^{42} - N_{p_y\sigma}^{41}) & \frac{1}{2}(N_{p_x\sigma}^{41} + N_{p_y\sigma}^{42}) & 0 & 0 & 0 \\ \frac{1}{2}(N_{p_x\sigma}^{52} + N_{p_y\sigma}^{51}) & -\frac{1}{2}(N_{p_x\sigma}^{51} - N_{p_y\sigma}^{52}) & 0 & 0 & 0 \end{pmatrix}, \quad (3.10d)$$

where we used the convenient shorthand notation $\{d_{xz}, d_{yz}, d_{x^2-y^2}, d_{xy}, d_{3z^2-r^2}\} \equiv \{1, 2, 3, 4, 5\}$.

Similarly we find the following symmetry breaking (sb) terms

$$N_{s\sigma, \text{sb}} = \begin{pmatrix} \frac{1}{2}(N_{s\sigma}^{11} - N_{s\sigma}^{22}) & \frac{1}{2}(N_{s\sigma}^{12} + N_{s\sigma}^{21}) & N_{s\sigma}^{13} & N_{s\sigma}^{14} & N_{s\sigma}^{15} \\ \frac{1}{2}(N_{s\sigma}^{12} + N_{s\sigma}^{21}) & -\frac{1}{2}(N_{s\sigma}^{11} - N_{s\sigma}^{22}) & N_{s\sigma}^{23} & N_{s\sigma}^{24} & N_{s\sigma}^{25} \\ N_{s\sigma}^{31} & N_{s\sigma}^{32} & 0 & 0 & N_{s\sigma}^{35} \\ N_{s\sigma}^{41} & N_{s\sigma}^{42} & 0 & 0 & N_{s\sigma}^{45} \\ N_{s\sigma}^{51} & N_{s\sigma}^{52} & N_{s\sigma}^{53} & N_{s\sigma}^{54} & 0 \end{pmatrix}, \quad (3.11a)$$

$$N_{d\sigma, \text{sb}} = \begin{pmatrix} \frac{1}{2}(N_{d\sigma}^{11} + N_{d\sigma}^{22}) & \frac{1}{2}(N_{d\sigma}^{12} - N_{d\sigma}^{21}) & N_{d\sigma}^{13} & N_{d\sigma}^{14} & N_{d\sigma}^{15} \\ \frac{1}{2}(N_{d\sigma}^{21} - N_{d\sigma}^{12}) & \frac{1}{2}(N_{d\sigma}^{11} + N_{d\sigma}^{22}) & N_{d\sigma}^{23} & N_{d\sigma}^{24} & N_{d\sigma}^{25} \\ N_{d\sigma}^{31} & N_{d\sigma}^{32} & N_{d\sigma}^{33} & N_{d\sigma}^{34} & 0 \\ N_{d\sigma}^{41} & N_{d\sigma}^{42} & N_{d\sigma}^{43} & N_{d\sigma}^{44} & 0 \\ N_{d\sigma}^{51} & N_{d\sigma}^{52} & 0 & 0 & N_{d\sigma}^{55} \end{pmatrix}, \quad (3.11b)$$

$$N_{p_x\sigma, \text{sb}} = \begin{pmatrix} N_{p_x\sigma}^{11} & N_{p_x\sigma}^{12} & \frac{1}{2}(N_{p_x\sigma}^{13} - N_{p_y\sigma}^{23}) & \frac{1}{2}(N_{p_x\sigma}^{14} - N_{p_y\sigma}^{24}) & \frac{1}{2}(N_{p_x\sigma}^{15} + N_{p_y\sigma}^{25}) \\ N_{p_x\sigma}^{21} & N_{p_x\sigma}^{22} & \frac{1}{2}(N_{p_x\sigma}^{23} + N_{p_y\sigma}^{13}) & \frac{1}{2}(N_{p_x\sigma}^{24} + N_{p_y\sigma}^{14}) & \frac{1}{2}(N_{p_x\sigma}^{25} - N_{p_y\sigma}^{15}) \\ \frac{1}{2}(N_{p_x\sigma}^{31} - N_{p_y\sigma}^{32}) & \frac{1}{2}(N_{p_x\sigma}^{32} + N_{p_y\sigma}^{31}) & N_{p_x\sigma}^{33} & N_{p_x\sigma}^{34} & N_{p_x\sigma}^{35} \\ \frac{1}{2}(N_{p_x\sigma}^{41} - N_{p_y\sigma}^{42}) & \frac{1}{2}(N_{p_x\sigma}^{42} + N_{p_y\sigma}^{41}) & N_{p_x\sigma}^{43} & N_{p_x\sigma}^{44} & N_{p_x\sigma}^{45} \\ \frac{1}{2}(N_{p_x\sigma}^{51} + N_{p_y\sigma}^{52}) & \frac{1}{2}(N_{p_x\sigma}^{52} - N_{p_y\sigma}^{51}) & N_{p_x\sigma}^{53} & N_{p_x\sigma}^{54} & N_{p_x\sigma}^{55} \end{pmatrix}, \quad (3.11c)$$

$$N_{p_y\sigma, \text{sb}} = \begin{pmatrix} N_{p_y\sigma}^{11} & N_{p_y\sigma}^{12} & \frac{1}{2}(N_{p_x\sigma}^{23} + N_{p_y\sigma}^{13}) & \frac{1}{2}(N_{p_x\sigma}^{24} + N_{p_y\sigma}^{14}) & -\frac{1}{2}(N_{p_x\sigma}^{25} - N_{p_y\sigma}^{15}) \\ N_{p_y\sigma}^{21} & N_{p_y\sigma}^{22} & -\frac{1}{2}(N_{p_x\sigma}^{13} - N_{p_y\sigma}^{23}) & -\frac{1}{2}(N_{p_x\sigma}^{14} - N_{p_y\sigma}^{24}) & \frac{1}{2}(N_{p_x\sigma}^{15} + N_{p_y\sigma}^{25}) \\ \frac{1}{2}(N_{p_x\sigma}^{32} + N_{p_y\sigma}^{31}) & -\frac{1}{2}(N_{p_x\sigma}^{31} - N_{p_y\sigma}^{32}) & N_{p_y\sigma}^{33} & N_{p_y\sigma}^{34} & N_{p_y\sigma}^{35} \\ \frac{1}{2}(N_{p_x\sigma}^{42} + N_{p_y\sigma}^{41}) & -\frac{1}{2}(N_{p_x\sigma}^{41} - N_{p_y\sigma}^{42}) & N_{p_y\sigma}^{43} & N_{p_y\sigma}^{44} & N_{p_y\sigma}^{45} \\ -\frac{1}{2}(N_{p_x\sigma}^{52} - N_{p_y\sigma}^{51}) & \frac{1}{2}(N_{p_x\sigma}^{51} + N_{p_y\sigma}^{52}) & N_{p_y\sigma}^{53} & N_{p_y\sigma}^{54} & N_{p_y\sigma}^{55} \end{pmatrix}. \quad (3.11d)$$

These fields, combined with the basis functions $f_{\mathbf{k}}^\gamma$, enter in the mean-field decoupled Hamiltonian in the following way, see also eqn. (3.5)

$$H_{\text{int}} \approx H_{\text{int}}^{\text{MF}} = V \sum_{\mathbf{k}} c_{\mathbf{k}\mu\sigma}^\dagger \left[f_{\mathbf{k}}^s \left(N_{s\sigma, \text{br}}^{\mu\nu} + \beta N_{s\sigma, \text{sb}}^{\mu\nu} \right) + f_{\mathbf{k}}^d \left(N_{d\sigma, \text{br}}^{\mu\nu} + \beta N_{d\sigma, \text{sb}}^{\mu\nu} \right) \right. \\ \left. + f_{\mathbf{k}}^{p_x} \left(N_{p_x\sigma, \text{br}}^{\mu\nu} + \beta N_{p_x\sigma, \text{sb}}^{\mu\nu} \right) + f_{\mathbf{k}}^{p_y} \left(N_{p_y\sigma, \text{br}}^{\mu\nu} + \beta N_{p_y\sigma, \text{sb}}^{\mu\nu} \right) \right] c_{\mathbf{k}\nu\sigma}. \quad (3.12)$$

The Hamiltonian becomes bilinear in creation and annihilation operators upon approximating $H_{\text{int}} \approx H_{\text{int}}^{\text{MF}}$, and we can thus easily express the fermionic operators in the diagonal basis of the Hamiltonian $c_{\mathbf{k}\mu\sigma} = \sum_{\alpha} \gamma_{\mathbf{k}\alpha\sigma} \langle \mathbf{k}\mu\sigma | \mathbf{k}\alpha\sigma \rangle$, where $\gamma_{\mathbf{k}\alpha\sigma}$ are the operators related to the eigenstates of

the Hamiltonian $\mathcal{H}\gamma_{\mathbf{k}\alpha\sigma}^\dagger|0\rangle = E_{\mathbf{k}\alpha\sigma}|\mathbf{k}\alpha\sigma\rangle$. Here \mathcal{H} is the single particle Hamiltonian, see eqn. (1.1). In this diagonal basis the electron density $\langle n \rangle$ takes the simple form

$$\langle n \rangle = \frac{1}{\mathcal{N}} \sum_{\mathbf{k}} \sum_{\sigma} \sum_{\alpha} n_F(E_{\mathbf{k}\alpha\sigma}), \quad (3.13)$$

where $n_F(E_{\mathbf{k}\alpha\sigma})$ is the Fermi-Dirac distribution function. Furthermore, we find that the terms entering in the matrix elements in eqns. (3.10) and (3.11) are expressed as

$$N_{\gamma\sigma}^{\mu\nu} = -\frac{1}{\mathcal{N}} \sum_{\mathbf{k}'} [f_{\mathbf{k}'}^\gamma]^* \langle c_{\mathbf{k}'\nu\sigma}^\dagger c_{\mathbf{k}'\mu\sigma} \rangle = -\frac{1}{\mathcal{N}} \sum_{\mathbf{k}',\alpha} [f_{\mathbf{k}'}^\gamma]^* \langle \mathbf{k}'\alpha\sigma | \mathbf{k}'\nu\sigma \rangle n_F(E_{\mathbf{k}'\alpha\sigma}) \langle \mathbf{k}'\mu\sigma | \mathbf{k}'\alpha\sigma \rangle. \quad (3.14)$$

By calculating the above self-consistently with the parameters used in fig. 3.1(b) and 3.1(c), we arrive at the band renormalizing and S_4 symmetry breaking fields displayed in fig. 3.6 and fig. 3.7, respectively. Only fields coupled to $f_{\mathbf{k}}^s$ and $f_{\mathbf{k}}^d$ are discussed in the main text, since the remaining ones lead to minimal effects on the low-energy t_{2g} orbitals. This is obviously true for $N_{p_x\sigma, sb}^{\mu\nu}$ since all these are zero, while for the remaining band renormalizing terms and $N_{p_y\sigma, sb}^{\mu\nu}$ it is the form factors which are eliminating the effects, since $f_{\mathbf{k}=(0,k_y)}^{p_x} = f_{\mathbf{k}=(k_x,0)}^{p_y} = 0$. This can be seen by considering the field $N_{p_x\sigma, br}^{xz\ xy} = -0.27$ ($N_{p_y\sigma, br}^{yz\ xy} = -0.27$) which introduces inter-orbital $d_{xz} - d_{xy}$ ($d_{yz} - d_{xy}$) hybridization terms, however, the form factor for this field goes to zero on the orbitally-relevant electron pocket at Y (X), thus rendering the effect minimal. Same argument holds for $N_{p_y\sigma, sb}^{xz\ yz}$, which should be relevant at Γ , however $f_{\Gamma}^{p_y} = 0$.

3.B Irreducible Representation of Bond-Order Fields

Although the above classification of band renormalizing and symmetry breaking fields suffices in describing the occurrence of nematic order, it fails to express the exact symmetry of the emergent nematic order. In other words, the band renormalizing and symmetry breaking fields transform as a sum of IRs, specifically

$$N_{\mathbf{k}\sigma, br}^{\mu\nu} \sim A_1 \oplus A_2, \quad N_{\mathbf{k}\sigma, sb}^{\mu\nu} \sim B_1 \oplus B_2 \oplus E, \quad (3.15)$$

and it is therefore not obvious whether the nematic order parameter transforms as B_1 , B_2 or E .

In order to shed light on this ambiguity, we will in the following perform a thorough classification of the bond-order fields, and further segregate these into IRs. In doing so, we project out the various IRs of $N_{\gamma\sigma}^{\mu\nu}$, in the following way, see eqn. (1.22)

$$D[N_{\gamma, \Gamma_i}] = P_i^\Gamma D[N_\gamma] = \frac{\ell_\Gamma}{8} \sum_{g \in D_{2d}} (D^\Gamma[g]^{ii})^* D[g] D[N_\gamma] D^\dagger[g], \quad (3.16)$$

where $D[N_{\gamma, \Gamma}]$ represents a matrix in combined orbital and spin space transforming as the IR Γ of the group D_{2d} . The γ -subscript indicates that the matrix couples to the form factor $f_{\mathbf{k}}^\gamma$. Similarly, $D[N_\gamma]$ is a matrix containing the elements $N_{\gamma\sigma}^{\mu\nu}$. As discussed in app. 3.A, $D[g]$ is the matrix representation of $g \in D_{2d}$ in combined orbital and spin space.

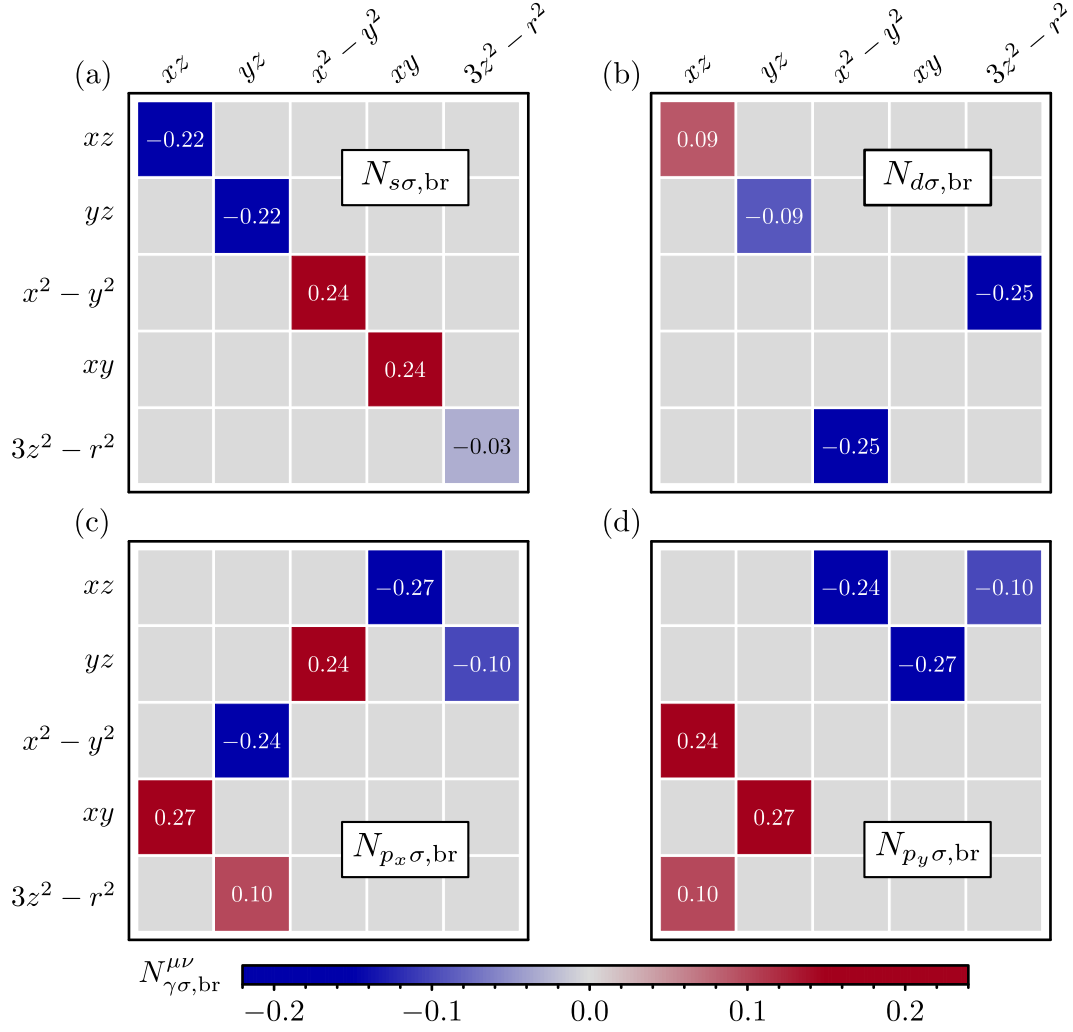


Figure 3.6: Band renormalizing bond-order fields, $N_{\gamma\sigma,br}^{\mu\nu}$, calculated self-consistently with the parameters used in fig. 3.1(b) and 3.1(d). A given field $N_{\gamma\sigma,br}^{\mu\nu}$ couples to the appropriate form factor $f_{\mathbf{k}}^{\gamma}$, see eqn. (3.8). (a) and (b) are discussed in the main text, while (c) and (d) only lead to minimal effects on the low-energy band structure. All numbers appearing in the matrices have for clarity been rounded to the second decimal place.

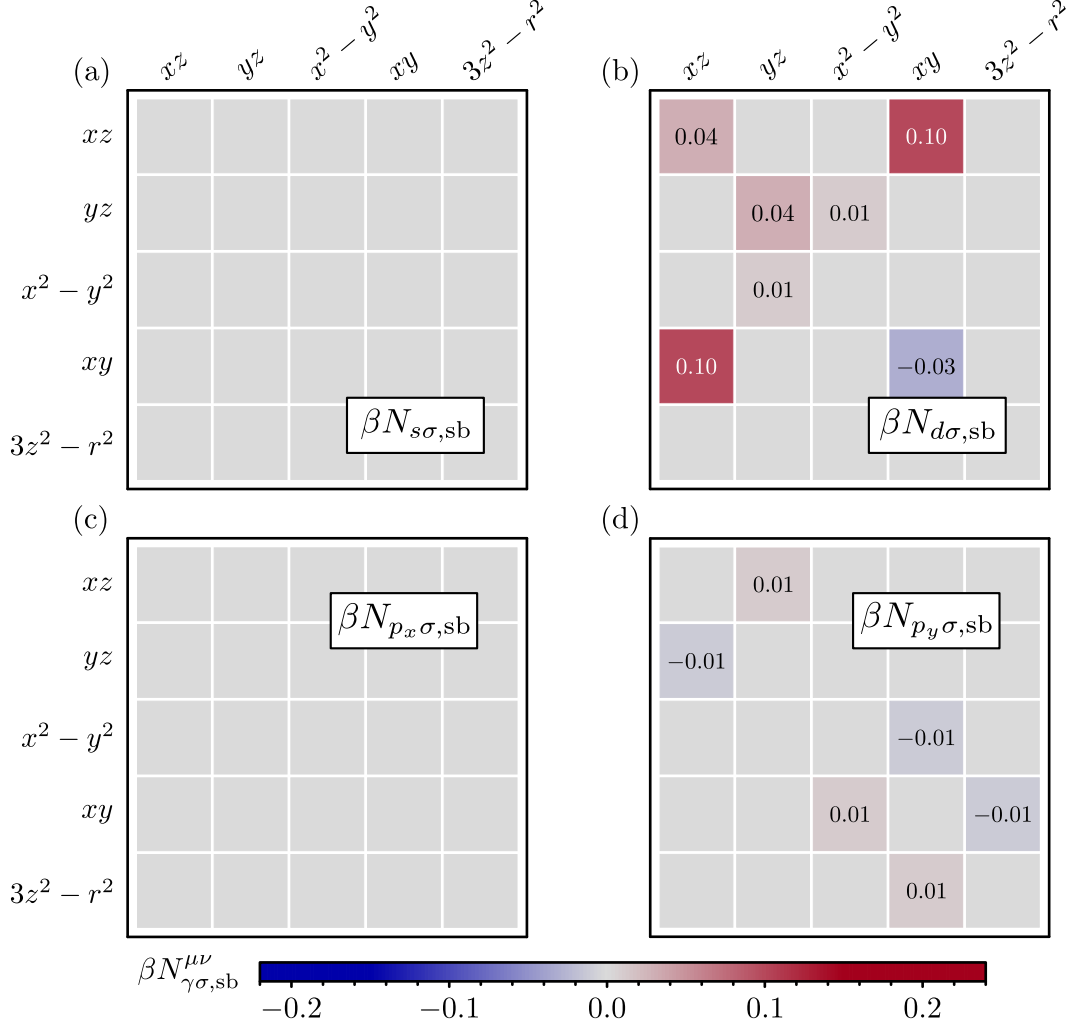


Figure 3.7: Symmetry breaking fields, $N_{\gamma\sigma, sb}^{\mu\nu}$, calculated self-consistently with the parameters used in fig. 3.1(b) and 3.1(d). Each field is coupled to the belonging form factor listed in eqn. (3.8). Only (b) and (d) display non-zero solutions, and the former will ultimately give rise to the highly anisotropic FS shown in fig. 3.1(b). Similar to figs. 3.2 and 3.6, also here we rounded the values of the matrix elements to the second decimal place.

By explicitly performing these averages for the 2D system under consideration, we get the following matrices $N_{\gamma\sigma,\Gamma}$ in orbital space for a given spin projection $\sigma = \{\uparrow, \downarrow\} \equiv \{1, -1\}$

$$N_{\gamma\sigma,A_1} = \begin{pmatrix} \frac{1}{2}(n_\gamma^{11} + n_\gamma^{22}) & \frac{\sigma}{2}(m_\gamma^{12} - m_\gamma^{21}) & 0 & 0 & 0 \\ -\frac{\sigma}{2}(m_\gamma^{12} - m_\gamma^{21}) & \frac{1}{2}(n_\gamma^{11} + n_\gamma^{22}) & 0 & 0 & 0 \\ 0 & 0 & n_\gamma^{33} & \sigma m_\gamma^{34} & 0 \\ 0 & 0 & \sigma m_\gamma^{43} & n_\gamma^{44} & 0 \\ 0 & 0 & 0 & 0 & n_\gamma^{55} \end{pmatrix}, \quad (3.17a)$$

$$N_{\gamma\sigma,A_2} = \begin{pmatrix} \frac{\sigma}{2}(m_\gamma^{11} + m_\gamma^{22}) & \frac{1}{2}(n_\gamma^{12} - n_\gamma^{21}) & 0 & 0 & 0 \\ -\frac{1}{2}(n_\gamma^{12} - n_\gamma^{21}) & \frac{\sigma}{2}(m_\gamma^{11} + m_\gamma^{22}) & 0 & 0 & 0 \\ 0 & 0 & \sigma m_\gamma^{33} & n_\gamma^{34} & 0 \\ 0 & 0 & n_\gamma^{43} & \sigma m_\gamma^{44} & 0 \\ 0 & 0 & 0 & 0 & \sigma m_\gamma^{55} \end{pmatrix}, \quad (3.17b)$$

$$N_{\gamma\sigma,B_1} = \begin{pmatrix} \frac{1}{2}(n_\gamma^{11} - n_\gamma^{22}) & \frac{\sigma}{2}(m_\gamma^{12} + m_\gamma^{21}) & 0 & 0 & 0 \\ \frac{\sigma}{2}(m_\gamma^{12} + m_\gamma^{21}) & -\frac{1}{2}(n_\gamma^{11} - n_\gamma^{22}) & 0 & 0 & 0 \\ 0 & 0 & 0 & 0 & n_\gamma^{35} \\ 0 & 0 & 0 & 0 & \sigma m_\gamma^{45} \\ 0 & 0 & n_\gamma^{53} & \sigma m_\gamma^{54} & 0 \end{pmatrix}, \quad (3.17c)$$

$$N_{\gamma\sigma,B_2} = \begin{pmatrix} \frac{\sigma}{2}(m_\gamma^{11} - m_\gamma^{22}) & \frac{1}{2}(n_\gamma^{12} + n_\gamma^{21}) & 0 & 0 & 0 \\ \frac{1}{2}(n_\gamma^{12} + n_\gamma^{21}) & -\frac{\sigma}{2}(m_\gamma^{11} - m_\gamma^{22}) & 0 & 0 & 0 \\ 0 & 0 & 0 & 0 & \sigma m_\gamma^{35} \\ 0 & 0 & 0 & 0 & n_\gamma^{45} \\ 0 & 0 & \sigma m_\gamma^{53} & n_\gamma^{54} & 0 \end{pmatrix}, \quad (3.17d)$$

$$N_{\gamma\sigma,E_x} = \begin{pmatrix} 0 & 0 & \frac{\sigma}{2}(m_\gamma^{13} + m_\gamma^{23}) & \frac{1}{2}(n_\gamma^{14} + n_\gamma^{24}) & \frac{\sigma}{2}(m_\gamma^{15} - m_\gamma^{25}) \\ 0 & 0 & \frac{1}{2}(-n_\gamma^{13} + n_\gamma^{23}) & \frac{\sigma}{2}(-m_\gamma^{14} + m_\gamma^{24}) & \frac{1}{2}(n_\gamma^{15} + n_\gamma^{25}) \\ \frac{\sigma}{2}(m_\gamma^{31} + m_\gamma^{32}) & \frac{1}{2}(-n_\gamma^{31} + n_\gamma^{32}) & 0 & 0 & 0 \\ \frac{1}{2}(n_\gamma^{41} + n_\gamma^{42}) & \frac{\sigma}{2}(-m_\gamma^{41} + m_\gamma^{42}) & 0 & 0 & 0 \\ \frac{\sigma}{2}(m_\gamma^{51} - m_\gamma^{52}) & \frac{1}{2}(n_\gamma^{51} + n_\gamma^{52}) & 0 & 0 & 0 \end{pmatrix}, \quad (3.17e)$$

$$N_{\gamma\sigma, E_y} = \begin{pmatrix} 0 & 0 & \frac{1}{2}(n_\gamma^{13} - n_\gamma^{23}) & \frac{\sigma}{2}(m_\gamma^{14} - m_\gamma^{24}) & \frac{1}{2}(n_\gamma^{15} + n_\gamma^{25}) \\ 0 & 0 & \frac{\sigma}{2}(m_\gamma^{13} + m_\gamma^{23}) & \frac{1}{2}(n_\gamma^{14} + n_\gamma^{24}) & \frac{\sigma}{2}(-m_\gamma^{15} + m_\gamma^{25}) \\ \frac{1}{2}(n_\gamma^{31} - n_\gamma^{32}) & \frac{\sigma}{2}(m_\gamma^{31} + m_\gamma^{32}) & 0 & 0 & 0 \\ \frac{\sigma}{2}(m_\gamma^{41} - m_\gamma^{42}) & \frac{1}{2}(n_\gamma^{41} + n_\gamma^{42}) & 0 & 0 & 0 \\ \frac{1}{2}(n_\gamma^{51} + n_\gamma^{52}) & \frac{\sigma}{2}(-m_\gamma^{51} + m_\gamma^{52}) & 0 & 0 & 0 \end{pmatrix}, \quad (3.17f)$$

$$N_{\gamma\sigma, E_{L_x}} = \begin{pmatrix} 0 & 0 & \frac{\sigma}{2}(m_\gamma^{13} - m_\gamma^{23}) & \frac{1}{2}(n_\gamma^{14} - n_\gamma^{24}) & \frac{\sigma}{2}(m_\gamma^{15} + m_\gamma^{25}) \\ 0 & 0 & \frac{1}{2}(n_\gamma^{13} + n_\gamma^{23}) & \frac{\sigma}{2}(m_\gamma^{14} + m_\gamma^{24}) & \frac{1}{2}(-n_\gamma^{15} + n_\gamma^{25}) \\ \frac{\sigma}{2}(m_\gamma^{31} - m_\gamma^{32}) & \frac{1}{2}(n_\gamma^{31} + n_\gamma^{32}) & 0 & 0 & 0 \\ \frac{1}{2}(n_\gamma^{41} - n_\gamma^{42}) & \frac{\sigma}{2}(m_\gamma^{41} + m_\gamma^{42}) & 0 & 0 & 0 \\ \frac{\sigma}{2}(m_\gamma^{51} + m_\gamma^{52}) & \frac{1}{2}(-n_\gamma^{51} + n_\gamma^{52}) & 0 & 0 & 0 \end{pmatrix}, \quad (3.17g)$$

$$N_{\gamma\sigma, E_{L_y}} = \begin{pmatrix} 0 & 0 & \frac{1}{2}(n_\gamma^{13} + n_\gamma^{23}) & \frac{\sigma}{2}(m_\gamma^{14} + m_\gamma^{24}) & \frac{1}{2}(n_\gamma^{15} - n_\gamma^{25}) \\ 0 & 0 & \frac{\sigma}{2}(-m_\gamma^{13} + m_\gamma^{23}) & \frac{1}{2}(-n_\gamma^{14} + n_\gamma^{24}) & \frac{\sigma}{2}(m_\gamma^{15} + m_\gamma^{25}) \\ \frac{1}{2}(n_\gamma^{31} + n_\gamma^{32}) & \frac{\sigma}{2}(-m_\gamma^{31} + m_\gamma^{32}) & 0 & 0 & 0 \\ \frac{\sigma}{2}(m_\gamma^{41} + m_\gamma^{42}) & \frac{1}{2}(-n_\gamma^{41} + n_\gamma^{42}) & 0 & 0 & 0 \\ \frac{1}{2}(n_\gamma^{51} - n_\gamma^{52}) & \frac{\sigma}{2}(m_\gamma^{51} + m_\gamma^{52}) & 0 & 0 & 0 \end{pmatrix}, \quad (3.17h)$$

where we introduced the following quantities for brevity

$$n_\gamma^{\mu\nu} = (N_{\gamma\uparrow}^{\mu\nu} + N_{\gamma\downarrow}^{\mu\nu})/2, \quad m_\gamma^{\mu\nu} = (N_{\gamma\uparrow}^{\mu\nu} - N_{\gamma\downarrow}^{\mu\nu})/2, \quad (3.18)$$

Note furthermore that the matrices labeled by the IR $E_{x,y}$ transform as the basis functions (x, y) , while $N_{\gamma\sigma, E_{L_x}}$ and $N_{\gamma\sigma, E_{L_y}}$ instead transform as the angular momentum pseudovector (L_x, L_y) . In general we allow for magnetic terms, i.e. $m_{\gamma\sigma}^{\mu\nu} \neq 0$, however, we find these fields to be orders of magnitude smaller than the density terms $n_{\gamma\sigma}^{\mu\nu}$. Nonetheless, for completeness our calculations and classification include all terms, so not to miss any subtle details.

We can then, after having performed the various averages in eqn. (3.16), express $N_{\mathbf{k}\sigma}^{\mu\nu}$ in terms of the IRs in the following way

$$N_{\mathbf{k}\sigma}^{\mu\nu} = \sum_\gamma f_{\mathbf{k}}^\gamma (N_{\gamma\sigma, \text{br}}^{\mu\nu} + N_{\gamma\sigma, \text{sb}}^{\mu\nu}) = \sum_\gamma \sum_\Gamma f_{\mathbf{k}}^\gamma N_{\gamma\sigma, \Gamma}^{\mu\nu}. \quad (3.19)$$

This informs us that a single term $f_{\mathbf{k}}^\gamma N_{\gamma\sigma, \Gamma}^{\mu\nu}$ must transform as the product of the two IRs γ and Γ , e.g. for $\gamma = d \sim B_1$ and $\Gamma = A_1$, the term altogether transforms as $B_1 \otimes A_1 = B_1$. With this in mind, we can collect terms that transform equivalently, and get

$$N_{\mathbf{k}\sigma, A_1}^{\mu\nu} = f_{\mathbf{k}}^s N_{s\sigma, A_1}^{\mu\nu} + f_{\mathbf{k}}^d N_{d\sigma, B_1}^{\mu\nu} + f_{\mathbf{k}}^{p_x} (N_{p_x\sigma, E_x} + N_{p_x\sigma, E_{L_x}}) + f_{\mathbf{k}}^{p_y} (N_{p_x\sigma, E_y} - N_{p_x\sigma, E_{L_y}}) \\ + f_{\mathbf{k}}^{p_x} (N_{p_y\sigma, E_x} - N_{p_y\sigma, E_{L_x}}) + f_{\mathbf{k}}^{p_y} (N_{p_y\sigma, E_y} + N_{p_y\sigma, E_{L_y}}), \quad (3.20)$$

$$N_{\mathbf{k}\sigma, A_2}^{\mu\nu} = f_{\mathbf{k}}^s N_{s\sigma, A_2}^{\mu\nu} + f_{\mathbf{k}}^d N_{d\sigma, B_2}^{\mu\nu} + f_{\mathbf{k}}^{p_x} (N_{p_x\sigma, E_y} + N_{p_x\sigma, E_{L_y}}) - f_{\mathbf{k}}^{p_y} (N_{p_x\sigma, E_x} - N_{p_x\sigma, E_{L_x}}) - f_{\mathbf{k}}^{p_x} (N_{p_y\sigma, E_y} - N_{p_y\sigma, E_{L_y}}) + f_{\mathbf{k}}^{p_y} (N_{p_y\sigma, E_x} + N_{p_y\sigma, E_{L_x}}), \quad (3.21)$$

$$N_{\mathbf{k}\sigma, B_1}^{\mu\nu} = f_{\mathbf{k}}^s N_{s\sigma, B_1}^{\mu\nu} + f_{\mathbf{k}}^d N_{d\sigma, A_1}^{\mu\nu} + f_{\mathbf{k}}^{p_x} (N_{p_x\sigma, E_x} + N_{p_x\sigma, E_{L_x}}) - f_{\mathbf{k}}^{p_y} (N_{p_x\sigma, E_y} - N_{p_x\sigma, E_{L_y}}) - f_{\mathbf{k}}^{p_x} (N_{p_y\sigma, E_x} - N_{p_y\sigma, E_{L_x}}) + f_{\mathbf{k}}^{p_y} (N_{p_y\sigma, E_y} + N_{p_y\sigma, E_{L_y}}), \quad (3.22)$$

$$N_{\mathbf{k}\sigma, B_2}^{\mu\nu} = f_{\mathbf{k}}^s N_{s\sigma, B_2}^{\mu\nu} + f_{\mathbf{k}}^d N_{d\sigma, A_2}^{\mu\nu} + f_{\mathbf{k}}^{p_x} (N_{p_x\sigma, E_y} + N_{p_x\sigma, E_{L_y}}) + f_{\mathbf{k}}^{p_y} (N_{p_x\sigma, E_x} - N_{p_x\sigma, E_{L_x}}) + f_{\mathbf{k}}^{p_x} (N_{p_y\sigma, E_y} - N_{p_y\sigma, E_{L_y}}) + f_{\mathbf{k}}^{p_y} (N_{p_y\sigma, E_x} + N_{p_y\sigma, E_{L_x}}), \quad (3.23)$$

for the IRs A_1 , A_2 , B_1 and B_2 , respectively, and finally for the 2D IR we arrive at

$$N_{\mathbf{k}\sigma, E_x}^{\mu\nu} = f_{\mathbf{k}}^s (N_{s\sigma, E_x}^{\mu\nu} + N_{s\sigma, E_{L_x}}^{\mu\nu}) + f_{\mathbf{k}}^d (N_{d\sigma, E_x}^{\mu\nu} + N_{d\sigma, E_{L_x}}^{\mu\nu}) + f_{\mathbf{k}}^{p_x} (N_{p_x\sigma, A_1}^{\mu\nu} + N_{p_x\sigma, B_1}^{\mu\nu}) + f_{\mathbf{k}}^{p_y} (N_{p_y\sigma, A_2}^{\mu\nu} + N_{p_y\sigma, B_2}^{\mu\nu}). \quad (3.24)$$

$$N_{\mathbf{k}\sigma, E_y}^{\mu\nu} = f_{\mathbf{k}}^s (N_{s\sigma, E_y}^{\mu\nu} + N_{s\sigma, E_{L_y}}^{\mu\nu}) + f_{\mathbf{k}}^d (N_{d\sigma, E_y}^{\mu\nu} + N_{d\sigma, E_{L_y}}^{\mu\nu}) + f_{\mathbf{k}}^{p_x} (N_{p_x\sigma, A_2}^{\mu\nu} + N_{p_x\sigma, B_2}^{\mu\nu}) + f_{\mathbf{k}}^{p_y} (N_{p_y\sigma, A_1}^{\mu\nu} + N_{p_y\sigma, B_1}^{\mu\nu}). \quad (3.25)$$

From the above, we are able to pinpoint exactly what fields give rise to the nematic order. For example, if a non-zero B_1 term appears in our self-consistent calculations, then we know that the nematic order transforms as B_1 , and that the resulting crystalline point group must be $D_2 \triangleleft D_{2d}$.

From our self-consistent calculations, we find that all A_2 and B_2 terms are identically zero, i.e. $N_{\mathbf{k}\sigma, A_2}^{\mu\nu} = N_{\mathbf{k}\sigma, B_2}^{\mu\nu} = 0$, which immediately implies that $N_{\mathbf{k}\sigma, \text{br}}^{\mu\nu} \equiv N_{\mathbf{k}\sigma, A_1}^{\mu\nu}$, thus the band renormalizing terms all transform as the IR A_1 . See fig. 3.6 for the values of $N_{\mathbf{k}\sigma, A_1}^{\mu\nu}$, where we straightforwardly conclude that

$$N_{s\sigma, \text{br}}^{\mu\nu} \equiv N_{s\sigma, A_1}^{\mu\nu}, \quad N_{d\sigma, \text{br}}^{\mu\nu} \equiv N_{d\sigma, B_1}^{\mu\nu}. \quad (3.26)$$

Similarly we conclude

$$N_{p_x\sigma, \text{br}}^{\mu\nu} \equiv N_{p_x\sigma, E_x}^{\mu\nu} + N_{p_x\sigma, E_{L_x}}^{\mu\nu} + N_{p_y\sigma, E_x}^{\mu\nu} - N_{p_x\sigma, E_{L_x}}^{\mu\nu}, \quad (3.27)$$

$$N_{p_y\sigma, \text{br}}^{\mu\nu} \equiv N_{p_x\sigma, E_y}^{\mu\nu} - N_{p_x\sigma, E_{L_y}}^{\mu\nu} + N_{p_y\sigma, E_y}^{\mu\nu} + N_{p_x\sigma, E_{L_y}}^{\mu\nu},$$

which can be inferred from fig. 3.8(a) and (b), where we show the matrices with the form factors $f_{\mathbf{k}}^{p_x}$ and $f_{\mathbf{k}}^{p_y}$ in eqn. (3.20).

We can furthermore extract from fig. 3.8(a) and (b) that $N_{\mathbf{k}\sigma, B_1}^{\mu\nu}$ only involve terms coupling to $f_{\mathbf{k}}^s$ and $f_{\mathbf{k}}^d$, since

$$(N_{p_x\sigma, E_x}^{\mu\nu} + N_{p_x\sigma, E_{L_x}}^{\mu\nu}) - (N_{p_y\sigma, E_x}^{\mu\nu} - N_{p_x\sigma, E_{L_x}}^{\mu\nu}) = (N_{p_y\sigma, E_y}^{\mu\nu} + N_{p_x\sigma, E_{L_y}}^{\mu\nu}) - (N_{p_x\sigma, E_y}^{\mu\nu} - N_{p_x\sigma, E_{L_y}}^{\mu\nu}) = 0, \quad (3.28)$$

i.e. all terms coupling to $f_{\mathbf{k}}^{p_x, y}$ cancel in this IR channel. From our self-consistent calculations, we also find that $N_{s\sigma, B_1}^{\mu\nu} = 0$, leaving us with only a single remaining term in $N_{\mathbf{k}\sigma, B_1}^{\mu\nu}$, namely $N_{d\sigma, A_1}^{\mu\nu}$. See

fig. 3.8(c) and (d) for an illustration of the matrices $N_{s\sigma, B_1}$ and $N_{d\sigma, A_1}$. The non-zero matrix elements of the latter can serve as order parameters for our nematic phase, since these break S_4 symmetry and reduce the crystalline point group symmetry to the group D_2 . Specifically, we define the B_1 nematic order parameter as

$$\begin{aligned} N_{B_1} &= (N_{d\sigma, A_1}^{11} + N_{d\sigma, A_1}^{22})/2 \\ &= (N_{d\sigma}^{11} + N_{d\bar{\sigma}}^{11} + N_{d\sigma}^{22} + N_{d\bar{\sigma}}^{22})/4 \\ &= (N_{d\sigma, sb}^{11} + N_{d\bar{\sigma}, sb}^{11} + N_{d\sigma, sb}^{22} + N_{d\bar{\sigma}, sb}^{22})/4. \end{aligned} \quad (3.29)$$

$\sigma = -\bar{\sigma}$. Alternatively, one could also define the order parameter as $N_{d\sigma, A_1}^{44}$, however, we choose to focus on N_{B_1} since it acquires a slightly higher value.

For the terms transforming as the 2D IR E, we find the non-zero matrices displayed in fig. 3.9, which ultimately result in a simplified expression for $N_{\mathbf{k}\sigma, E}$, namely

$$N_{\mathbf{k}\sigma, E}^{\mu\nu} = f_{\mathbf{k}}^d (N_{d\sigma, E_x}^{\mu\nu} + N_{d\sigma, E_{L_x}}^{\mu\nu}) + f_{\mathbf{k}}^{p_y} (N_{p_y\sigma, A_2}^{\mu\nu} + N_{p_y\sigma, B_2}^{\mu\nu}). \quad (3.30)$$

Similar to the B_1 terms, also here we can adopt the non-zero elements of $N_{\mathbf{k}\sigma, E}^{\mu\nu}$ as an order parameter of the system. Specifically we define the following two component order parameter

$$\begin{aligned} N_E &= \left(N_{d\sigma, E_x}^{14} + N_{d\sigma, E_{L_x}}^{14}, N_{d\sigma, E_y}^{24} + N_{d\sigma, E_{L_y}}^{24} \right) \\ &= ([N_{d\sigma}^{14} + N_{d\bar{\sigma}}^{14}], [N_{d\sigma}^{24} + N_{d\bar{\sigma}}^{24}]) / 2 \\ &= ([N_{d\sigma, sb}^{14} + N_{d\bar{\sigma}, sb}^{14}], [N_{d\sigma, sb}^{24} + N_{d\bar{\sigma}, sb}^{24}]) / 2 \\ &\equiv (N_{E_x}, N_{E_y}). \end{aligned} \quad (3.31)$$

The order parameters $N_{E_{x,y}}$ will enter on equal footing in a Landau free energy expansion, since they are interrelated by symmetry, and the system can thus display either $N_{E_x} \neq 0$ or $N_{E_y} \neq 0$. Through our self-consistent calculations we find in fact both solutions, depending on the initialization of our computations, i.e. where in the energy landscape the calculations start. Throughout the paper we have focused on solutions with $N_{E_x} \neq 0$.

Conclusively, we see that the presence of two non-zero order parameters, belonging to distinct IRs, hints at the following two phase transition scenarios: *i*) By lowering of the temperature, N_E becomes non-zero which imposes the symmetry point group transition $D_{2d} \rightarrow C_2$. For this specific point group N_{B_1} transform trivially, and is thus allowed to enter simultaneously with N_E , i.e. N_E and N_B emerges at the same transition temperature. The other scenario is *ii*) The system undergoes two consecutive phase transitions, with N_{B_1} entering prior to N_E when lowering the temperature, leading to two transition temperatures and the following point group reduction scheme $D_{2d} \rightarrow D_2 \rightarrow C_2$. For the specific system under consideration, we find scenario *ii*) to be true, see fig. 3.3 where we display the order parameters N_B and N_E at various temperatures. Nonetheless, we stress that case *i*) potentially also could arise in experiments.

3.C Susceptibility and Spin-Fluctuation Pairing from a Partially Incoherent Electronic Structure

Adopting the properties of a correlated electron gas which is characterized by a reduced quasiparticle weight $Z_{\mathbf{k}_F}$ at the Fermi level, it seems a good approximation at low energies to parametrize the Green

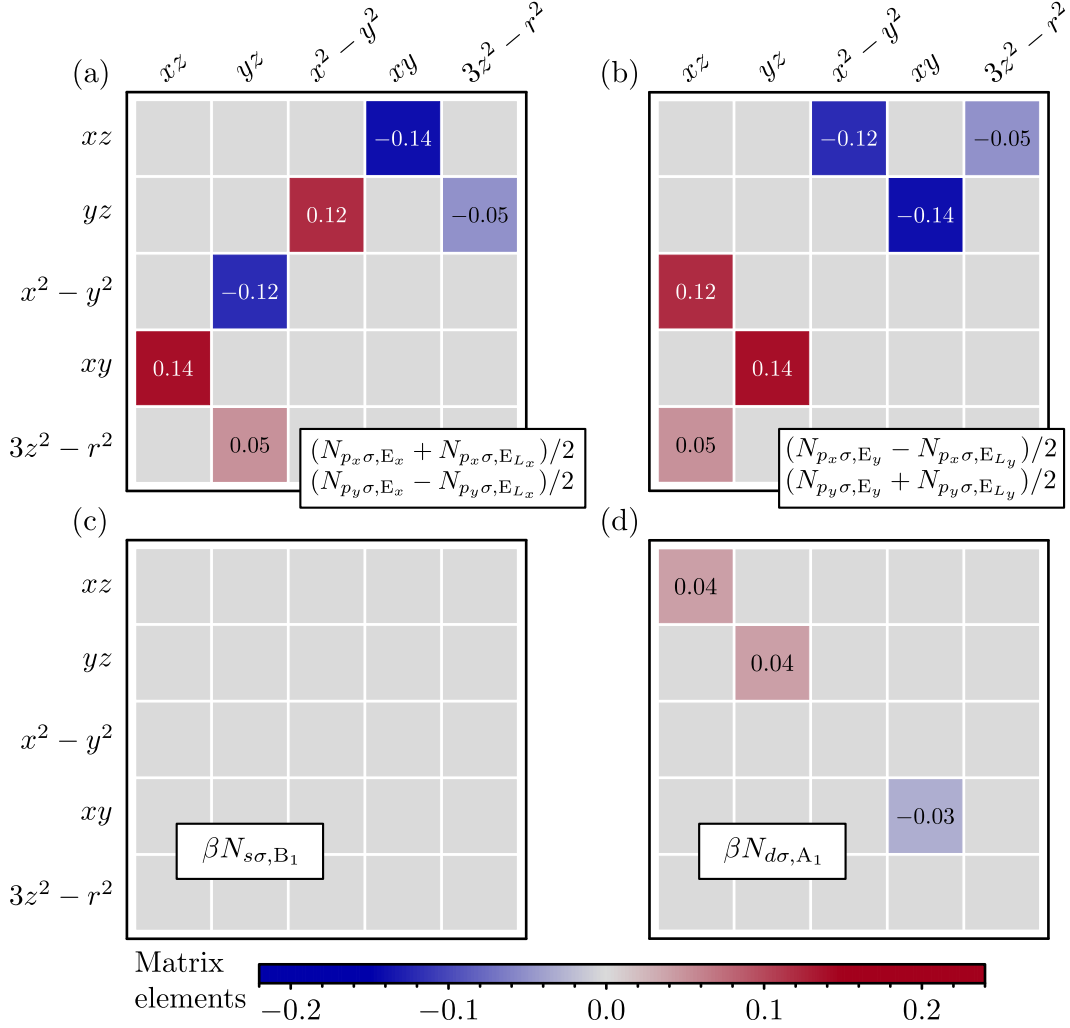


Figure 3.8: (a) and (b) Matrix structure of fields coupled to the p -wave form factors $f_{\mathbf{k}}^{p_x}$ and $f_{\mathbf{k}}^{p_y}$, respectively. These fields enter both in $N_{\mathbf{k}\sigma, A_1}$ and $N_{\mathbf{k}\sigma, B_1}$, but only lead to a non-zero contribution in the former, see eqns. (3.20) and (3.22). (c) and (d) Remaining contributions entering in $N_{\mathbf{k}\sigma, B_1}$. The non-zero elements in (d), can be utilized as the nematic order parameter, since they break S_4 symmetry. See eqn. (3.29) for the resulting B_1 nematic order parameter. All values in the figure have been rounded to the second decimal place.

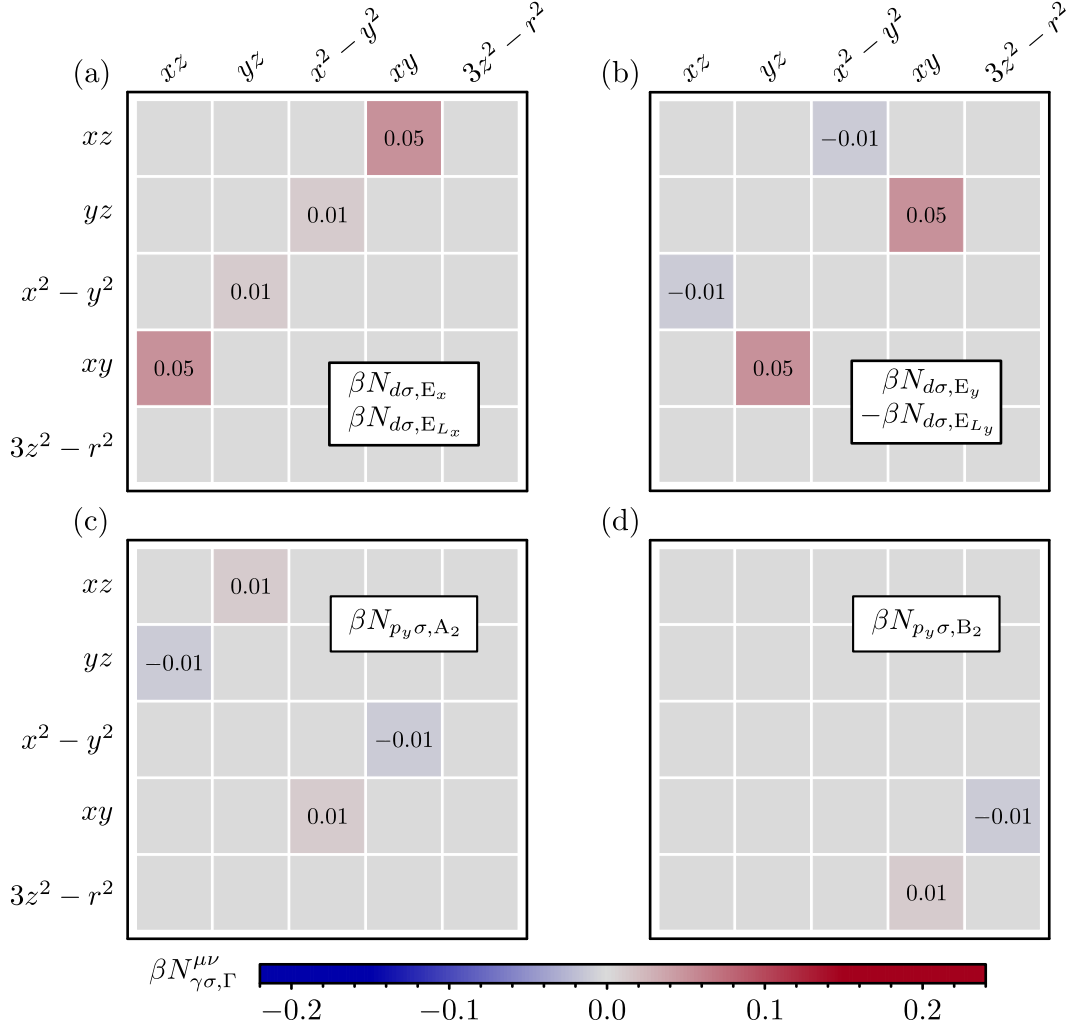


Figure 3.9: Non-zero matrices entering in the 2D IR fields in eqn. (3.24) and (3.25). The matrices in (a) and (b) [(c) and (d)] couple to the form factor $f_{\mathbf{k}}^d$ ($f_{\mathbf{k}}^{p_y}$). As for the B_1 field, also here the non-zero elements allow us to define an order parameter, see eqn. (3.31), which can be used as an indicator for when the symmetries of the system are described by the monoclinic point group C_2 . All values in the figure have been rounded to the second decimal place.

function as

$$G_{\mathbf{k},k_n}^{\mu\nu} = \sqrt{Z_\mu Z_\nu} \sum_{\alpha} \langle \mathbf{k}\mu | \mathbf{k}\alpha \rangle \langle \mathbf{k}\alpha | \mathbf{k}\nu \rangle G_{\mathbf{k},k_n}^{\alpha}, \quad (3.32)$$

where Z_μ are quasiparticle weights in orbital μ , $E_{\mathbf{k}\alpha}$ are the eigenenergies of band α of the mean field Hamiltonian in eqn. (3.5), and $G_{\mathbf{k},k_n}^{\alpha} = [ik_n - E_{\mathbf{k}\alpha}]^{-1}$ the Green function of band α . Adopting the usual local interactions from the Hubbard-Hund Hamiltonian

$$H = U \sum_i n_{i\mu\uparrow} n_{i\mu\downarrow} + \frac{U'}{2} \sum_i n_i n_i + \frac{J}{2} \sum_i c_{i\mu\sigma}^\dagger c_{i\nu\sigma'}^\dagger c_{i\mu\sigma'} c_{i\nu\sigma} + J' \sum_i c_{i\mu\uparrow}^\dagger c_{i\mu\downarrow}^\dagger c_{i\nu\downarrow} c_{i\nu\uparrow}, \quad (3.33)$$

where the parameters U , U' , J , J' are given in the notation of Kuroki *et al.* [266], we stay in the regime where $U' = U - 2J$, $J = J'$ and use the overall interaction magnitude U as free parameter to tune close to the magnetic instability and fix $J/U = 1/6$ as it has been used earlier for FeSe [216]. Within this current ansatz, the orbital susceptibility in the normal state is given by

$$\tilde{\chi}_{\mathbf{q},q_n;\mu_1\mu_2\mu_3\mu_4}^0 = - \sum_{\mathbf{k},k_n} \sum_{\alpha,\alpha'} M_{\mathbf{k},\mathbf{q};\mu_1\mu_2\mu_3\mu_4}^{\alpha\alpha'} G_{\mathbf{k}+\mathbf{q},k_n+q_n}^{\alpha} G_{\mathbf{k},k_n}^{\alpha'}, \quad (3.34)$$

where we have defined the abbreviation

$$M_{\mathbf{k},\mathbf{q};\mu_1\mu_2\mu_3\mu_4}^{\alpha\alpha'} = \sqrt{Z_{\mu_1} Z_{\mu_2} Z_{\mu_3} Z_{\mu_4}} \langle \mathbf{k}\mu_4 | \mathbf{k}\alpha' \rangle \langle \mathbf{k}\alpha' | \mathbf{k}\mu_2 \rangle \langle \mathbf{k} + \mathbf{q}\mu_1 | \mathbf{k} + \mathbf{q}\alpha \rangle \langle \mathbf{k} + \mathbf{q}\alpha | \mathbf{k} + \mathbf{q}\mu_3 \rangle. \quad (3.35)$$

To evaluate the susceptibility, we perform the frequency summation analytically and numerically sum over the full Brillouin zone using 400×400 \mathbf{k} points. Note that the susceptibility is just related by

$$\tilde{\chi}_{\mathbf{q};\mu_1\mu_2\mu_3\mu_4}^0 = \sqrt{Z_{\mu_1} Z_{\mu_2} Z_{\mu_3} Z_{\mu_4}} \chi_{\mathbf{q};\mu_1\mu_2\mu_3\mu_4}^0, \quad (3.36)$$

to the one from a fully coherent electronic structure, i.e. the quasiparticle weights enter as prefactors and renormalize each component of the susceptibility tensor. Finally, we treat the interactions in a random phase approximation (RPA) to calculate the spin (1) and charge (0) susceptibilities

$$\tilde{\chi}_{1\mathbf{q};\mu_1\mu_2\mu_3\mu_4}^{\text{RPA}} = \left[\tilde{\chi}_{\mathbf{q},iq_n}^0 (1 - \bar{U}^s \tilde{\chi}_{\mathbf{q},iq_n}^0)^{-1} \right]_{\mu_1\mu_2\mu_3\mu_4}, \quad (3.37a)$$

$$\tilde{\chi}_{0\mathbf{q};\mu_1\mu_2\mu_3\mu_4}^{\text{RPA}} = \left[\tilde{\chi}_{\mathbf{q},iq_n}^0 (1 + \bar{U}^c \tilde{\chi}_{\mathbf{q},iq_n}^0)^{-1} \right]_{\mu_1\mu_2\mu_3\mu_4}. \quad (3.37b)$$

The total spin susceptibility as measured experimentally is given by the sum

$$\tilde{\chi}_{\mathbf{q},\omega} = \frac{1}{2} \sum_{\mu\nu} \tilde{\chi}_{1\mathbf{q},\omega;\mu\mu\nu\nu}^{\text{RPA}}. \quad (3.38)$$

Note that the interaction matrices \bar{U}^s and \bar{U}^c contain linear combinations of the parameters U , U' , J , J' , for details see for example ref. [267].

To calculate the superconducting instability in the spin-singlet channel (the dominant one for the present models), we use the vertex for pair scattering between bands α and α' ,

$$\tilde{\Gamma}_{\mathbf{k},\mathbf{k}'}^{\alpha\alpha'} = \text{Re} \langle \mathbf{k}\alpha | \mathbf{k}\mu_1 \rangle \langle -\mathbf{k}\alpha | -\mathbf{k}\mu_4 \rangle \tilde{\Gamma}_{\mathbf{k},\mathbf{k}';\mu_1\mu_2\mu_3\mu_4} \langle \mathbf{k}'\mu_2 | \mathbf{k}'\alpha' \rangle \langle -\mathbf{k}'\mu_3 | -\mathbf{k}'\alpha' \rangle, \quad (3.39)$$

where \mathbf{k} and \mathbf{k}' are wave-vectors restricted to the pockets $\mathbf{k} \in C_\alpha$ and $\mathbf{k}' \in C_{\alpha'}$, and is defined in terms of the orbital space vertex function

$$\tilde{\Gamma}_{\mathbf{k},\mathbf{k}';\mu_1\mu_2\mu_3\mu_4} = \left[\frac{3}{2} \bar{U}^s \tilde{\chi}_{1\mathbf{k}-\mathbf{k}'}^{\text{RPA}} \bar{U}^s + \frac{1}{2} \bar{U}^s - \frac{1}{2} \bar{U}^c \tilde{\chi}_{0\mathbf{k}-\mathbf{k}'}^{\text{RPA}} \bar{U}^c + \frac{1}{2} \bar{U}^c \right]_{\mu_1\mu_2\mu_3\mu_4}. \quad (3.40)$$

Then, the linearized gap equation

$$-\frac{1}{V_G} \sum_{\alpha} \int_{\text{FS}_{\alpha}} dS' \tilde{\Gamma}_{\mathbf{k},\mathbf{k}'}^{\alpha'\alpha} \frac{g_{\mathbf{k}';i}}{|v_{F\alpha;\mathbf{k}'}|} = \lambda_i g_{\mathbf{k};i} \quad (3.41)$$

describes the superconducting gap $\Delta_{\mathbf{k}} \propto g_{\mathbf{k}}$ for the largest eigenvalue λ at least at T_c . The integration is over the Fermi surface FS_{α} , the Fermi velocity $v_{F\alpha;\mathbf{k}'}$ enters as weights in the denominator and V_G is the volume of the Brillouin zone. For the uncorrelated case [figs. 3.4, 3.5(a)] we have used $Z_{\mu} = 1$, while for the weakly correlated case we start with $\sqrt{Z_{\mu}} = \{0.72, 0.89, 0.77, 0.77, 0.85\}$ [220], subsequently reduce $\sqrt{Z_{xy}}$ by steps of 0.1, figs. 3.4, 3.5(b), and finally split $\sqrt{Z_{xz,yz}} = 0.77 \mp 0.02s$, $s = \{1, 2, 3, 4\}$, figs. 3.4, 3.5(c).

Part II

Topological Phases of Multi-Orbital Systems

“Sure, this will probably end up being another in a long line of emotionally crippling misadventures... but let’s try to have some fun along the way.”

– Yorick Brown

4

Majorana Zero Modes in Magnetic Texture Vortices



Info: This chapter has been submitted for publication, and can be found as an [arXiv preprint](#) [[arXiv:2008.10626](#) [[cond-mat.mes-hall](#)]] by me, Brian M. Andersen and Panagiotis Kotetes.

4.1 Introduction

The experimental study of bound states in superconductors (SCs) has recently witnessed a reheated interest. This came after a series of theory proposals, which designated how to induce non-Abelian anyons in 0D defects [7, 8, 12, 269–272], as well as termination edges in certain SCs featuring p -wave pairing [13, 273], antisymmetric SOC [274–279], Landau levels [280, 281], noncollinear magnetism [102, 103, 105, 106, 108–111, 113, 115, 119, 121], or collinear magnetism [124, 282–284]. Majorana zero modes (MZMs) are so far the most sought-after excitations of this genre [107, 285–294]. They are charge-neutral, spatially localized, pinned to zero energy, and enjoy a topological protection. In addition, they adhere to Ising exchange statistics, which open perspectives for fault-tolerant quantum computing [92–94]. The charge neutrality of MZMs brings SCs forward as ideal candidates to look for them, since their quasiparticle excitations arise from hybridized electrons and holes. Experimental evidences for MZMs have been already captured in nanowire [295–306], topological insulator [307–310], magnetic adatom [311–318] and FeSC [87–91] systems.

It has been shown that MZMs appear in vortices induced in chiral $p_x + ip_y$ SCs [7, 8], and conventional SCs in proximity to time-reversal invariant topological insulators [12]. In fact, the vortices

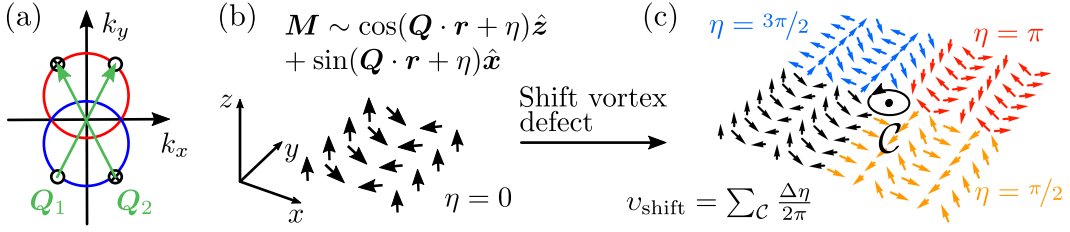


Figure 4.1: (a) Example of a bulk energy spectrum for the type of nodal superconductors discussed in this chapter. We consider $n \in \mathbb{N}$ pairs of nodes with opposite momenta $\pm \mathbf{k}_n$ and spin projections \uparrow, \downarrow . Thus, the nodes of such a pair carry the same helicity $\zeta = \pm 1$ ($\{\otimes, \odot\}$), and are assumed to be gapped out by a magnetic helix/stripe texture with a wave vector \mathbf{Q}_n . (b) Sketch of a magnetic helix with $\mathbf{Q} = (2\pi/3, 0)$. (c) Same as in (b), but for a discrete shift defect with vorticity $v_{\text{shift}} = 1$.

do not need to be introduced in the pairing term, but can also arise in the phase of another complex field or the angle of a two-component vector entering the Hamiltonian [27, 29, 319–323], e.g. in the complex order parameter of superfluid [319] and axion-string [320] condensates, or in the angle of a two-component SOC vector field [317, 321]. To obtain robust MZMs, a fully-gapped bulk energy spectrum is required. To achieve this, all the above proposals strictly require a fully-gapped pairing term. As a result, this prerequisite has so far excluded the MZM pursuit in an equally abundant category of SCs, which instead contain point nodes. Hence, a question naturally arises: under what conditions can MZMs become accessible if our starting point is a nodal SC instead?

In this chapter, we unveil that MZMs can be indeed trapped in a nodal SC by inducing so-called spin and shift vortices in magnetic textures which are exchange-coupled to the electrons. Here, we explore textures consisting of magnetic helices and/or stripes, with suitable wave vectors \mathbf{Q}_n which ensure that all nodes at $\pm \mathbf{k}_n$ momenta become pairwise coupled and gapped out (see fig. 4.1). While a fully-gapped bulk spectrum emerges in our mechanism as well, we prove that MZMs appear in the cores of the magnetic-texture vortices *only* when nodes are present in the spectrum of the host SC. Our theory applies to generic nodal SCs with spin-singlet, -triplet or mixed [324] pairing, thus covering a broad range of materials and hybrid structures. Remarkably, for systems with antisymmetric SOC, MZMs can be trapped by inducing vortices in textures as simple as magnetic stripes.

4.2 Microscopic Continuum Model

To model the physical situations of interest, we employ the following continuum BdG Hamiltonian

$$H = \frac{1}{2} \int d\mathbf{r} \Psi^\dagger(\mathbf{r}) \mathcal{H}(\mathbf{p}, \mathbf{r}) \Psi(\mathbf{r}), \quad (4.1)$$

with the spinor $\Psi^\dagger(\mathbf{r}) = (\psi_\uparrow^\dagger(\mathbf{r}), \psi_\downarrow^\dagger(\mathbf{r}), \psi_\downarrow(\mathbf{r}), -\psi_\uparrow(\mathbf{r}))$. Here, $\psi_\sigma(\mathbf{r})$ annihilates an electron at position \mathbf{r} with spin projection σ , while $\mathbf{p} = -i\nabla$ with $\hbar = 1$. The BdG matrix representation of $\mathcal{H}(\mathbf{p}, \mathbf{r})$ is as

	Symmetries			$\delta = d - D$							
	Θ^2	Ξ^2	Π^2	0	1	2	3	4	5	6	7
A	0	0	0	\mathbb{Z}	0	\mathbb{Z}	0	\mathbb{Z}	0	\mathbb{Z}	0
AIII	0	0	$\mathbb{1}$	0	\mathbb{Z}	0	\mathbb{Z}	0	\mathbb{Z}	0	\mathbb{Z}
AI	$\mathbb{1}$	0	0	\mathbb{Z}	0	0	0	$2\mathbb{Z}$	0	\mathbb{Z}_2	\mathbb{Z}_2
BDI	$\mathbb{1}$	$\mathbb{1}$	$\mathbb{1}$	\mathbb{Z}_2	\mathbb{Z}	0	0	0	$2\mathbb{Z}$	0	\mathbb{Z}_2
D	0	$\mathbb{1}$	0	\mathbb{Z}_2	\mathbb{Z}_2	\mathbb{Z}	0	0	0	$2\mathbb{Z}$	0
DIII	$-\mathbb{1}$	$\mathbb{1}$	$\mathbb{1}$	0	\mathbb{Z}_2	\mathbb{Z}_2	\mathbb{Z}	0	0	0	$2\mathbb{Z}$
AII	$-\mathbb{1}$	0	0	$2\mathbb{Z}$	0	\mathbb{Z}_2	\mathbb{Z}_2	\mathbb{Z}	0	0	0
CII	$-\mathbb{1}$	$-\mathbb{1}$	$\mathbb{1}$	0	$2\mathbb{Z}$	0	\mathbb{Z}_2	\mathbb{Z}_2	\mathbb{Z}	0	0
C	0	$-\mathbb{1}$	0	0	0	$2\mathbb{Z}$	0	\mathbb{Z}_2	\mathbb{Z}_2	\mathbb{Z}	0
CI	$\mathbb{1}$	$-\mathbb{1}$	$\mathbb{1}$	0	0	0	$2\mathbb{Z}$	0	\mathbb{Z}_2	\mathbb{Z}_2	\mathbb{Z}

Table 4.1: Periodic table of the ten symmetry classes, based on the square of three discrete non-spatial symmetries, i.e. Θ^2 , Ξ^2 and Π^2 . If a symmetry is broken, it is indicated by a 0. For a given set of symmetries, and the spatial dimensions δ , one can read of the type of invariant which can be defined for the system. In the absence of topological defects, the dimension reduces to $\delta \mapsto d$.

follows

$$D_{\text{BdG}}[\mathcal{H}(\mathbf{p}, \mathbf{r})] = D_{\text{BdG}}[\mathcal{H}_0(\mathbf{p})] + \sum_n \left(2M_n \cos[\mathbf{Q}_n \cdot \mathbf{r} + \eta_n(\mathbf{r})] \hat{\mathbf{e}}_n \cdot \boldsymbol{\sigma} - 2M'_n \sin[\mathbf{Q}_n \cdot \mathbf{r} + \eta_n(\mathbf{r})] \hat{\mathbf{e}}'_n \cdot \boldsymbol{\sigma} \right) e^{-i\omega_n(\mathbf{r})\sigma_z}, \quad (4.2)$$

and is represented using the $\boldsymbol{\tau}$ ($\boldsymbol{\sigma}$) Pauli matrices defined in Nambu (spin) space, supplemented with the respective unit matrix $\mathbb{1}_\tau$ ($\mathbb{1}_\sigma$). In chap. 1 we adopted the notation $D_{\text{BdG}}[\mathcal{H}]$ in order to distinguish abstract operators from matrices, however, in the following we will solely focus on BdG matrix representations of the Hamiltonian, and we can thus simply replace $D_{\text{BdG}}[\mathcal{H}] \rightarrow \mathcal{H}$. For simplicity, we omit writing unit matrices throughout. In the above, $\hat{\mathbf{e}}_n \cdot \hat{\mathbf{e}}'_n = 0$ for all n . The nonmagnetic part of the BdG Hamiltonian reads

$$\mathcal{H}_0(\mathbf{p}) = \tau_3 [\xi_s(\mathbf{p}) + \xi_t(\mathbf{p})\sigma_z] + \tau_1 [\Delta_s(\mathbf{p}) + \Delta_t(\mathbf{p})\sigma_z] \quad (4.3)$$

where $f_s(-\mathbf{p}) = f_s(\mathbf{p})$ and $f_t(-\mathbf{p}) = -f_t(\mathbf{p})$ for $f = \xi, \Delta$. $\mathcal{H}_0(\mathbf{p})$ is invariant under z -axis spin rotations [translations] associated with the angles $\omega_n(\mathbf{r})$ [phases $\eta_n(\mathbf{r})$]. In 3D coordinate space, we define $\mathbf{r} = (x, y, z)$, $\tan \phi = y/x$, $\cos \theta = z/r$, $r = \sqrt{\rho^2 + z^2}$ and $\rho = \sqrt{x^2 + y^2}$. Vortices can be independently introduced in all $\omega_n(\mathbf{r})$ angles and $\eta_n(\mathbf{r})$ phases labeled by n , at the same or different positions. For a shift [spin] vortex defect with vorticity v_{shift} [v_{spin}] we set $\eta(\mathbf{r}) = v_{\text{shift}}\phi$ [$\omega(\mathbf{r}) = v_{\text{spin}}\phi$]. In fig. 4.1(c) we depict the spatial profile of a magnetic helix with a discrete shift vortex. A shift vortex defect in $\eta(\mathbf{r})$ implies that this phase shows discontinuous jumps by an integer multiple of 2π after traversing a path around the core of the defect, which is identified with the region where the magnetic texture vanishes. This is reflected in the definition of the vorticity $v_{\text{shift}} = \oint_C d\eta/2\pi \in \mathbb{Z}$,

where \mathcal{C} denotes a closed contour enclosing the core of the defect. A similar behavior emerges for $\omega(\mathbf{r})$ in the presence of a spin vortex with vorticity $v_{\text{spin}} = \oint_{\mathcal{C}} d\omega/2\pi \in \mathbb{Z}$.

To proceed, we employ standard classification methods, cf. refs. [27, 29] and table 4.1, where Θ , Ξ and Π are generalizations of the non-spatial symmetries T , C and S discussed in chap. 1. The topological classification of the system in the presence of defects is carried out using the BdG Hamiltonian in combined momentum-coordinate space $\mathcal{H}(\mathbf{k}, \mathbf{r})$, which is obtained by assuming that the defect builds up in a sufficiently smooth manner in space, so that the momentum $\mathbf{p} \rightarrow \mathbf{k}$ and the position \mathbf{r} appearing in $\eta_n(\mathbf{r})$ and $\omega_n(\mathbf{r})$ commute. This approach suffices to predict the appearance of MZMs, but generally fails to accurately describe the complete bound state spectrum that we observe in our numerics using abrupt defects. The relevant Majorana symmetry class, i.e., BDI, D or DIII, is inferred in the presence of the defect-containing variables. The effective classification dimension δ is obtained by the spatial dimensionality of the system d , after subtracting the dimension of the surface that can enclose the defect, i.e., here $\delta = d - 1$ since a circle \mathbb{S}^1 can enclose a vortex. Based on the tenfold classification [24–26], we find the topologically-nontrivial scenarios $\{\text{BDI, D, DIII}\} \rightarrow \{\mathbb{Z}, \mathbb{Z}_2, \mathbb{Z}_2\}$ in 2D, and $\{\text{D, DIII}\} \rightarrow \{\mathbb{Z}, \mathbb{Z}_2\}$ in 3D. To construct the topological invariants, we view ϕ as a synthetic momentum which extends the base space to (\mathbf{k}, ϕ) .

4.3 Topological Invariants and Numerical Results

Similar to ref. [323], which discusses MZMs trapped in superconducting vortices, also here, the outcome of the various topological invariants is tied to the local, instead of the global, \mathbf{k} -space topology of $\mathcal{H}_0(\mathbf{k})$. Therefore, to facilitate the calculation of the various topological invariants, we rely on low-energy models obtained after expanding the original Hamiltonian about pairs of nodes with momenta $\pm\mathbf{k}_n$, which are determined by

$$\mathcal{H}_0(\mathbf{k}) = \mathbf{0} \quad \Rightarrow \quad \xi_s(\mathbf{k}_n) \pm \sigma_z \xi_t(\mathbf{k}_n) = \Delta_s(\mathbf{k}_n) \pm \sigma_z \Delta_t(\mathbf{k}_n) = \mathbf{0}, \quad (4.4)$$

with $\mathbf{0}$ being the null matrix. Since $\{\xi_t(-\mathbf{k}), \Delta_t(-\mathbf{k})\} = -\{\xi_t(\mathbf{k}), \Delta_t(\mathbf{k})\}$ we find that nodes at opposite momenta $\pm\mathbf{k}_n$ carry opposite spin projections $\sigma_z = \pm 1$, i.e. possess the same helicity. See fig. 4.1(a). We now expand the Hamiltonian about the n -th pair of nodes by setting $\mathbf{k} \approx \pm\mathbf{k}_n + \mathbf{q}$ for small $|\mathbf{q}|$. By introducing the $\boldsymbol{\rho}$ Pauli matrices in $\{\mathbf{k}_n, -\mathbf{k}_n\}$ nodes space, the defect-free Hamiltonian in the vicinity of $\pm\mathbf{k}_n$ reads

$$\begin{aligned} \mathcal{H}^{(n)}(\mathbf{q}, \phi = 0) &= \tau_3 [\xi_s^{(n)} + \mathbf{v}_{\xi_t}^{(n)} \cdot \mathbf{q} \sigma_z] + \rho_3 \tau_3 [\mathbf{v}_{\xi_s}^{(n)} \cdot \mathbf{q} + \xi_t^{(n)} \sigma_z] \\ &+ M_n \rho_1 \hat{\mathbf{e}}_n \cdot \boldsymbol{\sigma} - M'_n \rho_2 \hat{\mathbf{e}}'_n \cdot \boldsymbol{\sigma} + \tau_1 [\Delta_s^{(n)} + \mathbf{v}_{\Delta_t}^{(n)} \cdot \mathbf{q} \sigma_z] + \rho_3 \tau_1 [\mathbf{v}_{\Delta_s}^{(n)} \cdot \mathbf{q} + \Delta_t^{(n)} \sigma_z], \end{aligned} \quad (4.5)$$

where we used the shorthand expressions for $f = \xi, \Delta$

$$f_{s,t}^{(n)} = f_{s,t}(\mathbf{k}_n) \quad \text{and} \quad \mathbf{v}_{f_{s,t}}^{(n)} = \nabla_{\mathbf{k}} f_{s,t}(\mathbf{k}) \Big|_{\mathbf{k}=\mathbf{k}_n}. \quad (4.6)$$

The nonmagnetic part of eqn. (4.5), that we denote $\mathcal{H}_0^{(n)}(\mathbf{q})$, is invariant under arbitrary ϕ -dependent shifts and spin rotations generated by the operators $\mathcal{L}_{\text{shift}}^{(n)} = \rho_3$ and $\mathcal{L}_{\text{spin}}^{(n)} = \sigma_z$. Thus, the defects are added as follows

$$\mathcal{H}^{(n)}(\mathbf{q}, \phi) = e^{i\phi \mathcal{L}^{(n)}/2} \mathcal{H}^{(n)}(\mathbf{q}, \phi = 0) e^{-i\phi \mathcal{L}^{(n)}/2}, \quad (4.7)$$

where we introduced $\mathcal{L}^{(n)} = v_{\text{shift}}^{(n)} \mathcal{L}_{\text{shift}}^{(n)} + v_{\text{spin}}^{(n)} \mathcal{L}_{\text{spin}}^{(n)}$.

For $M_n = M'_n = 0$, one defines the four states $|\rho_3 = \pm 1, \sigma_z = \pm 1\rangle$ in $\rho \otimes \sigma$ space. Two of these give rise to the pair of nodes at $\pm \mathbf{k}_n$, while the remaining two lie energetically away from zero. These two pairs of states can be distinguished by their helicity eigenvalue $\zeta = \rho_3 \sigma_z = \pm 1$. Hence, to obtain a Hamiltonian describing only the states related to the nodes, we project eqn. (4.5) onto a given helicity subspace, which fulfills: $\xi_s^{(n)} + \zeta \xi_t^{(n)} = \Delta_s^{(n)} + \zeta \Delta_t^{(n)} = 0$, resulting in

$$\mathcal{H}_\zeta^{(n)}(\mathbf{q}, \phi = 0) = \lambda_3 \mathbf{q} \cdot [\mathbf{v}_{\xi, \zeta}^{(n)} \tau_3 + \mathbf{v}_{\Delta, \zeta}^{(n)} \tau_1] + \mathbf{M}_\zeta^{(n)} \cdot \boldsymbol{\lambda}, \quad (4.8)$$

where $\mathbf{v}_{\xi, \zeta}^{(n)} = \zeta \mathbf{v}_{\xi_s}^{(n)} + \mathbf{v}_{\xi_t}^{(n)}$, $\mathbf{v}_{\Delta, \zeta}^{(n)} = \zeta \mathbf{v}_{\Delta_s}^{(n)} + \mathbf{v}_{\Delta_t}^{(n)}$, and

$$\mathbf{M}_\zeta^{(n)} = (\hat{e}_{n,x} M_n + \zeta \hat{e}'_{n,y} M'_n, \hat{e}_{n,y} M_n - \zeta \hat{e}'_{n,x} M'_n, 0). \quad (4.9)$$

The unit $\mathbf{1}_\lambda$ and Pauli $\boldsymbol{\lambda}$ matrices, not to be confused with the Gell Mann matrices, act in a given helicity subspace. The choice of basis for both $\zeta = \pm 1$ is such that the spin Pauli matrix σ_z coincides with λ_3 . Note that the terms $\hat{e}_n \cdot \hat{\mathbf{z}}$, $\hat{e}'_n \cdot \hat{\mathbf{z}}$ drop out after the projection. Projecting the operator which generates the vortices yields

$$\mathcal{L}_\zeta^{(n)} = [\zeta v_{\text{shift}}^{(n)} + v_{\text{spin}}^{(n)}] \lambda_3. \quad (4.10)$$

Notably, the emergence of MZMs is guaranteed by the structure of eqns. (4.8) and (4.10), which allow mapping our model to the Jackiw-Rossi model [325]. The latter is known to support zero-energy solutions in vortices, and also lies at the core of the Fu-Kane proposal [12, 326].

The fact that MZMs become accessible in the model of eqn. (4.7) is alternatively understood in terms of the chiral symmetry $\Pi = \lambda_3 \tau_2$ it possesses. As a result, the Hamiltonian resides in class BDI and is classified by the winding number $w_3^{(n)} \in \mathbb{Z}$ [27] defined in (q_x, q_y, ϕ) . This invariant is expressed in terms of the upper off-diagonal block $h_\zeta^{(n)}(\mathbf{q}, \phi)$ of $\mathcal{H}_\zeta^{(n)}(\mathbf{q}, \phi)$, in a basis where the latter is block off-diagonal. Notably, by further exploiting

$$h_\zeta^{(n)}(\mathbf{q}, \phi) = e^{i\phi \mathcal{L}_\zeta^{(n)}/2} h_\zeta^{(n)}(\mathbf{q}, \phi = 0) e^{-i\phi \mathcal{L}_\zeta^{(n)}/2}, \quad (4.11)$$

and taking into account that the upper off-diagonal block $h_{0;\zeta}^{(n)}(\mathbf{q})$ of $\mathcal{H}_{0;\zeta}^{(n)}(\mathbf{q})$ commutes with $\mathcal{L}^{(n)}$, leads to (see app. 4.A)

$$w_{3;\zeta}^{(n)} = \sum_{\lambda=\pm 1} \frac{\zeta v_{\text{shift}}^{(n)} + v_{\text{spin}}^{(n)}}{2} \lambda \int \frac{d\mathbf{q}}{2\pi} \mathfrak{O}_{q_x q_y} i \text{tr} \ln [h_{0;\zeta, \lambda}^{(n)}(\mathbf{q})], \quad (4.12)$$

where we employed the eigenstates $|\lambda\rangle$ of $\mathcal{L}_\zeta^{(n)}$, which here coincide with the eigenstates of $\lambda_3 = \pm 1$. In addition, we introduced the shorthand notation $\mathfrak{O}_{q_x q_y} = \partial_{q_x} \partial_{q_y} - \partial_{q_y} \partial_{q_x}$ for the differential operator associated with vorticity in \mathbf{q} space. We make use of the identity $\text{tr} \ln [h_{0;\zeta, \lambda}^{(n)}(\mathbf{q})] = \ln \det [h_{0;\zeta, \lambda}^{(n)}(\mathbf{q})]$ and set $\det [h_{0;\zeta, \lambda}^{(n)}(\mathbf{q})] = |\det [h_{0;\zeta, \lambda}^{(n)}(\mathbf{q})]| e^{-i\varphi_{\zeta, \lambda}^{(n)}(\mathbf{q})}$. The latter implies that eqn. (4.12) is nonzero only when the arguments $\varphi_{\zeta, \lambda}^{(n)}(\mathbf{q})$ contain vortex defects. These \mathbf{q} -space vortices correspond to the point nodes in the spectrum. The node with helicity ζ and z -axis spin projection $\sigma_z = \pm 1$, carries vorticity $v_{\zeta, \lambda=\pm 1}^{(n)}$, which is defined through the relation $\mathfrak{O}_{q_x q_y} \varphi_{\zeta, \lambda}^{(n)}(\mathbf{q}) = 2\pi v_{\zeta, \lambda}^{(n)} \delta(\mathbf{q})$, and leads to the expression

$$w_{3;\zeta}^{(n)} = \sum_{\lambda=\pm 1} \frac{\zeta v_{\text{shift}}^{(n)} + v_{\text{spin}}^{(n)}}{2} \lambda v_{\zeta, \lambda}^{(n)}. \quad (4.13)$$

To evaluate the above, it is required to determine the vorticities of the nodes. For this purpose, we consider the unitary transformation $(\Pi + \tau_3)/\sqrt{2}$ onto the projected Hamiltonians, and obtain the upper off-diagonal blocks

$$h_{\zeta}^{(n)}(\mathbf{q}, \phi = 0) = [\mathbf{M}_{\zeta}^{(n)} \times \hat{\mathbf{z}}] \cdot \boldsymbol{\lambda} - \mathbf{q} \cdot [\mathbf{v}_{\Delta, \zeta}^{(n)} \lambda_3 + i\mathbf{v}_{\xi, \zeta}^{(n)}]. \quad (4.14)$$

We use the eigenstates of $\lambda_z \rightarrow \lambda = \pm 1$ and diagonalize $h_{0; \zeta}^{(n)}(\mathbf{q})$ as $h_{0; \zeta, \lambda}^{(n)}(\mathbf{q}) = -\mathbf{q} \cdot [\lambda \mathbf{v}_{\Delta, \zeta}^{(n)} + i\mathbf{v}_{\xi, \zeta}^{(n)}]$. As long as $\mathbf{v}_{\xi, \zeta}^{(n)} \times \mathbf{v}_{\Delta, \zeta}^{(n)} \neq \mathbf{0}$, the vorticities of the nodes at $\mathbf{q} = \mathbf{0}$ are opposite and of a single unit, i.e., $v_{\zeta, -\lambda}^{(n)} = -v_{\zeta, \lambda}^{(n)}$ and $|v_{\zeta, \lambda}^{(n)}| = 1$, while they are independent of the helicity ζ . Under the above conditions, we finally obtain

$$w_{3; \zeta}^{(n)} = \text{sgn}[v_{\zeta, \lambda=\pm 1}^{(n)}] [\zeta v_{\text{shift}}^{(n)} + v_{\text{spin}}^{(n)}], \quad (4.15)$$

which implies that both spin and shift vortex defects can induce a \mathbb{Z} number of MZMs. Notably, the number of MZMs arising due to the simultaneous emergence of shift and spin vortices at the same position in coordinate space, are obtained by adding (for $\zeta = 1$) or subtracting (for $\zeta = -1$) the number of MZMs that would independently arise for each different type of defect.

The above analysis persists, *only* as long as also the full Hamiltonian is in class BDI. We find that the latter possesses a chiral symmetry effected by $\tau_2 \sigma_z$, when \mathbf{e}_n and \mathbf{e}'_n lie in the same spin plane for all n . When at least one of $\xi_t(\mathbf{k})$ or $\Delta_t(\mathbf{k})$ is present, this is identified with the xy spin plane. If the above condition is met, eqn. (4.15) remains valid. Instead, for a full Hamiltonian belonging to class D solely the parity $(-1)^{w_{3; \zeta}^{(n)}} \in \mathbb{Z}_2$ is well defined, and protects only a single MZM at a vortex defect. Hence, further caution needs to be paid now on the possible node degeneracies which can trivialize the \mathbb{Z}_2 invariant. This takes place, for instance, when only $\xi_s(\mathbf{k})$ and $\Delta_s(\mathbf{k})$ enter $\mathcal{H}_0(\mathbf{k})$. In this case, both helicities contribute, i.e., $w_3^{(n)} = \sum_{\zeta=\pm 1} w_{3; \zeta}^{(n)}$. This case is trivial in class D, since we find $|w_3^{(n)}| = 2|v_{\text{spin}}^{(n)}|$, while in class BDI it predicts spin-degenerate MZM pairs only for spin vortices, as a consequence of the spin-singlet character of the pairing. Analogous results with $|w_3^{(n)}| = 2|v_{\text{shift}}^{(n)}|$ are obtained when only $\xi_s(\mathbf{k})$ and $\Delta_t(\mathbf{k})$ are considered.

We numerically verify the above predictions by implementing a lattice model version of eqn. (4.3) with the following constituents

$$\begin{aligned} \xi_{\mathbf{k}; s} &= -2t(\cos k_x + \cos k_y) - \mu_0, & \xi_{\mathbf{k}; t} &= \beta \sin k_y, \\ \Delta_{\mathbf{k}; s} &= \Delta, & \Delta_{\mathbf{k}; t} &= d_z \sin k_y. \end{aligned} \quad (4.16)$$

In the absence of magnetism and for a suitable window of parameters, the lattice model supports a nodal energy spectrum of the form depicted in fig. 4.1(a). We consider that the two pairs of nodes are gapped out by a magnetic texture which consists of two helices $\mathbf{M}_{1,2}(\mathbf{r})$, with wave vectors $\mathbf{Q}_{1,2}$. In fig. 4.2, we present results for helices with $\{\hat{\mathbf{e}}_{1,2}, \hat{\mathbf{e}}'_{1,2}\} = \{\hat{\mathbf{x}}, \hat{\mathbf{y}}\}$, when one of these harbors a shift vortex defect of a single unit of vorticity. When considering open boundary conditions, see inset in fig. 4.2(a), we find a single MZM pair along with an edge Majorana flat band (MFB). To uncover the MZMs which are energetically buried inside the MFB, we employ instead periodic boundary conditions. Indeed, the MZM pair is clearly discerned in main panel fig. 4.2(a). One of the MZMs is trapped at the core of the shift defect, see fig. 4.2(b), while the other appears at the edge of the system, see fig. 4.2(c). Note that finite-size effects and a weak inter-MZM coupling lead to a small

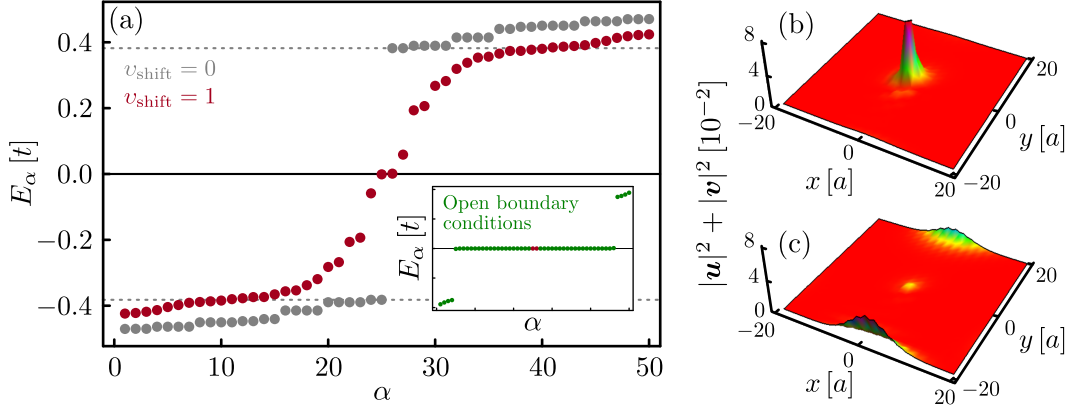


Figure 4.2: Numerical study of a BDI class model defined in eqn. (4.16). (a) 50 lowest eigenvalues in the absence (grey dots) and presence (red dots) of a single shift vortex with $v_{\text{shift}} = 1$. (b)-(c) Spatially-resolved MZM weight of the wavefunctions of (a) with electron (hole) column vectors \mathbf{u} (\mathbf{v}). We used the parameters $\Delta = 1/\sqrt{2}$, $\mu_0 = -5\Delta$, $d_z = \beta = 1$ and $\{M_{1,2}, M'_{1,2}\} = \{0.5, 0.1\}$, all in units of t , on a 40×40 square lattice with the lattice constant set to unity.

but nonzero MZM weight at the defect in (c). In app. 4.B we present additional results for BDI class models with higher values for the vorticity of the defect, as well as various 2D class D scenarios.

Our preceding analysis can be directly extended to 3D class D systems, which are classified by the 2nd Chern number \mathcal{C}_2 defined in (q_x, q_y, q_z, ϕ) space. \mathcal{C}_2 predicts the number of chiral Majorana modes emerging in the core of a vortex line. By evaluating \mathcal{C}_2 as a surface integral of the Chern-Simons 3 form, cf. ref. [27] and app. 4.A, and after exploiting eqn. (4.7), we find

$$\mathcal{C}_{2;\zeta}^{(n)} = \sum_{\lambda=\pm 1} \frac{\zeta v_{\text{shift}}^{(n)} + v_{\text{spin}}^{(n)}}{2} \lambda Q_{\zeta,\lambda}^{(n)}, \quad (4.17)$$

where $Q_{\zeta,\lambda}^{(n)}$ defines the monopole charge for the nodes of the n -th pair with helicity ζ and z -axis spin projection $\lambda = \pm 1$. As the simplest extension, one can consider the continuum model $\mathcal{H}_0(\mathbf{k}) = -k_y^2 \tau_3 + \beta(k_y \tau_3 + k_x \tau_1 - k_z \tau_2) \sigma_z$. The combined anisotropy and SOC yield two helical branches and two pair of nodes at $k_y = 0$ and $k_y = \pm\beta$. Here, the inner helical branch at $k_y = 0$ can be gapped out by a Zeeman field which is oriented orthogonally to the SOC vector [275, 276]. The two nodes of the outer helical branch can get gapped out by a magnetic stripe $\mathbf{M}(\mathbf{r}) = M \cos(2\beta y) \hat{x}$. Similarly to eqn. (4.15), here we find that a number of $|\mathcal{C}_2| = |v_{\text{shift}} + v_{\text{spin}}|$ chiral Majorana modes emerge in the core of a vortex line extending along the z -axis.

We numerically verify this results, by extending the model used in fig. 4.2 to 3D space, in the following way

$$\begin{aligned} \mathcal{H}_{\mathbf{k};0}^{3\text{D}} &= \tau_3 [\xi_{\mathbf{k};s}^{3\text{D}} + \xi_{\mathbf{k};t} \sigma_z] + \Delta (\tau_1 \sin k_x - \tau_2 \sin k_z) \sigma_z, \\ \text{with } \xi_{\mathbf{k};s}^{3\text{D}} &= -2t (\cos k_x + \cos k_y) - \Lambda (1 - \cos k_z) / 2 - \mu_0. \end{aligned} \quad (4.18)$$

We consider the limit $\Lambda \gg t$, for which the pairs of nodes in the nonmagnetic phase are located only in the $k_z = 0$ plane. After including the magnetic terms of the Hamiltonian and consider a vortex

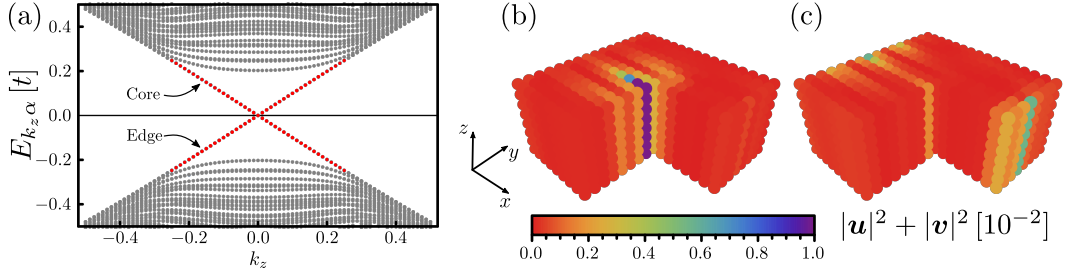


Figure 4.3: Chiral Majorana modes of the 3D class D model in eqn. (4.18). (a) Edge spectrum for the 3D model with a single shift vortex defect $v_{\text{shift}} = 1$. The spectrum is obtained with periodic (open) boundary conditions in the z (x and y) direction, and clearly displays chiral Majorana modes. The spatially-resolved weight of the two chiral branches are displayed in (b) and (c), and reveals a single Majorana mode at the core of the vortex defect, and its counterpart located at the edge of the system. Note that the nonzero wavefunction weight at the defect in (c), is a consequence of inter-Majorana mode coupling and finite-size effects. The figures were obtained with the parameters: $\Delta = 1$, $\mu_0 = -2\sqrt{2}$, $\beta = 2(\sqrt{2} - 1)$, $\Lambda = 8$ and $\{M_{1,2}, M'_{1,2}\} = \{0.5, 0.1\}$, all in units of t .

line extending uniformly in the z axis, we observe that k_z is a good quantum since $\tan \phi = y/x$. In fact, for small k_z , we can linearize the above Hamiltonian and see that for $k_z = 0$ it coincides with the model of fig. 4.2, where $\Pi = \tau_2 \sigma_3$ is conserved and gives rise to a pair of zero energy states. Away from $k_z = 0$ the chiral symmetry is broken, lifting the states away from zero energy, ultimately resulting into dispersive chiral Majorana modes, as seen fig. 4.3(a). Here, a single mode is dispersing along the vortex core while the other is on the outer edge of the system, see fig. 4.3(b) and (c), respectively.

Despite that magnetic textures break the standard time-reversal symmetry T , Majorana Kramers pairs are still accessible when a generalized time-reversal symmetry Θ with $\Theta^2 = -\mathbf{1}$ appears [107]. In this event, the Hamiltonian is of the DIII type and is classified by a \mathbb{Z}_2 topological invariant which now predicts the emergence of a single Majorana Kramers pair in a shift/spin vortex. Such a symmetry emerges in the previously examined models when we consider two bands which feel identical nonmagnetic terms, but opposite magnetic texture terms. After introducing the κ Pauli matrices in band space, we find $\Theta = \kappa_1 T$. When the bands are completely decoupled, they yield pairs of Majorana solutions in the core of the defect. Out of those, only a single Kramers pair survives upon the addition of band mixing terms which respect Θ and set the system in DIII class. A concrete example is detailed in app. 4.B.

4.4 Summary and Conclusions

Our theory applies to various intrinsic nodal SCs, such as, unconventional spin-singlet (-triplet) d -wave (p -wave) SCs [327], and noncentrosymmetric SCs with mixed spin pairing [101, 328–330]. Fe-based systems appear as prime spin-singlet SC candidates, because they can exhibit nodal superconductivity [64, 65], single- and double- \mathbf{Q} magnetic stripe order [66–76], and microscopic coexistence of magnetism and superconductivity [66, 80–85]. Moreover, recent theoretical studies [77] predict single- and double-

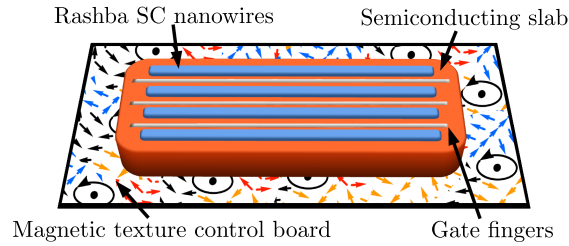


Figure 4.4: Hybrid Rashba SC-2DEG MZM platform. The SC filaments can be obtained by etching away strips in a SC layer epitaxially grown on top of the 2DEG slab, as in ref. [332]. Gate fingers, ideally buried under the slab, define loosely tunnel-coupled hybrid nanowires. MZMs can be pinned in the slab by inducing magnetic texture vortices in the 2D substrate.

Q magnetic textures in doped 122 and 1111 compounds. Note also, that, while Rashba SOC is usually negligible in these compounds, a given pair of nodes can still feel an effective Rashba SOC [331] that is generated by other helices comprising the magnetic texture.

The potential candidates moreover include a 2D electron gas (2DEG) or magnetic adatom lattices, in proximity to a conventional SC with strong Rashba SOC, such as Pb [311, 314]. The former scenario can arise for semiconducting slabs [332], or, coupled epitaxial nanowire hybrids [333, 334] based on semiconductors or carbon nanotubes. See fig. 4.4(b). Instead, in the second approach, the adatoms induce a lattice of Yu-Shiba-Rusinov (YSR) states [335–337]. While the underlying mechanisms differ, the proximity to the SC induces a self-energy to the 2DEG system/YSR lattice which leads to eqn. (4.3) [282, 284, 318, 324]. The arising nodes can be gapped out by magnetic stripes/helices and Zeeman fields (only for the inner helical branch). In 2DEGs, these textures can be engineered using nanomagnets [103, 119, 120, 122, 305], while in YSR lattices they are provided by the magnetization of the adatoms. Thus, being in a position to spatially control these textures in the above platforms, appears as a promising new route to trap and manipulate MZMs.

Concluding, we note that certain types of previously-studied topological defects in magnetic textures, i.e. disclinations [338, 339], have already been experimentally observed in helimagnets [340–344]. Similarly, we expect that the shift/spin vortices proposed in this work may arise either spontaneously or get pinned by disorder. Moreover, the magnetic-texture vortices discussed here are topologically distinct to the magnetic skyrmion bubbles that have been discussed in refs. [317, 345–349], and have been shown to act as smooth defects which can pin various types of bound states in fully-gapped SCs. Among these bound states one also finds MZMs [317, 346–348]. In our work, we do not view the texture itself as the defect, but instead consider singular defects in the texture. Hence, our mechanism to trap MZMs from a nodal SC, opens a novel path to explain the recent observations in 2D magnetic lattice-SC hybrids [317].

Appendices for Chapter 5

4.A Derivations for the w_3 and \mathcal{C}_2 Topological Invariants

The winding number w_3 is defined in 3D (\mathbf{q}, ϕ) space and is expressed as

$$w_3 = \int_0^{2\pi} \frac{d\phi}{2\pi} \int \frac{d\mathbf{q}}{2\pi} \text{tr} \left(h^{-1}(\mathbf{q}, \phi) [\partial_{q_x} h(\mathbf{q}, \phi)] h^{-1}(\mathbf{q}, \phi) [\partial_{q_y} h(\mathbf{q}, \phi)] h^{-1}(\mathbf{q}, \phi) [\partial_\phi h(\mathbf{q}, \phi)] \right). \quad (4.19)$$

By employing the relation $hh^{-1} = \mathbf{1} \Rightarrow \partial h^{-1} = -h^{-1}(\partial h)h^{-1}$ and the cyclic property of the trace, we find

$$w_3 = - \int_0^{2\pi} \frac{d\phi}{2\pi} \int \frac{d\mathbf{q}}{2\pi} \text{tr} \left([\partial_{q_x} h(\mathbf{q}, \phi)] h^{-1}(\mathbf{q}, \phi) [\partial_{q_y} h(\mathbf{q}, \phi)] \partial_\phi h^{-1}(\mathbf{q}, \phi) \right). \quad (4.20)$$

When the following relation holds: $h(\mathbf{q}, \phi) = e^{i\phi\mathcal{L}/2} h(\mathbf{q}, \phi = 0) e^{-i\phi\mathcal{L}/2}$, we also find the expression $h^{-1}(\mathbf{q}, \phi) = e^{i\phi\mathcal{L}/2} h^{-1}(\mathbf{q}, \phi = 0) e^{-i\phi\mathcal{L}/2}$. In this event, the winding number obtains the following simple form

$$\begin{aligned} w_3 &= i \int \frac{d\mathbf{q}}{2\pi} \text{tr} \left(\frac{\mathcal{L}}{2} ([\partial_{q_x} h^{-1}(\mathbf{q}, \phi = 0)] [\partial_{q_y} h(\mathbf{q}, \phi = 0)] - h \leftrightarrow h^{-1}) - q_x \leftrightarrow q_y \right) / 2 \\ &= \int \frac{d\mathbf{q}}{2\pi} \text{tr} \left(\frac{\mathcal{L}}{2} \mathcal{O}_{q_x q_y} i \ln [h(\mathbf{q}, \phi = 0)] \right). \end{aligned} \quad (4.21)$$

The above is nonzero even for a vanishing magnetic texture, in which case, $h(\mathbf{q}, \phi = 0) \rightarrow h_0(\mathbf{q})$. When $[\mathcal{L}, h_0(\mathbf{q})] = \mathbf{0}$, we evaluate the trace by introducing the eigenstates of \mathcal{L} , in which basis, $h_0(\mathbf{q})$ is block diagonal.

The 2nd Chern number \mathcal{C}_2 is defined in 4D $(q_x, q_y, \phi, q_z) \equiv (p_1, p_2, p_3, p_4)$ space and it is given by the expression

$$\mathcal{C}_2 = - \int \frac{d^4 p}{32\pi^2} \epsilon_{nm\ell s} \text{tr} [F_{nm} F_{\ell s}] \quad \text{with} \quad n, m, \ell, s = 1, 2, 3, 4. \quad (4.22)$$

We introduced the non-Abelian field strength tensor $F_{nm} = \partial_{p_n} A_m - \partial_{p_m} A_n - i[A_n, A_m]$, that is defined in terms of the Berry vector potential $A_n^{ab}(\mathbf{p}) = i\langle \Phi_a(\mathbf{p}) | \partial_{p_n} | \Phi_b(\mathbf{p}) \rangle$, which is a matrix in the occupied eigenstates $|\Phi(\mathbf{p})\rangle$ subspace. The Chern number can be equivalently expressed as a surface integral over the Chern-Simons 3 form. Here, we choose a surface $\mathcal{S} = \mathbb{S}^2 \times \mathbb{T}^1$ which is a \mathbb{S}^2 sphere in \mathbf{q} space. We thus find

$$\mathcal{C}_2 = - \oint_{\mathcal{S}} \frac{d^3 p}{8\pi^2} \epsilon_{nm\ell} \text{tr} \left(A_n \partial_{p_m} A_\ell - i \frac{2}{3} A_n A_m A_\ell \right) \quad \text{with} \quad n, m, \ell = 1, 2, 3. \quad (4.23)$$

When $\mathcal{H}(\mathbf{q}, \phi) = e^{i\phi\mathcal{L}/2}\mathcal{H}(\mathbf{q}, \phi = 0)e^{-i\phi\mathcal{L}/2}$, we find $|\Phi(\mathbf{q}, \phi)\rangle = e^{i\phi\mathcal{L}/2}|\Phi(\mathbf{q}, \phi = 0)\rangle$, which implies $A_{\mathbf{q}}(\mathbf{q}, \phi) = A_{\mathbf{q}}(\mathbf{q}, \phi = 0)$ and $A_{\phi}^{ab}(\mathbf{q}, \phi) = -\langle\Phi_a(\mathbf{q}, \phi = 0)|\mathcal{L}|\Phi_b(\mathbf{q}, \phi = 0)\rangle/2$. These lead to the simplified expression

$$\mathcal{C}_2 = \oint_{\mathbb{S}^2} \frac{d\mathbf{q}}{2\pi} \cdot \text{tr} \left[\frac{\mathcal{L}}{2} \Omega(\mathbf{q}, \phi = 0) \right] \quad (4.24)$$

where we introduced the matrix Berry curvature $\Omega(\mathbf{q}, \phi = 0)$. The above is generally nonzero also for vanishing magnetic texture strength. Under the assumption $[\mathcal{L}, \mathcal{H}_0(\mathbf{q})] = \mathbf{0}$, we evaluate the trace by introducing the eigenstates of \mathcal{L} , i.e. $\mathcal{L}|\lambda\rangle = v_{\text{defect}}\lambda|\lambda\rangle$, in which basis, $\mathcal{H}_0(\mathbf{q})$ and the respective Berry curvature matrix of the nonmagnetic system $\Omega_0(\mathbf{q})$ are block diagonal. Thus, we have

$$\mathcal{C}_2 = v_{\text{defect}} \sum_{\lambda} \frac{\lambda}{2} \oint_{\mathbb{S}^2} \frac{d\mathbf{q}}{2\pi} \cdot \text{tr}_{\lambda} [\Omega_{0;\lambda}(\mathbf{q})], \quad (4.25)$$

with the trace acting in a given λ block. Since we assume that the SCs under examination possess a zero 1st Chern number, the 2nd Chern number above becomes nonzero only in the presence of monopoles in the Berry curvature of the SC. These monopoles correspond to \mathbf{q} -space nodes in 3D space, which carry a topological charge defined through $\text{tr}_{\lambda} [\Omega_{0;\lambda}(\mathbf{q})] = Q_{\lambda}\mathbf{q}/(2|\mathbf{q}|^3)$. For a 2×2 λ block, these monopoles define Weyl points, which carry a topological charge given by $\Omega_{0;\lambda}(\mathbf{q}) = Q_{\lambda}\mathbf{q}/(2|\mathbf{q}|^3)$. Hence

$$\mathcal{C}_{2;\zeta}^{(n)} = \sum_{\lambda=\pm 1} \frac{\zeta v_{\text{shift}}^{(n)} + v_{\text{spin}}^{(n)}}{2} \lambda Q_{\zeta,\lambda}^{(n)}, \quad (4.26)$$

with $Q_{\zeta,\lambda}^{(n)}$ the monopole charge of the nodes of the n -th pair with helicity ζ and z -axis spin projection $\lambda = \pm 1$.

4.B Additional Numerical Investigations for BDI, D, and DIII Class Models

MZMs in Magnetic Texture Vortices for 2D Class BDI and D Models

In the main text we derived the topological invariant for a 2D BDI model, cf. eqn. (4.15), which predicts the appearance of multiple MZMs at the core of a shift/spin defect. To further verify this result, we study various cases numerically, by implementing the same lattice Hamiltonian used in fig. 4.2 in the main text. In fig. 4.5(a),(c) we confirm that $v_{\text{shift}} = 2$ results into two pairs of MZMs, with two at the center of the defect, and their two partners on the edge. Additionally we confirm that spin defects also lead to MZMs. See fig. 4.5(d) with 3 pairs of MZMs for $v_{\text{spin}} = 3$.

We can induce the class transition BDI \rightarrow D, by explicitly breaking the chiral symmetry $\Pi = \lambda_3\tau_2$ of eqn. (4.7) in the main text, which can be achieved either by applying a magnetic field in the z direction or by having \mathbf{e}_n and \mathbf{e}'_n lying in different spin planes. By virtue of the symmetry class reduction, it is only the parity $(-1)^{w_{3;\zeta}^{(n)}}$ which can protect MZMs. This is reflected in fig. 4.5(b) where we display the energy spectrum for $v_{\text{shift}} = 2$ in the presence of a magnetic field in the z direction. For this case $(-1)^{w_{3;\zeta}^{(n)}} = 1$, ultimately resulting in the hybridization of the MZMs, lifting them away from

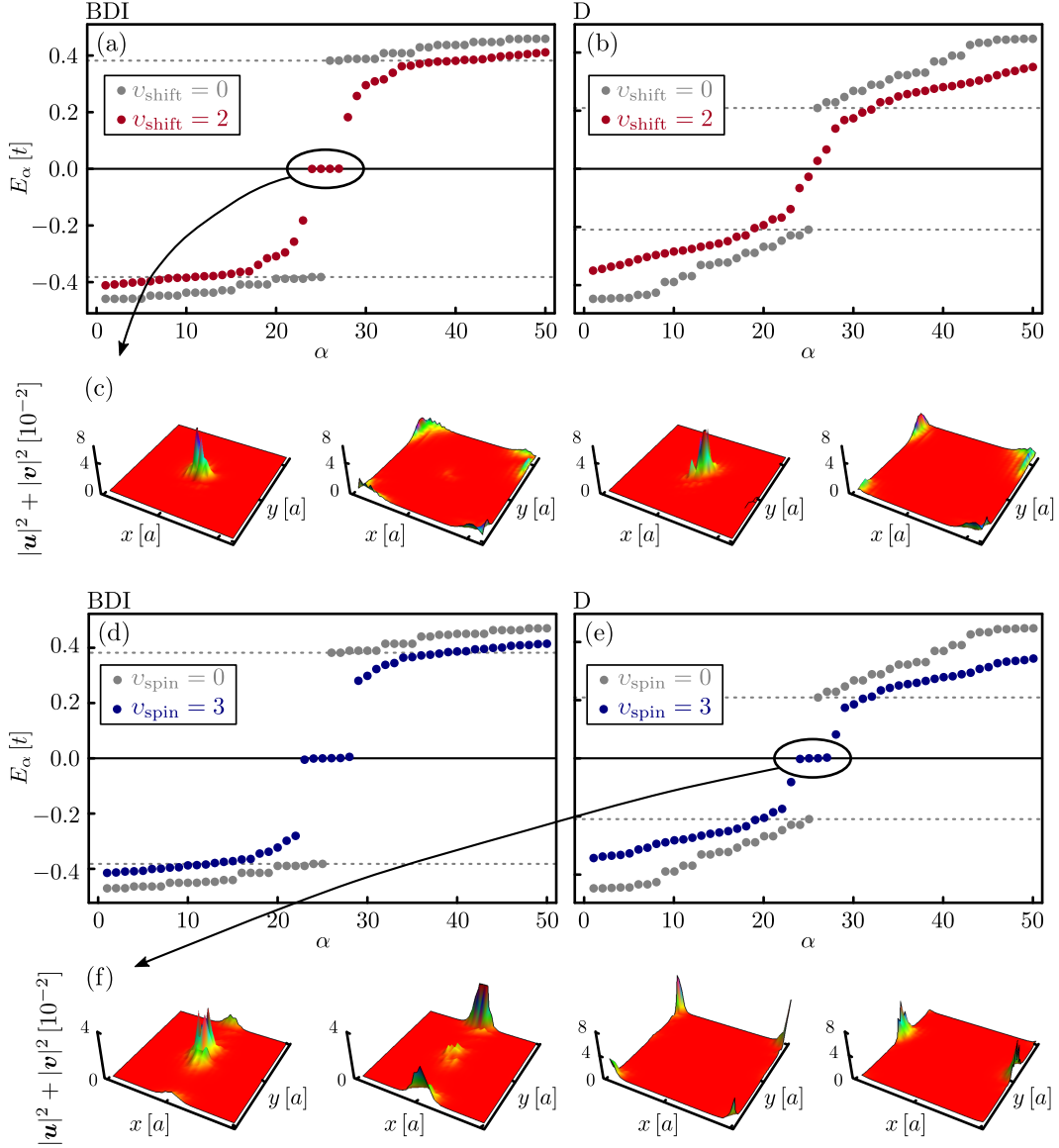


Figure 4.5: Numerical investigation of class BDI and D models in 2D. (a)-(b) The 50 lowest eigenvalues in the absence (grey dots) and presence (red dots) of a double shift vortex defect $v_{\text{shift}} = 2$ for a class BDI and D model, respectively. In (b) we observe that a class D model does not support MZMs for $v_{\text{shift}} = 2$, in agreement with the invariant defined as the parity of $w_{3;\zeta}^{(n)}$. As indicated by the arrow, we show in (c) the weight of the MZM wavefunctions, where we clearly see two states located at the defect and their charge-conjugate counterparts at the edge of the system. (d)-(f) Same as in (a)-(c) but in the case of a triple spin defect $v_{\text{spin}} = 3$. For the class D model in (e) we expect a single MZM pair, in agreement with the parity of $w_{3;\zeta}^{(n)}$, yet we observe four zero energy states. The additional two states, see the two last panels in (f), are an artifact of the phase jump at the edges of the system, and are therefore not located at the defect. The figures were obtained using the same parameters as in fig. 4.2. For the class D figures in (b) and (e) we added the Zeeman term $B_z \sigma_z$ to the Hamiltonian, with the field strength $B_z = 0.4t$. Note that finite-size effects, and inter MZM-coupling result in weights at the defect in the second panel in (f).

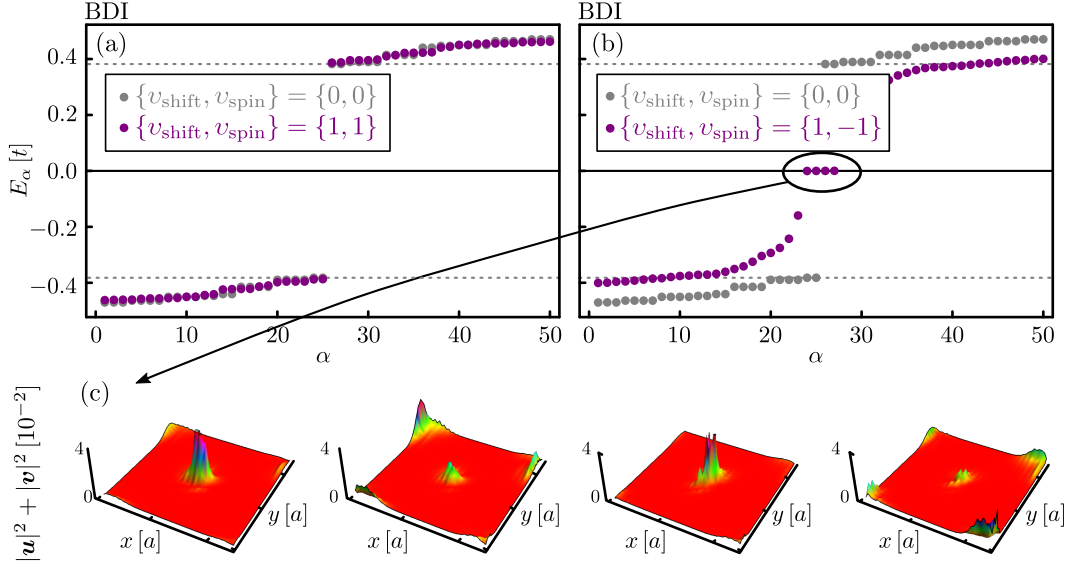


Figure 4.6: Numerical determination of helicity eigenvalue ζ . (a) and (b) same as in fig. 4.5(a) and (b), but for $\{v_{\text{shift}}, v_{\text{spin}}\} = \{1, \pm 1\}$, respectively. Clearly the system has helicity eigenvalue $\zeta = -1$, since only the latter leads to MZMs, cf. eqn. (4.15). In (c) we display the weights of the MZM wavefunctions found in (b). The figures were obtained with the same parameters as in fig. 4.2. Once more, inter MZM-coupling result in MZM weights at the defect in the second and fourth panel in (c).

zero energy. In stark contrast, if we have an odd number of MZMs, i.e. $(-1)^{w_{3;\zeta}^{(n)}} = -1$, a single pair of MZM persists in the presence of a magnetic field in z direction, as seen in fig. 4.5(d),(f). Despite the fact that in fig. 4.5(d) we find four in-gap states, only a single pair corresponds to topologically protected MZMs, with one having its wavefunction weight localized at the defect, see fig. 4.5(f).

Lastly we confirm that different types of defects arising at the same coordinate in real space are added (for $\zeta = +1$) or subtracted (for $\zeta = -1$) depending on the helicity eigenvalue, see again eqn. (4.15). Specifically for our model we find $\zeta = -1$, as seen in fig. 4.6(a) and (b) where we display the energy spectrum for $\{v_{\text{shift}}, v_{\text{spin}}\} = \{1, \pm 1\}$, respectively, with only the latter leading to MZM located at the center of the defect, see fig. 4.6(c).

MZMs in Magnetic Texture Vortices for a Class DIII Model in 2D

In order to numerically study class DIII models in 2D, we perform a two-band extension of the BDI model studied in fig. 4.2 in the main text, and consider two bands labelled by a and b. To represent matrices in band space we employ the Pauli matrices κ and the respective unit matrix $\mathbb{1}_\kappa$. For the sake of simplicity, in the following we consider identical bands, i.e. $\zeta_{\mathbf{k};s,t}^a = \zeta_{\mathbf{k};s,t}^b$ and $\Delta_{\mathbf{k};s,t}^a = \Delta_{\mathbf{k};s,t}^b$. The magnetic texture terms of the BdG Hamiltonian get promoted to matrices in band space, allowing for intra- and inter-band magnetic scattering terms proportional to $\mathbb{1}_\kappa$, κ_3 and κ_1 , respectively. In the remainder, we consider solely intraband magnetic scattering, with the magnetic texture term being proportional to κ_3 .

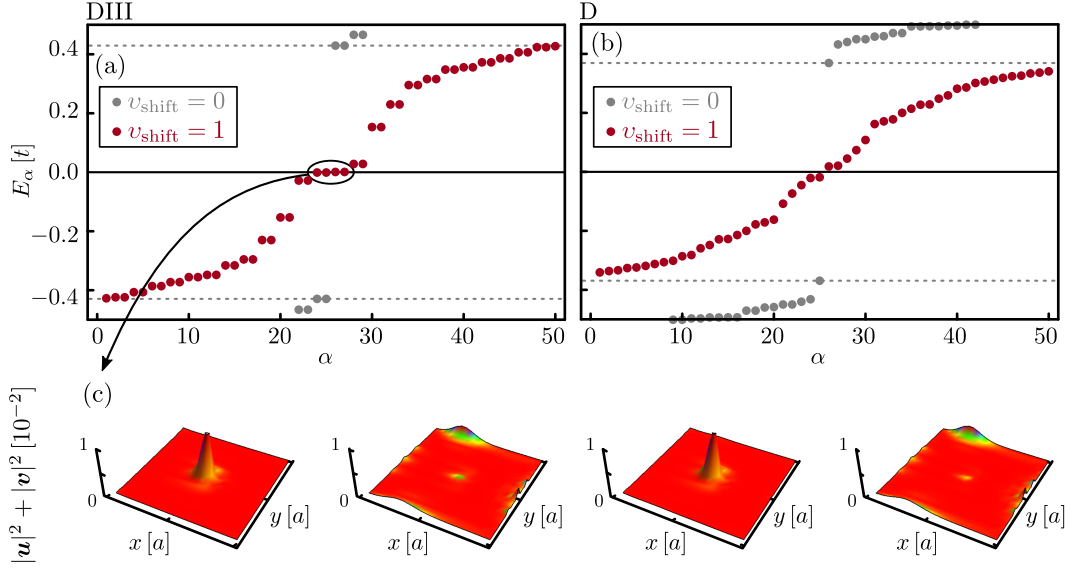


Figure 4.7: Numerical investigation of a class DIII model in 2D. (c) displays the resulting four zero energy states from the MZM Kramers pair in (a), and (b) shows how these get lifted in the presence of a magnetic field $B_z = 0.6t$. Here we used $\xi_{\mathbf{k};t}^a = \xi_{\mathbf{k};t}^b = \xi_{\mathbf{k};t}$, $\Delta_{\mathbf{k};s}^a = \Delta_{\mathbf{k};s}^b = 0$ and $\Delta_{\mathbf{k};t}^a = \Delta_{\mathbf{k};t}^b = d_z \sin k_x$, and the following parameters $\mu_0 = -2\sqrt{2}$, $\beta = 2 + \mu_0$, $d_z = 1$, $\{M_1, M'_1\} = \{1, 0.2\}$ and $\{M_2, M'_2\} = \{0.5, 0.5\}$ in units of t . Lastly, in order to enforce the DIII symmetry class, we added the band mixing term $\sim \delta_0 \tau_3 \kappa_1$, with $\delta_0 = 0.2$.

In the absence of band-mixing terms, the total Hamiltonian enjoys the generalized time-reversal symmetry $\Theta = \kappa_1 T$, as well as the unitary symmetry κ_3 . The latter allows the block diagonalization of the Hamiltonian into two blocks, with each block belonging to the symmetry class BDI. Nevertheless, the Hamiltonian is generally not block-diagonalizable in the presence of band mixing terms. Here, we consider weak band mixing terms $\tau_3 \kappa_1$ which preserve Θ , thus enlisting the Hamiltonian in the DIII symmetry class. Our numerics confirm the emergence of a MZM Kramers pair when considering a single shift/spin vortex defect, as seen in fig. 4.7(a) where we observe four MZMs. The spatially-resolved MZM wavefunction weights in fig. 4.7(c) show that one MZM Kramers pair is localized at the defect and another at the outer edge of the system. Similarly to the BDI models in 2D, we can also here reduce the symmetry of the system by adding a homogeneous external magnetic field. In fig. 4.7(b) we indeed see that the MZM Kramers pair is lifted away from zero energy by adding a magnetic field in the z direction, which makes the time-reversal-invariant system undergo a symmetry-class transition to class D. The latter supports a \mathbb{Z}_2 invariant and cannot sustain the MZM Kramers pair.

5

Topological Superconductivity Induced by Magnetic Textures



Info: This chapter has been submitted for publication, and can be found as an [arXiv preprint \[arXiv:2012.09691 \[cond-mat.supr-con\]\]](#) by me, Morten H. Christensen, Brian M. Andersen and Panagiotis Kotetes. Parts of this chapter are based on my master’s thesis [“[Topological Magnetic Superconductors](#),” University of Copenhagen (2017)].

5.1 Introduction

Since its discovery, superconductivity has served as an inspiration for countless new concepts and applications. A recent development in the field concerns the material discovery and synthetic engineering of topological superconductors [285–294, 351–353], which harbor charge-neutral Majorana fermion quasiparticles [7, 8, 13, 24–27, 269, 319, 354–356]. Remarkably, 0D defects can trap MZMs [24–27, 356], which adhere to non-Abelian exchange statistics [92–94, 269] and open perspectives for cutting-edge quantum manipulations [92–94]. MZMs are sought after in a variety of systems, such as those containing singular defects, e.g. vortices [7, 8, 12, 96, 269–272, 319–321, 323, 357] (see chap. 4), disclinations [358, 359], hedgehogs [322], and nonsingular defects unfolding in one direction, e.g., termination edges [13, 273, 358, 359], domain walls [12, 319], and magnetic skyrmion bubbles [345–349, 360].

In the majority of the most prominent engineered quasi-1D topological superconductors, where fingerprints of MZMs have already been experimentally recorded [88, 295–300, 302, 305–307, 309, 311–317, 361], the presence of an inversion symmetry breaking SOC is crucial. Its role is to split the initially-

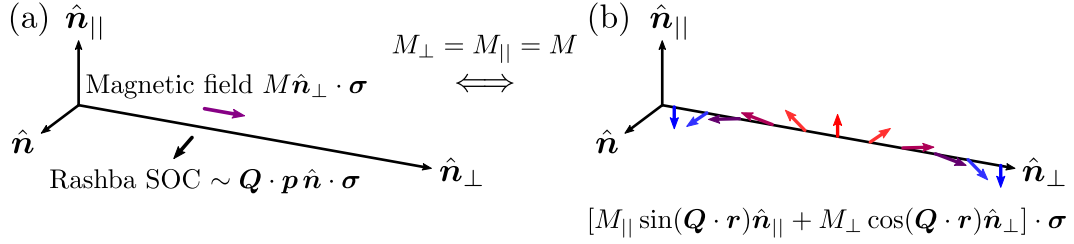


Figure 5.1: Sketch illustrating the mapping between Rashba SOC in the presence of a perpendicular external Zeeman/exchange field, and a magnetic helix crystal (MHC). (a) Schematic illustration of inversion symmetry breaking SOC pointing in the $\hat{n} = \hat{n}_{\perp} \times \hat{n}_{\parallel}$ spin direction, in the presence of a homogeneous magnetic field pointing in the \hat{n}_{\perp} direction. (b) depicts the profile of a MHC with wave vector $\mathbf{Q} = Q\hat{n}_{\perp}$, winding in the plane spanned by \hat{n}_{\parallel} and \hat{n}_{\perp} . Note that (a) and (b) map to each other for $M_{\parallel} = M_{\perp}$, see fig. 5.2.

degenerate spin bands, with the only remaining degeneracies surviving at inversion-symmetric points k_I , which satisfy $k_I \equiv -k_I$. In superconductor-semiconductor nanowires [274–276] and collinear magnetic chains [282–284, 311, 362], the additional presence of a Zeeman/exchange field lifts the residual Kramers degeneracies, as sketched in figs. 5.1(a) and 5.2(a)-(c). The inclusion of spin-singlet pairing gaps out the remnant FS and compensates the magnetic gaps at k_I , thus effecting the transition to a topological superconducting phase.

However, there is still a large number of proposals for engineered quasi-1D topological superconductors which instead rely on a synthetic SOC, which is either induced by a magnetic texture [102–123], or alternatively, by antiferromagnetism [124] or ferromagnetism [125] in the presence of currents and external or stray Zeeman fields. When it comes to magnetic textures, a magnetic helix crystal (MHC) is the minimal profile that can induce topological superconductivity, since it simultaneously generates the required inversion symmetry breaking SOC and the perpendicular exchange field mentioned above [331]. This is sketched in figs. 5.1(b) and 5.2(d)-(f). While a MHC is sufficient to guarantee the occurrence of topological superconductivity in 1D, engineering strong topological superconductors with a fully-gapped bulk energy spectrum in $d > 1$ dimensions requires a magnetic profile which winds in all d directions. Thus, while a MHC leads to spinless p -wave pairing in 1D, a spin skyrmion crystal (SSC) phase is necessary to generate an effective spinless chiral $p + ip$ topological superconductor in 2D [106]. Remarkably, the key role of magnetic textures in topological superconductors has been recently highlighted by the experimental observations of refs. [305, 316, 363] where textures were shown to be pivotal for stabilizing topological superconductivity. This is also the case in ref. [317], where the possible involvement of a skyrmion defect was invoked to explain the appearance of a pair of MZMs in topological magnetic-island heterostructures.

In this chapter, we provide a classification of the various 1D and 2D topological superconductors which emerge from the coexistence of magnetic textures with unconventional and multiband spin-singlet superconductivity. Thus our starting point is the synthetic SOC mechanism displayed in figs. 5.1(b) and 5.2(d)-(f), which opens the door to new and interesting topologically nontrivial phases. In fact, depending on the type of texture and the strengths of the magnetic and superconducting gaps, we find either a fully-gapped or a nodal bulk energy spectrum, which give rise to a diversity of

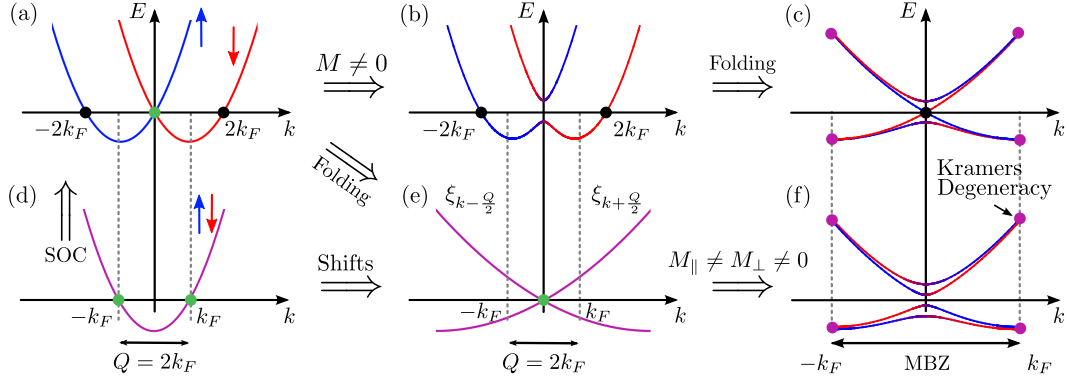


Figure 5.2: (a)-(c) Standard mechanism to achieve 1D topological superconducting phases, which relies on Rashba-like SOC. (d)-(f) Reconstruction of the bulk spectrum of a spin-degenerate electron gas due to a magnetic helix crystal (MHC). (a) Spin-split bands of an electron gas in the absence of a Zeeman/exchange field, resulting in a degeneracy at the inversion-symmetric point $k_I = 0$. (b) The combination of SOC and a Zeeman/exchange field perpendicular to it lifts all spin degeneracies in (a). (c) Equivalent description of (b) after downfolding to the magnetic Brillouin zone (MBZ) of a MHC, see fig. 5.1(b). (d) shows the two Fermi points which become magnetically scattered in the presence of the MHC. Here, the magnetic wave number Q coincides with the FS nesting wave number Q_N . (e) Equivalent description of (d) in the MBZ. (f) The MHC opens a full gap at the intersecting green point in (e).

Majorana fermion edge modes. We present a classification for each type of topological band structure, and account for both strong and weak topological superconducting phases, as well as possible strong topological crystalline phases stabilized by additional magnetic point/space group symmetries.

The present work aims at setting a paradigmatic and general framework to study the topological properties arising from the interplay between magnetic textures and spin-singlet superconductivity. It is applicable to a broad range of materials and hybrid devices, including platforms involving magnetic adatoms deposited on top of superconductors, alongside intrinsic topological superconductors that do not rely on inversion symmetry breaking SOC. Our analysis naturally addresses topological superconducting phases in which magnetism and superconductivity are assumed to originate from the same electronic degrees of freedom. Such a scenario may be of a direct relevance to FeSCs, which feature co-existence of various magnetic phases and superconductivity [66–68,70–73,75,76,80–85,364]. Among the experimentally discovered phases, one is of a yet-unresolved nature [80], and does not match with any of the three well-established commensurate magnetic phases known to exist in FeSCs [253,365–372]. This commensurate framework was recently extended in ref. [77] to include incommensurate magnetic textures. Given the currently inconclusive status of the experimental observations, the phase discovered in ref. [80] may as well be a magnetic texture. This opens up new possibilities for topological superconducting phases in FeSCs, which are distinct to the ones that have so far been theoretically [96,271,272] and experimentally [87–91] explored.

Motivated by the above, in the following we focus on the accessible topological superconductors in layered tetragonal itinerant magnets, which possess a D_{4h} point group symmetry in the nonmagnetic

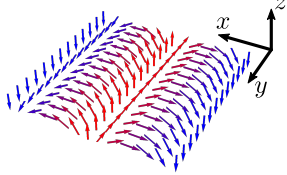
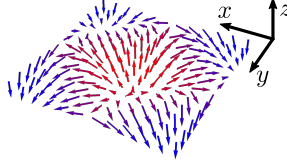
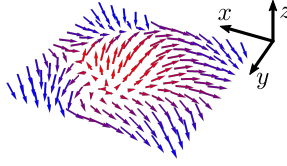
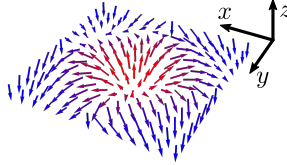
Magnetic texture	Spatial profile	Symmetries
<p>Magnetic Helix Crystal (MHC)</p> $\mathbf{M}(\mathbf{r}) = (M_{\parallel} \sin(Qx), 0, M_{\perp} \cos(Qx))$		$\begin{aligned} \mathcal{M}_{\text{MHC}} &= \text{M}_{\text{MHC}} \\ &+ \text{M}_{\text{MHC}}\{T (\pi/Q, 0)\} \\ \text{M}_{\text{MHC}} &= C_2 + (C_{2v} - C_2)T \end{aligned}$
<p>Spin Whirl Crystal (SWC_4)</p> $\begin{aligned} \mathbf{M}(\mathbf{r}) &= (M_{\parallel} \sin(Qx), 0, M_{\perp} \cos(Qx)) \\ &+ (0, M_{\parallel} \sin(Qy), M_{\perp} \cos(Qy)) \end{aligned}$		$\begin{aligned} \mathcal{M}_{\text{SWC}_4} &= \text{M}_{\text{SWC}_4} \\ &+ \text{M}_{\text{SWC}_4}\{T (\pi/Q, \pi/Q)\} \\ \text{M}_{\text{SWC}_4} &= C_4 + (C_{4v} - C_4)T \end{aligned}$
<p>Spin Whirl Crystal and inplane B field (SWCB_2)</p> $\begin{aligned} \mathbf{M}(\mathbf{r}) &= (M_{\parallel} \sin(Qx), 0, M_{\perp} \cos(Qx)) \\ &+ (B_{\parallel}, M_{\parallel} \sin(Qy), M_{\perp} \cos(Qy)) \end{aligned}$		$\begin{aligned} \mathcal{M}_{\text{SWCB}_2} &= \text{M}_{\text{SWCB}_2} \\ &+ \text{M}_{\text{SWCB}_2}\{\sigma_{yz} (\pi/Q, \pi/Q)\} \\ \text{M}_{\text{SWB}_2} &= C_1 + (D_1 - C_1)T \end{aligned}$
<p>Spin Whirl Crystal and out-of-plane B field (SWCB_4)</p> $\begin{aligned} \mathbf{M}(\mathbf{r}) &= (M_{\parallel} \sin(Qx), 0, M_{\perp} \cos(Qx)) \\ &+ (0, M_{\parallel} \sin(Qy), M_{\perp} \cos(Qy) + B_{\perp}) \end{aligned}$		$\text{M}_{\text{SWC}_4} = C_{4v} + (C_{4v} - C_4)T$

Table 5.1: Elements of the magnetic space (point) group \mathcal{M} (M) preserved for the different magnetic texture profiles studied in this work. These build upon the magnetic helix crystal (MHC) and the spin whirl crystal (SWC_4) textures. The SWC_4 profile is also investigated in the presence of an in (out-of) -plane Zeeman field B_{\parallel} (B_{\perp}). Note that deviations from the above generally appear for multiband implementations of the magnetic texture profiles. Examples of such situations are explored in detail in the main text.

normal phase. We also consider that spin transforms according to the spatial symmetry operations, and we restrict to a single Kramers doublet of the double covering D_{4h} group. We additionally assume that inversion symmetry breaking SOC and spin anisotropies (cf. ref. [371]) are negligible. Reference [77] has mapped out the types of single- and double- \mathbf{Q} textures that such magnets support, and we here focus on the single- \mathbf{Q} MHC and the fourfold-symmetric double- \mathbf{Q} spin whirl crystal (SWC₄) profiles. We also consider the SWC₄ phase in the presence of an in- and out-of-plane Zeeman field, B_{\parallel} and B_{\perp} , leading to the here-termed SWCB₂ and SWCB₄ textures, respectively. Notably, for a range of B_{\perp} values, the SWCB₄ texture is equivalent to a fourfold-symmetry preserving SSC phase [77], which we here denote SSC₄. Table 5.1 provides an overview of these magnetic textures.

5.2 Summary of our Topological Classification Results

To perform the classification of the various topological superconducting phases induced by the magnetic textures presented in table 5.1, a number of aspects need to be taken into consideration in regards to the symmetry groups preserved by the magnetic and pairing terms.

As we have already discussed in chap. 1, a given magnetic texture preserves the so-called magnetic space group \mathcal{M} . Elements of M , i.e. the point group elements of \mathcal{M} , involving T give rise to antiunitary mirror symmetries [34, 373–375] which have nontrivial implications on the topological classification in high-symmetry planes (HSPs), and open the door to novel types of crystalline topological phases and Majorana fermions [28, 29, 31, 146, 150, 155, 376–383]. Further information about the symmetry properties of the various textures considered in this work is listed in table 5.1. Furthermore, the classification in HSPs is also affected by the compound symmetries of the magnetic space group [32, 80, 99, 107, 150, 384–389]. Here, elements of M are combined with translations which make the texture glide in the plane. These constitute exact symmetries of the system only as long as the involved translation also constitutes a lattice translation, which takes place when the magnetic vector is commensurate. Nonsymmorphic symmetries can enrich the topological classification in bulk HSPs and at edges which preserve them.

The final crucial factor which influences the topological properties is the type of pairing gap. In this chapter, we assume unconventional multiband spin-singlet pairing with possible symmetry-imposed or accidental nodes. Considering multiple bands and pairings allows us to capture salient features of realistic band structures of correlated magnets, such as the FeSCs [164, 250, 390–395]. Moreover, depending on which IR of D_{4h} enters the pairing term $\Delta_{\mathbf{k}}$, i.e. $\{A_{1g}, B_{1g}, B_{2g}, A_{2g}\}$, we generally find a different topological scenario in HSPs, since $\Delta_{\mathbf{k}}$ may possess symmetry-enforced zeros in these. More specifically, the symmetry relation $\Delta_{U^{-1}\mathbf{k}} = \chi\Delta_{\mathbf{k}}$ as derived in app. 1.B plays a crucial role in the topological classification, since it generally alters the matrix representation of the symmetry elements.

Our main findings regarding the rich diversity of topological superconducting phases are collected in tables 5.2 and 5.3, for general and interband-only magnetic scattering, respectively. 2D systems in the presence of a MHC texture exhibit protected nodal points which lead to edge Majorana/Andreev flat bands. Bulk nodal points are also present when considering the SWC₄ texture, but these are not protected. As a result, edge Majorana/Andreev flat bands are not accessible. Nonetheless, a new type of Majorana fermion edge modes arises, which we denote bidirectional (see also ref. [32]), since they do not possess a fixed helicity or chirality, and depend strongly on the edge termination. These Majorana

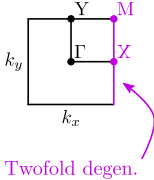
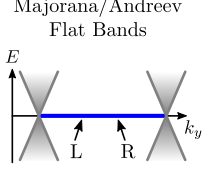
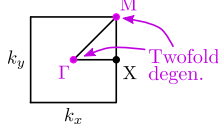
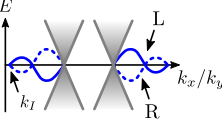
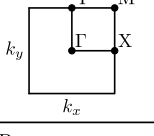
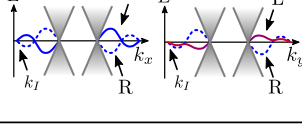
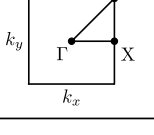
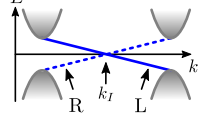
Magnetic Texture Properties	Topological Classification	Invariants Nodal Bulk	Invariants Fully-Gapped	Resulting Edge States
<p>MHC MBZ: $\mathbf{k} \in (-q, q] \times (-\pi, \pi]$ Protected degen.: XM</p> 	<ul style="list-style-type: none"> Full MBZ: BDI 	Strong: $v \in \mathbb{Z}$ Weak: $w_{k_x, y} \in \mathbb{Z}$	- Weak: $w_{k_x, y} \in \mathbb{Z}$	Majorana/Andreev Flat Bands 
<p>SWC₄ MBZ: $\mathbf{k} \in (-q, q] \times (-q, q]$ Protected degen.: Γ & M</p> 	<ul style="list-style-type: none"> Full MBZ: D 	- Weak: $\mathfrak{M}_{k_x, y=q} \in \mathbb{Z}_2$	Strong: $\mathcal{C}_1 \in \mathbb{Z}$ Weak: $\mathfrak{M}_{k_x, y=q} \in \mathbb{Z}_2$	Bidirectional Majorana Modes 
<p>SWCB₂ ($B_{ }\sigma_x$) MBZ: $\mathbf{k} \in (-q, q] \times (-q, q]$ Protected degen.: -</p> 	<ul style="list-style-type: none"> Full MBZ: D 	- Weak: $\mathfrak{M}_{k_x, y=q} \in \mathbb{Z}_2$	Strong: $\mathcal{C}_1 \in \mathbb{Z}$ Weak: $\mathfrak{M}_{k_x, y=q} \in \mathbb{Z}_2$	Bi- or Uni-directional Majorana Modes 
<p>SWCB₄ MBZ: $\mathbf{k} \in (-q, q] \times (-q, q]$ Protected degen.: -</p> 	<ul style="list-style-type: none"> Full MBZ: D 	- Weak: $\mathfrak{M}_{k_x, y=q} \in \mathbb{Z}_2$	Strong: $\mathcal{C}_1 \in \mathbb{Z}$ Weak: $\mathfrak{M}_{k_x, y=q} \in \mathbb{Z}_2$	Chiral Majorana Modes 

Table 5.2: Summarizing table of the broad variety of 2D topological superconducting phases induced by the magnetic textures in table 5.1. For each texture we display the relevant HSPs and the arising symmetry-protected degeneracies induced by the given magnetic point/space group, see table 5.1. Furthermore, we also list the symmetry classification for the full MBZ and the HSPs, the relevant topological invariants, and the resulting type of Majorana/Andreev edges states. We arrive at three distinct types of invariants which become nontrivial. For a gapless energy spectrum these consist of the vorticities v/ν of the arising nodes, while for a fully-gapped energy spectrum, we find the winding number w , the Majorana number \mathfrak{M} , and the 1st Chern number \mathcal{C}_1 . Each invariant is in addition labeled as strong, weak, mirror or glide, depending on its type. Note that the classification in HSPs presents all the possible topological scenarios obtained by assuming the presence of only a single crystalline symmetry at a time. We further elaborate on these in the proceeding sections. The table also includes the HSP classification in the presence of a pairing function $\Delta_{\mathbf{k}}$ transforming as one of the IRs $\{A_{1g}, B_{1g}, B_{2g}, A_{2g}\}$ of the group D_{4h} . Depending on the IR of $\Delta_{\mathbf{k}}$, the classification in HSPs splits into two branches, depending on whether $\Delta_{\mathbf{k}}$ is even or odd under the original D_{4h} mirror operation defined for the HSP of interest. In the former case ($\mathcal{Q} = \mathbb{1}_\tau$), $\Delta_{\mathbf{k}}$ remains invariant under the original mirror operation, while in the latter ($\mathcal{Q} = \tau_3$), $\Delta_{\mathbf{k}}$ is invariant under the mirror operation combined with a rotation in Nambu space, which is spanned by the unit $\mathbb{1}_\tau$ and Pauli τ matrices. Finally, the red/blue color coding is adopted throughout the text, and reflects the spin up/down orientation of the electronic spin polarization of the mode. Left (Right) edge modes are labeled by L (R) and sketched above with solid (dashed) lines.

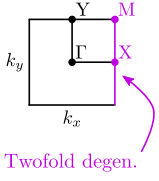
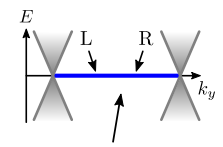
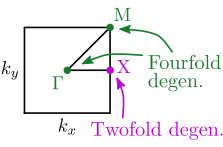
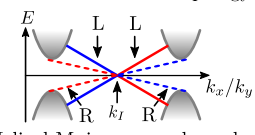
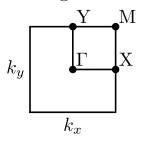
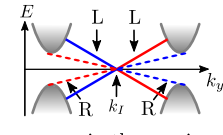
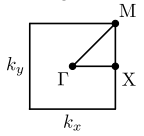
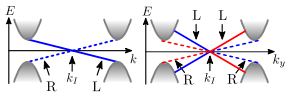
Magnetic Texture Properties	Topological Classification	Invariants Nodal Bulk	Invariants Fully-Gapped	Resulting Edge States
<p><u>MHC</u> MBZ: $\mathbf{k} \in (-q, q] \times (-\pi, \pi]$ Protected degen.: XM</p> 	<ul style="list-style-type: none"> Full MBZ: AIII \oplus AIII <p>Strong: $v \in \mathbb{Z}$ Weak: $w_{k_x, y} \in \mathbb{Z}$</p> <p>$\mathcal{Q} = \mathbf{1}_\tau (\tau_3)$</p> <ul style="list-style-type: none"> ΓY & XM: CI \oplus CI or \bigoplus_4 AIII (BDI \oplus BDI or \bigoplus_4 AIII) ΓX & YM: AIII \oplus AIII (\bigoplus_4 AIII) 	<p>Strong: $v \in \mathbb{Z}$ Weak: $w_{k_x, y} \in \mathbb{Z}$</p> <p>(Mirror: $\tilde{w}_{M, \text{HSP}} \in \mathbb{Z}$) (Glide: $w_{G, k_x=0, q} \in \mathbb{Z}$)</p>	<p>Andreev/Majorana Flat Bands</p>  <p>Majorana flat bands: twofold degeneracy per edge</p>	
<p><u>SWC₄</u> MBZ: $\mathbf{k} \in (-q, q] \times (-q, q]$ Protected degen.: Γ, X & M</p> 	<ul style="list-style-type: none"> Full MBZ: DIII <p>Strong: $v \in \mathbb{Z}$ Weak: $w_{k_x, y} \in \mathbb{Z}$</p> <p>$\mathcal{Q} = \mathbf{1}_\tau (\tau_3)$</p> <ul style="list-style-type: none"> $\Gamma X, XM$ & $M\Gamma$: AIII \oplus AIII (D \oplus D) 	<p>Strong: $\mathfrak{M}^{\text{KP}} \in \mathbb{Z}_2$ Weak: $\mathfrak{M}_{k_x, y=q}^{\text{KP}} \in \mathbb{Z}_2$</p> <p>Mirror: $w_{M, \text{HSP}} \in \mathbb{Z}$ (Mirror: $\mathfrak{M}_{M, \text{HSP}} \in \mathbb{Z}_2$)</p>	<p>Quasi-helical Majorana modes from weak or mirror topology</p>  <p>Helical Majorana modes only for broken C_4 symmetry</p>	
<p><u>SWCB₂ ($B_{ }\sigma_x$)</u> MBZ: $\mathbf{k} \in (-q, q] \times (-q, q]$ Protected degen.: Γ, X</p> 	<ul style="list-style-type: none"> Full MBZ: D <p>Strong: $v \in \mathbb{Z}$ Weak: $\mathfrak{M}_{k_x, y=q} \in \mathbb{Z}_2$</p> <p>$\mathcal{Q} = \mathbf{1}_\tau (\tau_3)$</p> <ul style="list-style-type: none"> ΓX & YM: BDI (BDI) 	<p>Strong: $C_1 \in \mathbb{Z}$ Weak: $\mathfrak{M}_{k_x, y=q} \in \mathbb{Z}_2$</p> <p>Mirror: $\tilde{w}_{M, \text{HSP}} \in \mathbb{Z}$ (Mirror: $\tilde{w}_{M, \text{HSP}} \in \mathbb{Z}$)</p>	<p>Quasi-helical Majorana modes from weak or mirror topology</p>  <p>a gap opens in the x-axis modes</p>	
<p><u>SWCB₄</u> MBZ: $\mathbf{k} \in (-q, q] \times (-q, q]$ Protected degen.: Γ, X</p> 	<ul style="list-style-type: none"> Full MBZ: D <p>Strong: $v \in \mathbb{Z}$ Weak: $\mathfrak{M}_{k_x, y=q} \in \mathbb{Z}_2$</p> <p>$\mathcal{Q} = \mathbf{1}_\tau (\tau_3)$</p> <ul style="list-style-type: none"> $\Gamma X, XM$ & $M\Gamma$: BDI (BDI) 	<p>Strong: $C_1 \in \mathbb{Z}$ Weak: $\mathfrak{M}_{k_x, y=q} \in \mathbb{Z}_2$</p> <p>Mirror: $\tilde{w}_{M, \text{HSP}} \in \mathbb{Z}$ (Mirror: $\tilde{w}_{M, \text{HSP}} \in \mathbb{Z}$)</p>	<p>Chiral/Quasi-helical Majorana modes from strong/weak or mirror topology</p> 	

Table 5.3: Summarizing table of the accessible topological phases induced by interband-only magnetic textures. As in table 5.2, also here, we list the topological symmetry classification in the full MBZ and in HSPs, the relevant topological invariants and the resulting edge states, for all four magnetic textures of interest. Note that the topological invariants in the MHC case are identical for the two AIII blocks. Hence, we only enlist the invariants for a single AIII block.

fermion edge modes emerge due to mirror-symmetry protected degeneracies at inversion-symmetric points, or alternatively due to weak topological superconducting phases. The addition of a magnetic field can either render the bidirectional Majorana fermion edge modes unidirectional [396–398], or open a bulk gap and mediate a transition to a chiral topological superconductor, analogous to a $p+ip$ superconductor. Remarkably, we find that the multiband character of the systems considered here not only allows for a more realistic description, but also results in novel topological superconducting phases and Majorana fermion edge modes. In particular, we show that two-band systems under the influence of multiband magnetic textures harbor Kramers (mirror-symmetry protected) pairs of (quasi-)helical Majorana fermion edge modes, although time-reversal symmetry is broken. In fact, these pairs of Majorana fermions constitute topologically-protected Andreev zero modes in 1D [399–402]. While Andreev zero modes have been poorly explored, their topological nature also renders them prominent candidates for quantum computing applications [403, 404].

The remainder of this chapter is organized as follows. In sec. 5.3 we describe the modeling assumptions that we use throughout this work. In sec. 5.4, we investigate topological superconductors in 1D systems induced by a MHC. While TSCs from MHCs appear to have been widely discussed, cf. refs. [103–105, 107–111, 113, 116–119, 122, 123], here we provide a so-far-lacking complete topological classification of the accessible phases by also accounting for crystalline symmetries, and uncover a number of novel phases and properties. This section motivates and introduces the general formalism and methodology that we employ for the exploration of the 2D topological superconductors. In sec. 5.5 we extend our study to 2D, and explore the full variety of possible topological superconductors and protected Majorana fermion edge modes induced by the SWC_4 phase. Section 5.6 presents our conclusions and outlook. Lastly, apps. 5.A–5.E contain various definitions, summarizing tables, further technical details, and complementary numerical calculations.

5.3 Modeling Considerations

Before proceeding, we specify the modeling assumptions employed in the upcoming analysis. While our analytical and numerical investigations also aim at predicting possible topological phases relevant to unconventional superconductors, we here treat these cases only in a qualitative fashion. Correlated systems generally exhibit complex band structures, which is an aspect that hinders a transparent discussion of the topological properties as pursued here. For example, an accurate description of the FeSCs typically requires five- or ten-band models [392, 393]. Therefore, in order to ensure a balance between analytical tractability and faithful modeling, we focus on simplified one- and two-band models¹ which exhibit hole and electron pockets, as well as FS nesting. These features are similar to those exhibited by some FeSCs, see also fig. 5.3. The one-band (two-band) models are particularly suitable for exploring topological properties arising from intra-pocket (inter-pocket) nesting.

Another aspect of realistic systems that needs to be accounted for, is the fact that the magnetic wave vectors may be incommensurate or exhibit a high-order degree of commensurability. As a result, such cases require an infinite or very large number of bands for an accurate description after downfolding to the magnetic Brillouin zone (MBZ). To avoid such a complication, we consider commensurate magnetic wave vectors $\mathbf{Q}_{1,2}$, with the property $\mathbf{k} + 4\mathbf{Q}_{1,2} \equiv \mathbf{k}$. More precisely $\mathbf{Q}_1 = Q\hat{x}$

¹Note that each one of the band dispersions employed in the upcoming models is chosen to be independently invariant under all the D_{4h} point group operations.

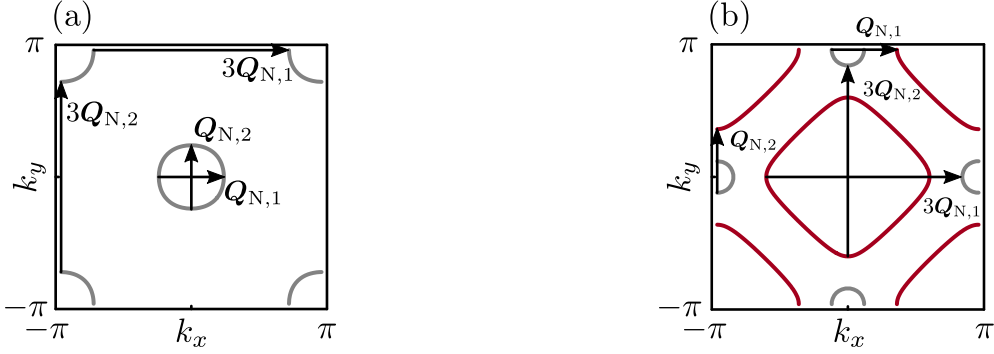


Figure 5.3: One-band (a) and two-band (b) FSs studied here. In (a) the two pockets possess the same character, while in (b) the pockets centered at the Γ and M (X and Y) points are of the hole (electron) type. The chosen electron- and hole-characters for the pockets in (a) and (b) allow a qualitative connection with the band structures of certain FeSCs [392, 393]. Notably, our results for the two-band model and the general mechanisms underlying the topological superconductor phases can be directly generalized to system with more bands.

with $Q = -3\pi/2 \equiv \pi/2$, with the lattice constant set to unity throughout, and $\mathbf{Q}_2 = Q\hat{y}$, since the latter is obtained via a counter-clockwise fourfold rotation of \mathbf{Q}_1 . In most cases we consider that the magnetic wave vectors coincide with the FS nesting wave vectors $\mathbf{Q}_{N,1}$ and $\mathbf{Q}_{N,2}$, see fig. 5.3, which is a realistic assumption within the itinerant picture of magnetism adopted here. We note that our choice of Q does not affect the generality of the qualitative conclusions regarding the topological features of the systems under discussion, as the above wave vectors can be adiabatically connected to incommensurate ones. This is achieved by only deforming the FS of the system without modifying its topology, i.e., assuming that a Lifshitz transition [405, 406] does not occur. In fact, the analytical tractability which is ensured in this manner, allows for a deeper and transparent understanding of the underlying mechanisms. Our conclusions thus serve as a basis for the study of more realistic multiband magnetic superconductors.

Furthermore, we point out that the upcoming analysis is not self-consistent with respect to the magnetic and superconducting order parameters. While our starting point builds upon the results of ref. [77], which have been derived using microscopic models, we do not further examine the fate of the textured magnetic order and its interplay with superconductivity. The present work has a more explorative character, and thus, we allow for our search to be unconstrained. In fact, we seek to perform an exhaustive study for the combinations of the magnetic and superconducting orders, in order to identify the most prominent routes for achieving topological superconductors.

Concluding this section, we wish to emphasize that we have confirmed the validity of all the analytical results presented in the upcoming sections by means of numerical investigations of the respective lattice models in 1D and 2D, with open boundary conditions, and observed the predicted edge states. We also wish to stress that the crystalline topological properties induced by the magnetic point and space group symmetries, only give rise to topologically-protected modes at boundaries which preserve the symmetries in question. This is in stark contrast to strong topological phases, for which the bulk-edge correspondence enforces the edge states to appear for a boundary of an arbitrary direction. For this reason, in the upcoming sections we first carry out the classification of the strong

topological superconductor phases, and subsequently discuss the possible crystalline ones which result from the magnetic point and space group symmetries.

Finally, to facilitate the readability of the upcoming analysis, we collect in table 5.4 of app. 5.A all the topological invariants employed here.

5.4 1D Topological Superconductors

In the following analysis we first explore possible topological phases in 1D. Apart from being simple to investigate, the 1D case sets the stage and the formalism employed in the study of 2D systems, which is the main goal of this work. In 1D we consider the topological effects arising from the coexistence of either a conventional or an unconventional superconducting pairing with a MHC phase with either a constant or a spatially-varying magnitude of the magnetic moment.

One-Band Models

We begin our study with one-band models, which are defined on a lattice and describe electrons with a band dispersion ξ_k set by the hopping matrix elements $t_{R,R'}$. After including the chemical potential μ_0 , we have

$$H_{\text{kin}} = - \sum_{R,R'} c_R^\dagger (t_{R,R'} + \mu_0 \delta_{R,R'}) c_{R'}, \quad (5.1)$$

where R labels the position on the direct lattice, and $\mathbf{c}_R = (c_{R\uparrow}, c_{R\downarrow})$. The magnetic part of the Hamiltonian describes a MHC texture winding in the xz spin plane

$$H_{\text{mag}} = \sum_R c_R^\dagger [M_{\parallel} \sin(QR) \sigma_x + M_{\perp} \cos(QR) \sigma_z] c_R. \quad (5.2)$$

Here, $Q = \pi/2$ denotes the magnetic ordering wave number, which in low-dimensional itinerant magnets it often happens to coincide with the nesting wave number Q_N . The texture mediates scattering between two distinct pairs of points. In this work, one pair usually lies at high energies and the other at low. When the condition $Q_N = Q$ is met, the latter pair is identified with the two nested Fermi points. See fig. 5.4(a) for a concrete example. We observe that when $|M_{\perp}| \neq |M_{\parallel}|$ ($|M_{\perp}| = |M_{\parallel}|$) the MHC leads to a spatially varying (constant) magnetic moment. Below we examine each case separately.

MHC with a Spatially Constant Magnetic Moment: $|M_{\perp}| = |M_{\parallel}|$

In this case, we follow ref. [331] and gauge away the spatial dependence of the magnetization profile through a unitary transformation $\mathbf{c}_R \rightarrow U \mathbf{c}_R$ with $U = \exp(iqR\sigma_y)$, where $q = Q/2$. By employing the plane-wave basis, the single-particle Hamiltonian reads

$$h_{k_x} = \xi_{k_x - q} \sigma_y + M \sigma_z = \xi_{k_x; q}^+ + \xi_{k_x; q}^- \sigma_y + M \sigma_z, \quad (5.3)$$

with $M_{\perp} = M_{\parallel} = M > 0$. The dispersions read $\xi_{k_x; q}^{\pm} = (\xi_{k_x - q} \pm \xi_{k_x + q})/2$. One observes that the spin-dependent shift of the wave number splits the dispersion into an even and an odd function under inversion, i.e., $\xi_{-k_x; q}^{\pm} = \pm \xi_{k_x; q}^{\pm}$. The emergence of the odd function reflects the induction of a



Figure 5.4: Example of a one-band model in 1D, obtained by considering a nearest neighbor hopping with strength t and a chemical potential value $\mu_0 = -\sqrt{2}t < 0$. (a) The resulting dispersion $\xi_{k_x} = -2t \cos k_x - \mu_0$ contains two Fermi points at $k_x = \pm\pi/4$ of the 1st BZ, which are connected by $Q_N = Q = \pi/2 \equiv -3\pi/2 = -3Q$. The texture also mediates the scattering between two points lying at $E = 2|\mu_0|$. (b) The resulting four bands of the dispersion in the MBZ. The points connected by the magnetic wave vectors are depicted with green dots.

Rashba-type SOC. By further considering a generic spin-singlet pairing gap Δ_{k_x} , we obtain the BdG Hamiltonian

$$\mathcal{H}_{k_x} = \tau_3(\xi_{k_x;q}^+ + \xi_{k_x;q}^- \sigma_y) + M\sigma_z + \tau_1(\Delta_{k_x;q}^+ + \Delta_{k_x;q}^- \sigma_y), \quad (5.4)$$

where we introduced the superconducting gaps $\Delta_{k_x;q}^\pm$ in a similar fashion to $\xi_{k_x;q}^\pm$, as well as the spinor

$$\mathcal{C}_{k_x}^\dagger = (c_{k_x;\uparrow}^\dagger, c_{k_x;\downarrow}^\dagger, c_{-k_x;\downarrow}, -c_{-k_x;\uparrow}). \quad (5.5)$$

Hence, the mean-field decoupled Hamiltonian reads $H^{\text{MF}} = \frac{1}{2} \sum_{k_x} \mathcal{C}_{k_x}^\dagger \mathcal{H}_{k_x} \mathcal{C}_{k_x}$. In the above, we employed the $\tau_{1,2,3}$ Pauli matrices defined in Nambu electron-hole space.

Leaving aside for the moment the magnetic space group symmetries present, the BdG Hamiltonian in eqn. (5.4) resides in the BDI symmetry class with generalized time-reversal, charge-conjugation and chiral symmetries effected by the operators $\Theta = K$, $\Xi = \tau_2 \sigma_y K$ and $\Pi = \tau_2 \sigma_y$, respectively. When Δ_{k_x} leads to a fully-gapped spectrum, the system harbors an integer number of topologically protected MZMs per edge, with the corresponding \mathbb{Z} topological invariant given by the winding number w [407]. To define the winding number, we rely on the chiral symmetry dictating the Hamiltonian and block off-diagonalize it via the unitary transformation $\mathcal{S} = (\Pi + \tau_3)/\sqrt{2}$

$$\mathcal{S} \mathcal{H}_{k_x} \mathcal{S}^\dagger = \begin{pmatrix} 0 & A_{k_x} \\ A_{k_x}^\dagger & 0 \end{pmatrix}. \quad (5.6)$$

Given the above, we calculate $\det A_{k_x}$, which reads

$$\det A_{k_x} = (\xi_{k_x;q}^+)^2 + (\Delta_{k_x;q}^+)^2 - (\xi_{k_x;q}^-)^2 - (\Delta_{k_x;q}^-)^2 - M^2 + 2i(\xi_{k_x;q}^- \Delta_{k_x;q}^+ - \xi_{k_x;q}^+ \Delta_{k_x;q}^-) \quad (5.7)$$

and allows us to define the normalized complex function

$$z_{k_x} = \det(A_{k_x}) / |\det(A_{k_x})|, \quad (5.8)$$

and the associated winding number in the complex plane

$$w = \frac{1}{2\pi i} \int_{\text{BZ}} \frac{dz_{k_x}}{z_{k_x}}. \quad (5.9)$$

To facilitate the evaluation of w , one relies on its invariance under smooth deformations of the Hamiltonian, i.e. deformations that do not lead to any gap closings of the bulk spectrum. Hence, one assumes that the parameters take such values, so that the system is close to topological phase transitions. In such cases the main contributions to w arise from the gap-closing points k_c of the bulk energy spectrum, determined by $|\det A_{k_c}| = 0$. This equation yields the conditions $\text{Im}[\det A_{k_c}] = 0$ and $\text{Re}[\det A_{k_c}] = 0$, whereof the first one reads

$$\text{Im}[\det A_{k_c}] = \xi_{k_c; q}^- \Delta_{k_c; q}^+ - \xi_{k_c; q}^+ \Delta_{k_c; q}^- = 0 \quad \Rightarrow \quad \xi_{k_c - q} \Delta_{k_c + q} = \xi_{k_c + q} \Delta_{k_c - q}. \quad (5.10)$$

The above is always satisfied at the inversion-symmetric points ($k_I \equiv -k_I$). If we momentarily assume that the k_x dependence of the pairing gap does not lead to any additional gap closings besides the ones at the inversion-symmetric points, and take into account the remaining gap-closing condition $\text{Re}[\det A_{k_c}] = 0$, we obtain the topological phase transition criterion

$$M = \sqrt{(\xi_{k_I; q}^+)^2 + (\Delta_{k_I; q}^+)^2}, \quad (5.11)$$

because $\xi_{k_I; q}^- = \Delta_{k_I; q}^- = 0$. Since the 1D BZ contains only the two inversion-symmetric points $k_I = \{0, \pi\}$, the winding number reads

$$w = \sum_{k_I=0, \pi} \text{sgn} \left(\Delta_{k_x; q}^+ \frac{d\xi_{k_x; q}^-}{dk_x} - \xi_{k_x; q}^+ \frac{d\Delta_{k_x; q}^-}{dk_x} \right) \bigg|_{k_x=k_I} \frac{\text{sgn}[M^2 - (\Delta_{k_I; q}^+)^2 - (\xi_{k_I; q}^+)^2]}{2}. \quad (5.12)$$

We note that when the magnetic wave vector Q coincides with the FS nesting vector Q_N , the expression for the topological invariant further simplifies since $\xi_{k_I; q}^+ = 0$ for at least one of the two inversion-symmetric points. Remarkably, this special, but actually realistic situation, appears to be the sweet spot for entering the topologically nontrivial phase, since the minimum magnetic gap $M_c = |\Delta_{k_I; q}^+|$ is required in this case. Away from this special point, the critical magnetic gap increases, and its value is controlled by the degree of the $|Q - Q_N|$ detuning, which is reflected in the size of $|\xi_{k_I; q}^+|$. Therefore, a topological phase transition still occurs even if the special condition $Q = Q_N$ is not met. We thus conclude that the system exhibits gap closings at wave numbers for which $\xi_{k_x + Q} = \xi_{k_x}$ and $d\xi_{k_x + Q}/dk_x = -d\xi_{k_x}/dk_x$. Notably both conditions hold trivially for two nested Fermi points given that $Q = Q_N$.

For a one-band model with $\xi_{0; q}^+ = 0$ and $\xi_{\pi; q}^+ = 2|\mu_0|$, which happens to hold for the one-band model in fig. 5.4, eqn. (5.12) yields

$$w = \frac{1}{2} \sum_{k_I=0, \pi} e^{ik_I} \text{sgn} \left[M^2 - (\xi_{k_I; q}^+)^2 - (\Delta_{k_I; q}^+)^2 \right], \quad (5.13)$$

which implies that the topologically nontrivial regime is realized in the interval

$$\sqrt{(\xi_{0; q}^+)^2 + (\Delta_{0; q}^+)^2} < M < \sqrt{(\xi_{\pi; q}^+)^2 + (\Delta_{\pi; q}^+)^2}. \quad (5.14)$$

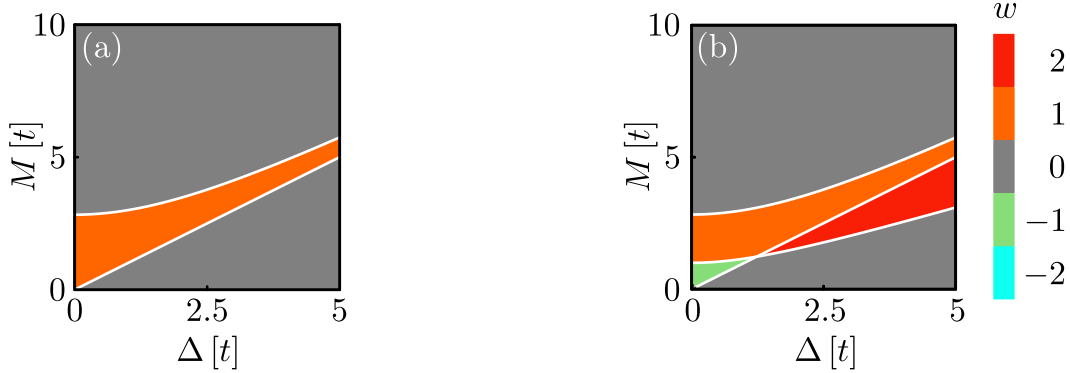


Figure 5.5: Topological phase diagrams for the one-band model in fig. 5.4 in the MHC phase for: (a) a constant pairing gap $\Delta_{k_x} = \Delta$ and (b) an unconventional pairing gap $\Delta_{k_x} = \Delta[1 + 2 \cos(2k_x)]$, which leads to additional gap-closing points. Both (a) and (b) were obtained for $Q = Q_N$ and a spatially-constant magnetic moment, i.e. $M_{\perp} = M_{\parallel} = M > 0$.

Note, however, that the upper boundary may not be reached in practice, since for this purpose, magnetic gap values larger than the Fermi energy are required.

In fig. 5.5(a), we numerically determine the topological phase diagram for a conventional s -wave pairing gap $\Delta_{k_x} = \Delta > 0$, given the dispersion in fig. 5.4. The orange region displays the parameter space, for which, the system is in a topologically nontrivial phase with $w = 1$. For the parameters used in the figure, eqn. (5.14) reduces to $\Delta < M < \sqrt{8t^2 + \Delta^2}$, and coincides with the numerically-obtained upper and lower bounds of the nontrivial region.

We conclude this section by addressing the case of an unconventional superconducting order parameter which generates additional gap closings away from inversion-symmetric points. As a result of chiral and charge-conjugation symmetries, the additional gap closings come in pairs $\pm k_*$ [284], and thus each pair of gap-closing points of this type generally contributes with ± 1 units to w . For an illustration, we consider the gap function $\Delta_{k_x} = \Delta[1 + 2 \cos(2k_x)]$ which features a single pair of such nodes. The latter nodes have an accidental origin, since they are not imposed by the presence of a symmetry, and further contribute to the winding number of eqn. (5.13). A numerically-obtained example for this case is depicted in fig. 5.5(b). The regions with $w = -1$ and $w = +2$ appear due to the fact that the signs of the fractional contributions arising from the $k_I = 0, \pi$ points are no longer determined by eqn. (5.13), as a result of the unconventional pairing. Therefore, the contributions of the k_I points for $w = -1$ ($w = +2$) cancel out (add up to $+1$), while the contribution from the $\pm k_*$ gap-closing points is -1 ($+1$). Thus, the inclusion of an unconventional pairing function which leads to additional gap closings at $\pm k_*$, does not significantly alter the nontrivial region here, but does increase the overall complexity of the phase diagram.

We conclude this section by discussing the impact of the various magnetic point group symmetries on the topological classification, given that the nonmagnetic part of the BdG Hamiltonian is invariant under the symmetry group of the normal phase. The addition of magnetism reduces the initial point group down to the magnetic point group $M_{\text{MHC}} = C_2 + (C_{2v} - C_2)T$, whose elements are presented in table 5.1. Any possible implications of the magnetic point group on the topological properties of the system are associated with the emergence of the two *antiunitary* mirror symmetries

$(C_{2v} - C_2)T = \{\sigma_{xz}T, \sigma_{yz}T\}$. Their presence implies that the symmetry classes for the xz and yz HSPs generally differ from the BDI class which was obtained by solely considering the generalized time-reversal symmetry $\Theta = K$. This is because these antiunitary mirror symmetries act as additional generalized time-reversal symmetries in the HSPs. Furthermore, the presence of this set of three time-reversal symmetries induces two *unitary* symmetries $\{R_{xz}, R_{yz}\}$, whose presence allow for the block diagonalization of the Hamiltonian.

It is customary to describe these effects in terms of $\{\Theta, \Xi\}$ and their (anti)commutation relations with the generators of the induced unitary symmetries $\{R_{xz}, R_{yz}\}$ [28, 29, 146, 379], whose expressions are inferrable from the two *unitary* mirror symmetries

$$R = (C_{2v} - C_2)T\Theta \equiv \{R_{xz}, R_{yz}\}. \quad (5.15)$$

Hence, by restricting to the HSPs, we find the expressions $R_{xz} = \mathbb{1}_\sigma$ and $R_{yz} = \sigma_z$.

For the 1D system examined here R_{xz} is trivial, while R_{yz} is expected to only affect the bulk topological properties of the system, since it is violated when boundaries are introduced. Specifically, R_{yz} can influence the classification at the mirror-symmetry-invariant points $k_{R_{yz}} = \{0, \pi\}$ satisfying $R_{yz}k_{R_{yz}} \equiv k_{R_{yz}}$. For these points $\xi_{k_{R_{yz};q}}^- = \Delta_{k_{R_{yz};q}}^- = 0$, and the BdG Hamiltonian in eqn. (5.4) becomes block diagonal and reads

$$\mathcal{H}_{k_{R_{yz};\sigma}} = \sigma M + \xi_{k_{R_{yz};q}}^+ \tau_3 + \Delta_{k_{R_{yz};q}}^+ \tau_1, \quad (5.16)$$

where we used the eigenvectors of σ_z , which are labelled by $\sigma = \pm 1$. The above Hamiltonian belongs to symmetry class $\text{AI} \oplus \text{AI}$ with $\Theta = K$, which in 0D yields the mirror topological invariant $n_M \in \mathbb{Z}$. See refs. [28, 319].

To calculate n_M , we choose an approach which keeps the variety of the topological-invariant constructions used in this work to a minimum. This is achieved by evaluating the mirror invariant in an augmented space, which is spanned by the spatial dimensions relevant for the classification, and the continuous frequency $\epsilon \in (-\infty, \infty)$ obtained as the zero-temperature limit of the Matsubara frequencies. Adding ϵ compensates the reduction of the physical dimensions by one, which occurs when restricting to a HSP. As a result, this allows us to describe both bulk and HSPs using a winding number defined in the natural and augmented 1D spaces, respectively.

The topological invariant for the AI class in 0D is thus given here by the winding number of the normalized complex number Z_ϵ , obtained from the normalized determinant of the inverse single-particle Matsubara Green function $G_{\epsilon,\sigma}^{-1} = i\epsilon - \mathcal{H}_{k_{R_{yz};\sigma}}$. Hence, we have for each σ block

$$n_{k_{R_{yz};\sigma}} = \frac{1}{4\pi i} \int_{-\infty}^{+\infty} \frac{dZ_{\epsilon,\sigma}}{Z_{\epsilon,\sigma}}, \quad (5.17)$$

with $Z_{\epsilon,\sigma} = -\det(G_{\epsilon,\sigma}^{-1})/|\det(G_{\epsilon,\sigma}^{-1})|$. We thus find

$$-\det(G_{\epsilon,\sigma}^{-1}) = (\xi_{k_{R_{yz};q}}^+)^2 + (\Delta_{k_{R_{yz};q}}^+)^2 - (i\epsilon)^2 - M^2 + 2i\sigma\epsilon M, \quad (5.18)$$

which has a form similar to that of the determinant in eqn. (5.7), that was employed to calculate the winding number w in k_x space.² To be in accordance with ref. [28], given the definition in eqn. (5.17),

²Note that the Green function approach could have been also used to evaluate the winding number w in eqn. (5.9), by means of a 1st Chern number in the augmented (ϵ, k_x) space. This method has clear advantages if we wish to include possible self-energy effects.

we define the mirror invariant n_M using a single σ block of our choice as follows

$$n_M = 2 \operatorname{sgn}(n_{k_x=0,\sigma} - n_{k_x=\pi,\sigma}) (|n_{k_x=0,\sigma}| - |n_{k_x=\pi,\sigma}|). \quad (5.19)$$

n_M counts the number of mirror-symmetry protected edge states for edges preserving the respective mirror symmetry. However, as we announced, the above invariant becomes obsolete in 1D systems, since mirror symmetry is expected to be broken when termination edges are present. Nevertheless, here we rely on the translational invariance of the system and instead introduce a set of bulk mirror invariants. In analogy to the spin Chern number construction [15, 17, 408], we define

$$n_{M;k_{R_{yz}}} = \sum_{\sigma} \sigma n_{k_{R_{yz}},\sigma}. \quad (5.20)$$

After evaluating $n_{k_{R_{yz}},\sigma}$, we find that $n_{M;k_{R_{yz}}}$ becomes

$$2n_{M;k_{R_{yz}}} = \operatorname{sgn}[(\xi_{k_{R_{yz}};q}^+)^2 + (\Delta_{k_{R_{yz}};q}^+)^2 - M^2] - 1. \quad (5.21)$$

This bulk mirror invariant reflects the quantization of the z axis magnetization³ in HSPs, since $\langle \sigma_z \rangle_{k_x=k_{R_{yz}}} = n_{M;k_{R_{yz}}}$. One finds $|n_{M;k_{R_{yz}}}| = 1$ only after certain level crossings occur at $k_{R_{yz}}$, thus bearing similarities to parity-switching level crossings known for Yu-Shiba-Rusinov bound states [335–337, 409], which are induced by magnetic impurities in spin-singlet superconductors.

The measurement of the k_x -resolved magnetization appears experimentally feasible by means of spin-resolved angle resolved photoemission spectroscopy, which has already been successfully applied to map out the spin character of the surface states of time-reversal-invariant 3D topological insulators [410]. We thus find that, although the unitary mirror symmetry R_{yz} is generally broken when edges are introduced to the system, we can still use $n_{M;k_{R_{yz}}}$ as a bulk experimental probe for topological superconductivity. Furthermore, we remark that the above calculations also serve as a simple example of similar derivations that we plan to carry out in the upcoming sections.

MHC with a Spatially Varying Magnetic Moment: $|M_{\perp}| \neq |M_{\parallel}|$

We now extend the study of the previous section to the more general situation, in which $|M_{\perp}| \neq |M_{\parallel}|$. In this case, using a spin-dependent unitary transformation to gauge away the spatial dependence of the MHC is no longer possible, and one has to approach the problem in the MBZ, i.e. $k_x \in (-q, q]$, with $q = Q/2 = \pi/4$. To describe the downfolding to the MBZ, one can either consider a sublattice description which is briefly discussed in app. 5.B, or choose to express the Hamiltonian in $\{k_x, k_x + Q\}$ and $\{k_x, k_x + 2Q\}$ wave-number-transfer spaces. The former is advantageous for carrying out the topological classification, since the resulting BdG Hamiltonian is 2π -periodic and thus suitably compactified. The results presented in table 5.2 and 5.3 were obtained using this approach. However, throughout the main text we follow the second route, which is implemented by introducing the enlarged spinor

$$\mathbf{c}_{k_x}^{\dagger} = \mathbb{1}_{\eta} \frac{\rho_2 + \rho_3}{\sqrt{2}} \left(C_{k_x-q}^{\dagger}, C_{k_x+q}^{\dagger}, C_{k_x+3q}^{\dagger}, C_{k_x-3q}^{\dagger} \right) \quad (5.22)$$

³Recall that the above is expressed in the local spin frame. Rotating back with U^{\dagger} , implies that $n_{M;k_{R_{yz}}}$ leads to the quantization of the staggered magnetization in the xz spin plane.

where we introduced the Pauli matrices $(\rho_{1,2,3}) \eta_{1,2,3}$ defined in the $(Q-)$ $2Q$ -transfer space. The above basis reveals more transparently the mechanisms underlying the nontrivial topological properties induced by the magnetic textures, it highlights the emergent Dirac physics, and it provides a simpler and more convenient framework to evaluate the various topological invariants.

The wave-number shifts in the arguments of the above spinor were chosen to connect to the spinor obtained after performing the unitary transformation U in the case $|M_{\perp}| = |M_{\parallel}|$. See also fig. 5.4(b) and note that, given our spinor choice, the periodic magnetization opens gaps at $k_x = 0$ when $Q = Q_N$. The extended BdG Hamiltonian reads $\mathcal{H}_{k_x} = \mathcal{H}_{k_x}^0 + \mathcal{H}_{\text{mag}}$ with

$$\begin{aligned} \mathcal{H}_{k_x} &= \left[h_{k_x}^{(0)} + h_{k_x}^{(1)} \rho_2 + h_{k_x}^{(2)} \eta_3 + h_{k_x}^{(3)} \eta_3 \rho_2 \right] \tau_3 + \left[\Delta_{k_x}^{(0)} + \Delta_{k_x}^{(1)} \rho_2 + \Delta_{k_x}^{(2)} \eta_3 + \Delta_{k_x}^{(3)} \eta_3 \rho_2 \right] \tau_1, \\ \mathcal{H}_{\text{mag}} &= -(M_{\perp} \rho_1 \sigma_z + M_{\parallel} \rho_3 \sigma_x) / 2 - \eta_1 (M_{\perp} \rho_1 \sigma_z - M_{\parallel} \rho_3 \sigma_x) / 2 \end{aligned} \quad (5.23)$$

and the functions $h_{k_x}^{(s)}$ and $\Delta_{k_x}^{(s)}$ appearing above with $s = 0, 1, 2, 3$, constituting linear combinations of ξ_{k_x} and Δ_{k_x} , which follow from the general definitions

$$\begin{aligned} f_{k_x}^{(0)} &= (f_{k_x-q} + f_{k_x+q} + f_{k_x+3q} + f_{k_x-3q}) / 4, & f_{k_x}^{(1)} &= (f_{k_x-q} - f_{k_x+q} + f_{k_x+3q} - f_{k_x-3q}) / 4, \\ f_{k_x}^{(2)} &= (f_{k_x-q} + f_{k_x+q} - f_{k_x+3q} - f_{k_x-3q}) / 4, & f_{k_x}^{(3)} &= (f_{k_x-q} - f_{k_x+q} - f_{k_x+3q} + f_{k_x-3q}) / 4. \end{aligned} \quad (5.24)$$

The above construction further implies that inversion $k_x \rightarrow -k_x$, acts as $f_{-k_x}^{(s)} = (-1)^s f_{k_x}^{(s)}$. One observes that the four linear combinations resulting from the electron part $h_{k_x}^{(0)} + h_{k_x}^{(1)} \rho_2 + h_{k_x}^{(2)} \eta_3 + h_{k_x}^{(3)} \eta_3 \rho_2$ of the nonmagnetic BdG Hamiltonian, give rise to the four spin-degenerate band segments in the MBZ shown in fig. 5.4(b). We point out that the set of inversion-symmetric points in the MBZ reads $k_I = \{0, q \equiv -q\}$, while the $k_I = \pi$ of the original BZ coincides now with $k_I = 0$ in the MBZ. Note that the inversion-symmetric nature of $k_x = \pm q$ is established via the equivalence relation $-q \equiv q + nQ$ with $n \in \mathbb{Z}$.

The magnetic space group dictating the above BdG Hamiltonian is identical to the one for the MHC with a spatially-constant magnetic moment ($|M_{\perp}| = |M_{\parallel}|$). However, before discussing its implications on the topological classification, we point out that given the enlarged basis in eqn. (5.22), which is indispensable here for the description of the MHC, one needs to account for possible space group symmetries.

Specifically, as also presented in table 5.2, the additional space group symmetries $\{T | \pi/Q\}$ and $\{\sigma_{xz,yz} | \pi/Q\}$ become now relevant. Given our choice of basis, $\{E | \pi/Q\} = -ie^{ik_x \pi/Q} \rho_2$ and $T = i\sigma_y K$ as usual, while the mirror operations have the following $\rho \otimes \sigma$ space matrix structure $\sigma_{yz} = i\rho_1 \sigma_x$ and $\sigma_{xz} = i\sigma_y$. Hence, we find the unitary symmetries with $\{\sigma_{yz} | \pi/Q\} = ie^{ik_x \pi/Q} \rho_3 \sigma_x$, $\{\sigma_{xz} | \pi/Q\} = e^{ik_x \pi/Q} \rho_2 \sigma_y$, and the antiunitary symmetry $\tilde{\Theta}_{k_x} \equiv \{T | \pi/Q\} = ie^{ik_x \pi/Q} \rho_2 \sigma_y K$. In contrast to the physical time-reversal operation which satisfies $T^2 = -\mathbb{1}$, here $\tilde{\Theta}_{k_x}^2 = e^{i\pi k_x/q} \mathbb{1}$ and leads to a Kramers degeneracy only at the $k_x = q$ inversion-symmetric point in the MBZ [134, 135, 149]. Notably, this is the mechanism underlying the persistent Kramers degeneracies at the purple-colored points of the MBZ shown in fig. 5.2(h). As also discussed in app. 5.C, the above space-group symmetries do not lead to any further symmetry-protected degeneracies in the spectrum, and thus influence the topological classification only in HSPs. For this reason, their implications are discussed later, together with the magnetic point group symmetries.

The extended BdG Hamiltonian belongs to class BDI and is classified by a winding number $w \in \mathbb{Z}$. Applying the methods of sec. 5.4, and assuming for simplicity that $Q = Q_N$, and $\Delta_{k_x} = \Delta > 0$ so that

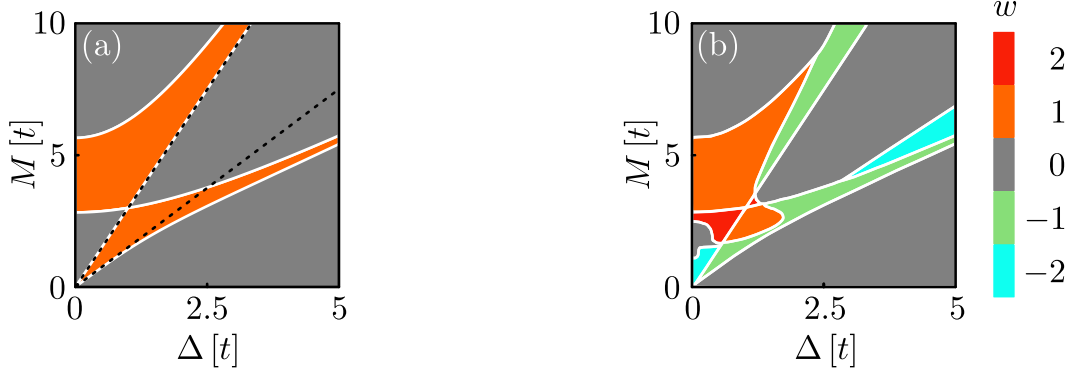


Figure 5.6: Topological phase diagrams for the one-band model in fig. 5.4 in the MHC phase with a spatially varying magnetic moment $M_{\perp} = M > 0$ and $M_{\parallel} = M/3$. (a) displays the phase diagram for a constant pairing gap $\Delta_{k_x} = \Delta$ while (b) uses an unconventional pairing gap $\Delta_{k_x} = \Delta[1 + 2 \cos(2k_x)]$, which leads to additional gap-closing points. The black dotted lines in (a) span the topologically nontrivial region in the weak-coupling limit, see eqn. (5.27). As one observes, this limit is only valid when $0 < M_{\parallel, \perp}, \Delta \ll 2|\mu_0|$ are satisfied.

$\Delta_{k_x}^{(0)} = \Delta$ and $\Delta_{k_x}^{(s)} = 0$ for $s = 1, 2, 3$, lead to (see app. 5.D for details)

$$w = \sum_{\nu} \frac{\nu}{2} \text{sgn} \left((M_{\nu}^2 - \Delta^2) - \frac{(M_{\perp}^2 - \Delta^2)(M_{\parallel}^2 - \Delta^2)}{(2\mu_0)^2} \right), \quad (5.25)$$

with $M_{\nu} = (M_{\parallel} + \nu M_{\perp})/2$ and $\nu = \pm 1$. Figure 5.6(a) depicts the topological phase diagram for the one-band model in fig. 5.4 when $M_{\perp} = M$ and $M_{\parallel} = M/3$. The orange regions are phases with a single MZM per edge. While the anisotropic nature of the MHC does not lead to the removal of the topologically nontrivial phase, it still significantly modifies the phase diagram. It is straightforward to verify that for $\Delta_{k_x} = \Delta$, the gap closings responsible for the topological phase transition take place only at $k_x = 0$. Nonetheless, eqn. (5.25) also holds for an unconventional superconducting order parameter after replacing $\Delta \rightarrow \Delta_{k_x=0}$, under the condition that additional gap-closing points do not emerge. Instead, for an unconventional pairing order parameter which leads to additional gap closings at $\pm k_*$, the topological phase diagram ends up to be quite complex. After obtaining w for a generic Δ_{k_x} (see app. 5.D), we focus on a pairing gap $\Delta_{k_x} = \Delta[1 + 2 \cos(2k_x)]$. The related topological phase diagram is depicted in fig. 5.6(b).

To gain deeper insight, we set $\Delta_{k_x} = \Delta > 0$ and restrict to the weak-coupling limit $|\Delta|, |M_{\parallel, \perp}| \ll 2|\mu_0|$. Since gap closings now occur only near the FS, eqn. (5.25) becomes

$$w = \frac{\text{sgn}(M_{+}^2 - \Delta^2) - \text{sgn}(M_{-}^2 - \Delta^2)}{2}. \quad (5.26)$$

Thus, the topological phases arising from gap closings occurring in the low-energy sector, are solely determined by the inequality

$$M_{-} < \Delta < M_{+} \quad \text{for} \quad M_{\perp, \parallel} \geq 0. \quad (5.27)$$

The spatial variation of the magnetic moment, which is reflected in the size of the difference $|M_{-}| = |M_{\parallel} - M_{\perp}|$, sets a maximum value for the magnetic anisotropy that can still allow for the system to

enter the nontrivial phase. For the specific parameters used in fig. 5.6(a), the above inequality reduces to $3\Delta/2 < M < 3\Delta$. The low-energy nontrivial region is therefore spanned by the black dotted lines in fig. 5.6(a), which verifies that eqn. (5.26) indeed describes the exact model well in the weak-coupling limit.

The results in the weak-coupling limit can be alternatively obtained by directly restricting the multicomponent spinor of eqn. (5.22) to the operators creating/annihilating electrons in the low-energy sector, i.e.

$$\mathbf{C}_{k_x}^\dagger = \frac{\rho_2 + \rho_3}{\sqrt{2}} (\mathbf{C}_{k_x-q}^\dagger, \mathbf{C}_{k_x+q}^\dagger). \quad (5.28)$$

The projection of the Hamiltonian in eqn. (5.23) onto this subspace is achieved by setting $\eta_3 = +1$, and dropping the term proportional to η_1 which connects the low- and high-energy sectors. These steps lead to the Hamiltonian

$$\mathcal{H}_{k_x}^{\text{low-en}} = \left(\xi_{k_x;q}^+ + \xi_{k_x;q}^- \rho_2 \right) \tau_3 - \left(M_\perp \rho_1 \sigma_z + M_\parallel \rho_3 \sigma_x \right) / 2 + \left(\Delta_{k_x;q}^+ + \Delta_{k_x;q}^- \rho_2 \right) \tau_1, \quad (5.29)$$

with $\xi_{k_x;q}^\pm$ and $\Delta_{k_x;q}^\pm$ following once again the general form $f_{k_x;q}^\pm = (f_{k_x-q} \pm f_{k_x+q})/2$.

We now discuss the impact of the unitary mirror $R_{xz,yz}$ and space group $\{\sigma_{xz,yz} | \pi/Q\}$ symmetries on the topological classification in HSPs. First of all, Θ_{k_x} imposes a twofold degeneracy at $k_x = q$, thus implying that the magnetic texture does not induce any new topologically nontrivial phases at $k_x = q$. See table 5.2 and app. 5.B for more details. Even more, as in sec. 5.4, also here, the effects of R_{xz} are trivial, since it leads to a unitary symmetry $R_{xz} = \mathbf{1}$. The remaining four symmetries modify the topological properties at $k_x = 0$. The symmetries R_{yz} and $\{\sigma_{yz} | \pi/Q\}$ ($\{T | \pi/Q\}$ and $\{\sigma_{xz} | \pi/Q\}$) lead to a AI \oplus AI (BDI \oplus BDI) class, thus providing an additional \mathbb{Z} (\mathbb{Z}_2) topological invariant to the winding number w .

The R_{yz} symmetry allows defining two types of mirror invariants, in analogy to eqns. (5.19) and (5.20). The block-diagonalization of the BdG Hamiltonian in eqn. (5.23), that is effected by the unitary transformation $(R_{yz} + \sigma_x)/\sqrt{2}$, yields in the weak-coupling limit (see also app. 5.D)

$$2n_{M,k_x=0} = \sum_{\nu=\pm 1} \nu \operatorname{sgn} [(\xi_{0;q}^+)^2 + (\Delta_{0;q}^+)^2 - M_\nu^2]. \quad (5.30)$$

It is straightforward to verify that $n_{M,k_x=0} = n_M$, since no topological gap closings can take place at $k_x = q$. In a similar fashion, the offcentered⁴ space-group symmetry $\{\sigma_{yz} | \pi/Q\}$ allows introducing the here-termed glide invariant $n_{G,k_x=0} \in \mathbb{Z}$, which is defined following eqns. (5.17) and (5.20). As pointed out in sec. 5.4 and footnote 3, also here, the staggered magnetization in the z (x) spin axis becomes quantized when $n_{M,k_x=0}$ ($n_{G,k_x=0}$) is nonzero, since $2n_{M,k_x=0} = \langle \rho_1 \sigma_z \rangle_{k_x=0}$ ($2n_{G,k_x=0} = \langle \rho_3 \sigma_x \rangle_{k_x=0}$). For the given model $|n_{M,k_x=0}| = |n_{G,k_x=0}|$.

We now proceed with the \mathbb{Z}_2 topological invariants which emerge from the $\{T | \pi/Q\}$ and $\{\sigma_{xz} | \pi/Q\}$ symmetries. In the presence of either one of these, the unitary symmetry $\tilde{R} = \rho_2 \sigma_y$ is induced, and allows us to block-diagonalize the Hamiltonian in eqn. (5.23) via the unitary transformation $(\tilde{R} + \sigma_z)/\sqrt{2}$. This yields the BDI blocks

$$\mathcal{H}_{k_x=0,\sigma} = \mathcal{H}_{k_x=0}^0 - \left(M_\sigma - M_{-\sigma} \eta_1 \right) \rho_1, \quad (5.31)$$

⁴The nonmenclature highlights that this symmetry is not nonsymmorphic, because we can choose a coordinate system in the direct lattice for which $\{\sigma_{yz} | \pi/Q\} \rightarrow \sigma_{yz}$. See also app. 5.C.

with $\sigma = \pm 1$ labeling the eigenstates of σ_z . The two blocks exhibit a chiral symmetry $\Pi = \rho_2 \tau_2$. Following the same approach that led to eqn. (5.6), we block-off diagonalize each σ block by means of the unitary transformation $(\Pi + \tau_3)/\sqrt{2}$, with the upper block denoted $A_{k_x=0,\sigma}$. The \mathbb{Z}_2 invariant, that we here term glide Majorana parity P_G , is constructed in app. 5.D and is defined as

$$P_{G,k_x=0} = \text{sgn} \prod_{\sigma=\pm 1} \det A_{k_x=0,\sigma}. \quad (5.32)$$

Within the weak-coupling limit, we obtain the result

$$P_{G,k_x=0} = \text{sgn} \prod_{\sigma=\pm 1} [(\xi_{0,q}^+)^2 + (\Delta_{0,q}^+)^2 - M_\sigma^2]. \quad (5.33)$$

Hence, here we end up with $P_{G,k_x=0} = (-1)^{n_{M,k_x=0}}$, which implies that in the present model $P_{G,k_x=0}$ is nontrivial, i.e. equal to -1 , when $n_{M,k_x=0} \in 2\mathbb{Z} + 1$.

Concluding this section, we remark once again that in strictly 1D systems the above point and space group symmetries affect only the bulk topological properties, since these are all broken when edges are introduced. When this takes place, it is only w together with the weak \mathbb{Z}_2 invariant of class BDI,⁵ which are capable of predicting the number of the arising MZMs. This is in stark contrast to 2D systems, where certain edges also support crystalline and/or weak invariants, as discussed further in later sections.

Two-Band Models

In this section, we extend the previous analysis to the case of two-band models with dispersions $\xi_{k_x}^{e,h}$, where the superscript e/h reflects the type of electron/hole pocket that arises from the respective band. An example of such a two-band model is shown in fig. 5.7. We employ the $\kappa_{1,2,3}$ Pauli matrices to represent Hamiltonian matrix elements in band space. This representation is also relevant for the magnetic and pairing terms, which now become matrices in this space. In particular, the real space lattice profile of the magnetization generally reads

$$\widehat{M}_R = \frac{M_R^e + M_R^h}{2} + \frac{M_R^e - M_R^h}{2} \kappa_3 + M_R^{eh} \kappa_1. \quad (5.34)$$

One notes that a term proportional to κ_2 is not allowed, since this violates the requirement that the magnetization field of the texture is odd under T . On the other hand, the spin-singlet pairing matrix reads

$$\widehat{\Delta}_{k_x} = \frac{\Delta_{k_x}^e + \Delta_{k_x}^h}{2} + \frac{\Delta_{k_x}^e - \Delta_{k_x}^h}{2} \kappa_3 + \frac{\Delta_{k_x}^{eh} + \Delta_{k_x}^{he}}{2} \kappa_1 - \frac{\Delta_{k_x}^{eh} - \Delta_{k_x}^{he}}{2i} \kappa_2. \quad (5.35)$$

The required antisymmetry of the superconducting matrix order parameter in the combined spin, band and k_x spaces, implies that the terms proportional to $\mathbb{1}_\kappa$, κ_3 and κ_1 are even under inversion, while the one proportional to κ_2 is odd. In the remainder, we focus on cases where the FSs associated with the various pockets do not overlap and, as a result, interband pairing is fully suppressed.

⁵We define the weak invariant $P_{\mathcal{M}} = \text{sgn} \prod_{k_I} \det A_{k_I} \equiv \text{sgn}[\det A_{k_x=0}]$, with A_{k_I} the upper off-diagonal block of the block off-diagonalized Hamiltonian in eqn. (5.23) evaluated at k_I . The arising equivalence is a result of the Kramers degeneracy at $k_x = q$. When either $\{T | \pi/Q\}$ or $\{\sigma_{xz} | \pi/Q\}$ is a symmetry, $P_{\mathcal{M}}$ coincides with the glide Majorana parity $P_{G,k_x=0}$ in eqn. (5.32).

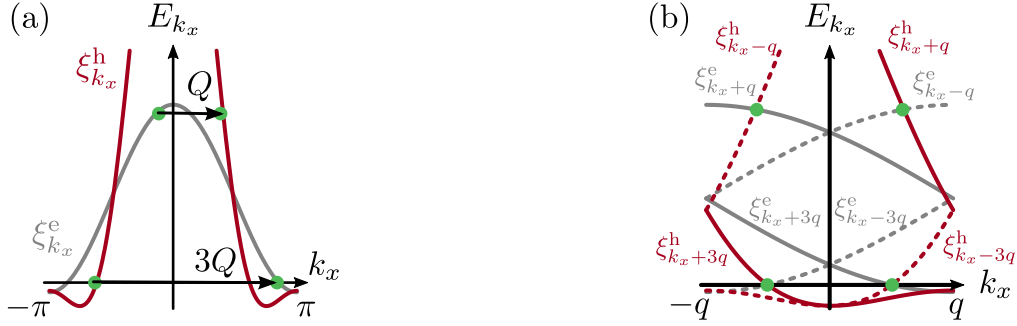


Figure 5.7: Example of a two-band model in 1D. (a) The dispersions $\xi_{k_x}^e = t_e \cos k_x - \varepsilon_e$ (gray) and $\xi_{k_x}^h = t_h \cos k_x + t'_h [1 + \cos(2k_x)] - \varepsilon_h$ (red) in the first BZ. We set the parameters values $t_h = 2.86 t_e$, $t'_h = t_e$, $\varepsilon_e \approx -0.92 t_e$ and $\varepsilon_h = -0.80 t_e$. We also show the nesting wave vector Q_N which, for the choice of parameters made here, coincides with the magnetic wave vector Q . Thus, Q connects two pairs of points at the Fermi level and two more pairs at higher energies. (b) The resulting eight band-segments in the MBZ. The points connected by the magnetic wave number ($3Q = -Q$) come in pairs due to C_2 symmetry, and are depicted by green dots. For clarity, (a) depicts half of the ordering wave numbers.

In the present case we also consider that the magnetization possesses a MHC form, with the $M_{\parallel, \perp}$ helix components of the previous section being upgraded to band-space matrices according to eqn. (5.34). In addition, we assume that the two intraband pairing order parameters $\Delta_{k_x}^{e, h}$ do not contain any zeros, and thus, we set them to be constants. Nonetheless, our results qualitatively hold for more complex unconventional gap structures, as long as these do not contain any zeros. We further note that, here, the inclusion of an additional band does not lower the symmetry of the Hamiltonian, and the system is therefore left invariant under the magnetic space group symmetries discussed in the previous section.

Since the two-band models bear similarities with the thoroughly-explored one-band models, we confine the analysis to the novel features brought about by the additional band. We extend the spinor defined in eqn. (5.22) as follows

$$\tilde{\mathbf{c}}_{k_x}^\dagger = \left(\mathbf{c}_{k_x; e}^\dagger, \mathbf{c}_{k_x; h}^\dagger \right). \quad (5.36)$$

and consider the Hamiltonian

$$\mathcal{H}_{k_x} = \sum_s^{\text{e, h}} \mathcal{P}_s \mathcal{H}_{k_x; 0}^s - (\widehat{M}_\perp \rho_1 \sigma_z + \widehat{M}_\parallel \rho_3 \sigma_x) / 2 - (\widehat{M}_\perp \eta_1 \rho_1 \sigma_z - \widehat{M}_\parallel \eta_1 \rho_3 \sigma_x) / 2 \quad (5.37)$$

where we introduced the electron-like [hole-like] band projectors $\mathcal{P}_e = (\mathbf{1}_\kappa + \kappa_3) / 2$ [$\mathcal{P}_h = (\mathbf{1}_\kappa - \kappa_3) / 2$]. Depending on the precise matrix form of the magnetization, one can interpolate between intra- and inter-band scattering. For $\widehat{M}_{\parallel, \perp} \propto \mathbf{1}_\kappa$, κ_3 , the magnetic scattering has only an intraband character, and the two bands are completely decoupled. Thus, the topological properties of the system follow from applying the results of the previous paragraphs separately to each band, and the symmetry class is $\text{BDI} \oplus \text{BDI}$. In contrast, when $\widehat{M}_\perp = M_\perp \kappa_1$ and $\widehat{M}_\parallel = M_\parallel \kappa_1$, the Hamiltonian exhibits an additional unitary symmetry with the generator $O = \kappa_3 \sigma_y$. Note that this symmetry is due to the specific form of

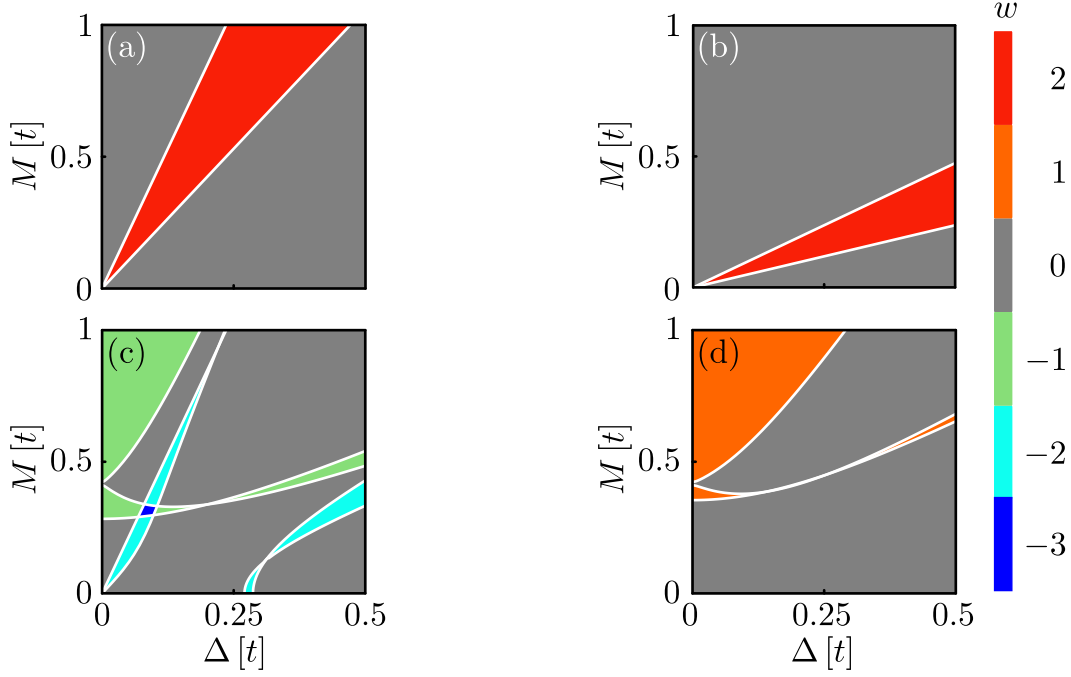


Figure 5.8: Topological phase diagrams for the two-band model in fig. 5.7 in the MHC phase, evaluated by projecting onto the low-energy sector. (a) Phase diagram when solely interband magnetic scattering is considered, and the order parameter values $\Delta^h = \Delta$ and $\Delta^e = \Delta/2$ are employed. (b) Same as in (a), but with $\Delta^h/\Delta^e = 1/10$. When $\Delta^h\Delta^e < 0$ the topologically nontrivial phase vanishes. (c) Same as in (a), but with the inclusion of intraband magnetic scattering, with $M_{\parallel,\perp}^e = M_{\parallel,\perp}^h = M$. (d) Here, $\Delta^h = -2\Delta^e$ and $M_{\parallel,\perp}^e = M_{\parallel,\perp}^h = M$. Notably, the inclusion of intraband magnetic scattering induces a topologically-nontrivial phase in an otherwise trivial region. We considered $M_{\perp}^{\text{eh}} = M$ and $M_{\parallel}^{\text{eh}} = M/3$ in all calculations.

the magnetic texture in band space, and intraband magnetic scattering terms $\widehat{M}_{\perp,\parallel} \propto \mathbf{1}_{\kappa}, \kappa_3$ generally violate it.

Assuming the presence of O , we block diagonalize the Hamiltonian using the transformation $\mathcal{S} = (O + \sigma_z)/\sqrt{2}$, and find that the nonmagnetic part of eqn. (5.37) remains unaltered, while the magnetic part becomes

$$\mathcal{H}_{\text{mag},\sigma} = -(\sigma M_{\perp} \kappa_1 \rho_1 + M_{\parallel} \kappa_2 \rho_3)/2 - (\sigma M_{\perp} \kappa_1 \eta_1 \rho_1 - M_{\parallel} \kappa_2 \eta_1 \rho_3)/2, \quad (5.38)$$

where $\sigma = \pm 1$ correspond to the eigenvalues of σ_z . Each Hamiltonian block belongs to the symmetry class AIII with $\Pi = \kappa_3 \tau_2$. The procedure for carrying out the 1D topological analysis is here identical to the one presented in sec. 5.4 for systems in the BDI symmetry class, since also the AIII class supports a \mathbb{Z} topological invariant in 1D, which is identified with a winding number.

Such an analysis, see app. 5.D, yields that the topological phase transition from the trivial to the nontrivial phase occurs when $\xi_{k_x \pm 3q}^e \Delta^h = \xi_{k_x \mp 3q}^h \Delta^e$ and $\xi_{k_x \pm 3q}^e \xi_{k_x \mp 3q}^h + \Delta^e \Delta^h = M_{\sigma}^2$, are simultaneously satisfied, for a given σ . When the magnetic wave vectors connect two points at the Fermi level,

we have $\xi_{k_x \pm 3q}^e = \xi_{k_x \mp 3q}^h = 0$ and the topological criterion reads $\Delta^e \Delta^h = M_\sigma^2$. Remarkably, the latter condition can be satisfied only when the two magnetically connected points exhibit the *same* sign for the pairing term. Figures 5.8(a)-(b) display the resulting phase diagrams for $\Delta^h/\Delta^e = \{2, 1/10\}$, respectively, with the topologically nontrivial regions marked in red. In agreement with the above criterion, we find that the nontrivial regime shrinks when $|\Delta^e - \Delta^h|$ increases.

We note the doubling of w compared to the case of the one-band models, cf. fig. 5.5(a) and 5.6(c). This is due to the doubling of the number of gap closing points k_c . Each one of the green dots in fig. 5.7(b) contributes with a single unit to w . The emergence of a number of $2\mathbb{Z}$ MZMs in conjunction with the AIII classification imply that each emergent pair of MZMs should be seen as a single topologically protected Andreev zero mode. Indeed, from the analyses of refs. [24, 356], it emerges that here a topological superconductor originating from an interband-only magnetic texture can be described with a spinor of halved dimensionality compared to the one defined in eqn. (5.36), since spin-up electrons of the electron-like pocket pair up only with spin-down electrons of the hole-like pocket, and vice versa. While so far there exists only a little theoretical activity on Andreev zero modes compared to MZMs, cf. ref. [123, 399–402], their experimental creation and manipulation is a fascinating topic on its own. Indeed, when these Andreev zero modes are topologically protected for an extended region in the parameter space, as found here, they in principle enable quantum information processing with long-lived quasiparticles [403, 404].

In the more general case, intraband terms which break the $O = \kappa_3 \sigma_y$ symmetry may also be present. These can be divided into nonmagnetic and magnetic. When these are nonmagnetic, e.g. various types of inversion symmetry breaking SOC, they stabilize a DIII symmetry class which supports MZM Kramers pairs. For a similar situation see ref. [268]. However, throughout this work we consider that all types of inversion symmetry breaking SOC have negligible strengths, thus implying that such a possibility is inaccessible here. Nonetheless, as we discuss later in this manuscript, DIII class Majorana fermions become generally accessible in 2D two-band models for a SWC_4 texture. On the other hand, when additional magnetic terms are considered, these restore the BDI class found in the one-band models, as well as the Majorana nature of the topologically-protected edge excitations.

We proceed by investigating the effects of intraband magnetic texture terms. For this purpose, we recalculate the winding number (see app. 5.D), and obtain the phase diagrams in fig. 5.8(c) and (d) for $\Delta^h/\Delta^e = \pm 2$, respectively. Strikingly, as seen in fig. 5.8(d), the inclusion of intraband magnetic scattering induces a topologically nontrivial phase, even when the connected points exhibit different signs for the pairing term. Once again, assuming that the transition occurs due to the gap closing at two magnetically-connected Fermi points, and that the magnetic moments are spatially constant, the topological criterion reads

$$(\Delta^e \pm M^e)(\Delta^h \pm M^h) = (M^{\text{eh}})^2. \quad (5.39)$$

This expression imposes severe constraints on the unconventional superconducting order parameter, as well as the relative contributions of intra- and inter-band magnetism, which can lead to topologically nontrivial phases in 1D. Nonetheless, this condition is not as stringent in higher-dimensional systems, since the pairing term may lead to a gap closing for some of the BZ points, which is a sufficient condition to allow, but not necessarily guarantee, the transition to a topological superconductor phase.

To this end, we remark that crystalline symmetries generally influence the bulk classification of multiband systems in a similar fashion to one-band models when inter- and intra-band magnetic

texture terms are simultaneously present. Instead, when only interband textures are considered, the presence of the O symmetry renders the effects of the crystalline symmetries trivial.

Before proceeding to the 2D cases, we here summarize what we learned from the 1D models, and how this will help us explore the 2D cases. First of all, we discussed that a system in the presence of a MHC with a spatially varying magnetic moment $|M_{||}| \neq |M_{\perp}|$ cannot be directly mapped onto the inversion symmetry breaking SOC mechanism in figs. 5.2(a)-(d), i.e. one cannot gauge away the spatial dependence of the MHC. Hence one needs to adopt either a sublattice description (see. app. 5.B), or perform a downfolding to the MBZ. The latter serves as a convenient basis for our calculations, and is adopted in the upcoming paragraphs. In this regard, the 1D cases additionally served as an introduction and motivation for our formalism in the more complicated 2D systems.

Concerning the topological classification, we established that one-band models and two-band models in the MHC phase generally reside in the BDI symmetry class, regardless of the type of spin-singlet pairing gap. However, by considering interband-only magnetic scattering, we found that the two-band models display an emergent unitary symmetry ultimately resulting in the class $AIII \oplus AIII$. This class supports Andreev zero modes, which however, can be converted back to MZMs by including intraband terms. Lastly, we also performed the topological classification in the presence of magnetic point and space group symmetries, introduced the relevant invariants, and discussed how these can lead to new topological phases. For 1D systems, the additional unitary symmetries proved to be obsolete when it comes to the prediction of edge modes, since edges generally break these. Nonetheless, their presence sets constraints on a number of bulk topological properties which can be harnessed to experimentally infer the topological superconductor phase of the system. In fact, the methodology employed in the study of unitary symmetries sets the stage and introduces the concepts for the upcoming 2D cases, where magnetic point group symmetries play instead an essential role in determining the type of Majorana or Andreev edge modes.

5.5 2D Topological Superconductors

We now extend our study to the case of 2D systems, which is the main topic on our agenda. We start with one-band models and afterwards consider two-band extensions. We find that 2D systems exhibit a rich variety of Majorana fermion-edge-mode types, i.e. flat, uni- and bi-directional modes when nodes are present in the bulk energy spectrum, or, quasi-helical, helical, and chiral modes when the bulk energy band structure is fully gapped. This Majorana fermion diversity is obtained by considering one-band models and two-band models in the presence of a MHC, a SWC_4 and, finally, a SWC_4 combined with an external in- and out-of-plane Zeeman field, where the latter situation also reproduces a SSC_4 phase.

One-Band Models

In this section we extend the one-band model dispersion ξ_{k_x} to its 2D analog $\xi_{\mathbf{k}}$, with a focus on models leading to two hole pockets centered at Γ and M . The two pockets are assumed to feature intra-pocket FS nesting at the mutually orthogonal wave vectors $\mathbf{Q}_{N,1}$ and $\mathbf{Q}_{N,2}$, thus generally supporting both single- \mathbf{Q} and double- \mathbf{Q} magnetic phases [77]. The magnetic vectors $\mathbf{Q}_{1,2}$ may coincide with the nesting wave vectors. Such a type of band structure is shown in fig. 5.9, and bears qualitative similarities to

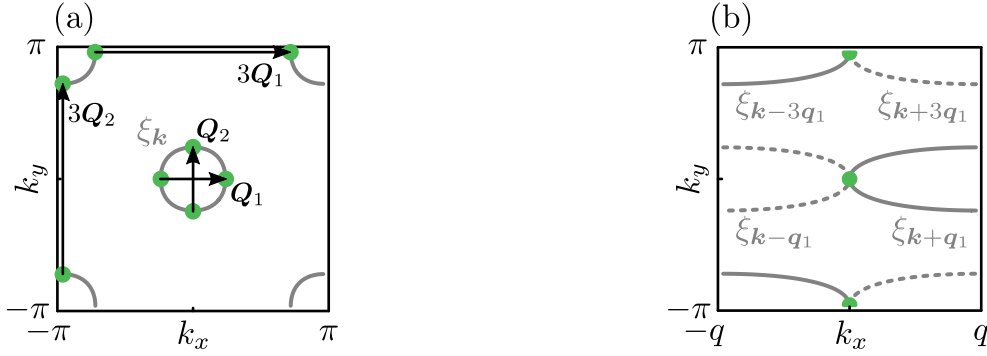


Figure 5.9: Example of a one-band model in 2D. (a) FSs in the BZ obtained for a dispersion $\xi_{\mathbf{k}} = -2t \cos k_x \cos k_y - \mu_0$ with $\mu_0 = -\sqrt{2}t < 0$. We show the magnetic ordering wave vectors $\mathbf{Q}_{1,2} = Q\{\hat{x}, \hat{y}\}$ and $3\mathbf{Q}_{1,2} \equiv -\mathbf{Q}_{1,2}$ connecting points of the FS. (b) depicts the resulting four FS segments after transferring to the MBZ for a MHC with the wave vector \mathbf{Q}_1 . Similar to fig. 5.4, also here there exist points at higher energy which are connected by $\mathbf{Q}_{1,2}$.

substantially hole doped FeSCs. In principle, for highly symmetric FSs other nesting vectors may play a substantial role in deciding the resulting magnetic phase. Nonetheless, for the explorative nature of this paper we simply restrict to the star $\pm\mathbf{Q}_{1,2}$.

MHC Texture - Majorana Flat Bands

The construction of the Hamiltonian in 2D is straightforward, and is obtained by replacing the 1D dispersion in eqn. (5.23) by its 2D analog. The MBZ is now defined as the set $\mathbf{k} \in (-q, q] \times (-\pi, \pi]$ and the inversion-symmetric points are $\mathbf{k}_I = \{(0, 0), (q, 0), (0, \pi), (q, \pi)\}$, where $\mathbf{q}_{1,2} = \mathbf{Q}_{1,2}/2$ and $q = |\mathbf{q}_{1,2}|$. Out of these four, $(q, 0)$ and (q, π) observe a Kramers degeneracy imposed by the antiunitary magnetic space group symmetry $\tilde{\Theta}_{\mathbf{k}} = \{T | (\pi/Q, 0)\}$.

The extension to 2D is complete after adding k_y as a second argument to $h_{\mathbf{k}}^{(s)}$ and $\Delta_{\mathbf{k}}^{(s)}$ defined in eqn. (5.24), which leads to $h_{\mathbf{k}}^{(s)}$ and $\Delta_{\mathbf{k}}^{(s)}$. Note, however, that this seemingly-trivial extension leads to a dichotomy in regards with the behavior of $\Delta_{\mathbf{k}}^{(s)}$ under mirror operations. Specifically, one can now distinguish two cases depending on whether $\Delta_{\mathbf{k}}$ transforms according to the $\{A_{1g}, B_{1g}\}$ or the $\{B_{2g}, A_{2g}\} \equiv B_{2g} \times \{A_{1g}, B_{1g}\}$ IRs of D_{4h} .⁶ Notably, pairing gaps transforming according to the former (latter) satisfy $\sigma_{xz, yz} \Delta_{\mathbf{k}} = \chi \Delta_{\mathbf{k}}$ with $\chi = +1$ (-1). While this difference does not diversify the BDI 2D symmetry classification for the two categories of pairing, it does lead to two distinct classifications in the HSPs depending on whether the magnetic and pairing point groups coincide or not. Below, we first focus on the 2D classification and study the influence of the magnetic point group at the end of this section.

In analogy to our previous analysis, we define the winding number for each k_y subsystem which, notably, for the BDI class in 2D defines a *weak*, instead of a strong, topological invariant [411, 412]. Under the condition that $\Delta_{\mathbf{k}}$ does not induce additional gap closings in the MBZ other than the ones

⁶For example: $\{A_{1g}, B_{1g}, B_{2g}\} \sim \{1, \cos k_x - \cos k_y, \sin k_x \sin k_y\}$.

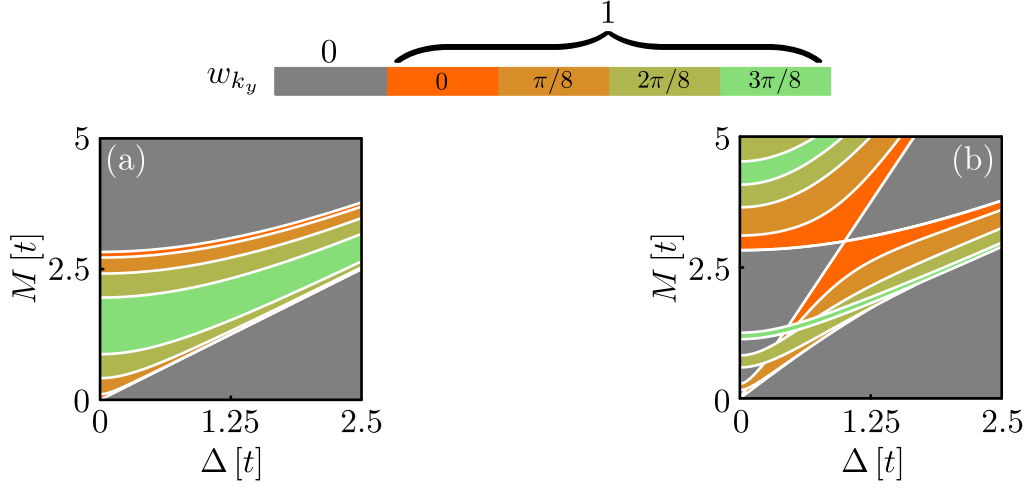


Figure 5.10: (a)-(b) Topological phase diagrams for the 2D one-band model in fig. 5.9, in the presence of a MHC texture with spatially-constant and -varying ($M_{\perp}/M_{\parallel} = 3$) moment, respectively. For a given $k_y = \{0, \pi/8, 2\pi/8, 3\pi/8\}$ value, we find one (no) MZMs per edge in the correspondingly-colored (gray) regions.

appearing for $\mathbf{k} = (0, k_y)$, we obtain

$$w_{k_y} = \sum_{k_c} \text{sgn} \left(\Delta_{\mathbf{k}; \mathbf{q}_1}^+ \frac{d\xi_{\mathbf{k}; \mathbf{q}_1}^-}{dk_x} - \xi_{\mathbf{k}; \mathbf{q}_1}^+ \frac{d\Delta_{\mathbf{k}; \mathbf{q}_1}^-}{dk_x} \right) \Big|_{k_x=k_c} \frac{\text{sgn} \left(M^2 - [\Delta_{(k_c, k_y); \mathbf{q}_1}^+]^2 - [\xi_{(k_c, k_y); \mathbf{q}_1}^+]^2 \right)}{2}, \quad (5.40)$$

where we considered $M_{\parallel, \perp} = M > 0$, exploited the property $\xi_{-k_x, k_y} = \xi_{k_x, k_y}$, and made use of the constraint on $\Delta_{\mathbf{k}}$. Evidently, the 1D criterion for a gap closing at a point k_c , for a given k_y , still holds, namely $M^2 = [\Delta_{(k_c, k_y); \mathbf{q}_1}^+]^2 + [\xi_{(k_c, k_y); \mathbf{q}_1}^+]^2$. Thus, gap closing points appear for $(k_x = 0, k_y)$ and suitable values of k_y .⁷

In fig. 5.10(a) we display topological phase diagrams for the model in fig. 5.9, for various k_y values which are depicted using a k_y -dependent color scale. In the weak-coupling limit, and for generally different $M_{\parallel, \perp}$, each k_y subsystem is dictated by the familiar criterion in eqn. (5.27)

$$M_- < \sqrt{(\xi_{\mathbf{k}_c; \mathbf{q}_1}^+)^2 + (\Delta_{\mathbf{k}_c; \mathbf{q}_1}^+)^2} < M_+. \quad (5.41)$$

However, in contrast to eqn. (5.27), here, not all gap-closing points \mathbf{k}_c are at the Fermi level, and this detuning introduces an effective chemical potential $\xi_{\mathbf{k}_c; \mathbf{q}_1}^+$ in the above criterion. As expected, for $k_y = 0$ we reproduce eqn. (5.27) after setting $\Delta_{\mathbf{k}} = \Delta$. Figure 5.10(b) presents the arising topological phase diagram for a system in the MHC phase with $|M_{\perp}| \neq |M_{\parallel}|$. Clearly, the phase diagram becomes significantly modified as k_y varies, and the various topologically nontrivial regions generally overlap.

⁷Note that the one-band model presented in fig. 5.9 features additional gap closings at $(k_x, \pm\pi/2)$. However, these solely stem from the next-nearest-neighbor character of the hopping term considered, and do not constitute universal properties. In fact, this band peculiarity can be removed by considering additional hopping matrix elements of a different range in the 2D version of eqn. (5.1).

Based on the criteria for a gap closing at the various k_y values, we infer that the nodes in the bulk spectrum move along the $k_x = 0$ line in the MBZ when varying the superconducting and magnetic gaps. This resembles a gapless-gapful transition in topological insulators which leads to a Weyl semimetallic phase [413]. In fact, such transitions have also been studied previously in: (i) $p \pm ip$ topological superconductors, where an in-plane magnetic field drives the transition [396], (ii) in nodal d -wave SCs [397], and (iii) in nodal superconducting phases of FeSCs [414, 415].

In fig. 5.11(a) we sketch the path followed by the nodes in the MBZ when varying the superconducting and magnetic gaps. Given the structure of the weak topological invariant w_{k_y} , we expect to find topologically-protected Majorana fermion modes at the edges parallel to the y direction, but no modes at the edges perpendicular to it. This is indeed verified in figs. 5.11(c) and 5.11(d), where we plot the spectrum with open boundary conditions along the x and y direction, respectively. Here, only the former edge spectrum displays topologically-protected Majorana fermion modes. This behavior is reminiscent of graphene and the appearance of flat bands only when the termination is of the zig-zag type [416]. We observe that nodes related to each other by the discrete symmetries Θ and Ξ , are connected by Majorana flat bands, in agreement with the values of w_{k_y} shown in fig. 5.11(b). In the direct-lattice representation, these Majorana flat bands manifest as standing Majorana fermion waves only at edges parallel to the y direction, i.e. they possess wave functions with a spatial part proportional to $\sin(n\pi R_y/\mathcal{N}_y)$ where $n \in \mathbb{N}^+$ and \mathcal{N}_y being the number of lattice sites in the y direction, cf. ref. [141].

So far, we studied the emergence of the Majorana flat bands by viewing k_y as a mere parameter which controls the topological properties of each 1D k_y subsystem. However, accounting for the correspondence of k_y to the spatial coordinate y , and considering the stable character of the nodes in the bulk energy spectrum, allows us to characterize the 2D nodal topological superconductor using *local* strong topological invariants [30, 154, 417, 418]. In fact, the BDI symmetry class ensures that the Majorana flat bands enjoy a topological protection, which is inherited from the respective robustness of the bulk nodes in the energy spectrum. Each node at \mathbf{k}_c possesses a \mathbb{Z} topological charge, i.e. its vorticity

$$v = \frac{1}{2\pi i} \oint_{\mathcal{C}} \frac{dz_{\mathbf{k}}}{z_{\mathbf{k}}}, \quad (5.42)$$

where \mathcal{C} is a contour encircling the node. Here, $z_{\mathbf{k}}$ corresponds to the 2D extension of eqn. (5.8). For the present model, linearizing the Hamiltonian about a node yields $v = \text{sgn}(\alpha\beta\Delta\xi_{\mathbf{k}_c; \mathbf{q}_1}^+)$, where we set $\Delta_{\mathbf{k}} = \Delta$, and expanded the shifted dispersions about \mathbf{k}_c as follows: $\xi_{\mathbf{k}; \mathbf{q}_1}^+ \approx \xi_{\mathbf{k}_c; \mathbf{q}_1}^+ + \alpha k_y$ and $\xi_{\mathbf{k}; \mathbf{q}_1}^- \approx \beta k_x$. The above result reveals that the vorticity is ill-defined at the inversion-symmetric points $(0, 0)$ and $(0, \pi)$ since, there, $\alpha = 0$.⁸

Let us now proceed and consider a superconducting order parameter which *does* generate new nodal points. In order to determine the location of these new nodes, we employ the 2D analog of eqn. (5.29), which describes the low-energy features about the Γ point in the MBZ. Alternatively, we can perform the shift $\mathbf{k} \rightarrow \mathbf{k} + 4\mathbf{q}_1$ to obtain a description about Y. By repeating the steps detailed in sec. 5.4, the gap closing points \mathbf{k}_c are given by $\text{Im}[\det A_{\mathbf{k}_c, \sigma}^{\text{low-en}}] = 0$ which yields the equation

$$\xi_{\mathbf{k}_c - \mathbf{q}_1} \Delta_{\mathbf{k}_c + \mathbf{q}_1} = \xi_{\mathbf{k}_c + \mathbf{q}_1} \Delta_{\mathbf{k}_c - \mathbf{q}_1}. \quad (5.43)$$

⁸For the model in fig. 5.9, v is also ill-defined for $k_y = \pm\pi/2$, since at these points $\xi_{\mathbf{k}_c; \mathbf{q}_1}^+ = 0$ which, however, is only an artifact of the next-nearest-neighbor nature of the hopping considered.

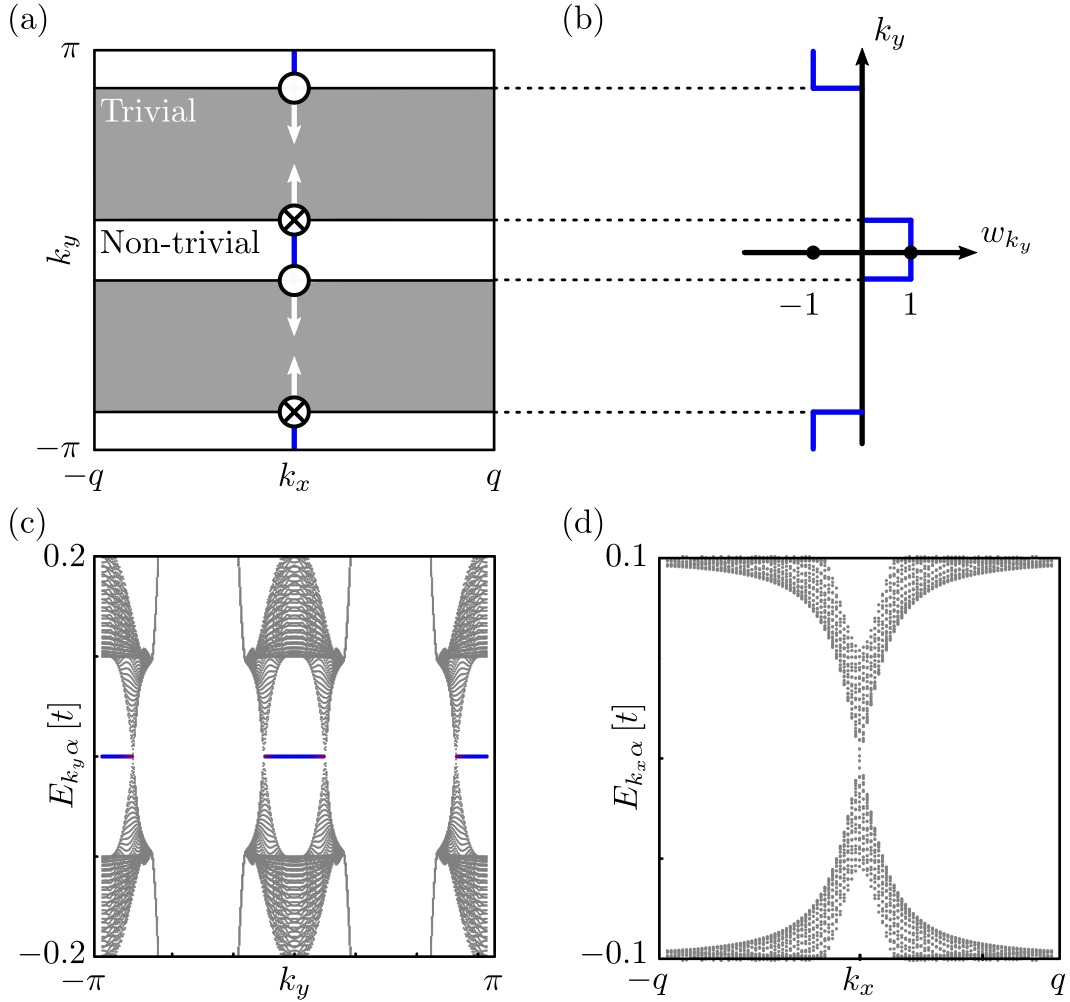


Figure 5.11: Properties of the topologically-stable nodes obtained in the gapless bulk energy spectrum of the one-band model in fig. 5.9 in the presence of the MHC texture. Here, nodes with vorticity $v = +1$ ($v = -1$) are discerned by a dot (cross). (a) Sketch of the path followed by the nodes when varying the superconducting and/or magnetic gaps. Nodes of opposite vorticities are connected by Majorana flat bands, in agreement with the winding number values in (b). (c) and (d) Numerically-obtained dispersions with open boundary conditions along the x and y direction, respectively. Parameter values used: $\Delta = 0.1t$, $M_{\perp} = M_{\parallel} = 0.2t$, and $\mathcal{N}_{x,y} = 401$ sites in the x, y direction.

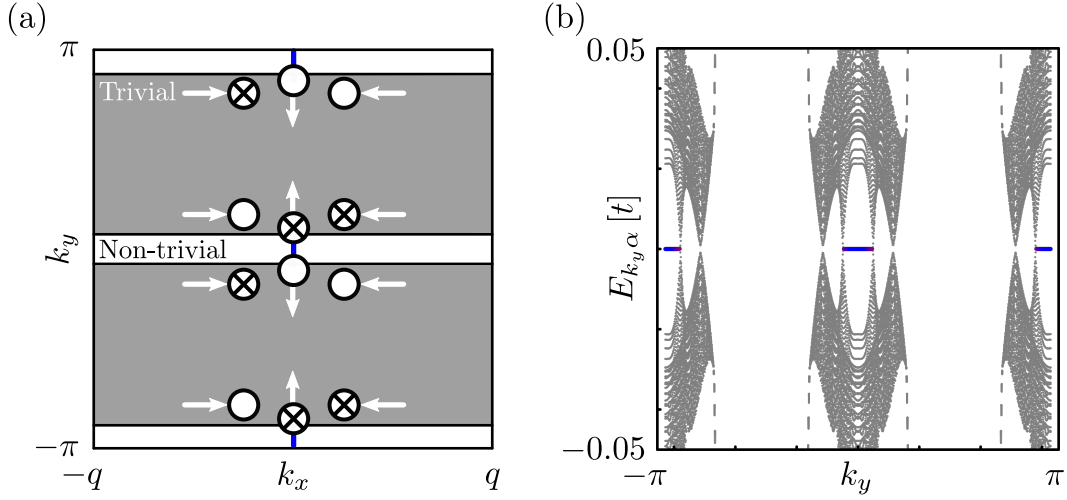


Figure 5.12: Modification of the nodal spectrum in fig. 5.11 due to the unconventional pairing function $\Delta_{\mathbf{k}} = \Delta(\cos k_x - \cos k_y)$. (a) The unconventional gap function induces 8 additional nodes in the bulk spectrum. In (b) we present the energy spectrum for open boundary conditions along the x direction and $\mathcal{N}_x = \mathcal{N}_y = 1001$. We do not find any new Majorana fermion bands since, for the given orientation of the termination edges, the contributions of the 8 additional nodes cancel out. Parameter values used: $\Delta = 0.1 t$ and $M_{\perp} = M_{\parallel} = 0.05 t$.

As an example, we consider the one-band model of fig. 5.9 and the d -wave gap function $\Delta_{\mathbf{k}} = \Delta(\cos k_x - \cos k_y)$. We find the gap-closing points $\mathbf{k}_c : \{k_x = 0 \text{ or } \cos(2k_y) = -1 - \mu_0/t\}$. For the given values of q and μ_0 , the additional nodes move on the lines $k_y \simeq \pm 0.18\pi, \pm 1.18\pi$. The complete information regarding the location of the above gap-closing points in the MBZ is found by further employing the remaining gap-closing condition $\text{Re}[\det A_{\mathbf{k}_c}^{\text{low-en}}] = 0$, which is equivalent to the criterion in eqn. (5.41). Analyzing the above yields nodes moving along different lines in the MBZ, as shown in fig. 5.12(a). Contrasting this to fig. 5.11, we clearly see the introduction of eight new nodes in addition to the four nodes for $k_x = 0$. Here, however, we do not find any additional Majorana fermion modes compared to fig. 5.11(c) when we consider open boundary conditions along the main x, y axes, as is evident in fig. 5.12(b) for open boundary conditions in the x direction. This is because, the contributions of the additional nodes cancel out by virtue of mirror symmetries when projected onto the edge where translational invariance persists. However, if the system were to be terminated along the, e.g., (11) surface, that would indeed allow for the presence of new Majorana fermion modes, cf. ref. [415].

We now consider the additional presence of the magnetic point/space group symmetries and the modifications that these bring to the topological classification. A common feature of the crystalline classifications in 1D and 2D for the MHC, is that the effects of R_{xz} are trivial in both. On the other hand, we find crucial differences which mainly relate to (i) the enhancement of the dimensionality which generally leads to different topological invariants even within the same symmetry class, and (ii) the structure of the pairing gap. Specifically, we find two distinct cases depending on whether $\chi = \pm 1$ for a given unitary operator $\Delta_{U^{-1}\mathbf{k}} = \chi\Delta_{\mathbf{k}}$. When $\Delta_{\mathbf{k}} \sim \{A_{1g}, B_{1g}\}$ ($\Delta_{\mathbf{k}} \sim \{B_{2g}, A_{2g}\}$), we

find $\chi = +1$ ($\chi = -1$). Notably, the pair of D_{4h} IRs bunched together in a given set are equivalent under the action of the magnetic point group.

Another key aspect of the crystalline classification in 2D, is that the Kramers degeneracy imposed by $\tilde{\Theta}_{\mathbf{k}}$ at $(q, 0)$ and (q, π) , extends to the entire $k_x = q$ HSP. As discussed in app. 5.C this is imposed by the pair of offcentered symmetries O_{yz} and $\{\sigma_{yz} | (\pi/Q, 0)\}$. Hence, MHC-driven gap closings cannot take place anywhere in the $k_x = q$ HSP. Therefore, any possible crystalline topological features arising in this HSP originate from the structure of the pairing gap. For this reason, the remainder of this section focuses only on the $k_x = 0$ HSP. The classification in the $k_x = q$ HSP appears in table 5.2 and the topological invariants connect to the analysis below.

For $\Delta_{\mathbf{k}} \sim \{A_{1g}, B_{1g}\}$ ($\chi = 1$), R_{yz} and $\{\sigma_{yz} | (\pi/Q, 0)\}$ lead to a $AI \oplus AI$ class in the $k_x = 0$ HSP. While a similar result was also encountered in sec. 5.4, here the topological consequences stemming from these symmetries differ because of the increased spatial dimensionality. Specifically, new topological features emerge only when the spectrum contains point nodes. In this case, the class AI allows defining an additional \mathbb{Z} crystalline topological invariant, which we denote ν_{k_I} , and associate with the following vorticity in (ϵ, k_y) space

$$\nu_{k_x=0} = \frac{1}{4\pi i} \sum_{\sigma=\pm 1} \sigma \oint_{\mathcal{C}} \frac{dZ_{\epsilon, k_y, \sigma}}{Z_{\epsilon, k_y, \sigma}}, \quad (5.44)$$

with \mathcal{C} a path enclosing the node, and $\sigma = \pm 1$ labeling the respective AI block. $Z_{\epsilon, k_y, \sigma}$ is obtained in a similar fashion to eqn. (5.17). We remark that for the nodes shown in fig. 5.11, we find $|\nu_{k_x=0}| = |v| = 1$.

The remaining two space group symmetries, i.e. $\{\sigma_{xz} | (\pi/Q, 0)\}$ and $\{T | (\pi/Q, 0)\}$, need to be treated more carefully, since the former only leaves inversion-symmetric points invariant, and thus does not introduce any changes to the topological classification in HSPs. The latter symmetry instead, combined with Θ , leads to a class $BDI \oplus BDI$ in the $k_x = 0$ HSP. Hence, it only influences the topological properties of the system for a fully-gapped spectrum, since the BDI class cannot protect nodes in 1D [30]. Therefore, in the case of a full gap, we define the glide winding number

$$w_{G, k_x=0} = \sum_{\sigma=\pm 1} \sigma w_{k_x=0, \sigma} \equiv \frac{1}{4\pi i} \sum_{\sigma=\pm 1} \sigma \int_{\text{BZ}} \frac{dz_{k_y, \sigma}}{z_{k_y, \sigma}}, \quad (5.45)$$

with $w_{k_x=0, \sigma}$ corresponding to the winding number of each BDI class Hamiltonian block of eqn. (5.31), after the suitable k_y dependence is accounted for, and the respective normalized complex function $z_{k_y, \sigma} = \det(A_{k_x=0, k_y, \sigma}) / |\det(A_{k_x=0, k_y, \sigma})|$ is constructed.

In contrast, when $\Delta_{\mathbf{k}}$ transforms according to the IRs $\{B_{2g}, A_{2g}\}$, we find deviations from the above behaviors. Notably, the magnetic and pairing point groups differ, since M_{MHC} acts on $\Delta_{\mathbf{k}} \sim \{B_{2g}, A_{2g}\}$ as

$$\{E, C_2, \sigma_{xz}T, \sigma_{yz}T\} \Delta_{\mathbf{k}} = \{1, 1, -1, -1\} \Delta_{\mathbf{k}}. \quad (5.46)$$

Nevertheless, the sign-changing behavior of $\Delta_{\mathbf{k}}$ under mirror operations still allows us to define a point group G_{MHC} , which is preserved by the total Hamiltonian and is isomorphic to M_{MHC} . This group consists of the elements

$$G_{\text{MHC}} = \{E, C_2, \sigma_{xz}^Q T, \sigma_{yz}^Q T\}, \quad (5.47)$$

with $\sigma_{xz,yz}^{\mathcal{Q}} = \mathcal{Q}\sigma_{xz,yz}$, where we introduced the dimensionless electric charge operator $\mathcal{Q} = \tau_3$. Such symmetries have also been previously discussed in connection to p -wave superconductors [319, 419]. There, these ensure that the energy spectrum is inversion symmetric, despite the fact that inversion itself is not preserved. Similarly here, G_{MHC} ensures that the energy spectrum is invariant under the original M_{MHC} magnetic point group. Note also that the space group symmetries $\{\sigma_{xz,yz} | (\pi/Q, 0)\}$, are correspondingly replaced by $\{\sigma_{xz,yz}^{\mathcal{Q}} | (\pi/Q, 0)\}$.

To infer the arising topological modifications, we block diagonalize the 2D extension of eqn. (5.23) according to the symmetry of interest. We immediately observe that the effects of $\{T | (\pi/Q, 0)\}$ and $\{\sigma_{xz}^{\mathcal{Q}} | (\pi/Q, 0)\}$ in HSPs remain the same, with the latter only affecting inversion-symmetric points once again. The presence of $R_{xz}^{\mathcal{Q}}$ establishes the class $\text{AI} \oplus \text{AI}$ in the $k_y = \{0, \pi\}$ HSPs, where however the pairing gap is zero. In these HSPs $R_{xz}^{\mathcal{Q}}$ can only protect nodes, with a \mathbb{Z} invariant given by eqn. (5.44) after interchanging k_x and k_y , and considering $k_y = \{0, \pi\}$. The remaining two symmetries, i.e. $\{\sigma_{yz}^{\mathcal{Q}} | (\pi/Q, 0)\}$ and $R_{yz}^{\mathcal{Q}}$ lead to a $\text{BDI} \oplus \text{BDI}$ class in the $k_x = \{0, q\}$ HSPs. When the spectrum is fully-gapped in these HSPs, one finds the glide $w_{G,\text{HSP}}$ and mirror $w_{M,\text{HSP}}$ winding numbers. These are correspondingly defined by, and in analogy to, eqn. (5.45). For details and concrete examples of the topological properties and the arising spectrum for a system with $\Delta_{\mathbf{k}} \sim \{\text{B}_{2g}, \text{A}_{2g}\}$, see app. 5.D.

Closing this section, we point out that one can also introduce the BDI class weak \mathbb{Z} invariants for k_x points with a fully-gapped spectrum. These are given by the winding numbers w_{k_x} , which are defined in an analogous manner to w_{k_y} in eqn. (5.40). The w_{k_x} invariants are expected to be particularly relevant when $\Delta_{\mathbf{k}} \sim \{\text{B}_{2g}, \text{A}_{2g}\}$. This is because, for a fixed k_x , the resulting pairing gap becomes effectively of the p_y -wave type, cf. app. 5.D.

SWC₄ Phase - Majorana Bidirectional Edge Modes

In this section, we consider the case of a double- \mathcal{Q} magnetic texture, with the ordering wave vectors depicted in fig. 5.13(a). Here, we focus on the SWC₄ profile which couples to the electrons through the exchange term

$$H_{\text{mag}} = \sum_n \mathbf{c}_n^\dagger [M_\perp \cos(\mathbf{Q}_1 \cdot \mathbf{R}_n) \sigma_z + M_\parallel \sin(\mathbf{Q}_1 \cdot \mathbf{R}_n) \sigma_x + M_\perp \cos(\mathbf{Q}_2 \cdot \mathbf{R}_n) \sigma_z + M_\parallel \sin(\mathbf{Q}_2 \cdot \mathbf{R}_n) \sigma_y] \mathbf{c}_n. \quad (5.48)$$

The double- \mathcal{Q} structure of the magnetic texture implies that the MBZ is obtained by folding in both k_x and k_y directions of the original BZ, and is defined as $\mathbf{k} \in (-q, q] \times (-q, q]$. The inversion-symmetric points span the set $\mathbf{k}_I = \{\Gamma, X, Y, M\}$. To proceed, we employ the wave-vector-transfer Pauli matrices $\boldsymbol{\eta}$ and $\boldsymbol{\rho}$ related to foldings in the k_x direction, as in sec. 5.4, and the Pauli matrices $\lambda_{1,2,3}$ and $\zeta_{1,2,3}$ related to foldings in the k_y direction, acting in $\{\mathbf{k}, \mathbf{k} + \mathbf{Q}_2\}$ and $\{\mathbf{k}, \mathbf{k} + 2\mathbf{Q}_2\}$ spaces, respectively. The resulting enlarged spinor reads

$$\mathbf{c}_{\mathbf{k};2\text{D}}^\dagger = \mathbb{1}_\zeta \frac{\lambda_2 + \lambda_3}{\sqrt{2}} \left(\mathbf{c}_{\mathbf{k}-\mathbf{q}_2}^\dagger, \mathbf{c}_{\mathbf{k}+\mathbf{q}_2}^\dagger, \mathbf{c}_{\mathbf{k}+3\mathbf{q}_2}^\dagger, \mathbf{c}_{\mathbf{k}-3\mathbf{q}_2}^\dagger \right) \quad (5.49)$$

where $\mathbf{c}_{\mathbf{k}}^\dagger$ is the 2D analog of eqn. (5.22). This yields the following class D ($\Xi = \tau_2 \sigma_y K$) bulk 2D Hamiltonian

$$\begin{aligned} \mathcal{H}_{\mathbf{k}} = & F(h_{\mathbf{k}}) \tau_3 + F(\Delta_{\mathbf{k}}) \tau_1 - (M_\perp \rho_1 \sigma_z + M_\parallel \rho_3 \sigma_x) / 2 - (M_\perp \eta_1 \rho_1 \sigma_z - M_\parallel \eta_1 \rho_3 \sigma_x) / 2 \\ & - (M_\perp \lambda_1 \sigma_z + M_\parallel \lambda_3 \sigma_y) / 2 - (M_\perp \zeta_1 \lambda_1 \sigma_z - M_\parallel \zeta_1 \lambda_3 \sigma_y) / 2, \end{aligned} \quad (5.50)$$

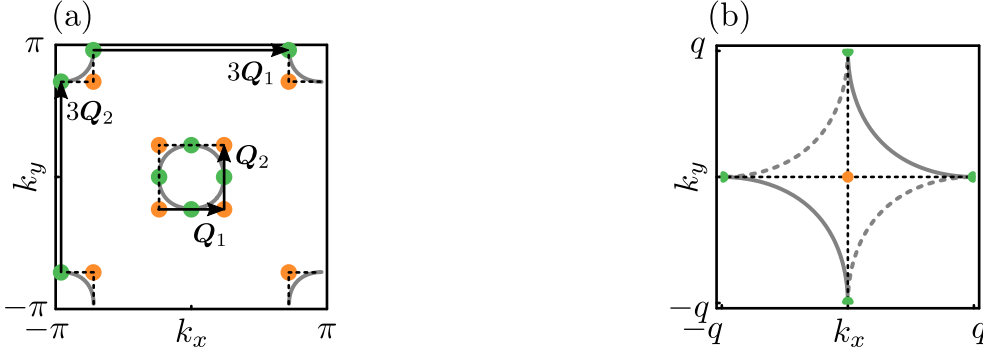


Figure 5.13: 2D one-band model of fig. 5.9 with a double- \mathbf{Q} magnetic texture. (a) FSs of the one-band model in the 1st BZ. We show the magnetic ordering wave vectors \mathbf{Q}_1 ($3\mathbf{Q}_1 \equiv -\mathbf{Q}_1$) and \mathbf{Q}_2 ($3\mathbf{Q}_2 \equiv -\mathbf{Q}_2$), connecting points at the Fermi level (green dots). As in the 1D case, cf. fig. 5.4, points at higher energies are also connected by $\mathbf{Q}_{1,2}$, which upon increasing the magnetic energy scale give rise to nodes whose locations trace the dotted black lines. (b) Resulting FS segments in the MBZ, where the points simultaneously experiencing magnetic scattering by both \mathbf{Q}_1 and \mathbf{Q}_2 (orange dots) are now centered at the Γ point.

where $F(h_{\mathbf{k}})$ and $F(\Delta_{\mathbf{k}})$ are defined in app. 5.E.

The band dispersions and the magnetic part of the BdG Hamiltonian of eqn. (5.50) are invariant under the magnetic point group $M_{\text{SWC}_4} = C_4 + (C_{4v} - C_4)T$, as well as the magnetic space group operations: $\{T, C_{4v} - C_4 | (\pi/q, \pi/q)\}$. See also table 5.1. Out of these five space group symmetries, the antiunitary $\tilde{\Theta}_{\mathbf{k}} = \{T | (\pi/q, \pi/q)\} = ie^{i\pi(k_x+k_y)/Q} \lambda_2 \rho_2 \sigma_y \mathcal{K}$ defines a time-reversal symmetry with $\tilde{\Theta}_{\mathbf{k}}^2 = -e^{i\pi(k_x+k_y)/q} \mathbb{1}$, and yields a Kramers degeneracy at $\mathbf{k}_{\tilde{\Theta}_{\mathbf{k}}} = \{\Gamma(0,0), M(q,q)\}$. The remaining space group symmetries do not lead to any additional symmetry-protected degeneracies in the spectrum. See app. 5.C for further clarifications.

Similar to the previous section, also here, the point group G_{SWC_4} preserved by the BdG Hamiltonian is decided by which *one* out of the possible four IRs $\{A_{1g}, B_{1g}, B_{2g}, A_{2g}\}$, is stabilized for $\Delta_{\mathbf{k}}$. In a one-to-one correspondence to these four IRs, we find the scenarios

$$\begin{aligned} G_{\text{SWC}_4}^{A_{1g}} &= \{E, C_2, 2C_4, 2\sigma_v \mathcal{T}, 2\sigma_d \mathcal{T}\}, & G_{\text{SWC}_4}^{B_{1g}} &= \{E, C_2, 2C_4^Q, 2\sigma_v \mathcal{T}, 2\sigma_d^Q \mathcal{T}\}, \\ G_{\text{SWC}_4}^{B_{2g}} &= \{E, C_2, 2C_4^Q, 2\sigma_v^Q \mathcal{T}, 2\sigma_d \mathcal{T}\}, & G_{\text{SWC}_4}^{A_{2g}} &= \{E, C_2, 2C_4, 2\sigma_v^Q \mathcal{T}, 2\sigma_d^Q \mathcal{T}\}. \end{aligned} \quad (5.51)$$

In a similar fashion, depending on the IR of $\Delta_{\mathbf{k}}$, we obtain four space group symmetries generated by products of $\{\mathbb{1} | (\pi/q, \pi/q)\}$ and the mirror operations preserved by $\Delta_{\mathbf{k}}$. Note that the topological class remains D, irrespectively of the given point group G_{SWC_4} . As it is customary in this work, the effects of the point and space groups are presented at the end of the section.

For the one-band model in fig. 5.13, we find two pairs of nodes upon modifying the various parameters, as sketched in fig. 5.14(a). These pairs move along mutually-orthogonal HSPs in the MBZ as indicated by the white arrows in the figure. Specifically, as the magnetic gap increases, the nodes first emerge at the X and Y points, and then move towards the Γ point of the MBZ.

Similar nodes emerged for a MHC texture in 2D, cf. fig. 5.11. Hence, we expect that in this nodal regime, the topological properties stemming from a SWC_4 texture are describable by superimposing

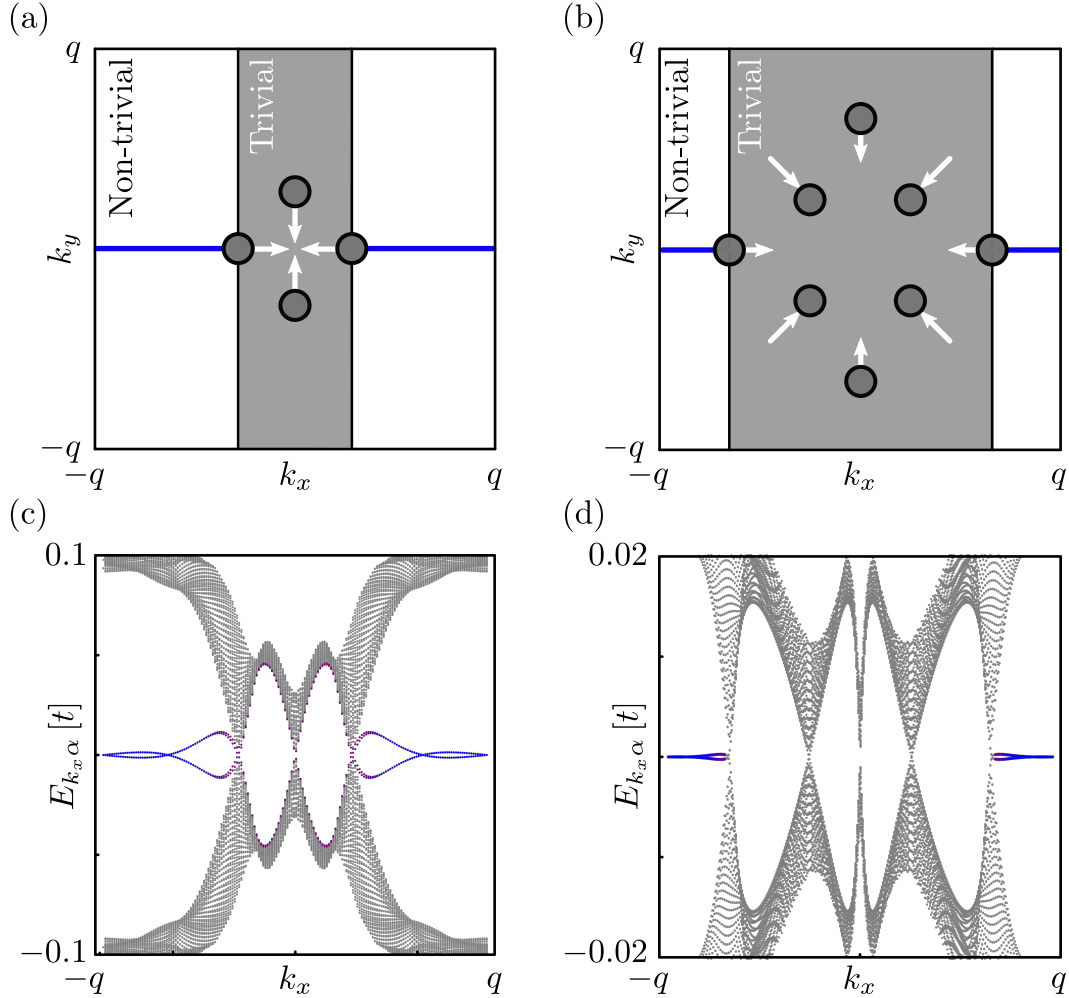


Figure 5.14: (a) and (b) depict the paths swept by the pairs of nodes emerging in the bulk energy spectrum for the one-band model in fig. 5.9 in the SWC_4 phase. In contrast to sec. 5.5, the nodes here are not topologically protected as reflected by the grey shading of the dots. (c) and (d) show the related dispersions for open boundary conditions in the y direction. (a) and (c) were obtained with $\Delta_{\mathbf{k}} = \Delta$ while for (b) and (d) we used the unconventional pairing gap $\Delta_{\mathbf{k}} = \Delta(\cos k_x - \cos k_y)$. For the latter we have four additional nodes in the spectrum compared to case (a). Note also that the resulting Majorana fermion modes in (d) are also lifted from zero energy away from inversion-symmetric points, but with a much flatter dispersion compared to the surface bands in (c). All the figures were obtained for $\Delta = 0.1 t$ and $\mathcal{N}_x = \mathcal{N}_y = 701$, while in (c) and (d) we used $M_{\perp} = M_{\parallel} = 0.2 t$ and $M_{\perp} = M_{\parallel} = 0.05 t$, respectively.

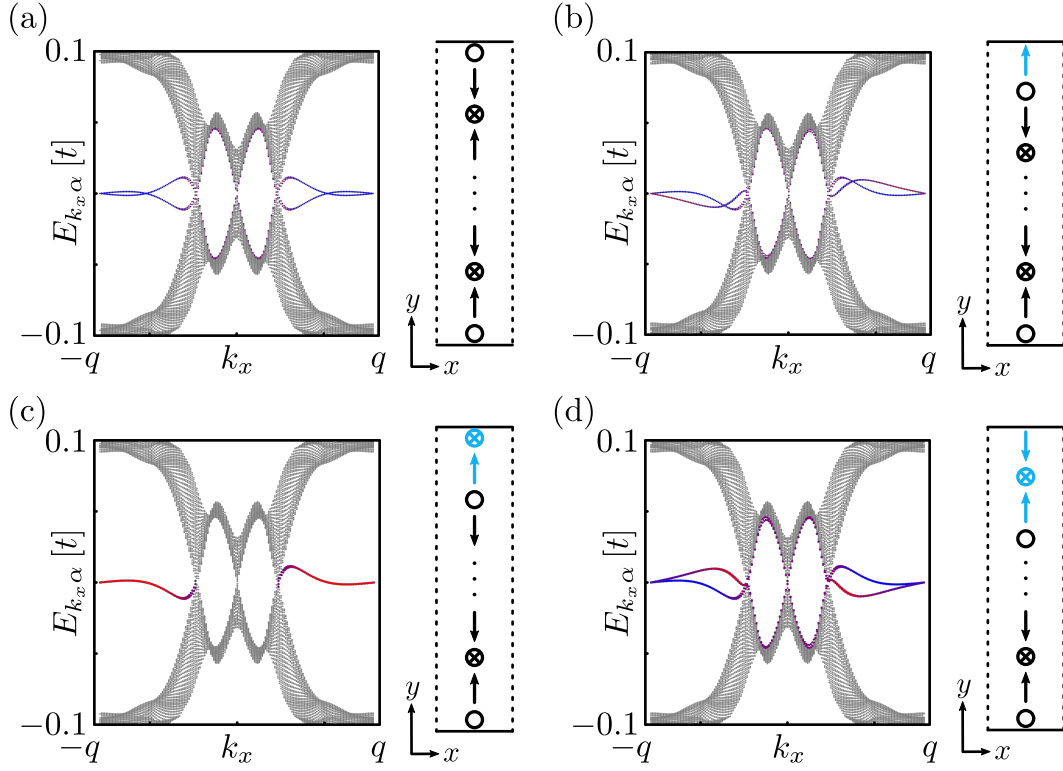


Figure 5.15: Influence of crystal termination on the dispersion of the bidirectional Majorana fermion edge modes in the one-band model in the SWC_4 phase. All spectra were obtained with open boundary conditions along the y direction. The insets show the termination of the magnetic texture for: (a) $\mathcal{N}_y = 701$, (b) $\mathcal{N}_y = 702$, (c) $\mathcal{N}_y = 703$ and (d) $\mathcal{N}_y = 704$. We see that only the termination in (a) leads to a symmetric spectrum, since in (b)-(d) a net magnetization is accumulated at one edge (see cyan colored spin symbols). We used the parameter values $\Delta = 0.1t$ and $M_{\perp} = M_{\parallel} = 0.2t$. The red/blue color coding is defined as in table 5.2.

the results originating from two MHC textures which wind in perpendicular spatial directions and different spin planes. In this sense, the underlying topological mechanism is essentially 1D and, as long as these nodes are present, we do not expect to obtain any genuine 2D topological superconducting phases. The latter become accessible only after the nodes meet at the Γ point and annihilate. However, the Kramers degeneracy enforced by $\tilde{\Theta}_{\mathbf{k}}$ prohibits that, thus imposing that *only nodal* topological superconductor phases become stabilized by a SWC_4 texture in such one-band models. Nonetheless, as we show in the next section, the consideration of additional perturbations which violate $\tilde{\Theta}_{\mathbf{k}}$ unlock the possibility of gapped 2D topological superconducting phases.

We anticipate that the gapping of these nodes becomes possible by considering suitable perturbations of even infinitesimally-weak strength. This is because class D does not protect nodes in 2D [30]. In fact, one would expect that the nodes could be protected by some crystalline symmetry, but as we find, this is also not the case. Let us further elaborate on this, through examining the impact of the crystalline symmetries on the topological classification. Each one of the $(C_{4v} - C_4)T$ symmetries acts as an effective time-reversal symmetry in the HSPs that they leave invariant. Each time-reversal symmetry operator in the HSPs squares to $+1$, thus establishing the BDI symmetry class in these high-symmetry lines. However, neither the BDI class is capable of providing protection to nodes appearing in these HSPs. Lastly, as explained in app. 5.C and ref. [32], nonsymmorphic symmetries in 2D systems can only affect the classification at inversion-symmetric points, and not in HSPs.

The absence of a topological protection for the nodes is reflected in the lack of Majorana flat bands in the energy spectrum obtained when open boundary conditions are imposed in one of the two main axes. Related numerical results for $\Delta_{\mathbf{k}} \sim \{1, \cos k_x - \cos k_y\}$ are discussed in fig. 5.14, where we assume open boundary conditions in the y direction⁹. Remarkably, instead of Majorana flat bands we find Majorana fermion edge modes with the distinctive feature that they do not have a fixed helicity or chirality. Even more remarkably, their spin-character and group velocity are k_x dependent and become strongly affected by the type of crystal termination. See ref. [32] for related findings, and fig. 5.15 where we display the edge spectrum in fig. 5.14 for various edge terminations. Clearly we see that the local spin content on a given edge modifies the Majorana fermion dispersion on that same edge. On these grounds, we here term this type of less familiar Majorana fermion edge modes as *bidirectional*.

The properties of the bidirectional Majorana fermion edge modes can be understood by viewing their presence as the outcome of the two coexisting MHCs. The MHC which winds spatially in the y direction gives rise to Majorana flat bands in the conserved k_x space, as long as the other MHC is completely neglected. In this ideal situation one obtains a spectrum similar to the one of fig. 5.11(c) after folding down to the MBZ. From this point of view, the secondary MHC mediates a BDI \rightarrow D symmetry-class transition for the 1D edge and, thus, lifts the protection of the Majorana flat bands. However, the presence of bidirectional Majorana fermion edge modes is ensured by topologically-protected degeneracies at inversion-symmetric points.

The emerging 1D physics implies that there should be suitable topological invariants that encode the presence of a persistent degeneracy at $k_x = q$, thus enforcing the presence of the bidirectional Majorana fermion edge modes. These are no other than the \mathbb{Z}_2 weak invariants of class D, which

⁹The particular choice of energy dispersion and pairing order parameter $\Delta_{\mathbf{k}}$, leads to an additional unitary symmetry and renders the spectra twofold degenerate. A weak violation of this symmetry gets the degeneracy lifted away from inversion-symmetric points, but preserves the number of Majorana fermion edge modes.

correspond to the Majorana numbers $\mathcal{M}_{k_x, y=q}$ [13, 31]

$$\mathfrak{M}_{k_x=q(k_y=q)} = \text{sgn} \prod_s^{\text{X, M (Y, M)}} \text{pf}(B_{\mathbf{k}_s}), \quad (5.52)$$

where $\text{pf}(B_{\mathbf{k}_s})$ is the pfaffian of the skew-symmetric matrix $B_{\mathbf{k}_I} = U_{\Xi} \mathcal{H}_{\mathbf{k}_I}$, where $\Xi = U_{\Xi} K$, with $U_{\Xi} = \tau_2 \sigma_y$. The presence of a C_4 -symmetric energy spectrum further renders the two invariants equal. Within the weak-coupling limit, these are nontrivial for $M_- < |\Delta_{\mathbf{k}=\mathbf{0}; \mathbf{q}_{1,2}}^+| < M_+$, which is satisfied only after a simultaneous gap closing takes place at X and Y. This mechanism stabilizes the degeneracies at the edge inversion-symmetric points.

Alternatively, as a consequence of the antiunitary magnetic point group elements $(C_{4v} - C_4)T$, each HSP resides in the 1D BDI class, for which, one can calculate the ensuing mirror winding number in 1D, $\tilde{w}_{M, \text{HSP}}$, similar to the weak invariant $w_{k_x, y}$ for the MHC models in 2D. $\tilde{w}_{M, \text{HSP}}$ is a crystalline topological invariant which is distinct from previously discussed mirror invariants in this paper, in the sense that the symmetries $(C_{4v} - C_4)T$ do not induce any block diagonal structure of the Hamiltonian in their respective HSPs, but rather an emergent time-reversal symmetry. Note lastly that the invariants for the $k_x, y = q$ HSPs fulfill the relation $\mathfrak{M}_{k_x, y=q} = (-1)^{\tilde{w}_{M, \text{HSP}}}$.

SWC₄ Texture - Genuine 2D Topological Superconductors

As we pointed out in the previous section, the Kramers degeneracy that the $\tilde{\Theta}_{\mathbf{k}}$ symmetry imposes at the Γ point of the MBZ, does not allow the nodes moving along the ΓX and ΓY lines to annihilate, therefore prohibiting the emergence of a fully-gapped bulk energy spectrum and genuinely 2D topological superconducting phases. Nonetheless, a fully-gapped bulk energy spectrum is obtainable in the presence of additional Hamiltonian terms which achieve at least one of the following two possibilities: (i) either preserve $\tilde{\Theta}_{\mathbf{k}}$ but enforce the nodes to meet and annihilate away from the Kramers degenerate points of the MBZ, i.e. away from $\mathbf{k}_{\Theta} = \{\Gamma, M\}$, or (ii) violate $\tilde{\Theta}_{\mathbf{k}}$.

In fig. 5.16, we present a situation in which the former scenario takes place. In this case, the addition of a term proportional to $\sin k_x \sin k_y$ to the dispersion preserves $\tilde{\Theta}_{\mathbf{k}}$ but violates C_4 symmetry. As a result, the nodes intersect away from Γ and annihilate, therefore allowing for a chiral topological superconductor. The second possibility is examined in the following section and is implemented by considering the presence of a constant Zeeman field \mathbf{B} , which is added to the Hamiltonian via the term $\mathbf{B} \cdot \boldsymbol{\sigma}$.

Depending on the orientation of the Zeeman field, the magnetic point/space group symmetries can be fully or partially violated, thus, also affecting the type of the accessible dispersive Majorana fermion edge modes. Specifically, we find that an inplane Zeeman field leads to unidirectional (bidirectional) Majorana fermion edge modes when its direction is parallel (orthogonal) to the translationally-invariant termination edge. In contrast, an out-of-plane field preserves the bidirectional character of the edge modes. We insist that such edge modes and inversion-symmetric point degeneracies are still accessible even when the crystalline symmetries are all broken, since these are protected by the weak invariants defined in eqn. (5.52), which still remain valid.

Apart from the abovementioned topological superconducting phases which have an underlying 1D character, the application of an out-of-plane field converts the SWC₄ phase into a SSC₄ for appropriate parameter regimes, and enables fully-gapped chiral topological superconducting phases. These are

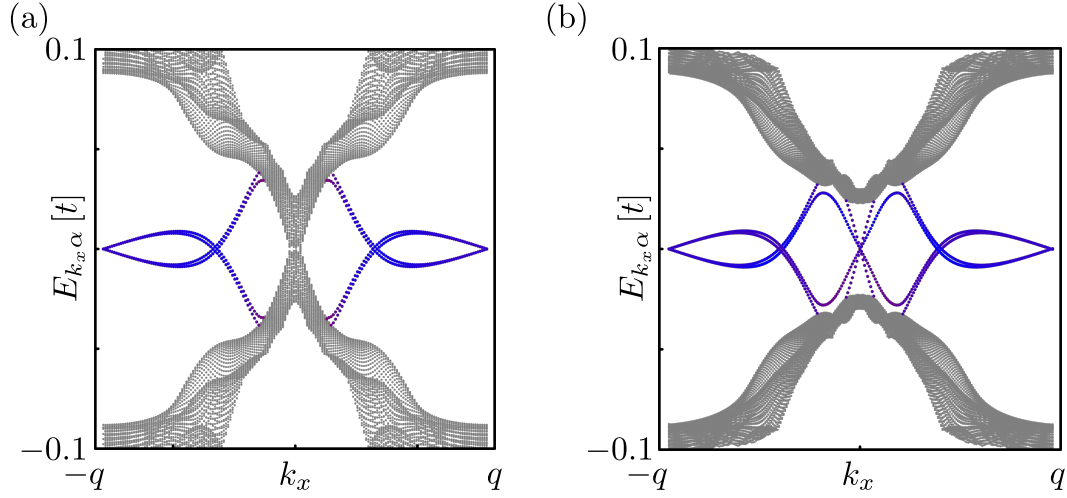


Figure 5.16: (a) The nodal spectrum at Γ is protected by $\tilde{\Theta}_{\mathbf{k}}$ for the one-band model in fig. 5.13 in the SWC_4 phase. (b) Resulting fully-gapped bulk spectrum for a broken C_4 symmetry due to a nematic dispersion $\xi_{\mathbf{k}}^{\text{nem}} = \xi_{\mathbf{k}} + t_{\text{nem}} \sin k_x \sin k_y$, where $\xi_{\mathbf{k}}$ is the dispersion used in (a). In the fully-gapped phase the preexisting bidirectional Majorana fermion modes in (a) get accompanied by chiral Majorana fermion modes. The figures were obtained using $\mathcal{N}_x = \mathcal{N}_y = 1001$, $\Delta_{\mathbf{k}} = \Delta = 0.1 t$, $M_{\parallel} = M_{\perp} = 0.3 t$ and $t_{\text{nem}} = 0.2 t$.

topologically equivalent to a $p + ip$ topological superconductor, and are classified according to the 1st Chern number \mathcal{C}_1 of the occupied bands [319].

Concluding this section, we remark that the introduction of the above perturbations is expected to influence the structure of the considered magnetic texture when the latter is treated in a self-consistent manner. However, sticking to the spirit of the explorative nature of this work, we neglect these modifications as they are not qualitatively modify the topological properties.

SWCB₂ Texture - Majorana Uni/Bi-Directional Edge Modes

An inplane Zeeman field with a direction which is not aligned with the main or diagonal axes defined by the HSPs $\{xz, yz, d_{\pm}z\}$ leads to the complete violation of the magnetic point and space group symmetries. In this case, it is the weak class D \mathbb{Z}_2 invariants which predict the appearance of protected MZM crossings at edge inversion-symmetric points independently of the orientation of the termination edge. However, considering a magnetic field which is aligned with one of these axes, still allows for a nontrivial magnetic point group. For a Zeeman field in the x (y) direction, the resulting magnetic point group becomes $M_{\text{SWCB}_2} = \{E, \sigma_{xz}T\}$ ($M_{\text{SWCB}_2} = \{E, \sigma_{yz}T\}$), while the symmetry $\{\sigma_{yz(xz)} | (\pi/Q, \pi/Q)\}$ also remains intact. See also table 5.1. Hence, now, by virtue of the time-reversal-symmetry $\sigma_{xz, yz}T$ acting in the respective HSP, one can also define the BDI class mirror winding number $\tilde{w}_{M, \text{HSP}}$.

In figs. 5.17(a)-(b) we present the edge spectra for a B_x and a B_y Zeeman field, respectively, with the system being open in the y direction in both cases. By evaluating the respective weak invariant, we find protected degeneracies at the edge inversion-symmetric points $k_x = \{0, q\}$. These persist until

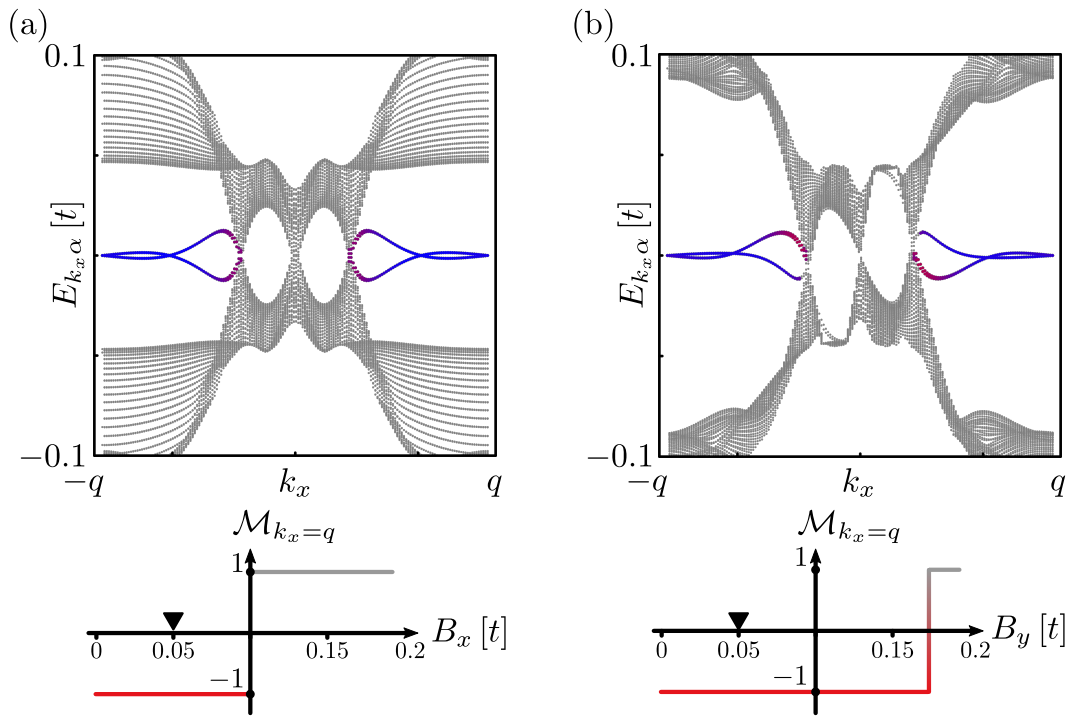


Figure 5.17: The effects of in-plane Zeeman/exchange fields on the one-band model in fig. 5.13 in the SWC_4 phase. (a)[(b)] Spectrum with the field in the x [y] direction with strength $0.05 t$. For the two figures we display the numerically calculated Majorana number eqn. (5.52) as a function of the magnetic field. The figures were obtained with open boundary conditions in the y direction and $\Delta_{\mathbf{k}} = \Delta = 0.1 t$, $M_{\parallel} = M_{\perp} = 0.2 t$ and $\mathcal{N}_x = \mathcal{N}_y = 1001$.

a gap closing takes place, which occurs for a Zeeman field value which depends on its orientation. Moreover, we observe the appearance of dispersive Majorana fermion edge modes. In the open-system geometry of fig. 5.17(a), the antiunitary mirror symmetry implies that every state vector ϕ_{n,k_x} corresponding to energy E_{n,k_x} possesses a mirror partner $\sigma_{xz}T\phi_{n,k_x}$ with energy $E_{n,-k_x}$, therefore resulting in a mirror symmetric spectrum. In contrast, the emergent antiunitary mirror symmetry $\sigma_{yz}T$ in fig. 5.17(b) relates a state vector ϕ_{n,k_x} with itself, thus, allowing for a mirror asymmetric spectrum and the emergence of unidirectional modes, see fig. 5.17(b).

SWCB₄ Texture - Majorana Bidirectional/Chiral Edge Modes

In the case of an out-of-plane B_z field, the resulting SWCB₄ texture possesses nontrivial topological properties itself. Indeed, it has been shown [77] that SWCB₄ is equivalent to a SSC₄ texture for $|B_z| < 2|M_\perp|$. This allows us to establish a connection to prior works [106, 420–424] which have focused on the emergence of chiral topological superconducting phases in other magnetic platforms. The above criterion also implies that, for $|B_z| > 2|M_\perp|$, SWCB₄ transforms into a ferromagnetic profile, which is expected to render the system trivial.

In connection to the detailed topological classification presented in the previous section for the SWC₄ phase, we observe that the addition of the B_z field leaves the magnetic point group M_{SWC_4} intact, but lifts the $\tilde{\Theta}_k$ and the space group symmetries $\{C_{4v} - C_4 | (\pi/Q, \pi/Q)\}$. As a consequence, the classification of the SWCB₄ texture follows from the classification performed for the topological superconductors induced by a SWC₄ magnetic texture. Indeed, we find that the presence of the B_z field still allows for Majorana fermion edge modes crossings at inversion-symmetric points, as seen in fig. 5.18(a). By evaluating the respective weak Majorana number, we find that for higher values of the external magnetic field, $B_z \sim 0.2t$, the edge mode crossings at inversion-symmetric points get lifted, while a band inversion at Γ takes place for slightly higher values of the field strength. Remarkably, the latter gives rise to two chiral Majorana fermion edge mode branches as displayed in fig. 5.18(b). The emergence of this chiral topological superconducting phase is also described by the Chern number $|\mathcal{C}_1| = 2$. Note that the Chern-number value $|\mathcal{C}_1| = 1$ is also generally accessible, as long as the accidental symmetry discussed in footnote 9 becomes lifted.

We now summarize the key results for one-band models in 2D. For a MHC the energy spectrum is nodal and leads to Majorana flat bands. Moreover, the classification in HSPs strongly depends on the IR of the pairing term. Nodes emerge also for a SWC₄ but they are not topologically stable. Nonetheless, degeneracies at inversion-symmetric points persist and give rise to weak and crystalline topological superconductor phases, which result into bidirectional Majorana fermion edge modes. In the SWC₄ case, a fully-gapped spectrum is accessible only by violating C₄ or time-reversal symmetries. Indeed, including a Zeeman field leaves the bidirectional modes intact, converts them into unidirectional modes, or, opens a gap in the spectrum and stabilizes chiral Majorana edge modes.

Two-Band Models

We now apply the classification methods discussed in the previous sections to 2D two-band models. For an example of such a model see fig. 5.19 which, for the chosen parameters, yields the FSs shown in fig. 5.19(a). Interband FS nesting, with the two ordering wave vectors $\mathbf{Q}_{1,2}$, takes place between

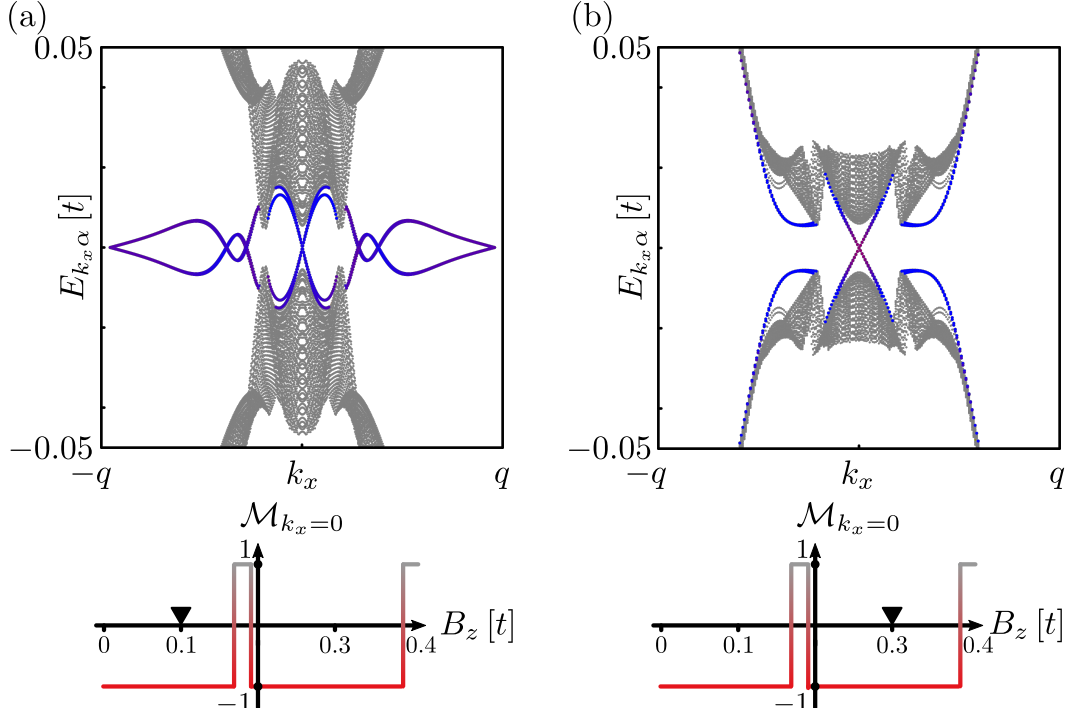


Figure 5.18: The one-band model of fig. 5.13 in the SWC_4 phase subjected to an out-of-plane Zeeman/exchange. (a) displays the effect of a field oriented in the z direction, thus, giving rise to a SSC_4 phase in the sufficiently-weak B_z regime. Here the field does not lower the magnetic point group symmetry of the system, but it does lift the unprotected nodes of the bulk spectrum. Here we used $B_z = 0.1t$. (d) Chiral edge modes for $B_z = 0.3t$, which become accessible only after a band inversion at $\Gamma(0,0)$ takes place. We show the numerically calculated Majorana number as a function of field strength. The invariant $\mathcal{M}_{k_x=0}$ is obtained by replacing (X, M) with (Y, Γ) in eqn. (5.52), and allows us to infer the transition to the chiral topological superconductor phase without resorting to the calculation of the related 1st Chern number \mathcal{C}_1 . The figures were obtained with $\Delta_{\mathbf{k}} = \Delta = 0.1t$, $M_{\parallel} = M_{\perp} = 0.2t$ and $\mathcal{N}_x = \mathcal{N}_y = 1001$ and open boundary conditions in the y direction.

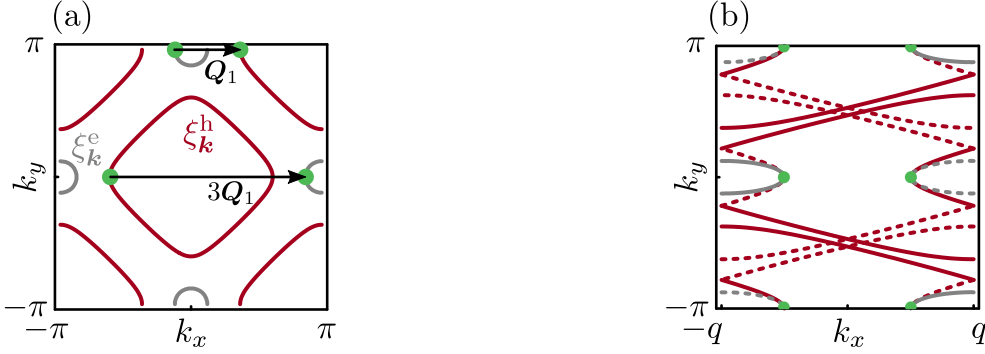


Figure 5.19: Example of a two-band model in 2D, described by the dispersions $\xi_{\mathbf{k}}^h = t_h \cos k_x \cos k_y + t'_h [\cos(2k_x) + \cos(2k_y)] - \varepsilon_h$ and $\xi_{\mathbf{k}}^e = t_e \cos k_x \cos k_y - \varepsilon_e$. We consider the parameters $t_h = 2.86 t_e$, $t'_h = t_e$, $\varepsilon_e \approx -0.92 t_e$ and $\varepsilon_h = -0.80 t_e$. (a) FSs of the two-band model in the first BZ. For clarity we only show half of the magnetic ordering wave vectors Q and $3Q = -Q$ connecting bands at the Fermi level. (b) FS segments for the two-band model in the MBZ for a MHC, where the nested points at the Fermi level are marked by green dots. Note that nested points at finite energy, away from the Fermi level, are also present.

the hole (fuchsia) and electron (navy blue) pockets. Hence, the system has the possibility to develop either a single- Q or a double- Q magnetic phase [77].

Recall from our previous discussion in sec. 5.4, that a multiband system allows for an interplay of interband and intraband magnetic scattering, as well as for a here-assumed intraband pairing gap which is a matrix in band space $\hat{\Delta}_{\mathbf{k}} = (\Delta_{\mathbf{k}}^e + \Delta_{\mathbf{k}}^h)/2 + \kappa_3(\Delta_{\mathbf{k}}^e - \Delta_{\mathbf{k}}^h)/2$. Even more importantly, we show here that the inclusion of the additional band, may in many realistic situations enrich the symmetry of the system. As we discuss below, a number of features that become unlocked for two-band models open perspectives for new phenomena and topological superconductor phases.

MHC Texture - Majorana and Andreev Flat Bands

The present section builds upon the analyses of the 1D two-band models and the 2D one-band models under the influence of a MHC. In the general case, in which intra- and inter-band magnetic scatterings are present, the system is dictated by the same magnetic point and space group symmetries discussed in sec. 5.5. The nodes in the bulk energy spectrum therefore possess a topological charge reflected in their vorticity v . Moreover, in HSPs one can also define the respective mirror vorticity $\nu_{\text{HSP}} \in \mathbb{Z}$ following the definition in eqn. (5.44). By further assuming spatially-constant pairing gaps $\Delta^{e,h}$ for the two pockets, we find that the edge spectrum contains Majorana flat bands, see fig. 5.20, whose topological protection can be genuinely described either by the strong local invariants mentioned above, or, by the weak invariant w_{k_y} .

As found previously for the two-band models in 1D, the topologically-stable bulk nodes and edge Majorana flat bands become accessible even for $\Delta^e \Delta^h < 0$, when intraband magnetic scattering is assumed. In fig. 5.20(a) and 5.20(c) we display the resulting path of the nodes in the MBZ and spectrum, respectively, for $\Delta^e = -\Delta^h$. For the chosen values of inter- and intraband scattering, the

topological properties are essentially determined only by the hole pocket, thus, exhibiting a similar phenomenology to fig. 5.11(a), with the nodes moving on straight lines.

If instead we restrict to an interband-only magnetic texture, we find that almost all the features of the two-band models in 2D are directly inherited from the 1D interband versions, namely: (i) the Hamiltonian is block-diagonalizable into an AIII \oplus AIII fashion [see eqn. (5.38) and fig. 5.20(b)], (ii) the number of gap closing points \mathbf{k}_c and edge modes double compared to the one-band models, (iii) the gap closing points are found through the relation $\xi_{\mathbf{k}\pm 3\mathbf{q}_1}^e \Delta^h = \xi_{\mathbf{k}\mp 3\mathbf{q}_1}^h \Delta^e$, and (iv) nodal topological superconducting phases are accessible only for $\Delta^e \Delta^h > 0$.

All the above features are reflected in fig. 5.20(b) and (d) where we display the path taken by the nodes upon variation of the magnetic and superconducting gaps, and the edge spectrum, respectively. Notably, here one obtains in most cases Andreev flat bands, which extend the Andreev zero modes discussed in sec. 5.4 to 2D. Andreev flat bands protected by the symmetry $\sigma_{xz}^Q T \Theta$ ($\{T \Theta | (\pi/Q, 0)\}$) are also accessible in $k_y = \{0, \pi\}$ for $\Delta_{\mathbf{k}} \sim \{B_{2g}, A_{2g}\}$ (for $\Delta_{\mathbf{k}}$ in any of the four D_{4h} IRs), in which case the symmetry class is \oplus_4 AIII, and the topological invariant is a mirror (glide) winding number $w_{M,\text{HSP}}$ ($w_{G,\text{HSP}}$). In contrast, Majorana fermion excitations become possible only in crystalline topological superconductor phases obtained for $\Delta_{\mathbf{k}} \sim \{B_{2g}, A_{2g}\}$, where the symmetry $\sigma_{yz}^Q T$ or $\{\sigma_{yz}^Q \Theta | (\pi/Q, 0)\}$ drives the symmetry-class transition $\text{AIII} \oplus \text{AIII} \rightarrow \text{BDI} \oplus \text{BDI}$, which in turn allows for Majorana flat bands. These are protected by a mirror winding number $\tilde{w}_{M,\text{HSP}}$, which is similar to the weak invariant $w_{k_x, y}$ for the one-band models in 2D in the presence of a MHC. See table 5.3.

Notably, a very crucial difference compared to the 2D one-band model is that, here, the paths along which the bulk nodes move in \mathbf{k} space do not coincide with the main axes of the MBZ. Remarkably, here the nodes generally move on arcs, as indicated by the white arrows in fig. 5.20(b). This enables the bulk nodes to meet and annihilate away from Kramers degenerate points, thus, opening the perspective for fully-gapped spectra for class D or DIII topological superconducting phases in the SWC_4 phase. This implies that here strong 2D topological superconductor phases seem to become accessible without the requirement of external perturbations, e.g., Zeeman fields, which was the case for one-band models.

SWC₄ Phase - Quasi-Helical Majorana Edge Modes

We now proceed by studying two-band models with an *interband-only* double- \mathbf{Q} SWC_4 texture. As in previous sections, we employ the usual set of wave-vector-transfer Pauli matrices $\boldsymbol{\zeta}$, $\boldsymbol{\lambda}$, $\boldsymbol{\eta}$ and $\boldsymbol{\rho}$, in order to account for the magnetic scattering taking place in the two orthogonal directions, as displayed in fig. 5.21(a). The MBZ is displayed in fig. 5.21(b), where points connected by a single \mathbf{Q} -vector at the FS and points connected by both \mathbf{Q} -vectors, are marked by green and orange dots, respectively.

Due to the interband nature of the magnetic scattering the BdG Hamiltonian now enjoys a time-reversal symmetry $\Theta = \kappa_3 T$. This satisfies $\Theta^2 = -\mathbb{1}$ and leads to Kramers pairs (KP) at all the inversion-symmetric points of the MBZ, thus enlisting the BdG Hamiltonian in the DIII symmetry class. Nodes in the bulk spectrum of a DIII Hamiltonian are topologically stable only at inversion-symmetric points, and are classified by a vorticity akin to the one in eqn. (5.42). For a fully-gapped bulk spectrum, class DIII supports one strong and two weak \mathbb{Z}_2 topological invariants [425–428], that

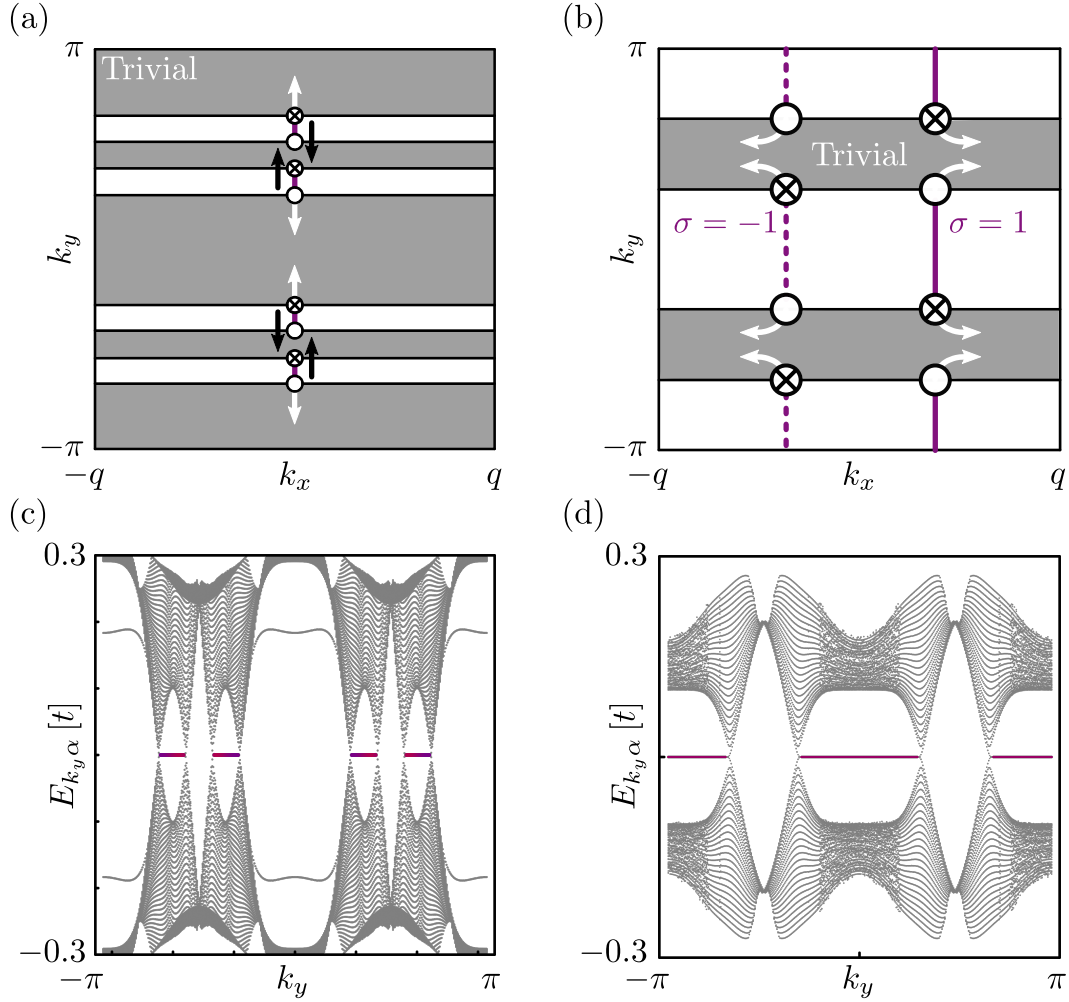


Figure 5.20: Sketches of nodes and the numerically-obtained dispersions for the two-band model of fig. 5.19 in the MHC phase. (a) and (c) $\Delta^e = t_e$, $\Delta^h = -t_e$ and $M_{\parallel, \perp}^{\text{eh}} = M_{\parallel, \perp}^e = M_{\parallel, \perp}^h = 1.1 t_e$. The nodes are moving on straight lines similar to the one-band model in 2D, cf. fig. 5.11. The number of nodes has increased with the number of nested points, see green points in fig. 5.19. (b) and (d) $\Delta^e = \Delta^h = t_e$, $M_{\parallel}^{\text{eh}} = M_{\perp}^{\text{eh}} = 1.1 t_e$ and $M_{\parallel, \perp}^e = M_{\parallel, \perp}^h = 0$. The nodes are now moving on arcs, due to the interband-only scattering mediated by the magnetic texture. Both dispersions are obtained with open boundary conditions along the x direction, and with $\mathcal{N}_x = \mathcal{N}_y = 401$. In (b) $\sigma = \pm 1$ labels the two blocks of the Hamiltonian after performing the unitary transformation with the operator \mathcal{S} in sec. 5.4.

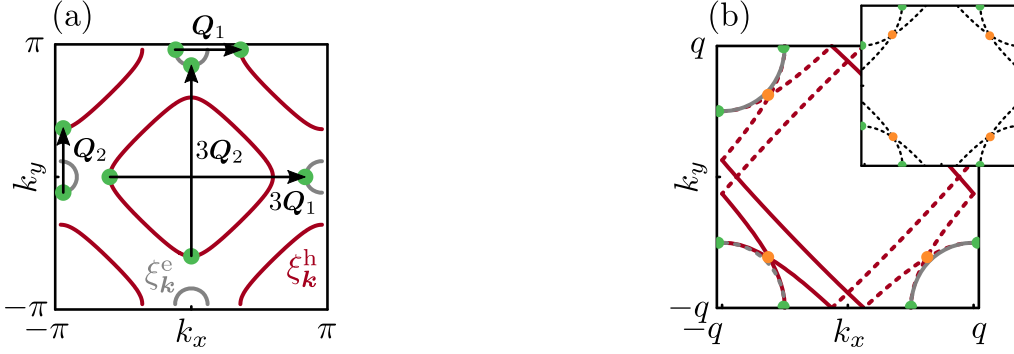


Figure 5.21: Two-band model of fig. 5.19 under the influence of a double- \mathbf{Q} magnetic texture. (a) FSs of the two-band model in the first BZ. We sketch the magnetic ordering wave vectors $\mathbf{Q}_{1,2}$ ($3\mathbf{Q}_{1,2} \equiv -\mathbf{Q}_{1,2}$), which connect points at the Fermi level (green dots). For clarity we only show half of the ordering wave vectors. (b) The resulting FS segments in the MBZ. As in fig. 5.13, we also display the points connected by both \mathbf{Q}_1 and \mathbf{Q}_2 (orange dots) at energies away from the Fermi level. Inset: The dotted black lines show the gap closing points \mathbf{k}_c in the MBZ.

we here construct as:

$$\mathfrak{M}^{\text{KP}} = \prod_s^{\Gamma, X, M, Y} \text{pf}(W_{\mathbf{k}_s}) / \sqrt{\det W_{\mathbf{k}_s}}, \quad (5.53)$$

$$\mathfrak{M}_{k_x=q(k_y=q)}^{\text{KP}} = \prod_s^{X, M(Y, M)} \text{pf}(W_{\mathbf{k}_s}) / \sqrt{\det W_{\mathbf{k}_s}}. \quad (5.54)$$

In the above, we defined the skew-symmetric “sewing” matrix $W_{\mathbf{k}_I} \equiv \mathcal{U}_\Theta A_{\mathbf{k}_I}$ at inversion-symmetric points \mathbf{k}_I only. The $W_{\mathbf{k}_I}$ matrix is the DIII analog of the AII class sewing matrix introduced by Fu and Kane [429]. The difference is that, here, $\mathcal{U}_\Theta = i\sigma_y$ corresponds to the unitary part of the block off-diagonal Θ , obtained in the diagonal basis of the chiral symmetry operator Π . In this basis, we identify the block off-diagonal part of the Hamiltonian as $A_{\mathbf{k}}$. The transition to this basis is here effected via the transformation $(\Pi + \tau_3)/\sqrt{2}$, which brings the arising chiral symmetry generator $\Pi = \kappa_3\tau_2$ into the form $\Pi = \tau_3$, and leads to

$$A_{\mathbf{k}} = - \sum_s^{\text{e,h}} \mathcal{P}_s \left[F(\Delta_{\mathbf{k}}^s) + i\kappa_3 F(h_{\mathbf{k}}^s) \right] - \kappa_2 (M_{\perp} \rho_1 \sigma_z + M_{\parallel} \rho_3 \sigma_x) / 2 \quad (5.55)$$

$$- \kappa_2 (M_{\perp} \eta_1 \rho_1 \sigma_z - M_{\parallel} \eta_1 \rho_3 \sigma_x) / 2 - \kappa_2 (M_{\perp} \lambda_1 \sigma_z + M_{\parallel} \lambda_3 \sigma_y) / 2 - \kappa_2 (M_{\perp} \zeta_1 \lambda_1 \sigma_z - M_{\parallel} \zeta_1 \lambda_3 \sigma_y) / 2,$$

with $\mathcal{P}_{\text{e,h}}$ (F) defined once again as in sec. 5.4 (app. 5.E).

We now move on with the discussion of the various crystalline symmetries, which are identical to the ones dictating the one-band models in sec. 5.5. Specifically, the antiunitary mirror symmetries $(C_{4v} - C_4)T$ belonging to the related G_{SWC_4} point group discussed in sec. 5.5, combine with Θ and give rise to the unitary mirror operations $R = (C_{4v} - C_4)T\Theta = \kappa_3(C_{4v} - C_4)$. These lead to a AIII \oplus AIII (D \oplus D) class in the corresponding HSP when the pairing gap $\Delta_{\mathbf{k}}$ is even (odd) under the given mirror operation, e.g., for $\Delta_{\mathbf{k}} \sim B_{1g}$ the symmetry class is AIII (D) in the xz ($x = y$) and

yz ($x = -y$) HSPs. Both AIII and D classes are nontrivial in 1D for a fully-gapped system. Thus, HSPs dictated by the symmetry class AIII \oplus AIII [D \oplus D] and at the same time exhibit a fully-gapped spectrum, are characterized by a \mathbb{Z} [\mathbb{Z}_2] mirror winding number $w_{M,\text{HSP}}$ [mirror Majorana number $\mathfrak{M}_{M,\text{HSP}}$].¹⁰ In contrast, nodes in HSPs dictated by either AIII \oplus AIII or D \oplus D are not protected.

On the other hand, nonsymmorphic symmetries can only influence the topological classification at inversion-symmetric points. Remarkably, the Γ and M points are under the simultaneous influence of two time-reversal symmetries which square to $-\mathbb{1}$, i.e. $\Theta = \kappa_3 T$ and $\{T | (\pi/Q, \pi/Q)\}$, thus observing a fourfold degeneracy. This can be understood in terms of the unitary symmetry $\{\kappa_3 | (\pi/Q, \pi/Q)\} = e^{i(k_x+k_y)\pi/Q} \kappa_3 \lambda_2 \rho_2$ which emerges at these two inversion-symmetric points.¹¹

We now investigate a concrete two-band model, specifically the model defined in fig. 5.21. Similar to the analysis of the one-band models in the SWC₄ phase, we identify two types of MBZ points, namely the points connected by a single \mathbf{Q} -vector (green dots) and the points connected by both ordering wave vectors (orange dots), cf. fig. 5.21(b). Based on the results of the previous paragraphs, we find that the nodes move on arcs determined by the intersection of the two bands connected by a single \mathbf{Q} -vector, e.g. $\xi_{\mathbf{k}+3\mathbf{q}_1-\mathbf{q}_2}^e = \xi_{\mathbf{k}-3\mathbf{q}_1-\mathbf{q}_2}^h$. The paths of the nodes upon variations of the magnetic or superconducting gaps are marked by the black dotted lines in the inset of fig. 5.21(b). Once again, bulk nodes appear strictly for $\Delta^e \Delta^h > 0$, since we here consider an interband-only texture.

The presence of bulk nodes goes hand in hand with the emergence of bidirectional Majorana fermion edge modes, as seen in fig. 5.22(a) and (c) where we display the nodes and edge spectrum. However, in the present situation, the bulk nodes are not topologically-protected, thus implying the same for the resulting bidirectional edge modes. Both nodes and edge modes are thus removable by considering additional Hamiltonian terms which do not modify the ensuing DIII class. Similar conclusions were drawn for the one-band models in the SWC₄, with the crucial distinction that there the edge modes had a topologically protected crossing at $k_{x,y} = q$. Such protected crossings do not arise for the bidirectional Majorana fermion modes in fig. 5.22(c).

By increasing the energy scale of the magnetic gaps the nodes move on arcs, as indicated by the white arrows in fig. 5.22(a), and meet up at the green points in the MBZ in fig. 5.21(b), when the familiar criterion is satisfied $\Delta^e \Delta^h = M_{\pm}^2$. In contrast to the one-band models, here the nodes *do* get lifted when they meet up, since they intersect away from inversion-symmetric points, as sketched in fig. 5.22(b). Beyond this point the spectrum is fully-gapped. In the present case, the fourfold degeneracies at Γ and M additionally imply that, there, $\text{pf}(W_{\mathbf{k}_s})$ features an even number of gap closings upon sweeping the various parameters. Hence, the above-mentioned invariants simplify as $\mathfrak{M}^{\text{KP}} = \mathfrak{M}_{k_x=q}^{\text{KP}} \mathfrak{M}_{k_y=q}^{\text{KP}}$ where $\mathfrak{M}_{k_x=q(k_y=q)}^{\text{KP}} = \text{sgn}[\text{pf}(W_{\mathbf{k}_{X(Y)}})]$. In the event of a C_4 -symmetric energy spectrum, which is actually the case here, the two invariants are equal. The two weak Majorana Kramers pair numbers generally become nontrivial simultaneously. Nonetheless, here we find that all three invariants remain trivial.

Despite of the fact that the DIII invariants are here all trivial, in fig. 5.22(d) we indeed find the here-termed quasi-helical edge modes centered at $k_x = q$, which are protected by the mirror symmetry $\sigma_{yz} T$. These come in pairs, and their electronic spin-polarization is opposite on opposite edges, similar

¹⁰ $\mathfrak{M}_{M,\text{HSP}}$ is defined as $\mathfrak{M}_{M,\text{HSP}} = \text{sgn} \prod_{\sigma} \mathfrak{M}_{\sigma,\text{HSP}}$, where $\sigma = \pm 1$ labels the D \oplus D blocks. Each $\mathfrak{M}_{\sigma,\text{HSP}}$ follows from eqn. (5.52).

¹¹Note that the above fourfold degeneracy does not lead to hourglass MFs. Following ref. [32], we can attribute this to the commutation relation $[\{\kappa_3 | (\pi/Q, \pi/Q)\}, \Pi] = 0$ which holds here.

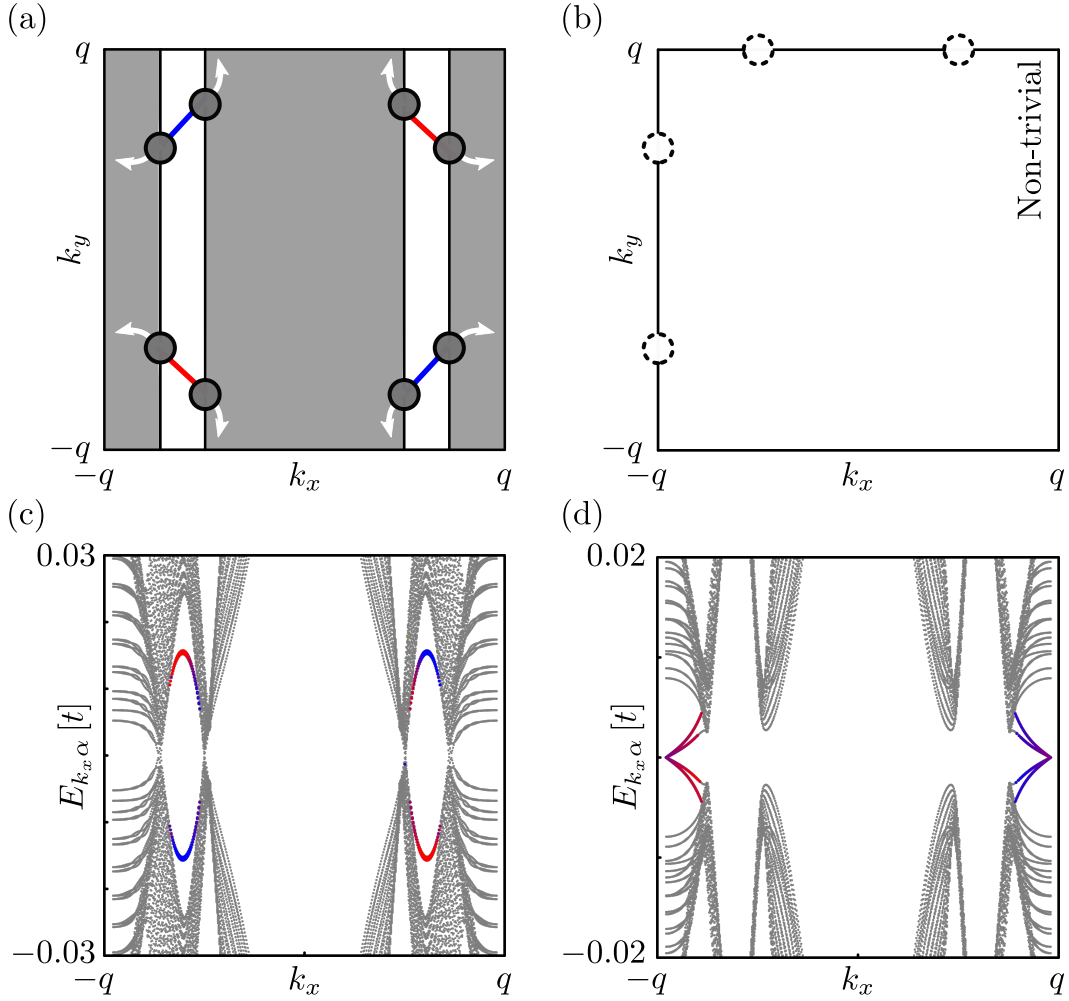


Figure 5.22: Bidirectional and mirror-symmetry-protected quasi-helical Majorana edge modes for the two-band model in the SWC_4 phase. (a) The bulk nodes move from the points connected by two \mathbf{Q} -vectors (orange dots in fig. 5.21(b)), and meet at points connected by a single \mathbf{Q} -vector (green dots in fig. 5.21(b)), as indicated by the white arrows. (c) The spectrum related to (a), with bidirectional Majorana edge modes ($M_{||,\perp}^{\text{eh}} = 0.095 t_e$). Note that here the bidirectional Majorana fermion modes are not topologically protected, due to the similar lack of protection seen by the bulk nodes. (b) Sketch of the MBZ after the nodes have met and annihilated at the points marked by the dotted circles. (d) Resulting quasi-helical edge modes connected to the sketch in (b), where we used $M_{||,\perp}^{\text{eh}} = 0.11 t_e$. For clarity, in (d), we show only the modes on a single edge, since the z spin axis electronic spin polarization of the modes on the other edge is exactly opposite. We note that both types of spectra are twofold degenerate for reasons discussed in footnote 9. We used open boundary conditions in the y direction, $\Delta^e = \Delta^h = 0.1 t_e$, $M_{z,\pm}^{\text{e,h}} = 0$ and $\mathcal{N}_x = \mathcal{N}_y = 501$.

to what is encountered for their helical counterparts. However, the quasi-helical ones appear only for edges preserving the respective mirror symmetry, in stark contrast to the helical edge modes stemming from the strong DIII invariant in 2D, which emerge for a termination of an arbitrary orientation. Since for the above numerical calculations we have considered $\Delta_{\mathbf{k}}^{\text{e,h}} \sim A_{1g}$, the HSP plane is dictated by the AIII \oplus AIII symmetry class. On the other hand, considering a pairing gap $\Delta_{\mathbf{k}}^{\text{e,h}} \sim B_{2g}$ imposes the D \oplus D symmetry class in the $k_x = q$ HSP, and allows instead for quasi-helical Majorana edge modes protected by a mirror \mathbb{Z}_2 invariant. The presence of two possible types of topological protection for the touching point, further suggests a different behaviour for the quasi-helical Majorana edge modes in response to external perturbations, e.g., Zeeman fields.

Magnetic-Field-Induced Phases: Majorana Uni/Bi-Directional, Quasi-Helical, and Chiral edge modes

We complete the study of the two-band models in 2D, by considering the effects of an additional Zeeman field on the system discussed in the previous paragraph. In this case, the system undergoes the symmetry class transition DIII \rightarrow D. Therefore, for a fully-gapped bulk energy spectrum, chiral edge modes become accessible. Even more, when the field is aligned with one of the HSPs, mirror-symmetry protected edge modes are also possible. For a magnetic field in the x (y) direction, the resulting magnetic point group becomes $M_{\text{SWCB}_2} = E + \sigma_{xz}T$ ($M_{\text{SWCB}_2} = E + \sigma_{yz}T$). HSPs now belong to the BDI symmetry class, since the antiunitary elements of the point group act as time-reversal symmetries. Hence, we can define the mirror winding numbers $\tilde{w}_{M,\text{HSP}} \in \mathbb{Z}$ similarly to the weak winding numbers $w_{k_{x,y}}$ introduced in eqn. (5.40).

For concreteness, below we focus on a system with open boundaries along the y direction, and assume that the pairing gap is nonzero in the xz and yz HSPs. For a magnetic field in the x direction, the time-reversal symmetry $\sigma_{xz}T$ is not preserved by the termination, thus not protecting the quasi-helical modes in the HSP. Evidently the quasi-helical Majorana edge modes in fig. 5.23(a), become lifted by the term $B_x\sigma_x$, as seen in fig. 5.23(b). If we instead consider a field perpendicular to the edge, i.e., a nonzero B_y or B_z field, we find that the time-reversal symmetry $\sigma_{yz}T$ is preserved by the termination, thus allowing for mirror-symmetry protected quasi-helical edge modes shown in fig. 5.23(c) for a field in the y -direction. Finally, we remark that results with a B_z field are not shown, since for the present model the transition to a chiral topological superconductor appears to occur for extremely large values of the magnetic field.

5.6 Conclusions and Outlook

We provide a systematic classification of the rich variety of accessible topological phases and Majorana excitations that appear due to the bulk interplay of spin-singlet superconductivity and representative magnetic texture crystals. This work aims at inspiring new developments in a field which has recently attracted significant interest from both theoretical [77, 102–123, 268, 284, 345–349, 359, 360, 362, 380] and experimental [305, 315–317, 361, 363] sides. Our work is novel in many ways, as it accounts for all possible strong, weak, and crystalline phases arising in topological superconductors induced by magnetic textures, and considers generally-multiband systems which harbor conventional or unconventional spin-singlet pairing. As we uncovered here, the concepts of the magnetic and pairing groups

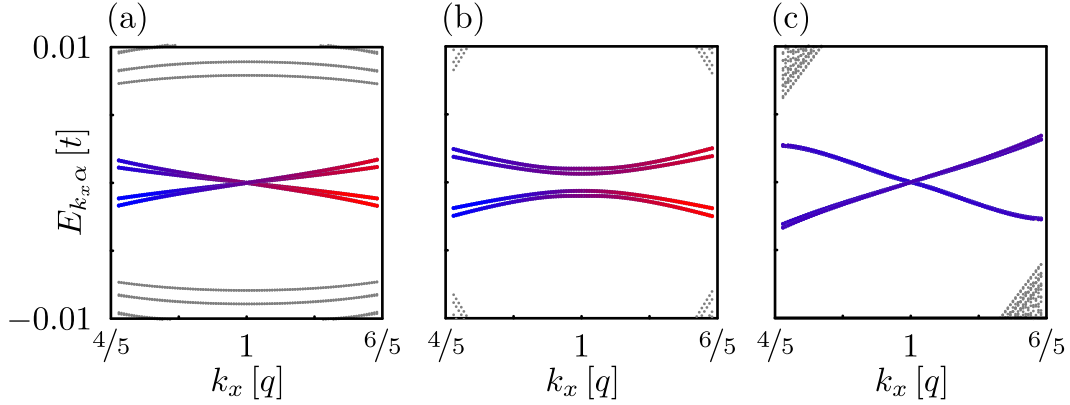


Figure 5.23: Impact of an applied Zeeman field on the quasi-helical Majorana modes of fig. 5.22(d). Once again, only modes on a single edge are also shown here for clarity. (a) Zoom in the edge mode spectrum of fig. 5.22(d). (b)[(c)] shows the resulting edge spectrum for an external magnetic field in the x [y] direction ($B_x = 0.04 t_e$) [($B_y = 0.05 t_e$)]. The quasi-helical edge modes are protected by the time-reversal symmetry $\sigma_{yz}T$, except in the case for a magnetic field in the x direction, where the modes get lifted. Hence, the addition of the Zeeman field modifies the symmetry properties at the touching point in such a way, so that the quasi-helical Majorana modes in (a) still are present in (c). The figures were obtained with open boundary conditions along the y direction, $\Delta^e = \Delta^h = 0.1 t_e$, $M_{||,\perp}^{eh} = 0.11 t_e$, $M_{z,\perp}^{e,h} = 0$ and $\mathcal{N}_x = \mathcal{N}_y = 501$.

play a crucial role in the symmetry classification of these systems, since their interplay controls the topological bulk and boundary properties. Our entire discussion unfolds by further assigning and calculating suitable topological invariants, with a number of them being concretely discussed here for the first time.

Our investigation first focuses on 1D systems. This allows bridging our work with previous known results [103–105, 107–112, 331] but also report new phenomena. Even more, it sets the stage for the formalism that we employ in 2D, which relies on a sublattice description, as well as on downfolding to the MBZ. While a complete and rigorous topological classification is extracted using the sublattice picture, the latter approach exposes transparently the key mechanisms which drive the nontrivial topology. In fact, the MBZ description is also computationally advantageous when studying the topological properties in the low-energy sector, since a few number of bands are required for this.

By following the above approaches, we find a number of new interesting results in 1D. First of all, we construct new crystalline topological invariants which reflect the quantization of the staggered magnetic moment in such systems. In addition, our analysis includes the study of unconventional pairing gaps and discusses how multiple Majorana zero modes appear on a given edge. Another important component of this study is the consideration of two-band models (two-band models). Remarkably, the multiband structure of the magnetization allows interpolating between different symmetry classes, i.e., BDI, AIII and DIII. The former appears when both interband and intraband magnetic scatterings are present. The second becomes relevant for interband-only scattering, in which case the Majorana edge excitations come in pairs. However, these do not obey a charge-conjugation symmetry and thus each

pair should be viewed as a single Andreev zero mode. On the other hand, true Majorana Kramers pairs appear when interband-only scattering is present and additional time-reversal-symmetry preserving intraband terms are included, e.g., inversion-symmetry-breaking spin-orbit coupling terms. See also ref. [268].

The emergence of Andreev edge modes in topologically nontrivial systems has recently attracted substantial attention [123, 399–402]. Noteworthy, here we obtain topologically-protected Andreev modes (cf ref. [402]) which are pinned to zero energy in an extended window in parameter space. As a result, these topologically-protected zero modes open perspectives for new quantum computing platforms, since they can constitute the hardware of long-lived Andreev qubits with enhanced protection against decoherence [403, 404]. Even more, engineering systems harboring topologically-protected Andreev zero modes, opens a new direction in synthesizing topological Andreev bandstructures in synthetic space [430–445]. Indeed, such a pursuit in topological superconductors has so far been unavoidably restricted to exploiting MZMs in multi-terminal devices [437–443], and theoretical works predict that it gives access to the observation of Weyl points, chiral anomaly, and a number of quantized Josephson transport phenomena. Being in a position to obtain Andreev zero modes in multi-terminal platforms such as the one experimentally investigated recently in ref. [446], provides an alternative and in some cases more robust and less demanding route for such types of synthetic topology.

The 2D investigation brings forward an equally rich list of results. By considering once again one- and two-band models, generally-unconventional multiband pairing, as well as various multiband implementations of representative textures, we uncover an intricate set of flat-band, uni/bi-directional, quasi-helical, helical, and chiral Majorana edge modes, that may be protected by strong, weak, or crystalline topology. Specifically, for a MHC we obtain Majorana and Andreev flat bands, which can be viewed as direct extensions of the 1D phenomena. However, new physics appears here due to the interplay of the magnetic and pairing point groups, thus revealing a dichotomy when it comes to the topological classification in HSPs. Depending on whether the IR of the pairing term belongs to either the $\{A_{1g}, B_{1g}\}$ or $\{B_{2g}, A_{2g}\}$ set, we find a different topological classification and, in turn, Majorana edge mode dispersions.

Considering instead a SWC_4 magnetic texture which eliminates the possibility of dispersionless edge modes, since the coexistence of two magnetic helix textures winding in different directions and spin planes, lifts almost all the degeneracies in the MBZ. Strikingly however, mirror and space-group symmetries consistent with the structure of the texture still impose a number of degeneracies in HSPs. These enable the conversion of the flat band edge modes into uni/bi-directional ones. The bidirectional modes constitute dispersive Majorana edge modes with neither a fixed chirality nor helicity, whose spin character depends on the conserved wave number. Notably, besides a few exceptions [32], this type of excitations has been poorly discussed so far in the literature.

We find that the emerging topological phases in 2D are mostly of the crystalline or weak type, and become manifest through the appearance of the here-called quasi-helical Majorana edge modes, which present a certain number of similarities with the standard helical edge modes in 2D. Remarkably, strong phases do not become accessible in 2D, because the crystalline symmetries present trivialize the respective strong topological invariants. Specifically, the presence of space-group symmetries imposes degeneracies at inversion-symmetric points which, in conjunction with the fourfold rotational symmetry (C_4) present, imposes a nodal bulk spectrum in the one-band models, and do not allow for

a strong \mathbb{Z}_2 invariant in two-band models despite the fact that a fully-gapped spectrum is accessible there. As we demonstrate, one possible route to unlock genuinely-2D topological phases, is by including terms which violate C_4 symmetry, while respecting the degeneracies imposed by the magnetic space group. Notably, the violation of C_4 symmetry can be either externally imposed via strain engineering, or spontaneously appear in systems with nematic correlations, cf. ref. [63, 203].

Another possibility is to consider the additional presence of a Zeeman/exchange field, which lifts the degeneracies at inversion-symmetric points, but still retains a number of crystalline symmetries. As a result, the arising bidirectional modes can be converted into unidirectional depending on the orientation of the field, Majorana chiral edge modes become accessible in one-band models, and mirror-symmetry-protected quasi-helical edge modes may persist or get gapped out. Despite the fact that space-group symmetries appear to be detrimental for the appearance of genuinely-2D topological phases, we remark that they still constitute a unique pathway to obtain multiply-degenerate Majorana excitations, such as, hourglass Majorana edge modes [32]. While such a possibility did not occur for the models examined, it still constitutes an interesting direction of research. Lastly, we remind that the presence of space-group symmetries are absent for magnetic textures with incommensurate magnetic ordering vectors [77], but may still be approximately preserved in itinerant magnets for low energies.

At this point, we wish to discuss in more detail prominent candidate physical systems that can host the above-mentioned phenomena. Our framework addresses a single Kramers doublet of the double covering D_{4h} point group, therefore allowing to describe tetragonal magnets. These systems may for instance correspond to correlated magnetic superconductors, where magnetism and superconductivity coexist microscopically. The desirable scenario is the one where a magnetic texture appears to partially gap out a well-nested FS [77], leaving behind reconstructed pockets, which can be subsequently gapped out by the emergence of superconductivity. Similar to ref. [108–110], in this situation, one expects that the resulting magnetic superconductor self-tunes into one of the topological phases discussed here.

Among the possible systems that promise to provide a fertile ground to materialize such a possibility, the family of doped FeSCs stands out. Some FeSCs are well known to exhibit a coexistence of magnetism and superconductivity [66–68, 70–73, 75, 76, 80–85, 364]. Reference [77] has identified all the possible single- and double- Q magnetic ground states that can appear in representative five-orbital models of FeSCs, and demonstrated that doping generally enables various magnetic textures, some of which we explore here. The possible subsequent emergence of conventional or unconventional spin-singlet superconductivity can give rise to a number of the topological scenarios discussed here. Moreover, accounting for a weak band dispersion in the third spatial dimension, which may be non-negligible in certain compounds, opens additional perspectives for realizing systems with topologically-protected Weyl and Dirac points [447], as well as nodal lines, rings and chains [448], thus leading to Majorana/Andreev arc and drumhead surface modes.

Other physical systems which our results may be applicable to, include hybrid systems [103, 105–123, 305, 316, 361] such as superconductor-semiconductor nanowire hybrids and topological magnetic lattices. In the former class of systems, it is desirable to impose on the system the desired magnetic texture by external means, i.e., using nanomagnets [305]. In this case, the magnetic wave vectors should be tailored to be comparable to the Fermi wave vectors of the underlying hybrid system, which in turn can be controlled by gating the device. On the other hand, the wave vectors describing the magnetic texture appearing in topological chains depends on up to which degree is the electronic spectral weight carried by the superconducting electrons of the substrate [282–284]. In the deep so-

called Yu-Shiba-Rusinov limit, the magnetic adatoms can be treated classically, and the modulation of the magnetic texture is determined by a number of factors. These include the spacing of the magnetic adatoms, the size of their moment, the strength of their coupling to the substrate electrons, the possible presence of inversion symmetry breaking in the substrate and/or crystal field effects. See ref. [284], for an analysis concerning a topological magnetic chain.

We continue with enumerating a number of possible experimental methods to infer the various topological phases discussed here, and detect the arising Majorana/Andreev modes. As mentioned already, spin- and angle-resolved photoemission spectroscopy [410] can provide information regarding protected degeneracies. Spectroscopic methods are also standard routes to detect Majorana/Andreev excitations [449–453]. Here we are particularly interested in spin-resolved scanning tunneling spectroscopy [452, 453] which can probe the spin character of the boundary excitations [454, 455]. The various Majorana fermion edge modes lead to a characteristic electronic edge spin polarization. For a topological superconductor induced by a MHC the presence of chiral symmetry confines the electronic spin polarization within a given spin plane, similar to what is encountered in superconductor-semiconductor nanowires [452–454], magnetic chains [124, 284], as well as charged [440] and neutral [455] p -wave superfluids. Topological superconductors engineered from the SWC_4 texture exhibit a wider range of possibilities. As we show in fig. 5.15, the type of termination is decisive for the spin character of the bidirectional Majorana fermion modes which possess neither fixed helicity nor chirality. In contrast, unidirectional modes tend to exhibit a higher degree of spin polarization. Chiral and (quasi-)helical Majorana fermions have instead a fixed spin character, since they stem from fully-gapped topological superconductors. Even more, the various dispersionless or dispersive Majorana and Andreev edge modes can be probed in suitably-designed generally-spin-resolved charge and thermal transport experiments [456–460]. Depending on whether we have electrically neutral (Majorana) or charged (Andreev) edge excitations one can correspondingly look for characteristic features and scaling behaviors in thermal and Hall responses [460].

Appendices for Chapter 6

5.A Summarizing Tables of Topological Invariants

Strong Topological Invariants	Hyperlinks
Winding number w	Eq. (5.9)
Vorticity v	Eq. (5.42)
1st Chern number \mathcal{C}_1	Ref. [319]
Majorana Kramers pair number \mathfrak{M}^{KP}	Eq. (5.53)
Weak Topological Invariants	
Majorana number parity $P_{\mathfrak{M}}$	Footnote 5
Winding number $w_{k_x, y}$	Eq. (5.40)
Majorana number $\mathfrak{M}_{\text{HSP}}$	Eq. (5.52)
Majorana Kramers Pair number $\mathfrak{M}_{\text{HSP}}^{\text{KP}}$	Eq. (5.54)
Mirror Topological Invariants	
Mirror winding number n_M	Eq. (5.19)
Mirror winding number at inversion-symmetric point n_{M, k_I}	Eq. (5.20)
Mirror vorticity in high symmetry plane ν_{HSP}	Eq. (5.44)
Mirror winding number in high symmetry plane $w_{M, \text{HSP}}$	Eq. (5.45)
Mirror winding number in high symmetry plane $\tilde{w}_{M, \text{HSP}}$	Eq. (5.40)
Glide Topological Invariants	
Glide invariant at inversion-symmetric point n_{G, k_I}	Eq. (5.20)
Glide Majorana parity at inversion-symmetric point P_{G, k_I}	Eq. (5.32)
Glide winding number in high symmetry plane $w_{G, \text{HSP}}$	Eq. (5.45)
Majorana number in high symmetry plane $\mathfrak{M}_{M, \text{HSP}}$	Footnote 10

Table 5.4: Summarizing table of the various types of topological invariants defined in the manuscript, and hyperlinks to the expressions that are used for their construction.

5.B Sublattice Formulation in 1D

In this appendix, we reformulate our analysis in terms of a four sublattice basis, which is more transparent in regards to the topological classification, since it leads to properly compactified 2π -periodic Hamiltonians. For illustrative purposes, we restrict to the 1D case, since the 2D description is obtainable in a straightforward manner. Within this framework a unit cell consists of 4 sites labelled as {A, B, C, D}, cf. fig. 5.24. We define the spinor

$$\bar{\mathbf{c}}_R^\dagger = \left(\mathbf{c}_{A,R}^\dagger, \mathbf{c}_{B,R}^\dagger, \mathbf{c}_{C,R}^\dagger, \mathbf{c}_{D,R}^\dagger \right), \quad (5.56)$$

where R now labels a 4-site unit cell. In this basis, a translation $\{E|a\}$, effects the shift $R \rightarrow R + \frac{1}{4}$. Hence, $\{E|a\}$ and $\{E|2a\} \equiv \{E|\pi/Q\}$ [for $Q = \pi/(2a)$] read in wave-number space $k_x \in (-\pi/4, \pi/4]$ (with $a = 1$)

$$\{\mathbb{1}|a\} = \begin{pmatrix} 0 & 0 & 0 & \beta^* \\ 1 & 0 & 0 & 0 \\ 0 & 1 & 0 & 0 \\ 0 & 0 & 1 & 0 \end{pmatrix}, \quad \{\mathbb{1}|\pi/Q\} = \begin{pmatrix} 0 & 0 & \beta^* & 0 \\ 0 & 0 & 0 & \beta^* \\ 1 & 0 & 0 & 0 \\ 0 & 1 & 0 & 0 \end{pmatrix}, \quad (5.57)$$

where we set $\beta = -e^{i4k_x}$ in order for the MBZs of the wave-number shifts and sublattice descriptions to match. Next we identify the action of inversion I about the center of inversion which is here set to be the A site of the $n = 0$ unit cell. For a Hamiltonian element \mathcal{H}_{k_x} defined in the respective wave-number spinor of eqn. (5.56), inversion acts as $[I\mathcal{H}_{k_x}I^\dagger]_{k_x \rightarrow -k_x}$ with

$$I = \begin{pmatrix} 1 & 0 & 0 & 0 \\ 0 & 0 & 0 & \beta \\ 0 & 0 & \beta & 0 \\ 0 & \beta & 0 & 0 \end{pmatrix}. \quad (5.58)$$

We note that the inversion of k_x takes place only after the matrix multiplications. This is because the matrix representation of inversion is k_x -dependent in this basis.

The kinetic energy operator describing first (t), second (t'), and third (t'') order neighbour hopping is represented as

$$\mathcal{H}_{\text{kin},k_x} = \quad (5.59)$$

$$-t \begin{pmatrix} 0 & 1 & 0 & \beta^* \\ 1 & 0 & 1 & 0 \\ 0 & 1 & 0 & 1 \\ \beta & 0 & 1 & 0 \end{pmatrix} - t' \begin{pmatrix} 0 & 0 & 1 + \beta^* & 0 \\ 0 & 0 & 0 & 1 + \beta^* \\ 1 + \beta & 0 & 0 & 0 \\ 0 & 1 + \beta & 0 & 0 \end{pmatrix} - t'' \begin{pmatrix} 0 & \beta^* & 0 & 1 \\ \beta & 0 & \beta^* & 0 \\ 0 & \beta & 0 & \beta^* \\ 1 & 0 & \beta & 0 \end{pmatrix}.$$

One verifies that the above kinetic part of the Hamiltonian is invariant under translations and inversion. The Hamiltonian for the MHC texture in eqn. (5.2), here reads

$$\mathcal{H}_{\text{mag}} = \begin{pmatrix} M_\perp \sigma_z & 0 & 0 & 0 \\ 0 & M_\parallel \sigma_x & 0 & 0 \\ 0 & 0 & -M_\perp \sigma_z & 0 \\ 0 & 0 & 0 & -M_\parallel \sigma_x \end{pmatrix}. \quad (5.60)$$

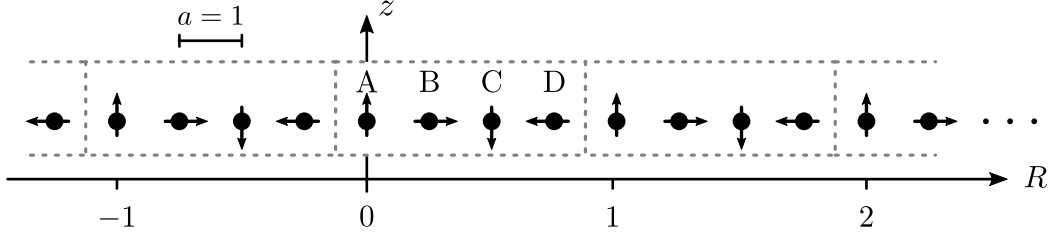


Figure 5.24: Unit cells for a 1D system experiencing a magnetic texture with a 4-site periodicity. The four sites of a unit cell are labelled as $\{A, B, C, D\}$ and the center of inversion is here chosen to be the site A of the $R = 0$ unit cell.

Main target of this appendix is to shed light to the topological classification at inversion-symmetric points/HSPs. At $k_x = 0$, we find that I and $\{E | \pi/Q\}$ possess the twofold degenerate eigenvalues ± 1 and $\pm i$, respectively. Instead, at $k_x = \pi/4$, we find that I possesses the eigenvalues $\{1, 1, 1, -1\}$, while $\{E | \pi/Q\}$ possesses the twofold degenerate eigenvalues ± 1 . The emergence of different eigenvalues for these symmetry operations at the two inversion-symmetric points implies that the respective symmetry classes generally differ. In contrast, these symmetry operators are k_x -independent in the wave-number-transfer description, thus implying that the various inversion-symmetric points and HSPs are dictated by the same symmetry and topological properties. The apparent discrepancy is attributed to the fact that the Hamiltonian in the wave-number-transfer description is not compactified. Therefore, caution is needed when performing the classification using this formalism. In fact, we find that the topological classifications coincide for the the inversion-symmetric points and HSPs where a magnetic gap opens. In contrast, at inversion-symmetric points/HSPs where a Kramers degeneracy appears and the magnetization becomes ineffective, only the sublattice-based topological classification is valid.

5.C Space Group Symmetry-Protected Degeneracies

Nonsymmorphic space group operations take the form $\{g | \mathbf{t}\}$, where g defines a point group operation and \mathbf{t} is a translation by a fraction of a Bravais lattice vector. A space group symmetry is referred to as nonsymmorphic, when no coordinate system can be chosen to remove the translation \mathbf{t} in $\{g | \mathbf{t}\}$ [32, 134, 135, 461, 462]. This is satisfied when $g\mathbf{t} = \mathbf{t}$, i.e., when the involved translation is along a HSP of g . If this is not the case, the component of \mathbf{t} which is perpendicular to the HSP of g is obsolete and can be removed. However, such a removal may result in the redefinition of other symmmorphic symmetry elements, which in the new basis may involve a translation. The elements that become simultaneously modified in such a process define the so-called set of “offcentered symmetry elements”. In the main text, we encounter pairs of such offcentered symmetries. As explained below, their presence introduces protected degeneracies in the spectrum. See also refs. [463–466].

The fact that a genuine nonsymmorphic symmetry requires that the equivalence $g\mathbf{t} = \mathbf{t}$ should be met, further restricts the systems in which nonsymmorphic symmetries can provide topological protection to boundary modes and thus stabilize crystalline topological phases. Since such a boundary is required to preserve both g and \mathbf{t} , only 3D systems can exhibit topological crystalline phases induced by nonsymmorphic symmetries. Indeed, edges of 2D systems generally fail to fulfill these criterion, and the presence of nonsymmorphic symmetries can only affect the bulk topological properties of the

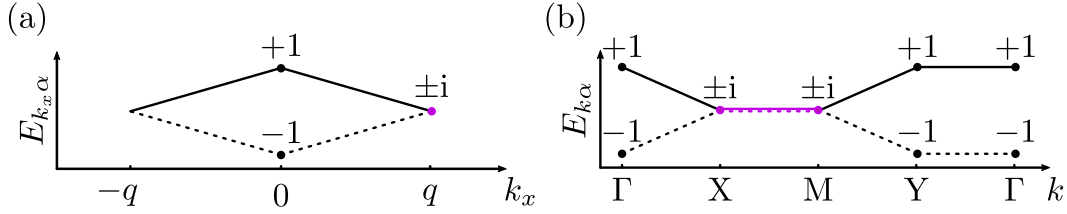


Figure 5.25: Sketches of degeneracies in the MBZ, in the case of a MHC in 1D and 2D [panels (a) and (b)]. The labels show the eigenvalues of the space group symmetry which commutes with the Hamiltonian in the given HSP. Degeneracies are colored in purple.

system. Consider, for example, a 2D system with the nonsymmorphic symmetry $\{\sigma_{xz} | (1,0)\}$. For this particular case, the edge (01) is invariant under σ_{xz} while (10) is preserving $\{E | (1,0)\}$, i.e., we can never find an edge which is invariant under the symmetry operation $\{\sigma_{xz} | (1,0)\}$. Extending the example to 3D systems, we immediately observe that the surface (001) preserves both σ_{xz} and $\{E | (1,0)\}$, and can thus potentially exhibit topological surface states protected by the nonsymmorphic symmetry. Hence we conclude that a nonsymmorphic symmetry cannot induce a crystalline topological phase in 2D systems, except in rare cases where $g\mathbf{k} = \mathbf{k}$ [32].

For the MHC texture in 1D, our system is invariant under a set of symmetries shown in table 5.1. Out of these, we find that the symmetry element $\{\sigma_{yz} | \pi/Q\}$ is rendered symmorphic after translating the magnetic unit cell by $\{E | a\}$. At the same time, the point group element $R_{yz} = \sigma_{yz}T\Theta$ is redefined and in the new basis involves a translation. Specifically, the two symmetry elements become redefined as follows

$$\{\sigma_{yz} | \pi/Q\} \rightarrow \sigma_{yz} \quad \text{and} \quad R_{yz} \rightarrow \{R_{yz} | \pi/Q\}. \quad (5.61)$$

In fact, it is not possible to choose a coordinate system for which both $\{\sigma_{yz} | \pi/Q\}$ and R_{yz} become regular point group elements. This leads to symmetry-protected degeneracies in the spectrum. To exemplify this, we rely on the relation: $\{\sigma_{yz} | \pi/Q\} R_{yz} = R_{yz} \{\sigma_{yz} | \pi/Q\} e^{ik_x \pi/q}$. By further taking into account that $\Theta^2 = +\mathbb{1}$, which holds in the here-relevant BDI symmetry class, we obtain $\{\sigma_{yz} | \pi/Q\}^2 = +\mathbb{1} e^{ik_I \pi/q}$ for $k_I = 0, q$. This leads to the two eigenvalue equations

$$\{\sigma_{yz} | \pi/Q\} |k_I, \pm\rangle = \pm e^{ik_I \pi/Q} |k_I, \pm\rangle, \quad \{\sigma_{yz} | \pi/Q\} R_{yz} |k_I, \pm\rangle = \pm e^{3ik_I \pi/Q} R_{yz} |k_I, \pm\rangle. \quad (5.62)$$

We thus observe that the two pairs $|k_I, \pm\rangle$ and $R_{yz} |k_I, \pm\rangle$ have the same (opposite) eigenvalues at $k_I = 0$ ($k_I = q$). The two states are therefore mutually “parallel” (orthogonal) at $k_I = 0$ ($k_I = q$), ultimately leading to a protected degeneracy at $k_x = q$, see fig. 5.25(a).

The above degeneracies appear at isolated points of the MBZ. This behavior has to be compared with the consequences of the genuinely nonsymmorphic symmetry $\{\sigma_{xz} | \pi/Q\}$ $k_x = k_x$. The latter can be employed to label the eigenstates of the Hamiltonian for all k_x in the 1D MBZ. Since the system is effectively spinless, $\Theta^2 = +\mathbb{1}$, we find

$$\{\sigma_{xz} | \pi/Q\} |k_x, \pm\rangle = \pm e^{ik_x \pi/Q} |k_x, \pm\rangle. \quad (5.63)$$

From the above eigenvalues, in combination with Θ , we know that the spectrum in the MBZ must follow the sketch in fig. 5.25(a), which is compatible with the degeneracies imposed by the pair of

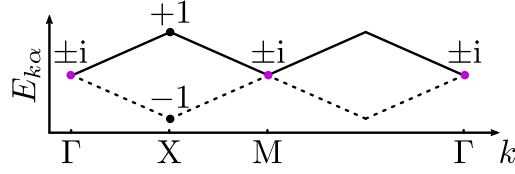


Figure 5.26: Sketch of the general band structure in the MBZ of a system in the SWC_4 magnetic phase.

offcentered symmetries. The twofold degeneracy at $k_x = q$ is enforced because the eigenvalues $\pm i$ are connected by the antiunitary symmetry Θ . Notably, this degeneracy can be alternatively seen as the result of the emergent time-reversal symmetry effected by $\tilde{\Theta} = \{\sigma_{xz} | \pi/Q\}\Theta \equiv \{T | \pi/Q\}$, with $\tilde{\Theta}^2 = \mathbb{1}e^{ik_x\pi/q}$.

Similar arguments for the MHC in 2D establish once again that the symmetries $\{\sigma_{yz} | \pi/Q\}$ and R_{yz} constitute a pair of offcentered ones, and impose a twofold degeneracy at $k_x = q$ for all $k_y \in [0, 2\pi)$. This gives insight about the key features of the generic band structure which is depicted in fig. 5.25(b), and reveals that the pairing gap cannot be compensated by the magnetic gap in this HSP. We conclude this section with a brief comment on the generic characteristics of the band structure for a 2D system under the influence of a SWC_4 texture. In this case, we do not find any offcentered symmetries. Nonetheless, twofold degeneracies still appear as the result of the presence of nonsymmorphic symmetries. See fig. 5.26 for a sketch of the general dispersion in the MBZ.

5.D Details on Topological Invariants

Winding Number in 1D One-Band Models for $\Delta_{k_x} = \Delta$

The calculation is facilitated by noticing the presence of the antiunitary time-reversal symmetry $\tilde{\Theta} = \rho_2\sigma_y K$ of the Hamiltonian in eqn. (5.23). Being k_x -independent, $\tilde{\Theta}$ influences the topological classification in the entire MBZ. Note that such a k_x -independent symmetry does not appear in the sublattice formulation of the problem. The product involving $\tilde{\Theta}$ and the preexisting $\Theta = K$ symmetry, induces the unitary symmetry $\tilde{\mathcal{O}} = \tilde{\Theta}\Theta = \rho_2\sigma_y$. In particular, this allows us to diagonalize the BdG Hamiltonian into blocks labelled by the eigenvalues of $\tilde{\mathcal{O}}$. By performing the unitary transformation induced by the operator $\tilde{\mathcal{S}} = (\tilde{\mathcal{O}} + \sigma_z)/\sqrt{2}$, we obtain the blocks

$$\begin{aligned} \mathcal{H}'_{k_x, \sigma} = & \left[h_{k_x}^{(0)} + h_{k_x}^{(1)}\rho_2 + h_{k_x}^{(2)}\eta_3 + h_{k_x}^{(3)}\eta_3\rho_2 \right] \tau_3 - M_\sigma\rho_1 + M_{-\sigma}\eta_1\rho_1 \\ & + \left[\Delta_{k_x}^{(0)} + \Delta_{k_x}^{(1)}\rho_2 + \Delta_{k_x}^{(2)}\eta_3 + \Delta_{k_x}^{(3)}\eta_3\rho_2 \right] \tau_1 \end{aligned} \quad (5.64)$$

where $M_\sigma = (M_{||} + \sigma M_{\perp})/2$, with $\sigma = \pm 1$ labeling the eigenvalues of σ_z in the new frame. Both blocks reside in BDI class with $\Theta = K$, $\Xi = \rho_2\tau_2 K$ and $\Pi = \rho_2\tau_2$. Consequently, the presence of the unitary symmetry effected the symmetry class transition $\text{BDI} \rightarrow \text{BDI} \oplus \text{BDI}$, which allows defining a winding number w_σ for each block.

One observes that each block leads to a fractional winding number $\pm 1/2$. As discussed previously in ref. [284], this peculiarity is due to the choice of the spinor, which, while being convenient, does not guarantee that the Hamiltonian blocks satisfy the compactification criteria required to define the \mathbb{Z}

index. As a result, the block winding numbers cannot define two independent topological invariants, but they have to be added or subtracted to provide the proper invariant. The correct way to combine them can be inferred based on a well-known limiting case, or, by adding infinitesimal terms which violate the unitary symmetry but preserve Θ , Ξ and Π . Nevertheless, here it is straightforward to infer how to combine the block invariants, by investigating their behavior in the already established result for $M_{\perp} = M_{\parallel} = M > 0$. In this known case, the block winding numbers become

$$w_{+}^{M_{\parallel}, \perp=M} = -\frac{\text{sgn}\left[(M^2 - \Delta^2)\left[1 + (\Delta^2 - M^2)/(2\mu)^2\right]\right]}{2}, \quad w_{-}^{M_{\parallel}, \perp=M} = 1/2. \quad (5.65)$$

In order to retrieve the topological invariant of eqn. (5.13), we verify that the winding number should be defined as

$$w = w_{-} - w_{+}. \quad (5.66)$$

Winding Number in 1D 1BMs for a generic Δ_{k_x}

Here we obtain an expression for the winding number in the case of a generic Δ_{k_x} . To facilitate the derivation of an analytical result, we restrict to the weak coupling limit. We block diagonalize the low-energy BdG Hamiltonian in eqn. (5.29) and find

$$\mathcal{H}_{k_x, \sigma}^{\text{low-en}} = \left(\xi_{k_x; q}^{+} + \xi_{k_x; q}^{-} \rho_2\right) \tau_3 - M_{\sigma} \rho_1 + \left(\Delta_{k_x; q}^{+} + \Delta_{k_x; q}^{-} \rho_2\right) \tau_1, \quad (5.67)$$

and define

$$\det A_{k_x, \sigma}^{\text{low-en}} = \left(\xi_{k_x; q}^{+}\right)^2 + \left(\Delta_{k_x; q}^{+}\right)^2 - \left(\xi_{k_x; q}^{-}\right)^2 - \left(\Delta_{k_x; q}^{-}\right)^2 - M_{\sigma}^2 + 2i\left(\xi_{k_x; q}^{-} \Delta_{k_x; q}^{+} - \xi_{k_x; q}^{+} \Delta_{k_x; q}^{-}\right), \quad (5.68)$$

which is of the exact same form as eqn. (5.7), with the crucial difference that here $k_x \in \text{MBZ}$, which implies that the contribution of the last term in the topological invariant of eqn. (5.25) drops out. In addition, when $k_x = 0$ constitutes the only wave number where a gap closing takes place, one directly retrieves the result of eqn. (5.26) after setting $\Delta_{k_x} = \Delta$.

Mirror Invariant in 1D One-Band Models

To evaluate the mirror invariant of eqn. (5.30) at $k_x = 0$, we restrict to the weak-coupling regime, and block diagonalize eqn. (5.29) by means of effecting the unitary transformation $(R_{yz} + \sigma_x)/\sqrt{2}$, which yield the blocks

$$\mathcal{H}_{k_x=0, \sigma}^{\text{low-en}} = \xi_{0; q}^{+} \tau_3 + \Delta_{0; q}^{+} \tau_1 - \sigma(M_{\perp} + M_{\parallel} \rho_3)/2. \quad (5.69)$$

The above is further block-diagonalizable by introducing the eigenstates of ρ_3 labelled by $\rho = \pm 1$. Straightforward manipulations following after the definitions of eqn. (5.17), yield the result for each $\mathcal{H}_{k_x=0, \sigma, \rho}^{\text{low-en}}$ block

$$n_{k_x=0, \sigma, \rho} = \sigma \rho \frac{1 + \text{sgn}\left[M_{\rho}^2 - \left(\xi_{0; q}^{+}\right)^2 - \left(\Delta_{0; q}^{+}\right)^2\right]}{2}. \quad (5.70)$$

Similar to the construction leading to eqn. (5.66), also here one has to consider combinations of the invariants stemming from the ρ blocks. Specifically, here we need to define $n_{k_x=0, \sigma} = -(n_{k_x=0, \sigma, -} + n_{k_x=0, \sigma, +})/2$.

Glide Majorana Parity

The glide Majorana parity is here defined as a \mathbb{Z}_2 invariant for the BDI class in 0D. This is given as the parity of the winding number for an interpolation \mathcal{H}_ℓ with $\ell \in [0, 2\pi)$ connecting the Hamiltonian of interest \mathcal{H}_π and a reference Hamiltonian \mathcal{H}_0 . The winding number reads

$$w_{\text{inter}} = \int_0^{2\pi} \frac{d\ell}{2\pi i} \text{tr} \left(A_\ell^{-1} \frac{d}{d\ell} A_\ell \right). \quad (5.71)$$

By virtue of the charge-conjugation symmetry, we obtain

$$i\pi w_{\text{inter}} = \ln \left[\det(A_\pi) / \det(A_0) \right] \quad \Rightarrow \quad P_G = \text{sgn} [(-1)^{w_{\text{inter}}}] = \text{sgn} \prod_{\ell=0, \pi} \det(A_\ell). \quad (5.72)$$

To obtain the result of eqn. (5.33), we employ the above equation, where each one of the two σ blocks of eqn. (5.31) is considered as a reference Hamiltonian for the other. In the weak-coupling limit, we project onto the $\eta_3 = 1$ block and obtain the Hamiltonian blocks

$$\mathcal{H}_{k_x=0, \sigma}^{\text{low-en}} = \xi_{0;q}^+ \tau_3 + \Delta_{0;q}^+ \tau_1 - M_\sigma \rho_1. \quad (5.73)$$

We block-off diagonalize the above blocks via the transformation $(\rho_2 \tau_2 + \tau_3) / \sqrt{2}$ and find

$$A_{k_x=0, \sigma} = -\Delta_{0;q}^+ - M_\sigma \rho_3 - i\xi_{0;q}^+ \rho_2. \quad (5.74)$$

By obtaining the determinant of the above upper off-diagonal blocks, we directly find the result of eqn. (5.33).

Winding Number in 1D Two-Band Models

To obtain the winding number for an interband-only MHC, we restrict to the low-energy sector of the system and consider the projected spinor

$$\tilde{\mathcal{C}}_{k_x}^\dagger = \frac{\rho_2 + \rho_3}{\sqrt{2}} (\mathcal{C}_{k_x+3q;e}^\dagger, \mathcal{C}_{k_x-3q;e}^\dagger, \mathcal{C}_{k_x+3q;h}^\dagger, \mathcal{C}_{k_x-3q;h}^\dagger), \quad (5.75)$$

as well as the corresponding Hamiltonian blocks:

$$\mathcal{H}_{k_x}^{\text{low-en}} = \sum_{s=e,h} \mathcal{P}_s \left[\left(\xi_{k_x;-3q}^{s,+} + \xi_{k_x;-3q}^{s,-} \right) \tau_3 + \Delta^s \tau_1 \right] - (\widehat{M}_\perp \rho_1 \sigma_z + \widehat{M}_\parallel \rho_3 \sigma_x) / 2. \quad (5.76)$$

By exploiting the $\tilde{\mathcal{O}} = \rho_2 \sigma_y$ symmetry, we can block diagonalize the Hamiltonian by means of $\tilde{\mathcal{S}} = (\tilde{\mathcal{O}} + \sigma_z) / \sqrt{2}$

$$\mathcal{H}_{k_x, \sigma}^{\text{low-en}} = \sum_{s=e,h} \mathcal{P}_s \left[\left(\xi_{k_x;-3q}^{s,+} + \xi_{k_x;-3q}^{s,-} \rho_2 \right) \tau_3 + \Delta^s \tau_1 \right] - \widehat{M}_\sigma \rho_1. \quad (5.77)$$

By solely considering interband magnetic scattering, i.e. $\widehat{M}_\sigma = M_\sigma \kappa_1$ we find the emergent unitary symmetry $O = \kappa_3 \sigma_y$ in the original basis, which allows for yet another block diagonalization via $(\tilde{\mathcal{S}}^\dagger O \tilde{\mathcal{S}} + \rho_1) / \sqrt{2}$

$$\mathcal{H}_{k_x, \rho}^{\text{low-en}} = \sum_{s=e,h} \mathcal{P}_s \left[\left(\xi_{k_x;-3q}^{s,+} + \rho \xi_{k_x;-3q}^{s,-} \kappa_3 \right) \tau_3 + \Delta^s \tau_1 \right] - \rho M_\sigma \kappa_1, \quad (5.78)$$

where $\rho = \pm 1$ label the eigenvalues of the matrix ρ_1 . Hence, we block off-diagonalize the Hamiltonian via the unitary transformation $(\Pi + \tau_3)/\sqrt{2}$, and obtain

$$\det A_{k_x, \sigma, \rho}^{\text{low-en}} = \xi_{k_x + \rho 3q}^e \xi_{k_x - \rho 3q}^h + \Delta^e \Delta^h - M_\sigma^2 + i (\xi_{k_x + \rho 3q}^e \Delta^h - \xi_{k_x - \rho 3q}^h \Delta^e). \quad (5.79)$$

A nonzero intraband magnetization components restores the $\text{BDI} \oplus \text{BDI}$ class found in one-band models and yields

$$A_{k_x, \sigma}^{\text{low-en}} = - \sum_{s=e,h} \mathcal{P}_s \left[i \left(\xi_{k_x; -3q}^{s,+} \rho_2 + \xi_{k_x; -3q}^{s,-} \right) + \Delta^s + M_\sigma^s \rho_3 \right] - \kappa_1 M_\sigma^{\text{eh}} \rho_3. \quad (5.80)$$

Invariants for 2D One-Band Models in the MHC phase and with $\Delta_{\mathbf{k}} \sim \{\mathbf{B}_{2g}, \mathbf{A}_{2g}\}$

For a gap function transforming as the B_{2g} or A_{2g} IR, the resulting point group becomes G_{MHC} accompanied by the space group symmetries $\{T, \sigma_{xz, yz}^Q | (\pi/Q, 0)\}$. As discussed in sec. 5.5, these modified symmetries lead to a $\text{BDI} \oplus \text{BDI}$ class in the $k_x = 0$ HSP and a $\text{AI} \oplus \text{AI}$ class for $k_y = \{0, \pi\}$, since, for the latter, the gap function vanishes. Specifically, for these HSPs, denoted by the wave-vectors $\mathbf{k}_{R_{xz}}$, the Hamiltonian takes the simple form in the weak-coupling regime

$$\mathcal{H}_{\mathbf{k}_{R_{xz}}, \sigma, \tau} = \tau \left[\xi_{\mathbf{k}_{R_{xz}}; \mathbf{q}_1}^+ + \xi_{\mathbf{k}_{R_{xz}}; \mathbf{q}_1}^- \rho_2 \right] - M_\sigma \rho_1, \quad (5.81)$$

where $\tau = \pm 1$ labels the two AI blocks. This class only supports a strong mirror \mathbb{Z} invariant for a nodal spectrum, with the associated invariant defined similar to eqn. (5.44). Specifically we find the normalized complex function entering in the invariant

$$Z_{\epsilon, k_x, \sigma, \tau} = \frac{\xi_{\mathbf{k}_{R_{xz}} - \mathbf{q}_1} \xi_{\mathbf{k}_{R_{xz}} + \mathbf{q}_1} + \epsilon^2 + M_\sigma^2 + 2i\tau\epsilon \xi_{\mathbf{k}_{R_{xz}}; \mathbf{q}_1}^+}{\sqrt{(\xi_{\mathbf{k}_{R_{xz}} - \mathbf{q}_1} \xi_{\mathbf{k}_{R_{xz}} + \mathbf{q}_1} + \epsilon^2 + M_\sigma^2)^2 + 4\epsilon^2 (\xi_{\mathbf{k}_{R_{xz}}; \mathbf{q}_1}^+)^2}}. \quad (5.82)$$

Instead for the $k_x = 0$ HSP, the BdG Hamiltonian in the weak-coupling limit becomes

$$\mathcal{H}_{\mathbf{k}=(0, k_y)} = \xi_{\mathbf{k}=(q, k_y)} \tau_3 - \Delta_{\mathbf{k}=(q, k_y)} \rho_2 \tau_1 - (M_\perp \rho_1 \sigma_z + M_\parallel \rho_3 \sigma_x)/2. \quad (5.83)$$

For this case we can only define a strong invariant for a fully gapped spectrum, namely the glide $w_{G, k_x=0}$ and mirror $w_{M, k_x=0}$ winding numbers, see eqns. (5.45) and (5.20), after replacing $\epsilon \rightarrow k_y$ in the latter. For the symmetry $\{T | (\pi/Q, 0)\} \Theta \equiv \tilde{\mathcal{O}}$ we block diagonalize the Hamiltonian via $\tilde{\mathcal{S}}$ and find

$$\mathcal{H}_{\mathbf{k}=(0, k_y), \sigma} = \xi_{\mathbf{k}=(q, k_y)} \tau_3 - \Delta_{\mathbf{k}=(q, k_y)} \rho_2 \tau_1 - M_\sigma \rho_1. \quad (5.84)$$

After block off-diagonalizing the above Hamiltonian by means of the unitary operator $(\rho_2 \tau_2 + \tau_3)/\sqrt{2}$, we obtain

$$\det A_{k_y, \sigma} = \xi_{\mathbf{k}=(q, k_y)}^2 - \Delta_{\mathbf{k}=(q, k_y)}^2 - M_\sigma^2 + 2i \xi_{\mathbf{k}=(q, k_y)} \Delta_{\mathbf{k}=(q, k_y)}. \quad (5.85)$$

For the remaining two symmetries $\{\sigma_{yz}^Q | (\pi/Q, 0)\}$ and R_{yz}^Q , which in fact commutes with $\tilde{\mathcal{O}}$, we find that their matrix representations coincide in each σ block. This leads to the additional block diagonalization by means of the unitary operator $(\rho_1 \tau_3 + \rho_2)/\sqrt{2}$

$$\mathcal{H}_{\mathbf{k}=(0, k_y), \sigma, \rho} = \xi_{\mathbf{k}=(q, k_y)} \tau_3 - \rho \Delta_{\mathbf{k}=(q, k_y)} \tau_1 - \rho M_\sigma \tau_3 \quad (5.86)$$

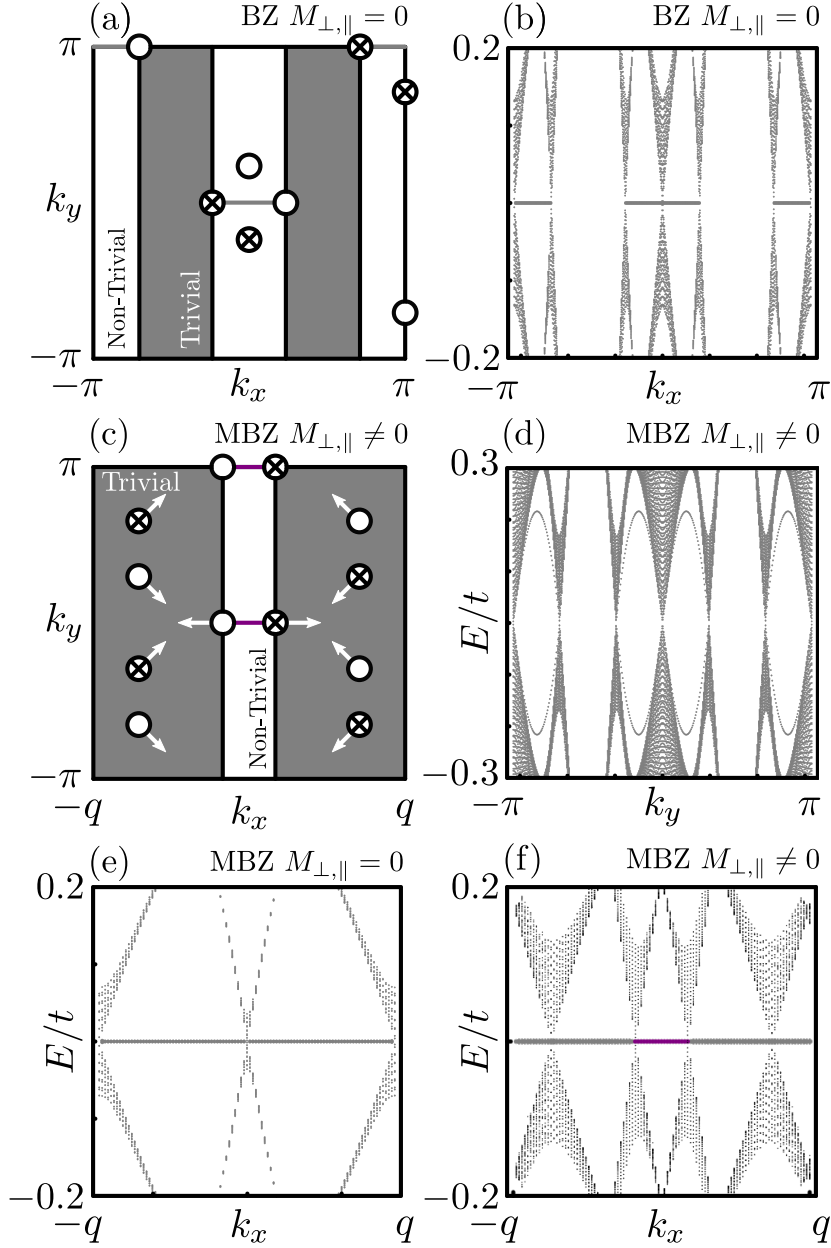


Figure 5.27: Nodal spectrum for the one-band model in fig. 5.9 in the MHC phase with $\Delta_{\mathbf{k}} = \Delta \sin k_x \sin k_y \sim B_{2g}$. (a) displays the nodes in the first BZ in the absence of magnetism. These symmetry enforced nodes give rise to Majorana flat bands, as seen in (b). (c) illustrates the same as in (a), after we include magnetism and downfold to the MBZ. We see that the initial nodes in (a) split and move on straight lines. This ultimately lifts the Majorana flat bands on edges perpendicular to the magnetic ordering wave-vector \mathbf{Q} , see (d), since the vorticity of the nodes cancel when projected onto this edge. In contrast, we see in (f) that new Majorana flat bands (marked in purple) are established on edges parallel to \mathbf{Q} in addition to the Majorana flat bands inherited from the case of $M_{\parallel} = M_{\perp} = 0$ (marked in gray), cf. (e). We used $L_x = L_y = 401$, $\Delta = 1t$ throughout, and $M_{\perp,||} = 0.8t$ in (d) and (f).

which we further block off-diagonalize with by means of a unitary transformation with operator $(\tau_2 + \tau_3)/\sqrt{2}$, and find $A_{\mathbf{k}=(0,k_y),\sigma,\rho} = -i[\xi_{\mathbf{k}=(q,k_y)} - \rho M_\sigma] + \rho \Delta_{\mathbf{k}=(q,k_y)}$.

In order to exemplify the above, we consider in the following the one-band model from fig. 5.9 in the MHC phase, with a pairing function transforming as the B_{2g} IR, specifically $\Delta_{\mathbf{k}} = \Delta \sin k_x \sin k_y$. Through relation eqn. (5.43), we find the gap closing points $\mathbf{k}_c : \{k_y = 0, \pi, \text{ or } k_x = \pm \arccos(-2t \cos k_y \cos q/\mu)\}$. For the values of q and μ used in fig. 5.9, we obtain the simple relation $\mathbf{k}_c : \{k_y = 0, \pi, \text{ or } k_x = \pm k_y\}$. For the gap closing points $\mathbf{k}_c = (k_x, 0)$ and (k_x, π) we straightforwardly find the gap closing criterion $\xi_{\mathbf{k}_{R_{xz}} - \mathbf{q}_1} \xi_{\mathbf{k}_{R_{xz}} + \mathbf{q}_1} = M_\sigma^2$. When the magnetic wave-vector \mathbf{Q}_1 coincides with the nesting vector \mathbf{Q}_N , we observe that the spectrum is nodal even for $M_\perp = M_\parallel = 0$ with $\mathbf{k}_c = (0, 0)$ and $(0, \pi)$. For a nonzero $M_{\perp,\parallel}$ the nodes move along the xz HSPs. The remaining set of nodes, i.e. the ones moving along the lines $k_x = \pm k_y$ appear for $M_\sigma^2 = \sqrt{\xi_{\mathbf{k}-\mathbf{q}_1} \xi_{\mathbf{k}+\mathbf{q}_1} + \Delta_{\mathbf{k}-\mathbf{q}_1} \Delta_{\mathbf{k}+\mathbf{q}_1}}$. Similar to the nodes moving along the HSPs $k_y = \{0, \pi\}$, also here we find a nodal spectrum for $M_\perp = M_\parallel = 0$ for $k_x = \pm k_y = q$ and $q + \pi$. Upon increasing $M_{\perp,\parallel}$ the nodes move along the lines $k_x = \pm k_y$.

In fig. 5.27 we sketch the path of the nodes, the vorticities and resulting edge spectra. As seen in (a), already in the absence of the MHC, the spectrum contains zeros which are enforced by the symmetry of $\Delta_{\mathbf{k}}$. These give rise to topologically-protected Majorana flat bands. This is exemplified in (b) using open boundary conditions in the y axis. Since in this case $M_{\perp,\parallel} = 0$, we show the original BZ. After switching on magnetism and transferring to the MBZ, we observe in (c) that the nodes split and start to move on straight lines as we vary the pairing and magnetic gaps. This splitting lifts the preexisting Majorana flat bands on edges perpendicular to the \mathbf{Q} vector, as a consequence of the cancelling vorticities. This becomes more transparent by comparing (b) and (d). Instead, for edges parallel to the \mathbf{Q} -vector, we recover the Majorana flat bands in (b), but we also obtain newly-established Majorana flat bands stemming from the split nodes. This is illustrated in (e), where we show the same as in (b) but now in the MBZ, and in (f) with $M_{\perp,\parallel} \neq 0$.

5.E Functions for the representation of the BdG Hamiltonian in 2D

The matrix function $F(f_{\mathbf{k}})$ has the form

$$\begin{aligned} F(f_{\mathbf{k}}) &= f_{\mathbf{k}}^{(0,0)} + f_{\mathbf{k}}^{(0,1)} \rho_3 + f_{\mathbf{k}}^{(0,2)} \eta_3 + f_{\mathbf{k}}^{(0,3)} \eta_3 \rho_3 \\ &+ \lambda_3 [f_{\mathbf{k}}^{(1,0)} + f_{\mathbf{k}}^{(1,1)} \rho_3 + f_{\mathbf{k}}^{(1,2)} \eta_3 + f_{\mathbf{k}}^{(1,3)} \eta_3 \rho_3] \\ &+ \zeta_3 [f_{\mathbf{k}}^{(2,0)} + f_{\mathbf{k}}^{(2,1)} \rho_3 + f_{\mathbf{k}}^{(2,2)} \eta_3 + f_{\mathbf{k}}^{(2,3)} \eta_3 \rho_3] \\ &+ \zeta_3 \lambda_3 [f_{\mathbf{k}}^{(3,0)} + f_{\mathbf{k}}^{(3,1)} \rho_3 + f_{\mathbf{k}}^{(3,2)} \eta_3 + f_{\mathbf{k}}^{(3,3)} \eta_3 \rho_3], \end{aligned} \quad (5.87)$$

with the functions $f_{\mathbf{k}}^{(t,s)} = (-1)^{s+t} f_{-\mathbf{k}}^{(t,s)}$ defined as

$$\begin{aligned} f_{\mathbf{k}}^{(0,s)} &= [f_{\mathbf{k}-\mathbf{q}_2}^{(s)} + f_{\mathbf{k}+\mathbf{q}_2}^{(s)} + f_{\mathbf{k}+3\mathbf{q}_2}^{(s)} + f_{\mathbf{k}-3\mathbf{q}_2}^{(s)}]/4, \\ f_{\mathbf{k}}^{(1,s)} &= [f_{\mathbf{k}-\mathbf{q}_2}^{(s)} - f_{\mathbf{k}+\mathbf{q}_2}^{(s)} + f_{\mathbf{k}+3\mathbf{q}_2}^{(s)} - f_{\mathbf{k}-3\mathbf{q}_2}^{(s)}]/4, \\ f_{\mathbf{k}}^{(2,s)} &= [f_{\mathbf{k}-\mathbf{q}_2}^{(s)} + f_{\mathbf{k}+\mathbf{q}_2}^{(s)} - f_{\mathbf{k}+3\mathbf{q}_2}^{(s)} - f_{\mathbf{k}-3\mathbf{q}_2}^{(s)}]/4, \\ f_{\mathbf{k}}^{(3,s)} &= [f_{\mathbf{k}-\mathbf{q}_2}^{(s)} - f_{\mathbf{k}+\mathbf{q}_2}^{(s)} - f_{\mathbf{k}+3\mathbf{q}_2}^{(s)} + f_{\mathbf{k}-3\mathbf{q}_2}^{(s)}]/4, \end{aligned} \quad (5.88)$$

with the functions $f_{\mathbf{k}}^{(s)}$ defined as in the main text eqn. (5.24)

$$\begin{aligned} f_{\mathbf{k}}^{(0)} &= (f_{\mathbf{k}-q} + f_{\mathbf{k}+q} + f_{\mathbf{k}+3q} + f_{\mathbf{k}-3q})/4, & f_{\mathbf{k}}^{(1)} &= (f_{\mathbf{k}-q} - f_{\mathbf{k}+q} + f_{\mathbf{k}+3q} - f_{\mathbf{k}-3q})/4, \\ f_{\mathbf{k}}^{(2)} &= (f_{\mathbf{k}-q} + f_{\mathbf{k}+q} - f_{\mathbf{k}+3q} - f_{\mathbf{k}-3q})/4, & f_{\mathbf{k}}^{(3)} &= (f_{\mathbf{k}-q} - f_{\mathbf{k}+q} - f_{\mathbf{k}+3q} + f_{\mathbf{k}-3q})/4. \end{aligned} \quad (5.89)$$

Conclusions and Outlook

In this thesis we have studied several aspects of the prototypical Hamiltonian presented in eqn. (4), with a particular focus on nematic order generated by nearest neighbor Coulomb interactions and topological superconductivity induced by magnetic textures. In the following we summarize some of our key findings, and discuss potential future directions.

In chap. 1 we derived a set of essential tools in the context of symmetries in condensed matter physics. By applying these tools on the mean-field decoupled Hamiltonian in eqn. (4), we found, in agreement with previous studies [126, 127], that the nearest neighbor Coulomb interactions give rise to two distinct effects, namely wave vector-dependent band renormalizations and nematic order. More specifically, refs. [126, 127] found that the leading nematic order parameter in mono-layer FeSe is of intra-orbital B_{1g} character. With this in mind, we performed in chap. 2 a phenomenological and microscopic study of B_{1g} nematicity in disorder systems, where we established that disorder locally induces nematicity in the bulk tetragonal phase. The latter can potentially explain the local detection of nematicity above T_{nem} in experiments [190–199]. Yet, due to the specific A_{1g} form of the impurity potential, disorder can generally not induce a global $\mathbf{Q} = \mathbf{0}$ nematic phase. On the other hand, we also found that under the right circumstances, a critical concentration of impurities can modify the Stoner criterion, and consequently increase the nematic transition temperature T_{nem} . Next, we performed in chap. 3 an extensive microscopic study of nematic order in FeSe driven by nearest-neighbor Coulomb interactions, in effort to settle some of the puzzling electronic properties of this material. In particular, we pursued a deeper understanding of the potential physical mechanism leading to the normal state nematicity, the anisotropic spin excitations found in experiments [211] and the associated gap structure. Within our approach, we found two consecutive phase transitions upon lowering of the temperature. The order parameter belonging to the high temperature phase transition was the usual intra-orbital B_1 nematic order, similar to the one previously found in refs. [126, 127], whereas the low-temperature order parameter was of a novel type. Specifically, we found the second phase transition to be accompanied by an inter-orbital E_x (or E_y) order parameter, which allowed for a hybridization gap at the Y (X) point of the 1-Fe Brillouin zone, ultimately removing the Y (X) pocket from the Fermi level altogether, as suggested by experiments [233, 234]. Although the here-established nematic Fermi surface qualitatively agrees with experiments, it does not lead to the highly anisotropic spin excitations found in experiments [211], as reflected in the calculated spin susceptibility, without invoking the physics of orbital selective correlations. At the moment, there are no experimental evidence advocating for a double phase transition in FeSe, and a direct extension of this study would therefore be to perform calculations similar to those presented in chap. 2, but for an order parameter transforming as the 2D IR E. Such calculations could open the door to new experimental hints to search for, and perhaps an alternative identification of the second phase transition, in contrast to the

usual specific heat measurements.

In part II of this thesis, we studied the potential topological phases of the prototypical Hamiltonian presented in eqn. (4), with a particular focus on topological superconductivity induced by magnetic textures. In chap. 4, we studied in great detail Majorana modes trapped by vortex defects in magnetic textures. The magnetic textures were considered to either coexist or be in proximity to a robust nodal superconductor. We found that 2D systems with magnetic shift and/or spin vortex defects can host MZMs, when the system resides in one of the three symmetry classes BDI, D or DIII. In 3D systems, on the other hand, it is only the classes D and DIII that supports Majorana modes. We confirmed these predictions by calculating the respective topological invariants analytically, followed by a numerical examination of the various relevant cases. Lastly, in chap. 5 we performed an extensive classification of topological superconductors induced by various magnetic textures. By addressing both strong, weak and crystalline topological phases in fully gapped and nodal systems, we found that the underlying symmetries of the magnetic textures played a fundamental role, and gave rise to a broad variety of topological excitations such as flat, uni- or bi-directional, quasi-helical and chiral Majorana edges modes. Although the results presented in chap. 4 and 5 are both novel and interesting, a natural extension of these studies, as a consequence of their explorative nature, would be to apply these on realistic models. Especially for the studies in chap. 5, since a prime candidate appears to be the FeSCs, for which one could perform a self-consistent study to determine whether one of the desired magnetic textures in fact can coexists with superconductivity, and thereby give rise to an intrinsic topological superconductor.

Bibliography

- [1] P. W. Anderson, “*More Is Different*,” *Science* **177**, 393–396 (1972) [doi: [10.1126/science.177.4047.393](https://doi.org/10.1126/science.177.4047.393)].
- [2] K. A. Brading and E. Castellani, “Symmetries in physics: philosophical reflections,” (2002).
- [3] E. Fradkin, S. A. Kivelson, M. J. Lawler, J. P. Eisenstein, and A. P. Mackenzie, “*Nematic Fermi Fluids in Condensed Matter Physics*,” *Annu. Rev. Condens. Matter Phys.* **1**, 153–178 (2010) [doi: [10.1146/annurev-conmatphys-070909-103925](https://doi.org/10.1146/annurev-conmatphys-070909-103925)].
- [4] S. E. Clifton, “*Collective electron ferronmagnetism*,” *Proc. R. Soc. London A - Math. Phys. Sci.* **165**, 372–414 (1938) [doi: [10.1098/rspa.1938.0066](https://doi.org/10.1098/rspa.1938.0066)].
- [5] J. Bardeen, L. N. Cooper, and J. R. Schrieffer, “*Theory of Superconductivity*,” *Phys. Rev.* **108**, 1175–1204 (1957) [doi: [10.1103/PhysRev.108.1175](https://doi.org/10.1103/PhysRev.108.1175)].
- [6] M. Nakahara, *Geometry, Topology and Physics, Second Edition (Graduate Student Series in Physics)*. CRC Press, (2003).
- [7] N. Read and D. Green, “*Paired states of fermions in two dimensions with breaking of parity and time-reversal symmetries and the fractional quantum Hall effect*,” *Phys. Rev. B* **61**, 10267–10297 (2000) [doi: [10.1103/PhysRevB.61.10267](https://doi.org/10.1103/PhysRevB.61.10267)].
- [8] G. E. Volovik, “*Fermion zero modes on vortices in chiral superconductors*,” *Jetp. Lett.* **70**, 609–614 (1999) [doi: [10.1134/1.568223](https://doi.org/10.1134/1.568223)].
- [9] R. Jackiw and C. Rebbi, “*Solitons with fermion number $\frac{1}{2}$* ,” *Phys. Rev. D* **13**, 3398–3409 (1976) [doi: [10.1103/PhysRevD.13.3398](https://doi.org/10.1103/PhysRevD.13.3398)].
- [10] W. P. Su, J. R. Schrieffer, and A. J. Heeger, “*Solitons in Polyacetylene*,” *Phys. Rev. Lett.* **42**, 1698–1701 (1979) [doi: [10.1103/PhysRevLett.42.1698](https://doi.org/10.1103/PhysRevLett.42.1698)].
- [11] K. v. Klitzing, G. Dorda, and M. Pepper, “*New Method for High-Accuracy Determination of the Fine-Structure Constant Based on Quantized Hall Resistance*,” *Phys. Rev. Lett.* **45**, 494–497 (1980) [doi: [10.1103/PhysRevLett.45.494](https://doi.org/10.1103/PhysRevLett.45.494)].
- [12] L. Fu and C. L. Kane, “*Superconducting Proximity Effect and Majorana Fermions at the Surface of a Topological Insulator*,” *Phys. Rev. Lett.* **100**, 096407 (2008) [doi: [10.1103/PhysRevLett.100.096407](https://doi.org/10.1103/PhysRevLett.100.096407)].

- [13] A. Y. Kitaev, “*Unpaired Majorana fermions in quantum wires*,” *Phys.-Usp.* **44**, 131–136 (2001) [doi: [10.1070/1063-7869/44/10s/s29](https://doi.org/10.1070/1063-7869/44/10s/s29)].
- [14] C. L. Kane and E. J. Mele, “ *Z_2 Topological Order and the Quantum Spin Hall Effect*,” *Phys. Rev. Lett.* **95**, 146802 (2005) [doi: [10.1103/PhysRevLett.95.146802](https://doi.org/10.1103/PhysRevLett.95.146802)].
- [15] C. L. Kane and E. J. Mele, “*Quantum Spin Hall Effect in Graphene*,” *Phys. Rev. Lett.* **95**, 226801 (2005) [doi: [10.1103/PhysRevLett.95.226801](https://doi.org/10.1103/PhysRevLett.95.226801)].
- [16] B. A. Bernevig and S.-C. Zhang, “*Quantum Spin Hall Effect*,” *Phys. Rev. Lett.* **96**, 106802 (2006) [doi: [10.1103/PhysRevLett.96.106802](https://doi.org/10.1103/PhysRevLett.96.106802)].
- [17] B. A. Bernevig, T. L. Hughes, and S.-C. Zhang, “*Quantum Spin Hall Effect and Topological Phase Transition in HgTe Quantum Wells*,” *Science* **314**, 1757–1761 (2006) [doi: [10.1126/science.1133734](https://doi.org/10.1126/science.1133734)].
- [18] M. König, S. Wiedmann, C. Brüne, A. Roth, H. Buhmann, L. W. Molenkamp, X.-L. Qi, and S.-C. Zhang, “*Quantum Spin Hall Insulator State in HgTe Quantum Wells*,” *Science* **318**, 766–770 (2007) [doi: [10.1126/science.1148047](https://doi.org/10.1126/science.1148047)].
- [19] J. M. Kosterlitz and D. J. Thouless, “*Long range order and metastability in two dimensional solids and superfluids. (Application of dislocation theory)*,” *J. Phys. C: Solid State Phys.* **5**, L124–L126 (1972) [doi: [10.1088/0022-3719/5/11/002](https://doi.org/10.1088/0022-3719/5/11/002)].
- [20] J. M. Kosterlitz and D. J. Thouless, “*Ordering, metastability and phase transitions in two-dimensional systems*,” *J. Phys. C: Solid State Phys.* **6**, 1181–1203 (1973) [doi: [10.1088/0022-3719/6/7/010](https://doi.org/10.1088/0022-3719/6/7/010)].
- [21] D. J. Thouless, M. Kohmoto, M. P. Nightingale, and M. Den Nijs, “*Quantized Hall Conductance in a Two-Dimensional Periodic Potential*,” *Phys. Rev. Lett.* **49**, 405–408 (1982) [doi: [10.1103/PhysRevLett.49.405](https://doi.org/10.1103/PhysRevLett.49.405)].
- [22] F. D. M. Haldane, “*Continuum dynamics of the 1-D Heisenberg antiferromagnet: Identification with the $O(3)$ nonlinear sigma model*,” *Phys. Lett. A* **93**, 464–468 (1983) [doi: [10.1016/0375-9601\(83\)90631-X](https://doi.org/10.1016/0375-9601(83)90631-X)].
- [23] F. D. M. Haldane, “*Model for a Quantum Hall Effect without Landau Levels: Condensed-Matter Realization of the "Parity Anomaly"*,” *Phys. Rev. Lett.* **61**, 2015–2018 (1988) [doi: [10.1103/PhysRevLett.61.2015](https://doi.org/10.1103/PhysRevLett.61.2015)].
- [24] A. Altland and M. R. Zirnbauer, “*Nonstandard symmetry classes in mesoscopic normal-superconducting hybrid structures*,” *Phys. Rev. B* **55**, 1142–1161 (1997) [doi: [10.1103/PhysRevB.55.1142](https://doi.org/10.1103/PhysRevB.55.1142)].
- [25] A. Kitaev, “*Periodic table for topological insulators and superconductors*,” *AIP Conference Proceedings* **1134**, 22–30 (2009) [doi: [10.1063/1.3149495](https://doi.org/10.1063/1.3149495)].
- [26] S. Ryu, A. P. Schnyder, A. Furusaki, and A. W. W. Ludwig, “*Topological insulators and superconductors: tenfold way and dimensional hierarchy*,” *New J. Phys.* **12**, 065010 (2010) [doi: [10.1088/1367-2630/12/6/065010](https://doi.org/10.1088/1367-2630/12/6/065010)].

- [27] J. C. Y. Teo and C. L. Kane, “*Topological defects and gapless modes in insulators and superconductors*,” Phys. Rev. B **82**, 115120 (2010) [doi: [10.1103/PhysRevB.82.115120](https://doi.org/10.1103/PhysRevB.82.115120)].
- [28] C.-K. Chiu, H. Yao, and S. Ryu, “*Classification of topological insulators and superconductors in the presence of reflection symmetry*,” Phys. Rev. B **88**, 075142 (2013) [doi: [10.1103/PhysRevB.88.075142](https://doi.org/10.1103/PhysRevB.88.075142)].
- [29] K. Shiozaki and M. Sato, “*Topology of crystalline insulators and superconductors*,” Phys. Rev. B **90**, 165114 (2014) [doi: [10.1103/PhysRevB.90.165114](https://doi.org/10.1103/PhysRevB.90.165114)].
- [30] S. Matsuura, P.-Y. Chang, A. P. Schnyder, and S. Ryu, “*Protected boundary states in gapless topological phases*,” New J. Phys. **15**, 065001 (2013) [doi: [10.1088/1367-2630/15/6/065001](https://doi.org/10.1088/1367-2630/15/6/065001)].
- [31] C.-K. Chiu and A. P. Schnyder, “*Classification of reflection-symmetry-protected topological semimetals and nodal superconductors*,” Phys. Rev. B **90**, 205136 (2014) [doi: [10.1103/PhysRevB.90.205136](https://doi.org/10.1103/PhysRevB.90.205136)].
- [32] K. Shiozaki, M. Sato, and K. Gomi, “*Topology of nonsymmorphic crystalline insulators and superconductors*,” Phys. Rev. B **93**, 195413 (2016) [doi: [10.1103/PhysRevB.93.195413](https://doi.org/10.1103/PhysRevB.93.195413)].
- [33] B. Bradlyn, L. Elcoro, J. Cano, M. G. Vergniory, Z. Wang, C. Felser, M. I. Aroyo, and B. A. Bernevig, “*Topological quantum chemistry*,” Nature **547**, 298–305 (2017) [doi: [10.1038/nature23268](https://doi.org/10.1038/nature23268)].
- [34] L. Elcoro, B. J. Wieder, Z. Song, Y. Xu, B. Bradlyn, and B. A. Bernevig, “*Magnetic Topological Quantum Chemistry*,” arXiv (2020)
- [35] M. Geier, P. W. Brouwer, and L. Trifunovic, “*Symmetry-based indicators for topological Bogoliubov–de Gennes Hamiltonians*,” Phys. Rev. B **101**, 245128 (2020) [doi: [10.1103/PhysRevB.101.245128](https://doi.org/10.1103/PhysRevB.101.245128)].
- [36] S. Ono, H. C. Po, and H. Watanabe, “*Refined symmetry indicators for topological superconductors in all space groups*,” Sci. Adv. **6**, eaaz8367 (2020) [doi: [10.1126/sciadv.aaz8367](https://doi.org/10.1126/sciadv.aaz8367)].
- [37] A. Altland and B. D. Simons, *Condensed Matter Field Theory*. Cambridge University Press, (2010).
- [38] J. Hubbard, “*Electron correlations in narrow energy bands*,” Proc. R. Soc. London A - Math. Phys. Sci. **276**, 238–257 (1963) [doi: [10.1098/rspa.1963.0204](https://doi.org/10.1098/rspa.1963.0204)].
- [39] P. W. Anderson, “*Antiferromagnetism. Theory of Superexchange Interaction*,” Phys. Rev. **79**, 350–356 (1950) [doi: [10.1103/PhysRev.79.350](https://doi.org/10.1103/PhysRev.79.350)].
- [40] N. F. Mott, “*The Basis of the Electron Theory of Metals, with Special Reference to the Transition Metals*,” Proc. Phys. Soc. A **62**, 416–422 (1949) [doi: [10.1088/0370-1298/62/7/303](https://doi.org/10.1088/0370-1298/62/7/303)].
- [41] J. G. Bednorz and K. A. Müller, “*Possible high T_c superconductivity in the Ba-La-Cu-O system*,” Z. Phys. B: Condens. Matter **64**, 189–193 (1986) [doi: [10.1007/BF01303701](https://doi.org/10.1007/BF01303701)].

- [42] Y. Maeno, H. Hashimoto, K. Yoshida, S. Nishizaki, T. Fujita, J. G. Bednorz, and F. Lichtenberg, “*Superconductivity in a layered perovskite without copper*,” *Nature* **372**, 532–534 (1994) [doi: [10.1038/372532a0](https://doi.org/10.1038/372532a0)].
- [43] Y. Kamihara, H. Hiramatsu, M. Hirano, R. Kawamura, H. Yanagi, T. Kamiya, and H. Hosono, “*Iron-Based Layered Superconductor: LaOFeP*,” *J. Am. Chem. Soc.* **128**, 10012–10013 (2006) [doi: [10.1021/ja063355c](https://doi.org/10.1021/ja063355c)].
- [44] D. Li, K. Lee, B. Y. Wang, M. Osada, S. Crossley, H. R. Lee, Y. Cui, Y. Hikita, and H. Y. Hwang, “*Superconductivity in an infinite-layer nickelate*,” *Nature* **572**, 624–627 (2019) [doi: [10.1038/s41586-019-1496-5](https://doi.org/10.1038/s41586-019-1496-5)].
- [45] M. A. Tanatar, E. C. Blomberg, A. Kreyssig, M. G. Kim, N. Ni, A. Thaler, S. L. Bud’ko, P. C. Canfield, A. I. Goldman, I. I. Mazin, and R. Prozorov, “*Uniaxial-strain mechanical detwinning of CaFe₂As₂ and BaFe₂As₂ crystals: Optical and transport study*,” *Phys. Rev. B* **81**, 184508 (2010) [doi: [10.1103/PhysRevB.81.184508](https://doi.org/10.1103/PhysRevB.81.184508)].
- [46] J.-H. Chu, J. G. Analytis, K. De Greve, P. L. McMahon, Z. Islam, Y. Yamamoto, and I. R. Fisher, “*In-Plane Resistivity Anisotropy in an Underdoped Iron Arsenide Superconductor*,” *Science* **329**, 824–826 (2010) [doi: [10.1126/science.1190482](https://doi.org/10.1126/science.1190482)].
- [47] J. J. Ying, X. F. Wang, T. Wu, Z. J. Xiang, R. H. Liu, Y. J. Yan, A. F. Wang, M. Zhang, G. J. Ye, P. Cheng, J. P. Hu, and X. H. Chen, “*Measurements of the Anisotropic In-Plane Resistivity of Underdoped FeAs-Based Pnictide Superconductors*,” *Phys. Rev. Lett.* **107**, 067001 (2011) [doi: [10.1103/PhysRevLett.107.067001](https://doi.org/10.1103/PhysRevLett.107.067001)].
- [48] J.-H. Chu, H.-H. Kuo, J. G. Analytis, and I. R. Fisher, “*Divergent Nematic Susceptibility in an Iron Arsenide Superconductor*,” *Science* **337**, 710–712 (2012) [doi: [10.1126/science.1221713](https://doi.org/10.1126/science.1221713)].
- [49] E. C. Blomberg, M. A. Tanatar, R. M. Fernandes, I. I. Mazin, B. Shen, H.-H. Wen, M. D. Johannes, J. Schmalian, and R. Prozorov, “*Sign-reversal of the in-plane resistivity anisotropy in hole-doped iron pnictides*,” *Nat. Commun.* **4**, 1–7 (2013) [doi: [10.1038/ncomms2933](https://doi.org/10.1038/ncomms2933)].
- [50] S. Ishida, M. Nakajima, T. Liang, K. Kihou, C.-H. Lee, A. Iyo, H. Eisaki, T. Kakeshita, Y. Tomioka, T. Ito, and S.-i. Uchida, “*Effect of doping on the magnetostructural ordered phase of iron arsenides: a comparative study of the resistivity anisotropy in doped BaFe₂As₂ with doping into three different sites*,” *J. Am. Chem. Soc.* **135**, 3158–3163 (2013) [doi: [10.1021/ja311174e](https://doi.org/10.1021/ja311174e)].
- [51] S. Ishida, M. Nakajima, T. Liang, K. Kihou, C. H. Lee, A. Iyo, H. Eisaki, T. Kakeshita, Y. Tomioka, T. Ito, and S. Uchida, “*Anisotropy of the In-Plane Resistivity of Underdoped Ba(Fe_{1-x}Co_x)₂As₂ Superconductors Induced by Impurity Scattering in the Antiferromagnetic Orthorhombic Phase*,” *Phys. Rev. Lett.* **110**, 207001 (2013) [doi: [10.1103/PhysRevLett.110.207001](https://doi.org/10.1103/PhysRevLett.110.207001)].
- [52] H.-H. Kuo and I. R. Fisher, “*Effect of Disorder on the Resistivity Anisotropy Near the Electronic Nematic Phase Transition in Pure and Electron-Doped BaFe₂As₂*,” *Phys. Rev. Lett.* **112**, 227001 (2014) [doi: [10.1103/PhysRevLett.112.227001](https://doi.org/10.1103/PhysRevLett.112.227001)].

- [53] M. Yi, D. Lu, J.-H. Chu, J. G. Analytis, A. P. Sorini, A. F. Kemper, B. Moritz, S.-K. Mo, R. G. Moore, M. Hashimoto, W.-S. Lee, Z. Hussain, T. P. Devereaux, I. R. Fisher, and Z.-X. Shen, “*Symmetry-breaking orbital anisotropy observed for detwinned $\text{Ba}(\text{Fe}_{1-x}\text{Co}_x)_2\text{As}_2$ above the spin density wave transition,*” Proc. Natl. Acad. Sci. U.S.A. **108**, 6878–6883 (2011) [doi: [10.1073/pnas.1015572108](https://doi.org/10.1073/pnas.1015572108)].
- [54] A. Kostin, P. O. Sprau, A. Kreisel, Y. X. Chong, A. E. Böhmer, P. C. Canfield, P. J. Hirschfeld, B. M. Andersen, and J. C. S. Davis, “*Imaging orbital-selective quasiparticles in the Hund’s metal state of FeSe ,*” Nat. Mater. **17**, 869–874 (2018) [doi: [10.1038/s41563-018-0151-0](https://doi.org/10.1038/s41563-018-0151-0)].
- [55] J. Zhao, D. T. Adroja, D.-X. Yao, R. Bewley, S. Li, X. F. Wang, G. Wu, X. H. Chen, J. Hu, and P. Dai, “*Spin waves and magnetic exchange interactions in CaFe_2As_2 ,*” Nat. Phys. **5**, 555–560 (2009) [doi: [10.1038/nphys1336](https://doi.org/10.1038/nphys1336)].
- [56] M. Nakajima, T. Liang, S. Ishida, Y. Tomioka, K. Kihou, C. H. Lee, A. Iyo, H. Eisaki, T. Kakeshita, T. Ito, and S. Uchida, “*Unprecedented anisotropic metallic state in undoped iron arsenide BaFe_2As_2 revealed by optical spectroscopy,*” Proc. Natl. Acad. Sci. U.S.A. **108**, 12238–12242 (2011) [doi: [10.1073/pnas.1100102108](https://doi.org/10.1073/pnas.1100102108)].
- [57] A. Dusza, A. Lucarelli, F. Pfuner, J.-H. Chu, I. R. Fisher, and L. Degiorgi, “*Anisotropic charge dynamics in detwinned $\text{Ba}(\text{Fe}_{1-x}\text{Co}_x)_2\text{As}_2$,*” EPL **93**, 37002 (2011) [doi: [10.1209/0295-5075/93/37002](https://doi.org/10.1209/0295-5075/93/37002)].
- [58] H. Z. Arham, C. R. Hunt, W. K. Park, J. Gillett, S. D. Das, S. E. Sebastian, Z. J. Xu, J. S. Wen, Z. W. Lin, Q. Li, G. Gu, A. Thaler, S. Ran, S. L. Bud’ko, P. C. Canfield, D. Y. Chung, M. G. Kanatzidis, and L. H. Greene, “*Detection of orbital fluctuations above the structural transition temperature in the iron pnictides and chalcogenides,*” Phys. Rev. B **85**, 214515 (2012) [doi: [10.1103/PhysRevB.85.214515](https://doi.org/10.1103/PhysRevB.85.214515)].
- [59] S. Kasahara, H. J. Shi, K. Hashimoto, S. Tonegawa, Y. Mizukami, T. Shibauchi, K. Sugimoto, T. Fukuda, T. Terashima, A. H. Nevidomskyy, and Y. Matsuda, “*Electronic nematicity above the structural and superconducting transition in $\text{BaFe}_2(\text{As}_{1-x}\text{P}_x)_2$,*” Nature **486**, 382–385 (2012) [doi: [10.1038/nature11178](https://doi.org/10.1038/nature11178)].
- [60] R. M. Fernandes, A. V. Chubukov, and J. Schmalian, “*What drives nematic order in iron-based superconductors?,*” Nat. Phys. **10**, 97–104 (2014) [doi: [10.1038/nphys2877](https://doi.org/10.1038/nphys2877)].
- [61] A. E. Böhmer and A. Kreisel, “*Nematicity, magnetism and superconductivity in FeSe ,*” J. Phys.: Condens. Matter **30**, 023001 (2017) [doi: [10.1088/1361-648x/aa9caa](https://doi.org/10.1088/1361-648x/aa9caa)].
- [62] A. I. Coldea and M. D. Watson, “*The Key Ingredients of the Electronic Structure of FeSe ,*” Annu. Rev. Condens. Matter Phys. **9**, 125–146 (2018) [doi: [10.1146/annurev-conmatphys-033117-054137](https://doi.org/10.1146/annurev-conmatphys-033117-054137)].
- [63] A. Kreisel, P. J. Hirschfeld, and B. M. Andersen, “*On the Remarkable Superconductivity of FeSe and Its Close Cousins,*” Symmetry **12**, 1402 (2020) [doi: [10.3390/sym12091402](https://doi.org/10.3390/sym12091402)].

- [64] C. de la Cruz, Q. Huang, J. W. Lynn, J. Li, W. R. I. I., J. L. Zarestky, H. A. Mook, G. F. Chen, J. L. Luo, N. L. Wang, and P. Dai, “Magnetic order close to superconductivity in the iron-based layered $LaO_{1-x}F_xFeAs$ systems,” *Nature* **453**, 899–902 (2008) [doi: 10.1038/nature07057].
- [65] C. Liu, T. Kondo, R. M. Fernandes, A. D. Palczewski, E. D. Mun, N. Ni, A. N. Thaler, A. Bostwick, E. Rotenberg, J. Schmalian, S. L. Bud’ko, P. C. Canfield, and A. Kaminski, “Evidence for a Lifshitz transition in electron-doped iron arsenic superconductors at the onset of superconductivity,” *Nat. Phys.* **6**, 419–423 (2010) [doi: 10.1038/nphys1656].
- [66] S. Avci, O. Chmaissem, J. M. Allred, S. Rosenkranz, I. Eremin, A. V. Chubukov, D. E. Bugaris, D. Y. Chung, M. G. Kanatzidis, J.-P. Castellán, J. A. Schlueter, H. Claus, D. D. Khalyavin, P. Manuel, A. Daoud-Aladine, and R. Osborn, “Magnetically driven suppression of nematic order in an iron-based superconductor,” *Nat. Commun.* **5**, 1–6 (2014) [doi: 10.1038/ncomms4845].
- [67] F. Waßer, A. Schneidewind, Y. Sidis, S. Wurmehl, S. Aswartham, B. Büchner, and M. Braden, “Spin reorientation in $Ba_{0.65}Na_{0.35}Fe_2As_2$ studied by single-crystal neutron diffraction,” *Phys. Rev. B* **91**, 060505 (2015) [doi: 10.1103/PhysRevB.91.060505].
- [68] E. Hassinger, G. Gredat, F. Valade, S. R. de Cotret, A. Juneau-Fecteau, J.-Ph. Reid, H. Kim, M. A. Tanatar, R. Prozorov, B. Shen, H.-H. Wen, N. Doiron-Leyraud, and L. Taillefer, “Pressure-induced Fermi-surface reconstruction in the iron-arsenide superconductor $Ba_{1-x}K_xFe_2As_2$: Evidence of a phase transition inside the antiferromagnetic phase,” *Phys. Rev. B* **86**, 140502 (2012) [doi: 10.1103/PhysRevB.86.140502].
- [69] A. E. Böhmer, F. Hardy, L. Wang, T. Wolf, P. Schweiss, and C. Meingast, “Superconductivity-induced re-entrance of the orthorhombic distortion in $Ba_{1-x}K_xFe_2As_2$,” *Nat. Commun.* **6**, 1–7 (2015) [doi: 10.1038/ncomms8911].
- [70] J. M. Allred, S. Avci, D. Y. Chung, H. Claus, D. D. Khalyavin, P. Manuel, K. M. Taddei, M. G. Kanatzidis, S. Rosenkranz, R. Osborn, and O. Chmaissem, “Tetragonal magnetic phase in $Ba_{1-x}K_xFe_2As_2$ from x-ray and neutron diffraction,” *Phys. Rev. B* **92**, 094515 (2015) [doi: 10.1103/PhysRevB.92.094515].
- [71] Y. Zheng, P. M. Tam, J. Hou, A. E. Böhmer, T. Wolf, C. Meingast, and R. Lortz, “Absence of nematic order in the pressure-induced intermediate phase of the iron-based superconductor $Ba_{0.85}K_{0.15}Fe_2As_2$,” *Phys. Rev. B* **93**, 104516 (2016) [doi: 10.1103/PhysRevB.93.104516].
- [72] B. P. P. Mallett, Yu. G. Pashkevich, A. Gusev, Th. Wolf, and C. Bernhard, “Muon spin rotation study of the magnetic structure in the tetragonal antiferromagnetic state of weakly underdoped $Ba_{1-x}K_xFe_2As_2$,” *EPL* **111**, 57001 (2015) [doi: 10.1209/0295-5075/111/57001].
- [73] B. P. P. Mallett, P. Marsik, M. Yazdi-Rizi, Th. Wolf, A. E. Böhmer, F. Hardy, C. Meingast, D. Munzar, and C. Bernhard, “Infrared Study of the Spin Reorientation Transition and Its Reversal in the Superconducting State in Underdoped $Ba_{1-x}K_xFe_2As_2$,” *Phys. Rev. Lett.* **115**, 027003 (2015) [doi: 10.1103/PhysRevLett.115.027003].

- [74] D. K. Pratt, M. G. Kim, A. Kreyssig, Y. B. Lee, G. S. Tucker, A. Thaler, W. Tian, J. L. Zarestky, S. L. Bud'ko, P. C. Canfield, B. N. Harmon, A. I. Goldman, and R. J. McQueeney, “*Incommensurate Spin-Density Wave Order in Electron-Doped BaFe₂As₂ Superconductors*,” *Phys. Rev. Lett.* **106**, 257001 (2011) [doi: [10.1103/PhysRevLett.106.257001](https://doi.org/10.1103/PhysRevLett.106.257001)].
- [75] J. M. Allred, K. M. Taddei, D. E. Bugaris, M. J. Krogstad, S. H. Lapidus, D. Y. Chung, H. Claus, M. G. Kanatzidis, D. E. Brown, J. Kang, R. M. Fernandes, I. Eremin, S. Rosenkranz, O. Chmaissem, and R. Osborn, “*Double-Q spin-density wave in iron arsenide superconductors*,” *Nat. Phys.* **12**, 493–498 (2016) [doi: [10.1038/nphys3629](https://doi.org/10.1038/nphys3629)].
- [76] W. R. Meier, Q.-P. Ding, A. Kreyssig, S. L. Bud'ko, A. Sapkota, K. Kothapalli, V. Borisov, R. Valentí, C. D. Batista, P. P. Orth, R. M. Fernandes, A. I. Goldman, Y. Furukawa, A. E. Böhrer, and P. C. Canfield, “*Hedgehog spin-vortex crystal stabilized in a hole-doped iron-based superconductor*,” *npj Quantum Mater.* **3**, 1–6 (2018) [doi: [10.1038/s41535-017-0076-x](https://doi.org/10.1038/s41535-017-0076-x)].
- [77] M. H. Christensen, B. M. Andersen, and P. Kotetes, “*Unravelling Incommensurate Magnetism and Its Emergence in Iron-Based Superconductors*,” *Phys. Rev. X* **8**, 041022 (2018) [doi: [10.1103/PhysRevX.8.041022](https://doi.org/10.1103/PhysRevX.8.041022)].
- [78] P. J. Hirschfeld, M. M. Korshunov, and I. I. Mazin, “*Gap symmetry and structure of Fe-based superconductors*,” *Rep. Prog. Phys.* **74**, 124508 (2011) [doi: [10.1088/0034-4885/74/12/124508](https://doi.org/10.1088/0034-4885/74/12/124508)].
- [79] J. Paglione and R. L. Greene, “*High-temperature superconductivity in iron-based materials*,” *Nat. Phys.* **6**, 645–658 (2010) [doi: [10.1038/nphys1759](https://doi.org/10.1038/nphys1759)].
- [80] Q.-Z. Wang and C.-X. Liu, “*Topological nonsymmorphic crystalline superconductors*,” *Phys. Rev. B* **93**, 020505 (2016) [doi: [10.1103/PhysRevB.93.020505](https://doi.org/10.1103/PhysRevB.93.020505)].
- [81] E. Wiesenmayer, H. Luetkens, G. Pascua, R. Khasanov, A. Amato, H. Potts, B. Banusch, H.-H. Klauss, and D. Johrendt, “*Microscopic Coexistence of Superconductivity and Magnetism in Ba_{1-x}K_xFe₂As₂*,” *Phys. Rev. Lett.* **107**, 237001 (2011) [doi: [10.1103/PhysRevLett.107.237001](https://doi.org/10.1103/PhysRevLett.107.237001)].
- [82] S. Avci, O. Chmaissem, E. A. Goremychkin, S. Rosenkranz, J.-P. Castellan, D. Y. Chung, I. S. Todorov, J. A. Schlueter, H. Claus, M. G. Kanatzidis, A. Daoud-Aladine, D. Khalyavin, and R. Osborn, “*Magnetoelastic coupling in the phase diagram of Ba_{1-x}K_xFe₂As₂ as seen via neutron diffraction*,” *Phys. Rev. B* **83**, 172503 (2011) [doi: [10.1103/PhysRevB.83.172503](https://doi.org/10.1103/PhysRevB.83.172503)].
- [83] P. Materne, S. Kamusella, R. Sarkar, T. Goltz, J. Spehling, H. Maeter, L. Harnagea, S. Wurmehl, B. Büchner, H. Luetkens, C. Timm, and H.-H. Klauss, “*Coexistence of superconductivity and magnetism in Ca_{1-x}Na_xFe₂As₂: Universal suppression of the magnetic order parameter in 122 iron pnictides*,” *Phys. Rev. B* **92**, 134511 (2015) [doi: [10.1103/PhysRevB.92.134511](https://doi.org/10.1103/PhysRevB.92.134511)].
- [84] N. Ni, M. E. Tillman, J.-Q. Yan, A. Kracher, S. T. Hannahs, S. L. Bud'ko, and P. C. Canfield, “*Effects of Co substitution on thermodynamic and transport properties and anisotropic H_{c2} in Ba(Fe_{1-x}Co_x)₂As₂ single crystals*,” *Phys. Rev. B* **78**, 214515 (2008) [doi: [10.1103/PhysRevB.78.214515](https://doi.org/10.1103/PhysRevB.78.214515)].

- [85] S. Nandi, M. G. Kim, A. Kreyssig, R. M. Fernandes, D. K. Pratt, A. Thaler, N. Ni, S. L. Bud'ko, P. C. Canfield, J. Schmalian, R. J. McQueeney, and A. I. Goldman, “*Anomalous Suppression of the Orthorhombic Lattice Distortion in Superconducting Ba(Fe_{1-x}Co_x)₂As₂ Single Crystals*,” Phys. Rev. Lett. **104**, 057006 (2010) [doi: [10.1103/PhysRevLett.104.057006](https://doi.org/10.1103/PhysRevLett.104.057006)].
- [86] P. O. Sprau, A. Kostin, A. Kreisel, A. E. Böhmer, V. Taufour, P. C. Canfield, S. Mukherjee, P. J. Hirschfeld, B. M. Andersen, and J. C. S. Davis, “*Discovery of orbital-selective Cooper pairing in FeSe*,” Science **357**, 75–80 (2017) [doi: [10.1126/science.aal1575](https://doi.org/10.1126/science.aal1575)].
- [87] J.-X. Yin, Z. Wu, J.-H. Wang, Z.-Y. Ye, J. Gong, X.-Y. Hou, L. Shan, A. Li, X.-J. Liang, X.-X. Wu, J. Li, C.-S. Ting, Z.-Q. Wang, J.-P. Hu, P.-H. Hor, H. Ding, and S. H. Pan, “*Observation of a robust zero-energy bound state in iron-based superconductor Fe(Te,Se)*,” Nat. Phys. **11**, 543–546 (2015) [doi: [10.1038/nphys3371](https://doi.org/10.1038/nphys3371)].
- [88] P. Zhang, K. Yaji, T. Hashimoto, Y. Ota, T. Kondo, K. Okazaki, Z. Wang, J. Wen, G. D. Gu, H. Ding, and S. Shin, “*Observation of topological superconductivity on the surface of an iron-based superconductor*,” Science **360**, 182–186 (2018) [doi: [10.1126/science.aan4596](https://doi.org/10.1126/science.aan4596)].
- [89] D. Wang, L. Kong, P. Fan, H. Chen, S. Zhu, W. Liu, L. Cao, Y. Sun, S. Du, J. Schneeloch, R. Zhong, G. Gu, L. Fu, H. Ding, and H.-J. Gao, “*Evidence for Majorana bound states in an iron-based superconductor*,” Science **362**, 333–335 (2018) [doi: [10.1126/science.aao1797](https://doi.org/10.1126/science.aao1797)].
- [90] L. Kong, S. Zhu, M. Papaj, H. Chen, L. Cao, H. Isobe, Y. Xing, W. Liu, D. Wang, P. Fan, Y. Sun, S. Du, J. Schneeloch, R. Zhong, G. Gu, L. Fu, H.-J. Gao, and H. Ding, “*Half-integer level shift of vortex bound states in an iron-based superconductor*,” Nat. Phys. **15**, 1181–1187 (2019) [doi: [10.1038/s41567-019-0630-5](https://doi.org/10.1038/s41567-019-0630-5)].
- [91] S. Zhu, L. Kong, L. Cao, H. Chen, M. Papaj, S. Du, Y. Xing, W. Liu, D. Wang, C. Shen, F. Yang, J. Schneeloch, R. Zhong, G. Gu, L. Fu, Y.-Y. Zhang, H. Ding, and H.-J. Gao, “*Nearly quantized conductance plateau of vortex zero mode in an iron-based superconductor*,” Science **367**, 189–192 (2020) [doi: [10.1126/science.aax0274](https://doi.org/10.1126/science.aax0274)].
- [92] A. Yu. Kitaev, “*Fault-tolerant quantum computation by anyons*,” Ann. Phys. **303**, 2–30 (2003) [doi: [10.1016/S0003-4916\(02\)00018-0](https://doi.org/10.1016/S0003-4916(02)00018-0)].
- [93] C. Nayak, S. H. Simon, A. Stern, M. Freedman, and S. Das Sarma, “*Non-Abelian anyons and topological quantum computation*,” Rev. Mod. Phys. **80**, 1083–1159 (2008) [doi: [10.1103/RevModPhys.80.1083](https://doi.org/10.1103/RevModPhys.80.1083)].
- [94] J. Alicea, Y. Oreg, G. Refael, F. von Oppen, and M. P. A. Fisher, “*Non-Abelian statistics and topological quantum information processing in 1D wire networks*,” Nat. Phys. **7**, 412 (2011) [doi: [10.1038/nphys1915](https://doi.org/10.1038/nphys1915)].
- [95] P. Zhang, Z. Wang, X. Wu, K. Yaji, Y. Ishida, Y. Kohama, G. Dai, Y. Sun, C. Bareille, K. Kuroda, T. Kondo, K. Okazaki, K. Kindo, X. Wang, C. Jin, J. Hu, R. Thomale, K. Sumida, S. Wu, K. Miyamoto, T. Okuda, H. Ding, G. D. Gu, T. Tamegai, T. Kawakami, M. Sato, and S. Shin, “*Multiple topological states in iron-based superconductors*,” Nat. Phys. **15**, 41–47 (2019) [doi: [10.1038/s41567-018-0280-z](https://doi.org/10.1038/s41567-018-0280-z)].

- [96] K. Jiang, X. Dai, and Z. Wang, “Quantum Anomalous Vortex and Majorana Zero Mode in Iron-Based Superconductor $Fe(Te,Se)$,” *Phys. Rev. X* **9**, 011033 (2019) [doi: 10.1103/PhysRevX.9.011033].
- [97] R.-X. Zhang, W. S. Cole, and S. Das Sarma, “Helical Hinge Majorana Modes in Iron-Based Superconductors,” *Phys. Rev. Lett.* **122**, 187001 (2019) [doi: 10.1103/PhysRevLett.122.187001].
- [98] M. Gray, J. Freudenstein, S. Y. F. Zhao, R. O’Connor, S. Jenkins, N. Kumar, M. Hoek, A. Kopec, S. Huh, T. Taniguchi, K. Watanabe, R. Zhong, C. Kim, G. D. Gu, and K. S. Burch, “Evidence for Helical Hinge Zero Modes in an Fe-Based Superconductor,” *Nano Lett.* **19**, 4890–4896 (2019) [doi: 10.1021/acs.nanolett.9b00844].
- [99] R.-X. Zhang, W. S. Cole, X. Wu, and S. Das Sarma, “Higher-Order Topology and Nodal Topological Superconductivity in $Fe(Se,Te)$ Heterostructures,” *Phys. Rev. Lett.* **123**, 167001 (2019) [doi: 10.1103/PhysRevLett.123.167001].
- [100] N. Heinsdorf, M. H. Christensen, M. Iraola, S. Zhang, F. Yang, T. Birol, C. D. Batista, R. Valentí, and R. M. Fernandes, “Prediction of Double-Weyl Points in the Iron-Based Superconductor $CaKFe_4As_4$,” arXiv (2021)
- [101] M. Sato and S. Fujimoto, “Topological phases of noncentrosymmetric superconductors: Edge states, Majorana fermions, and non-Abelian statistics,” *Phys. Rev. B* **79**, 094504 (2009) [doi: 10.1103/PhysRevB.79.094504].
- [102] T.-P. Choy, J. M. Edge, A. R. Akhmerov, and C. W. J. Beenakker, “Majorana fermions emerging from magnetic nanoparticles on a superconductor without spin-orbit coupling,” *Phys. Rev. B* **84**, 195442 (2011) [doi: 10.1103/PhysRevB.84.195442].
- [103] M. Kjaergaard, K. Wölms, and K. Flensberg, “Majorana fermions in superconducting nanowires without spin-orbit coupling,” *Phys. Rev. B* **85**, 020503 (2012) [doi: 10.1103/PhysRevB.85.020503].
- [104] I. Martin and A. F. Morpurgo, “Majorana fermions in superconducting helical magnets,” *Phys. Rev. B* **85**, 144505 (2012) [doi: 10.1103/PhysRevB.85.144505].
- [105] S. Nadj-Perge, I. K. Drozdov, B. A. Bernevig, and A. Yazdani, “Proposal for realizing Majorana fermions in chains of magnetic atoms on a superconductor,” *Phys. Rev. B* **88**, 020407 (2013) [doi: 10.1103/PhysRevB.88.020407].
- [106] S. Nakosai, Y. Tanaka, and N. Nagaosa, “Two-dimensional p-wave superconducting states with magnetic moments on a conventional s-wave superconductor,” *Phys. Rev. B* **88**, 180503 (2013) [doi: 10.1103/PhysRevB.88.180503].
- [107] P. Kotetes, “Classification of engineered topological superconductors,” *New J. Phys.* **15**, 105027 (2013) [doi: 10.1088/1367-2630/15/10/105027].
- [108] B. Braunecker and P. Simon, “Interplay between Classical Magnetic Moments and Superconductivity in Quantum One-Dimensional Conductors: Toward a Self-Sustained Topological Majorana Phase,” *Phys. Rev. Lett.* **111**, 147202 (2013) [doi: 10.1103/PhysRevLett.111.147202].

- [109] J. Klinovaja, P. Stano, A. Yazdani, and D. Loss, “*Topological Superconductivity and Majorana Fermions in RKKY Systems*,” Phys. Rev. Lett. **111**, 186805 (2013) [doi: [10.1103/PhysRevLett.111.186805](https://doi.org/10.1103/PhysRevLett.111.186805)].
- [110] M. M. Vazifeh and M. Franz, “*Self-Organized Topological State with Majorana Fermions*,” Phys. Rev. Lett. **111**, 206802 (2013) [doi: [10.1103/PhysRevLett.111.206802](https://doi.org/10.1103/PhysRevLett.111.206802)].
- [111] F. Pientka, L. I. Glazman, and F. von Oppen, “*Topological superconducting phase in helical Shiba chains*,” Phys. Rev. B **88**, 155420 (2013) [doi: [10.1103/PhysRevB.88.155420](https://doi.org/10.1103/PhysRevB.88.155420)].
- [112] F. Pientka, L. I. Glazman, and F. von Oppen, “*Unconventional topological phase transitions in helical Shiba chains*,” Phys. Rev. B **89**, 180505 (2014) [doi: [10.1103/PhysRevB.89.180505](https://doi.org/10.1103/PhysRevB.89.180505)].
- [113] K. Pöyhönen, A. Westström, J. Röntynen, and T. Ojanen, “*Majorana states in helical Shiba chains and ladders*,” Phys. Rev. B **89**, 115109 (2014) [doi: [10.1103/PhysRevB.89.115109](https://doi.org/10.1103/PhysRevB.89.115109)].
- [114] N. Sedlmayr, J. M. Aguiar-Hualde, and C. Bena, “*Flat Majorana bands in two-dimensional lattices with inhomogeneous magnetic fields: Topology and stability*,” Phys. Rev. B **91**, 115415 (2015) [doi: [10.1103/PhysRevB.91.115415](https://doi.org/10.1103/PhysRevB.91.115415)].
- [115] W. Chen and A. P. Schnyder, “*Majorana edge states in superconductor-noncollinear magnet interfaces*,” Phys. Rev. B **92**, 214502 (2015) [doi: [10.1103/PhysRevB.92.214502](https://doi.org/10.1103/PhysRevB.92.214502)].
- [116] J. Xiao and J. An, “*Chiral symmetries and Majorana fermions in coupled magnetic atomic chains on a superconductor*,” New J. Phys. **17**, 113034 (2015) [doi: [10.1088/1367-2630/17/11/113034](https://doi.org/10.1088/1367-2630/17/11/113034)].
- [117] M. Schechter, K. Flensberg, M. H. Christensen, B. M. Andersen, and J. Paaske, “*Self-organized topological superconductivity in a Yu-Shiba-Rusinov chain*,” Phys. Rev. B **93**, 140503 (2016) [doi: [10.1103/PhysRevB.93.140503](https://doi.org/10.1103/PhysRevB.93.140503)].
- [118] M. H. Christensen, M. Schechter, K. Flensberg, B. M. Andersen, and J. Paaske, “*Spiral magnetic order and topological superconductivity in a chain of magnetic adatoms on a two-dimensional superconductor*,” Phys. Rev. B **94**, 144509 (2016) [doi: [10.1103/PhysRevB.94.144509](https://doi.org/10.1103/PhysRevB.94.144509)].
- [119] G. L. Fatin, A. Matos-Abiague, B. Scharf, and I. Žutić, “*Wireless Majorana Bound States: From Magnetic Tunability to Braiding*,” Phys. Rev. Lett. **117**, 077002 (2016) [doi: [10.1103/PhysRevLett.117.077002](https://doi.org/10.1103/PhysRevLett.117.077002)].
- [120] T. Zhou, N. Mohanta, J. E. Han, A. Matos-Abiague, and I. Žutić, “*Tunable magnetic textures in spin valves: From spintronics to Majorana bound states*,” Phys. Rev. B **99**, 134505 (2019) [doi: [10.1103/PhysRevB.99.134505](https://doi.org/10.1103/PhysRevB.99.134505)].
- [121] P. Marra and M. Cuoco, “*Controlling Majorana states in topologically inhomogeneous superconductors*,” Phys. Rev. B **95**, 140504 (2017) [doi: [10.1103/PhysRevB.95.140504](https://doi.org/10.1103/PhysRevB.95.140504)].
- [122] N. Mohanta, T. Zhou, J.-W. Xu, J. E. Han, A. D. Kent, J. Shabani, I. Žutić, and A. Matos-Abiague, “*Electrical Control of Majorana Bound States Using Magnetic Stripes*,” Phys. Rev. Appl. **12**, 034048 (2019) [doi: [10.1103/PhysRevApplied.12.034048](https://doi.org/10.1103/PhysRevApplied.12.034048)].

- [123] G.-Y. Huang, B. Li, X.-F. Yi, J.-B. Fu, X. Fu, X.-G. Qiang, P. Xu, J.-J. Wu, C.-L. Yu, P. Kotetes, and M.-T. Deng, “*Field-Programmable Topological Array: Framework and Case-Studies*,” arXiv (2020)
- [124] A. Heimes, P. Kotetes, and G. Schön, “*Majorana fermions from Shiba states in an antiferromagnetic chain on top of a superconductor*,” *Phys. Rev. B* **90**, 060507 (2014) [doi: 10.1103/PhysRevB.90.060507].
- [125] G. Livanas, M. Sigrist, and G. Varelogiannis, “*Alternative paths to realize Majorana Fermions in Superconductor-Ferromagnet Heterostructures*,” *Sci. Rep.* **9**, 1–7 (2019) [doi: 10.1038/s41598-019-42558-3].
- [126] K. Jiang, J. Hu, H. Ding, and Z. Wang, “*Interatomic Coulomb interaction and electron nematic bond order in FeSe*,” *Phys. Rev. B* **93**, 115138 (2016) [doi: 10.1103/PhysRevB.93.115138].
- [127] D. D. Scherer, A. C. Jacko, C. Friedrich, E. Şaşıoğlu, S. Blügel, R. Valentí, and B. M. Andersen, “*Interplay of nematic and magnetic orders in FeSe under pressure*,” *Phys. Rev. B* **95**, 094504 (2017) [doi: 10.1103/PhysRevB.95.094504].
- [128] D. Steffensen, “*Topological Magnetic Superconductors*,” master’s thesis, The Niels Bohr Institute, University of Copenhagen, (2017). [<https://www.nbi.ku.dk/english/theses/masters-theses/daniel-steffensen/>].
- [129] E. P. Wigner, *Gruppentheorie und ihre Anwendung auf die Quanten mechanik der Atomspektren*. Braunschweig, Germany: Friedrich Vieweg und Sohn, (1931).
- [130] E. P. Wigner, *Group Theory and its Application to the Quantum Mechanics of Atomic Spectra (Translation from German by J. J. Griffin)*. New York: Academic Press, (1959).
- [131] G. F. Koster, “*Space Groups and Their Representations*,” in *Solid State Physics*, vol. 5, 173–256, Cambridge, MA, USA: Academic Press, (1957).
- [132] T. Inui, Y. Tanabe, and Y. Onodera, *Group Theory and Its Applications in Physics*. Berlin, Germany: Springer-Verlag, 1990.
- [133] M. Tinkham, *Group Theory and Quantum Mechanics (Dover Books on Chemistry)*. Mineola, NY, USA: Dover Publications, (2003).
- [134] M. S. Dresselhaus, G. Dresselhaus, and A. Jorio, *Group Theory - Application to the Physics of Condensed Matter*. Springer-Verlag Berlin Heidelberg, (2008).
- [135] C. Bradley and A. Cracknell, *The Mathematical Theory of Symmetry in Solids*. Oxford, England, UK: Oxford University Press, (2009).
- [136] J. J. Sakurai and J. J. Napolitano, *Modern Quantum Mechanics (2nd Edition)*. Pearson, (2010).
- [137] M. Lax, *Symmetry Principles in Solid State and Molecular Physics (Dover Books on Physics)*. Mineola, NY, USA: Dover Publications, (2012).

- [138] S. Rettrup, *Introduction to Group Theoretical Methods in Quantum Chemistry*. Department of Chemistry, University of Copenhagen, (2014).
- [139] M. Sigrist, “Solid State Theory,” (2014). (Online; accessed 27. Dec. 2020), [<http://edu.itp.phys.ethz.ch/fs14/sst/Lecture-Notes.pdf>].
- [140] A. Schnyder, “Lectures on "Topological band crossings in semimetals",” (2018). (Online; accessed 9. Dec. 2019), [https://www.fkf.mpg.de/6431357/topo_lecture_notes_schnyder_TMS18.pdf].
- [141] P. Kotetes, *Topological Insulators*. Morgan & Claypool Publishers, (2019).
- [142] E. Noether, “*Invariante Variationsprobleme*,” Nachrichten von der Gesellschaft der Wissenschaften zu Göttingen, Mathematisch-Physikalische Klasse **1918**, 235–257 1918
- [143] E. Wigner, “*On Unitary Representations of the Inhomogeneous Lorentz Group*,” Ann. Of Math. **40**, 149–204 (1939)
- [144] W. Pauli, “*The Connection Between Spin and Statistics*,” Phys. Rev. **58**, 716–722 (1940) [doi: 10.1103/PhysRev.58.716].
- [145] B. W. Roberts, *Time, Symmetry and Structure: A Study in the Foundations of Quantum Theory*. PhD thesis, University of Pittsburgh. [<http://d-scholarship.pitt.edu/12533/>].
- [146] C.-K. Chiu, J. C. Y. Teo, A. P. Schnyder, and S. Ryu, “*Classification of topological quantum matter with symmetries*,” Rev. Mod. Phys. **88**, 035005 (2016) [doi: 10.1103/RevModPhys.88.035005].
- [147] A. Altland, “10-Fold Classification and Disorder in Topological Systems - Lecture One,” 2017. (Online; accessed 9. Dec. 2020), [<http://tms17.dipc.org/lecture-notes/lecture-altland-1.pdf>].
- [148] J. O. Dimmock and R. G. Wheeler, “*Irreducible representations of magnetic groups*,” J. Phys. Chem. Solids **23**, 729–741 (1962) [doi: 10.1016/0022-3697(62)90531-0].
- [149] C. J. Bradley and B. L. Davies, “*Magnetic Groups and Their Corepresentations*,” Rev. Mod. Phys. **40**, 359–379 (1968) [doi: 10.1103/RevModPhys.40.359].
- [150] R.-X. Zhang and C.-X. Liu, “*Topological magnetic crystalline insulators and corepresentation theory*,” Phys. Rev. B **91**, 115317 (2015) [doi: 10.1103/PhysRevB.91.115317].
- [151] B. Sutherland, “*Localization of electronic wave functions due to local topology*,” Phys. Rev. B **34**, 5208–5211 (1986) [doi: 10.1103/PhysRevB.34.5208].
- [152] K. G. L. Pedersen, M. Strange, M. Leijnse, P. Hedegård, G. C. Solomon, and J. Paaske, “*Quantum interference in off-resonant transport through single molecules*,” Phys. Rev. B **90**, 125413 (2014) [doi: 10.1103/PhysRevB.90.125413].
- [153] R. Ortiz, R. A. Boto, N. García-Martínez, J. C. Sancho-García, M. Melle-Franco, and J. Fernández-Rossier, “*Exchange Rules for Diradical π -Conjugated Hydrocarbons*,” Nano Lett. **19**, 5991–5997 (2019) [doi: 10.1021/acs.nanolett.9b01773].
- [154] M. Sato, Y. Tanaka, K. Yada, and T. Yokoyama, “*Topology of Andreev bound states with flat dispersion*,” Phys. Rev. B **83**, 224511 (2011) [doi: 10.1103/PhysRevB.83.224511].

- [155] C. Fang, M. J. Gilbert, and B. A. Bernevig, “*New Class of Topological Superconductors Protected by Magnetic Group Symmetries*,” *Phys. Rev. Lett.* **112**, 106401 (2014) [doi: 10.1103/PhysRevLett.112.106401].
- [156] G. F. Koster, J. O. Dimmock, R. G. Wheeler, and H. Statz, *Properties of the Thirty-Two Point Groups. (M.I.T. Press Research Monographs No. 24)*. M.I.T. Press, (1966).
- [157] “Character tables for chemically important point groups,” (2019). (Online; accessed 29. Dec. 2020), [<http://symmetry.jacobs-university.de>].
- [158] “Character Tables for Point Groups Cn, Cnv, Cnh, Dn, Dnh, Dnd, S2n etc.,” (2016). (Online; accessed 29. Dec. 2020), [http://genot-katzers-spice-pages.com/character_tables/index.html].
- [159] “Bilbao Crystallographic Server,” (2021). [Online; accessed 13. Jan. 2021].
- [160] “(International Tables) Home page,” (2020). [Online; accessed 13. Jan. 2021].
- [161] G. Frobenius and I. Schur, *Über die reellen Darstellungen der endlichen Gruppen*. S.B. Dtsch. Akad. Wiss., (1906).
- [162] C. Herring, “*Effect of Time-Reversal Symmetry on Energy Bands of Crystals*,” *Phys. Rev.* **52**, 361–365 (1937) [doi: 10.1103/PhysRev.52.361].
- [163] C. Herring, “*Character tables for two space groups*,” *J. Franklin Inst.* **233**, 525–543 (1942) [doi: 10.1016/S0016-0032(42)90462-9].
- [164] V. Cvetkovic and O. Vafek, “*Space group symmetry, spin-orbit coupling, and the low-energy effective Hamiltonian for iron-based superconductors*,” *Phys. Rev. B* **88**, 134510 (2013) [doi: 10.1103/PhysRevB.88.134510].
- [165] H. Bruus and K. Flensberg, *Many-Body Quantum Theory in Condensed Matter Physics: An Introduction (Oxford Graduate Texts)*. Oxford University Press, (2004).
- [166] D. Steffensen, P. Kotetes, I. Paul, and B. M. Andersen, “*Disorder-induced electronic nematicity*,” *Phys. Rev. B* **100**, 064521 (2019) [doi: 10.1103/PhysRevB.100.064521].
- [167] M. P. Lilly, K. B. Cooper, J. P. Eisenstein, L. N. Pfeiffer, and K. W. West, “*Evidence for an Anisotropic State of Two-Dimensional Electrons in High Landau Levels*,” *Phys. Rev. Lett.* **82**, 394–397 (1999) [doi: 10.1103/PhysRevLett.82.394].
- [168] R. R. Du, D. C. Tsui, H. L. Stormer, L. N. Pfeiffer, K. W. Baldwin, and K. W. West, “*Strongly anisotropic transport in higher two-dimensional Landau levels*,” *Solid State Commun.* **109**, 389–394 (1999) [doi: 10.1016/S0038-1098(98)00578-X].
- [169] R. A. Borzi, S. A. Grigera, J. Farrell, R. S. Perry, S. J. S. Lister, S. L. Lee, D. A. Tennant, Y. Maeno, and A. P. Mackenzie, “*Formation of a Nematic Fluid at High Fields in Sr₃Ru₂O₇*,” *Science* **315**, 214–217 (2007) [doi: 10.1126/science.1134796].
- [170] V. Hinkov, D. Haug, B. Fauqué, P. Bourges, Y. Sidis, A. Ivanov, C. Bernhard, C. T. Lin, and B. Keimer, “*Electronic Liquid Crystal State in the High-Temperature Superconductor YBa₂Cu₃O_{6.45}*,” *Science* **319**, 597–600 (2008) [doi: 10.1126/science.1152309].

- [171] S. Yonezawa, K. Tajiri, S. Nakata, Y. Nagai, Z. Wang, K. Segawa, Y. Ando, and Y. Maeno, “*Thermodynamic evidence for nematic superconductivity in $Cu_xBi_2Se_3$* ,” *Nat. Phys.* **13**, 123–126 (2016) [doi: [10.1038/nphys3907](https://doi.org/10.1038/nphys3907)].
- [172] R. Tao, Y.-J. Yan, X. Liu, Z.-W. Wang, Y. Ando, Q.-H. Wang, T. Zhang, and D.-L. Feng, “*Direct Visualization of the Nematic Superconductivity in $Cu_xBi_2Se_3$* ,” *Phys. Rev. X* **8**, 041024 (2018) [doi: [10.1103/PhysRevX.8.041024](https://doi.org/10.1103/PhysRevX.8.041024)].
- [173] S. Yonezawa, “*Nematic Superconductivity in Doped Bi_2Se_3 Topological Superconductors*,” *Condens. Matter* **4**, 2 (2019) [doi: [10.3390/condmat4010002](https://doi.org/10.3390/condmat4010002)].
- [174] A. Kerelsky, L. J. McGilly, D. M. Kennes, L. Xian, M. Yankowitz, S. Chen, K. Watanabe, T. Taniguchi, J. Hone, C. Dean, A. Rubio, and A. N. Pasupathy, “*Maximized electron interactions at the magic angle in twisted bilayer graphene*,” *Nature* **572**, 95–100 (2019) [doi: [10.1038/s41586-019-1431-9](https://doi.org/10.1038/s41586-019-1431-9)].
- [175] Y. Gallais, R. M. Fernandes, I. Paul, L. Chauvière, Y.-X. Yang, M.-A. Méasson, M. Cazayous, A. Sacuto, D. Colson, and A. Forget, “*Observation of Incipient Charge Nematicity in $Ba(Fe_{1-x}Co_x)_2As_2$* ,” *Phys. Rev. Lett.* **111**, 267001 (2013) [doi: [10.1103/PhysRevLett.111.267001](https://doi.org/10.1103/PhysRevLett.111.267001)].
- [176] T.-M. Chuang, M. P. Allan, J. Lee, Y. Xie, N. Ni, S. L. Bud’ko, G. S. Boebinger, P. C. Canfield, and J. C. Davis, “*Nematic Electronic Structure in the “Parent” State of the Iron-Based Superconductor $Ca(Fe_{1-x}Co_x)_2As_2$* ,” *Science* **327**, 181–184 (2010) [doi: [10.1126/science.1181083](https://doi.org/10.1126/science.1181083)].
- [177] C.-L. Song, Y.-L. Wang, P. Cheng, Y.-P. Jiang, W. Li, T. Zhang, Z. Li, K. He, L. Wang, J.-F. Jia, H.-H. Hung, C. Wu, X. Ma, X. Chen, and Q.-K. Xue, “*Direct Observation of Nodes and Twofold Symmetry in $FeSe$ Superconductor*,” *Science* **332**, 1410–1413 (2011) [doi: [10.1126/science.1202226](https://doi.org/10.1126/science.1202226)].
- [178] X. Zhou, C. Ye, P. Cai, X. Wang, X. Chen, and Y. Wang, “*Quasiparticle Interference of C_2 -Symmetric Surface States in a $LaOFeAs$ Parent Compound*,” *Phys. Rev. Lett.* **106**, 087001 (2011) [doi: [10.1103/PhysRevLett.106.087001](https://doi.org/10.1103/PhysRevLett.106.087001)].
- [179] S. Grothe, S. Chi, P. Dosanjh, R. Liang, W. N. Hardy, S. A. Burke, D. A. Bonn, and Y. Pennek, “*Bound states of defects in superconducting $LiFeAs$ studied by scanning tunneling spectroscopy*,” *Phys. Rev. B* **86**, 174503 (2012) [doi: [10.1103/PhysRevB.86.174503](https://doi.org/10.1103/PhysRevB.86.174503)].
- [180] M. P. Allan, T.-M. Chuang, F. Massee, Y. Xie, N. Ni, S. L. Bud’ko, G. S. Boebinger, Q. Wang, D. S. Dessau, P. C. Canfield, M. S. Golden, and J. C. Davis, “*Anisotropic impurity states, quasiparticle scattering and nematic transport in underdoped $Ca(Fe_{1-x}Co_x)_2As_2$* ,” *Nat. Phys.* **9**, 220–224 (2013) [doi: [10.1038/nphys2544](https://doi.org/10.1038/nphys2544)].
- [181] E. P. Rosenthal, E. F. Andrade, C. J. Arguello, R. M. Fernandes, L. Y. Xing, X. C. Wang, C. Q. Jin, A. J. Millis, and A. N. Pasupathy, “*Visualization of electron nematicity and unidirectional antiferroic fluctuations at high temperatures in $NaFeAs$* ,” *Nat. Phys.* **10**, 225–232 (2014) [doi: [10.1038/nphys2870](https://doi.org/10.1038/nphys2870)].

- [182] X. Ren, L. Duan, Y. Hu, J. Li, R. Zhang, H. Luo, P. Dai, and Y. Li, “*Nematic Crossover in BaFe₂As₂ under Uniaxial Stress*,” Phys. Rev. Lett. **115**, 197002 (2015) [doi: 10.1103/PhysRevLett.115.197002].
- [183] S.-H. Baek, D. V. Efremov, J. M. Ok, J. S. Kim, J. van den Brink, and B. Büchner, “*Nematicity and in-plane anisotropy of superconductivity in β -FeSe detected by ⁷⁷Se nuclear magnetic resonance*,” Phys. Rev. B **93**, 180502(R) (2016) [doi: 10.1103/PhysRevB.93.180502].
- [184] M. N. Gastiasoro, I. Paul, Y. Wang, P. J. Hirschfeld, and B. M. Andersen, “*Emergent Defect States as a Source of Resistivity Anisotropy in the Nematic Phase of Iron Pnictides*,” Phys. Rev. Lett. **113**, 127001 (2014) [doi: 10.1103/PhysRevLett.113.127001].
- [185] Y. Wang, M. N. Gastiasoro, B. M. Andersen, M. Tomić, H. O. Jeschke, R. Valentí, I. Paul, and P. J. Hirschfeld, “*Effects of Lifshitz Transition on Charge Transport in Magnetic Phases of Fe-Based Superconductors*,” Phys. Rev. Lett. **114**, 097003 (2015) [doi: 10.1103/PhysRevLett.114.097003].
- [186] C.-C. Chen, B. Moritz, J. van den Brink, T. P. Devereaux, and R. R. P. Singh, “*Finite-temperature spin dynamics and phase transitions in spin-orbital models*,” Phys. Rev. B **80**, 180418(R) (2009) [doi: 10.1103/PhysRevB.80.180418].
- [187] Y. Inoue, Y. Yamakawa, and H. Kontani, “*Impurity-induced electronic nematic state and C₂-symmetric nanostructures in iron pnictide superconductors*,” Phys. Rev. B **85**, 224506 (2012) [doi: 10.1103/PhysRevB.85.224506].
- [188] M. N. Gastiasoro, P. J. Hirschfeld, and B. M. Andersen, “*Origin of electronic dimers in the spin-density wave phase of Fe-based superconductors*,” Phys. Rev. B **89**, 100502(R) (2014) [doi: 10.1103/PhysRevB.89.100502].
- [189] M. Hoyer, R. M. Fernandes, A. Levchenko, and J. Schmalian, “*Disorder-promoted C₄-symmetric magnetic order in iron-based superconductors*,” Phys. Rev. B **93**, 144414 (2016) [doi: 10.1103/PhysRevB.93.144414].
- [190] T. Iye, M.-H. Julien, H. Mayaffre, M. Horvatić, C. Berthier, K. Ishida, H. Ikeda, S. Kasahara, T. Shibauchi, and Y. Matsuda, “*Emergence of Orbital Nematicity in the Tetragonal Phase of BaFe₂(As_{1-x}Px)₂*,” J. Phys. Soc. Jpn. **84**, 043705 (2015) [doi: 10.7566/JPSJ.84.043705].
- [191] R. Zhou, L. Y. Xing, X. C. Wang, C. Q. Jin, and G.-q. Zheng, “*Orbital order and spin nematicity in the tetragonal phase of the electron-doped iron pnictides NaFe_{1-x}Co_xAs*,” Phys. Rev. B **93**, 060502(R) (2016) [doi: 10.1103/PhysRevB.93.060502].
- [192] P. S. Wang, P. Zhou, S. S. Sun, Y. Cui, T. R. Li, H. Lei, Z. Wang, and W. Yu, “*Robust short-range-ordered nematicity in FeSe evidenced by high-pressure NMR*,” Phys. Rev. B **96**, 094528 (2017) [doi: 10.1103/PhysRevB.96.094528].
- [193] P. Wiecki, M. Nandi, A. E. Böhrer, S. L. Bud’ko, P. C. Canfield, and Y. Furukawa, “*NMR evidence for static local nematicity and its cooperative interplay with low-energy magnetic fluctuations in FeSe under pressure*,” Phys. Rev. B **96**, 180502(R) (2017) [doi: 10.1103/PhysRevB.96.180502].

- [194] M. Toyoda, Y. Kobayashi, and M. Itoh, “Nematic fluctuations in iron arsenides NaFeAs and LiFeAs probed by ^{75}As NMR,” *Phys. Rev. B* **97**, 094515 (2018) [doi: [10.1103/PhysRevB.97.094515](https://doi.org/10.1103/PhysRevB.97.094515)].
- [195] W. Wang, Y. Song, C. Cao, K.-F. Tseng, T. Keller, Y. Li, L. W. Harriger, W. Tian, S. Chi, R. Yu, A. H. Nevidomskyy, and P. Dai, “Local orthorhombic lattice distortions in the paramagnetic tetragonal phase of superconducting $\text{NaFe}_{1-x}\text{Ni}_x\text{As}$,” *Nat. Commun.* **9**, 1–9 (2018) [doi: [10.1038/s41467-018-05529-2](https://doi.org/10.1038/s41467-018-05529-2)].
- [196] P. Zhang, T. Qian, P. Richard, X. P. Wang, H. Miao, B. Q. Lv, B. B. Fu, T. Wolf, C. Meingast, X. X. Wu, Z. Q. Wang, J. P. Hu, and H. Ding, “Observation of two distinct d_{xz}/d_{yz} band splittings in FeSe ,” *Phys. Rev. B* **91**, 214503 (2015) [doi: [10.1103/PhysRevB.91.214503](https://doi.org/10.1103/PhysRevB.91.214503)].
- [197] C.-W. Luo, P. Chung Cheng, S.-H. Wang, J.-C. Chiang, J.-Y. Lin, K.-H. Wu, J.-Y. Juang, D. A. Chareev, O. S. Volkova, and A. N. Vasiliev, “Unveiling the hidden nematicity and spin subsystem in FeSe ,” *npj Quantum Mater.* **2**, 1–6 (2017) [doi: [10.1038/s41535-017-0036-5](https://doi.org/10.1038/s41535-017-0036-5)].
- [198] R. J. Koch, T. Konstantinova, M. Abeykoon, A. Wang, C. Petrovic, Y. Zhu, E. S. Bozin, and S. J. L. Billinge, “Room temperature local nematicity in FeSe superconductor,” *Phys. Rev. B* **100**, 020501 (2019) [doi: [10.1103/PhysRevB.100.020501](https://doi.org/10.1103/PhysRevB.100.020501)].
- [199] B. A. Frandsen, Q. Wang, S. Wu, J. Zhao, and R. J. Birgeneau, “Quantitative characterization of short-range orthorhombic fluctuations in FeSe through pair distribution function analysis,” *Phys. Rev. B* **100**, 020504 (2019) [doi: [10.1103/PhysRevB.100.020504](https://doi.org/10.1103/PhysRevB.100.020504)].
- [200] G. Livanas, A. Aperis, P. Kotetes, and G. Varelogiannis, “Nematicity from mixed $S_{\pm} + d_{x^2-y^2}$ states in iron-based superconductors,” *Phys. Rev. B* **91**, 104502 (2015) [doi: [10.1103/PhysRevB.91.104502](https://doi.org/10.1103/PhysRevB.91.104502)].
- [201] R. M. Fernandes and A. J. Millis, “Nematicity as a Probe of Superconducting Pairing in Iron-Based Superconductors,” *Phys. Rev. Lett.* **111**, 127001 (2013) [doi: [10.1103/PhysRevLett.111.127001](https://doi.org/10.1103/PhysRevLett.111.127001)].
- [202] E. I. Timmons, M. A. Tanatar, K. Willa, S. Teknowijoyo, K. Cho, M. Kończykowski, O. Cavani, Y. Liu, T. A. Lograsso, U. Welp, and R. Prozorov, “Competition between orthorhombic and re-entrant tetragonal phases in underdoped $\text{Ba}_{1-x}\text{K}_x\text{Fe}_2\text{As}_2$ probed by the response to controlled disorder,” *Phys. Rev. B* **99**, 054518 (2019) [doi: [10.1103/PhysRevB.99.054518](https://doi.org/10.1103/PhysRevB.99.054518)].
- [203] Y. Gallais and I. Paul, “Charge nematicity and electronic Raman scattering in iron-based superconductors,” *C. R. Phys.* **17**, 113–139 (2016) [doi: [10.1016/j.crhy.2015.10.001](https://doi.org/10.1016/j.crhy.2015.10.001)].
- [204] B. M. Andersen, P. J. Hirschfeld, A. P. Kampf, and M. Schmid, “Disorder-Induced Static Antiferromagnetism in Cuprate Superconductors,” *Phys. Rev. Lett.* **99**, 147002 (2007) [doi: [10.1103/PhysRevLett.99.147002](https://doi.org/10.1103/PhysRevLett.99.147002)].
- [205] A. T. Rømer, S. Graser, T. S. Nunner, P. J. Hirschfeld, and B. M. Andersen, “Local modulations of the spin-fluctuation-mediated pairing interaction by impurities in d -wave superconductors,” *Phys. Rev. B* **86**, 054507 (2012) [doi: [10.1103/PhysRevB.86.054507](https://doi.org/10.1103/PhysRevB.86.054507)].

- [206] M. N. Gastiasoro, P. J. Hirschfeld, and B. M. Andersen, “*Impurity states and cooperative magnetic order in Fe-based superconductors*,” Phys. Rev. B **88**, 220509(R) (2013) [doi: 10.1103/PhysRevB.88.220509].
- [207] A. F. Ho and A. J. Schofield, “*Effect of disorder on a Pomeranchuk instability*,” EPL **84**, 27007 (2008) [doi: 10.1209/0295-5075/84/27007].
- [208] I. Khavkine, C.-H. Chung, V. Oganesyan, and H.-Y. Kee, “*Formation of an electronic nematic phase in interacting fermion systems*,” Phys. Rev. B **70**, 155110 (2004) [doi: 10.1103/PhysRevB.70.155110].
- [209] H. Yamase, V. Oganesyan, and W. Metzner, “*Mean-field theory for symmetry-breaking Fermi surface deformations on a square lattice*,” Phys. Rev. B **72**, 035114 (2005) [doi: 10.1103/PhysRevB.72.035114].
- [210] D. Steffensen, A. Kreisel, P. J. Hirschfeld, and B. M. Andersen, “*Inter-orbital nematicity and the origin of a single electron Fermi pocket in FeSe*,” arXiv (2020)
- [211] T. Chen, Y. Chen, A. Kreisel, X. Lu, A. Schneidewind, Y. Qiu, J. T. Park, T. G. Perring, J. R. Stewart, H. Cao, R. Zhang, Y. Li, Y. Rong, Y. Wei, B. M. Andersen, P. J. Hirschfeld, C. Broholm, and P. Dai, “*Anisotropic spin fluctuations in detwinned FeSe*,” Nat. Mater. **18**, 709–716 (2019) [doi: 10.1038/s41563-019-0369-5].
- [212] A. E. Böhmer, F. Hardy, F. Eilers, D. Ernst, P. Adelman, P. Schweiss, T. Wolf, and C. Meingast, “*Lack of coupling between superconductivity and orthorhombic distortion in stoichiometric single-crystalline FeSe*,” Phys. Rev. B **87**, 180505 (2013) [doi: 10.1103/PhysRevB.87.180505].
- [213] M. A. Tanatar, A. E. Böhmer, E. I. Timmons, M. Schütt, G. Drachuck, V. Taufour, K. Kothapalli, A. Kreyssig, S. L. Bud’ko, P. C. Canfield, R. M. Fernandes, and R. Prozorov, “*Origin of the Resistivity Anisotropy in the Nematic Phase of FeSe*,” Phys. Rev. Lett. **117**, 127001 (2016) [doi: 10.1103/PhysRevLett.117.127001].
- [214] A. Kostin, P. O. Sprau, A. Kreisel, Y. X. Chong, A. E. Böhmer, P. C. Canfield, P. J. Hirschfeld, B. M. Andersen, and J. C. S. Davis, “*Imaging orbital-selective quasiparticles in the Hund’s metal state of FeSe*,” Nat. Mater. **17**, 869–874 (2018) [doi: 10.1038/s41563-018-0151-0].
- [215] R. Zhou, D. D. Scherer, H. Mayaffre, P. Toulemonde, M. Ma, Y. Li, B. M. Andersen, and M.-H. Julien, “*Singular magnetic anisotropy in the nematic phase of FeSe*,” npj Quantum Mater. **5**, 1–9 (2020) [doi: 10.1038/s41535-020-00295-1].
- [216] A. Kreisel, B. M. Andersen, P. O. Sprau, A. Kostin, J. C. S. Davis, and P. J. Hirschfeld, “*Orbital selective pairing and gap structures of iron-based superconductors*,” Phys. Rev. B **95**, 174504 (2017) [doi: 10.1103/PhysRevB.95.174504].
- [217] L. Benfatto, B. Valenzuela, and L. Fanfarillo, “*Nematic pairing from orbital-selective spin fluctuations in FeSe*,” npj Quantum Mater. **3**, 1–7 (2018) [doi: 10.1038/s41535-018-0129-9].
- [218] H. Hu, R. Yu, E. M. Nica, J.-X. Zhu, and Q. Si, “*Orbital-selective superconductivity in the nematic phase of FeSe*,” Phys. Rev. B **98**, 220503 (2018) [doi: 10.1103/PhysRevB.98.220503].

- [219] L. De' Medici, G. Giovannetti, and M. Capone, “*Selective Mott Physics as a Key to Iron Superconductors*,” Phys. Rev. Lett. **112**, 177001 (2014) [doi: [10.1103/PhysRevLett.112.177001](https://doi.org/10.1103/PhysRevLett.112.177001)].
- [220] K. Björnson, A. Kreisel, A. T. Rømer, and B. M. Andersen, “*Orbital-dependent self-energy effects and consequences for the superconducting gap structure in multi-orbital correlated electron systems*,” arXiv (2020)
- [221] H. Cercellier, P. Rodière, P. Toulemonde, C. Marcenat, and T. Klein, “*Influence of the quasiparticle spectral weight in FeSe on spectroscopic, magnetic, and thermodynamic properties*,” Phys. Rev. B **100**, 104516 (2019) [doi: [10.1103/PhysRevB.100.104516](https://doi.org/10.1103/PhysRevB.100.104516)].
- [222] P. K. Biswas, A. Kreisel, Q. Wang, D. T. Adroja, A. D. Hillier, J. Zhao, R. Khasanov, J.-C. Orain, A. Amato, and E. Morenzoni, “*Evidence of nodal gap structure in the basal plane of the FeSe superconductor*,” Phys. Rev. B **98**, 180501 (2018) [doi: [10.1103/PhysRevB.98.180501](https://doi.org/10.1103/PhysRevB.98.180501)].
- [223] A. Georges, L. d. Medici, and J. Mravlje, “*Strong Correlations from Hund’s Coupling*,” Annu. Rev. Condens. Matter Phys. **4**, 137–178 (2013) [doi: [10.1146/annurev-conmatphys-020911-125045](https://doi.org/10.1146/annurev-conmatphys-020911-125045)].
- [224] A. van Roekeghem, P. Richard, H. Ding, and S. Biermann, “*Spectral properties of transition metal pnictides and chalcogenides: Angle-resolved photoemission spectroscopy and dynamical mean-field theory*,” C. R. Phys. **17**, 140–163 (2016) [doi: [10.1016/j.crhy.2015.11.003](https://doi.org/10.1016/j.crhy.2015.11.003)].
- [225] M. Yi, Y. Zhang, Z.-X. Shen, and D. Lu, “*Role of the orbital degree of freedom in iron-based superconductors*,” npj Quantum Mater. **2**, 1–12 (2017) [doi: [10.1038/s41535-017-0059-y](https://doi.org/10.1038/s41535-017-0059-y)].
- [226] D. Guterding, S. Backes, M. Tomić, H. O. Jeschke, and R. Valentí, “*Ab initio perspective on structural and electronic properties of iron-based superconductors*,” Phys. Status Solidi B **254**, 1600164 (2017) [doi: [10.1002/pssb.201600164](https://doi.org/10.1002/pssb.201600164)].
- [227] E. Pavarini, E. Koch, R. Martin, and R. Scalettar, *The Physics of Correlated Insulators, Metals, and Superconductors*. Forschungszentrum Jülich GmbH Zentralbibliothek, Verlag, 2017.
- [228] A. Kreisel, B. M. Andersen, and P. J. Hirschfeld, “*Itinerant approach to magnetic neutron scattering of FeSe: Effect of orbital selectivity*,” Phys. Rev. B **98**, 214518 (2018) [doi: [10.1103/PhysRevB.98.214518](https://doi.org/10.1103/PhysRevB.98.214518)].
- [229] M. D. Watson, A. A. Haghighirad, L. C. Rhodes, M. Hoesch, and T. K. Kim, “*Electronic anisotropies revealed by detwinned angle-resolved photo-emission spectroscopy measurements of FeSe*,” New J. Phys. **19**, 103021 (2017) [doi: [10.1088/1367-2630/aa8a04](https://doi.org/10.1088/1367-2630/aa8a04)].
- [230] H. Pfau, S. D. Chen, M. Yi, M. Hashimoto, C. R. Rotundu, J. C. Palmstrom, T. Chen, P.-C. Dai, J. Straquadine, A. Hristov, R. J. Birgeneau, I. R. Fisher, D. Lu, and Z.-X. Shen, “*Momentum Dependence of the Nematic Order Parameter in Iron-Based Superconductors*,” Phys. Rev. Lett. **123**, 066402 (2019) [doi: [10.1103/PhysRevLett.123.066402](https://doi.org/10.1103/PhysRevLett.123.066402)].
- [231] L. C. Rhodes, M. D. Watson, A. A. Haghighirad, D. V. Evtushinsky, and T. K. Kim, “*Revealing the single electron pocket of FeSe in a single orthorhombic domain*,” Phys. Rev. B **101**, 235128 (2020) [doi: [10.1103/PhysRevB.101.235128](https://doi.org/10.1103/PhysRevB.101.235128)].

- [232] D. Liu, C. Li, J. Huang, B. Lei, L. Wang, X. Wu, B. Shen, Q. Gao, Y. Zhang, X. Liu, Y. Hu, Y. Xu, A. Liang, J. Liu, P. Ai, L. Zhao, S. He, L. Yu, G. Liu, Y. Mao, X. Dong, X. Jia, F. Zhang, S. Zhang, F. Yang, Z. Wang, Q. Peng, Y. Shi, J. Hu, T. Xiang, X. Chen, Z. Xu, C. Chen, and X. J. Zhou, “*Orbital Origin of Extremely Anisotropic Superconducting Gap in Nematic Phase of FeSe Superconductor*,” *Phys. Rev. X* **8**, 031033 (2018) [doi: 10.1103/PhysRevX.8.031033].
- [233] M. Yi, H. Pfau, Y. Zhang, Y. He, H. Wu, T. Chen, Z. R. Ye, M. Hashimoto, R. Yu, Q. Si, D.-H. Lee, P. Dai, Z.-X. Shen, D. H. Lu, and R. J. Birgeneau, “*Nematic Energy Scale and the Missing Electron Pocket in FeSe*,” *Phys. Rev. X* **9**, 041049 (2019) [doi: 10.1103/PhysRevX.9.041049].
- [234] S. S. Huh, J. J. Seo, B. S. Kim, S. H. Cho, J. K. Jung, S. Kim, C. I. Kwon, J. S. Kim, Y. Y. Koh, W. S. Kyung, J. D. Denlinger, Y. H. Kim, B. N. Chae, N. D. Kim, Y. K. Kim, and C. Kim, “*Absence of Y-pocket in 1-Fe Brillouin zone and reversed orbital occupation imbalance in FeSe*,” *Commun. Phys.* **3**, 1–7 (2020) [doi: 10.1038/s42005-020-0319-1].
- [235] S. Mukherjee, A. Kreisel, P. J. Hirschfeld, and B. M. Andersen, “*Model of Electronic Structure and Superconductivity in Orbitally Ordered FeSe*,” *Phys. Rev. Lett.* **115**, 026402 (2015) [doi: 10.1103/PhysRevLett.115.026402].
- [236] Y. Liang, X.-X. Wu, and J.-P. Hu, “*Electronic Structure Properties in the Nematic Phases of FeSe**,” *Chin. Phys. Lett.* **32**, 117402 (2015) [doi: 10.1088/0256-307x/32/11/117402].
- [237] Y. Suzuki, T. Shimojima, T. Sonobe, A. Nakamura, M. Sakano, H. Tsuji, J. Omachi, K. Yoshioka, M. Kuwata-Gonokami, T. Watashige, R. Kobayashi, S. Kasahara, T. Shibauchi, Y. Matsuda, Y. Yamakawa, H. Kontani, and K. Ishizaka, “*Momentum-dependent sign inversion of orbital order in superconducting FeSe*,” *Phys. Rev. B* **92**, 205117 (2015) [doi: 10.1103/PhysRevB.92.205117].
- [238] M. D. Watson, T. K. Kim, L. C. Rhodes, M. Eschrig, M. Hoesch, A. A. Haghighirad, and A. I. Coldea, “*Evidence for unidirectional nematic bond ordering in FeSe*,” *Phys. Rev. B* **94**, 201107 (2016) [doi: 10.1103/PhysRevB.94.201107].
- [239] L. Fanfarillo, J. Mansart, P. Toulemonde, H. Cercellier, P. Le Fèvre, F. Bertran, B. Valenzuela, L. Benfatto, and V. Brouet, “*Orbital-dependent Fermi surface shrinking as a fingerprint of nematicity in FeSe*,” *Phys. Rev. B* **94**, 155138 (2016) [doi: 10.1103/PhysRevB.94.155138].
- [240] A. Fedorov, A. Yaresko, T. K. Kim, Y. Kushnirenko, E. Haubold, T. Wolf, M. Hoesch, A. Grüneis, B. Büchner, and S. V. Borisenko, “*Effect of nematic ordering on electronic structure of FeSe*,” *Sci. Rep.* **6**, 1–7 (2016) [doi: 10.1038/srep36834].
- [241] S. Onari, Y. Yamakawa, and H. Kontani, “*Sign-Reversing Orbital Polarization in the Nematic Phase of FeSe due to the C₂ Symmetry Breaking in the Self-Energy*,” *Phys. Rev. Lett.* **116**, 227001 (2016) [doi: 10.1103/PhysRevLett.116.227001].
- [242] R.-Q. Xing, L. Classen, M. Khodas, and A. V. Chubukov, “*Competing instabilities, orbital ordering, and splitting of band degeneracies from a parquet renormalization group analysis of a four-pocket model for iron-based superconductors: Application to FeSe*,” *Phys. Rev. B* **95**, 085108 (2017) [doi: 10.1103/PhysRevB.95.085108].

- [243] P. M. Eugenio and O. Vafek, “*Classification of symmetry derived pairing at the M point in FeSe*,” Phys. Rev. B **98**, 014503 (2018) [doi: [10.1103/PhysRevB.98.014503](https://doi.org/10.1103/PhysRevB.98.014503)].
- [244] M. H. Christensen, J. Kang, and R. M. Fernandes, “*Intertwined spin-orbital coupled orders in the iron-based superconductors*,” Phys. Rev. B **100**, 014512 (2019) [doi: [10.1103/PhysRevB.100.014512](https://doi.org/10.1103/PhysRevB.100.014512)].
- [245] M. H. Christensen, R. M. Fernandes, and A. V. Chubukov, “*Orbital transmutation and the electronic spectrum of FeSe in the nematic phase*,” Phys. Rev. Res. **2**, 013015 (2020) [doi: [10.1103/PhysRevResearch.2.013015](https://doi.org/10.1103/PhysRevResearch.2.013015)].
- [246] L. C. Rhodes, J. Böker, M. A. Müller, M. Eschrig, and I. M. Eremin, “*Non-local d_{xy} nematicity and the missing electron pocket in FeSe*,” arXiv (2020)
- [247] X. Long, S. Zhang, F. Wang, and Z. Liu, “*A first-principle perspective on electronic nematicity in FeSe*,” npj Quantum Mater. **5**, 1–9 (2020) [doi: [10.1038/s41535-020-00253-x](https://doi.org/10.1038/s41535-020-00253-x)].
- [248] K. Zantout, S. Backes, and R. Valentí, “*Effect of Nonlocal Correlations on the Electronic Structure of LiFeAs*,” Phys. Rev. Lett. **123**, 256401 (2019) [doi: [10.1103/PhysRevLett.123.256401](https://doi.org/10.1103/PhysRevLett.123.256401)].
- [249] S. Bhattacharyya, P. J. Hirschfeld, T. A. Maier, and D. J. Scalapino, “*Effects of momentum-dependent quasiparticle renormalization on the gap structure of iron-based superconductors*,” Phys. Rev. B **101**, 174509 (2020) [doi: [10.1103/PhysRevB.101.174509](https://doi.org/10.1103/PhysRevB.101.174509)].
- [250] H. Eschrig and K. Koepf, “*Tight-binding models for the iron-based superconductors*,” Phys. Rev. B **80**, 104503 (2009) [doi: [10.1103/PhysRevB.80.104503](https://doi.org/10.1103/PhysRevB.80.104503)].
- [251] A. V. Chubukov, M. Khodas, and R. M. Fernandes, “*Magnetism, Superconductivity, and Spontaneous Orbital Order in Iron-Based Superconductors: Which Comes First and Why?*,” Phys. Rev. X **6**, 041045 (2016) [doi: [10.1103/PhysRevX.6.041045](https://doi.org/10.1103/PhysRevX.6.041045)].
- [252] S. Bhattacharyya, K. Björnson, K. Zantout, D. Steffensen, L. Fanfarillo, A. Kreisel, R. Valentí, B. M. Andersen, and P. J. Hirschfeld, “*Nonlocal correlations in iron pnictides and chalcogenides*,” Phys. Rev. B **102**, 035109 (2020) [doi: [10.1103/PhysRevB.102.035109](https://doi.org/10.1103/PhysRevB.102.035109)].
- [253] M. N. Gastiasoro and B. M. Andersen, “*Competing magnetic double-Q phases and superconductivity-induced reentrance of C_2 magnetic stripe order in iron pnictides*,” Phys. Rev. B **92**, 140506 (2015) [doi: [10.1103/PhysRevB.92.140506](https://doi.org/10.1103/PhysRevB.92.140506)].
- [254] M. C. Rahn, R. A. Ewings, S. J. Sedlmaier, S. J. Clarke, and A. T. Boothroyd, “*Strong $(\pi, 0)$ spin fluctuations in β -FeSe observed by neutron spectroscopy*,” Phys. Rev. B **91**, 180501 (2015) [doi: [10.1103/PhysRevB.91.180501](https://doi.org/10.1103/PhysRevB.91.180501)].
- [255] Q. Wang, Y. Shen, B. Pan, Y. Hao, M. Ma, F. Zhou, P. Steffens, K. Schmalzl, T. R. Forrest, M. Abdel-Hafiez, X. Chen, D. A. Chareev, A. N. Vasiliev, P. Bourges, Y. Sidis, H. Cao, and J. Zhao, “*Strong interplay between stripe spin fluctuations, nematicity and superconductivity in FeSe*,” Nat. Mater. **15**, 159–163 (2016) [doi: [10.1038/nmat4492](https://doi.org/10.1038/nmat4492)].

- [256] L. Fanfarillo, L. Benfatto, and B. Valenzuela, “Orbital mismatch boosting nematic instability in iron-based superconductors,” *Phys. Rev. B* **97**, 121109 (2018) [doi: 10.1103/PhysRevB.97.121109].
- [257] A. Kreisel, S. Mukherjee, P. J. Hirschfeld, and B. M. Andersen, “Spin excitations in a model of *FeSe* with orbital ordering,” *Phys. Rev. B* **92**, 224515 (2015) [doi: 10.1103/PhysRevB.92.224515].
- [258] M. H. Christensen, J. Kang, B. M. Andersen, and R. M. Fernandes, “Spin-driven nematic instability of the multiorbital Hubbard model: Application to iron-based superconductors,” *Phys. Rev. B* **93**, 085136 (2016) [doi: 10.1103/PhysRevB.93.085136].
- [259] T. Miyake, K. Nakamura, R. Arita, and M. Imada, “Comparison of *Ab initio* Low-Energy Models for *LaFePO*, *LaFeAsO*, *BaFe₂As₂*, *LiFeAs*, *FeSe*, and *FeTe*: Electron Correlation and Covalency,” *J. Phys. Soc. Jpn.* **79**, 044705 (2010) [doi: 10.1143/JPSJ.79.044705].
- [260] Z. P. Yin, K. Haule, and G. Kotliar, “Kinetic frustration and the nature of the magnetic and paramagnetic states in iron pnictides and iron chalcogenides,” *Nat. Mater.* **10**, 932–935 (2011) [doi: 10.1038/nmat3120].
- [261] L. Jiao, C.-L. Huang, S. Rößler, C. Koz, U. K. Rößler, U. Schwarz, and S. Wirth, “Superconducting gap structure of *FeSe*,” *Sci. Rep.* **7**, 1–8 (2017) [doi: 10.1038/srep44024].
- [262] A. V. Muratov, A. V. Sadakov, S. Yu. Gavrilkin, A. R. Prishchepa, G. S. Epifanova, D. A. Chareev, and V. M. Pudalov, “Specific heat of *FeSe*: Two gaps with different anisotropy in superconducting state,” *Physica B* **536**, 785–789 (2018) [doi: 10.1016/j.physb.2017.10.041].
- [263] A. E. Böhmer, T. Arai, F. Hardy, T. Hattori, T. Iye, T. Wolf, H. v. Löhneysen, K. Ishida, and C. Meingast, “Origin of the Tetragonal-to-Orthorhombic Phase Transition in *FeSe*: A Combined Thermodynamic and NMR Study of Nematicity,” *Phys. Rev. Lett.* **114**, 027001 (2015) [doi: 10.1103/PhysRevLett.114.027001].
- [264] Z. Wang, X.-G. Zhao, R. Koch, S. J. L. Billinge, and A. Zunger, “Understanding electronic peculiarities in tetragonal *FeSe* as local structural symmetry breaking,” *Phys. Rev. B* **102**, 235121 (2020) [doi: 10.1103/PhysRevB.102.235121].
- [265] C. Eckberg, D. J. Campbell, T. Metz, J. Collini, H. Hodovanets, T. Drye, P. Zavalij, M. H. Christensen, R. M. Fernandes, S. Lee, P. Abbamonte, J. W. Lynn, and J. Paglione, “Sixfold enhancement of superconductivity in a tunable electronic nematic system,” *Nat. Phys.* **16**, 346–350 (2020) [doi: 10.1038/s41567-019-0736-9].
- [266] K. Kuroki, S. Onari, R. Arita, H. Usui, Y. Tanaka, H. Kontani, and H. Aoki, “Unconventional Pairing Originating from the Disconnected Fermi Surfaces of Superconducting *LaFeAsO_{1-x}F_x*,” *Phys. Rev. Lett.* **101**, 087004 (2008) [doi: 10.1103/PhysRevLett.101.087004].
- [267] A. F. Kemper, T. A. Maier, S. Graser, H.-P. Cheng, P. J. Hirschfeld, and D. J. Scalapino, “Sensitivity of the superconducting state and magnetic susceptibility to key aspects of electronic structure in ferropnictides,” *New J. Phys.* **12**, 073030 (2010) [doi: 10.1088/1367-2630/12/7/073030].

- [268] D. Steffensen, B. M. Andersen, and P. Kotetes, “*Majorana Zero Modes in Magnetic Texture Vortices*,” arXiv (2020)
- [269] D. A. Ivanov, “*Non-Abelian Statistics of Half-Quantum Vortices in p -Wave Superconductors*,” Phys. Rev. Lett. **86**, 268–271 (2001) [doi: [10.1103/PhysRevLett.86.268](https://doi.org/10.1103/PhysRevLett.86.268)].
- [270] J. D. Sau, R. M. Lutchyn, S. Tewari, and S. Das Sarma, “*Generic New Platform for Topological Quantum Computation Using Semiconductor Heterostructures*,” Phys. Rev. Lett. **104**, 040502 (2010) [doi: [10.1103/PhysRevLett.104.040502](https://doi.org/10.1103/PhysRevLett.104.040502)].
- [271] Z. Wang, P. Zhang, G. Xu, L. K. Zeng, H. Miao, X. Xu, T. Qian, H. Weng, P. Richard, A. V. Fedorov, H. Ding, X. Dai, and Z. Fang, “*Topological nature of the $\text{FeSe}_{0.5}\text{Te}_{0.5}$ superconductor*,” Phys. Rev. B **92**, 115119 (2015) [doi: [10.1103/PhysRevB.92.115119](https://doi.org/10.1103/PhysRevB.92.115119)].
- [272] G. Xu, B. Lian, P. Tang, X.-L. Qi, and S.-C. Zhang, “*Topological Superconductivity on the Surface of Fe-Based Superconductors*,” Phys. Rev. Lett. **117**, 047001 (2016) [doi: [10.1103/PhysRevLett.117.047001](https://doi.org/10.1103/PhysRevLett.117.047001)].
- [273] M. Wimmer, A. R. Akhmerov, M. V. Medvedyeva, J. Tworzydło, and C. W. J. Beenakker, “*Majorana Bound States without Vortices in Topological Superconductors with Electrostatic Defects*,” Phys. Rev. Lett. **105**, 046803 (2010) [doi: [10.1103/PhysRevLett.105.046803](https://doi.org/10.1103/PhysRevLett.105.046803)].
- [274] J. Alicea, “*Majorana fermions in a tunable semiconductor device*,” Phys. Rev. B **81**, 125318 (2010) [doi: [10.1103/PhysRevB.81.125318](https://doi.org/10.1103/PhysRevB.81.125318)].
- [275] R. M. Lutchyn, J. D. Sau, and S. Das Sarma, “*Majorana Fermions and a Topological Phase Transition in Semiconductor-Superconductor Heterostructures*,” Phys. Rev. Lett. **105**, 077001 (2010) [doi: [10.1103/PhysRevLett.105.077001](https://doi.org/10.1103/PhysRevLett.105.077001)].
- [276] Y. Oreg, G. Refael, and F. von Oppen, “*Helical Liquids and Majorana Bound States in Quantum Wires*,” Phys. Rev. Lett. **105**, 177002 (2010) [doi: [10.1103/PhysRevLett.105.177002](https://doi.org/10.1103/PhysRevLett.105.177002)].
- [277] J. Klinovaja and D. Loss, “*Time-reversal invariant parafermions in interacting Rashba nanowires*,” Phys. Rev. B **90**, 045118 (2014) [doi: [10.1103/PhysRevB.90.045118](https://doi.org/10.1103/PhysRevB.90.045118)].
- [278] M. Hell, M. Leijnse, and K. Flensberg, “*Two-Dimensional Platform for Networks of Majorana Bound States*,” Phys. Rev. Lett. **118**, 107701 (2017) [doi: [10.1103/PhysRevLett.118.107701](https://doi.org/10.1103/PhysRevLett.118.107701)].
- [279] F. Pientka, A. Keselman, E. Berg, A. Yacoby, A. Stern, and B. I. Halperin, “*Topological Superconductivity in a Planar Josephson Junction*,” Phys. Rev. X **7**, 021032 (2017) [doi: [10.1103/PhysRevX.7.021032](https://doi.org/10.1103/PhysRevX.7.021032)].
- [280] R. S. K. Mong, D. J. Clarke, J. Alicea, N. H. Lindner, P. Fendley, C. Nayak, Y. Oreg, A. Stern, E. Berg, K. Shtengel, and M. P. A. Fisher, “*Universal Topological Quantum Computation from a Superconductor-Abelian Quantum Hall Heterostructure*,” Phys. Rev. X **4**, 011036 (2014) [doi: [10.1103/PhysRevX.4.011036](https://doi.org/10.1103/PhysRevX.4.011036)].
- [281] A. Vaezi, “*Superconducting Analogue of the Parafermion Fractional Quantum Hall States*,” Phys. Rev. X **4**, 031009 (2014) [doi: [10.1103/PhysRevX.4.031009](https://doi.org/10.1103/PhysRevX.4.031009)].

- [282] P. M. R. Brydon, S. Das Sarma, H.-Y. Hui, and J. D. Sau, “*Topological Yu-Shiba-Rusinov chain from spin-orbit coupling*,” *Phys. Rev. B* **91**, 064505 (2015) [doi: 10.1103/PhysRevB.91.064505].
- [283] J. Li, H. Chen, I. K. Drozdov, A. Yazdani, B. A. Bernevig, and A. H. MacDonald, “*Topological superconductivity induced by ferromagnetic metal chains*,” *Phys. Rev. B* **90**, 235433 (2014) [doi: 10.1103/PhysRevB.90.235433].
- [284] A. Heimes, D. Mandler, and P. Kotetes, “*Interplay of topological phases in magnetic adatom-chains on top of a Rashba superconducting surface*,” *New J. Phys.* **17**, 023051 (2015) [doi: 10.1088/1367-2630/17/2/023051].
- [285] M. Z. Hasan and C. L. Kane, “*Colloquium: Topological insulators*,” *Rev. Mod. Phys.* **82**, 3045–3067 (2010) [doi: 10.1103/RevModPhys.82.3045].
- [286] X.-L. Qi and S.-C. Zhang, “*Topological insulators and superconductors*,” *Rev. Mod. Phys.* **83**, 1057–1110 (2011) [doi: 10.1103/RevModPhys.83.1057].
- [287] J. Alicea, “*New directions in the pursuit of Majorana fermions in solid state systems*,” *Rep. Prog. Phys.* **75**, 076501 (2012) [doi: 10.1088/0034-4885/75/7/076501].
- [288] C. W. J. Beenakker, “*Search for Majorana Fermions in Superconductors*,” *Annu. Rev. Condens. Matter Phys.* **4**, 113–136 (2013) [doi: 10.1146/annurev-conmatphys-030212-184337].
- [289] M. Leijnse and K. Flensberg, “*Introduction to topological superconductivity and Majorana fermions*,” *Semicond. Sci. Technol.* **27**, 124003 (2012) [doi: 10.1088/0268-1242/27/12/124003].
- [290] S. R. Elliott and M. Franz, “*Colloquium: Majorana fermions in nuclear, particle, and solid-state physics*,” *Rev. Mod. Phys.* **87**, 137–163 (2015) [doi: 10.1103/RevModPhys.87.137].
- [291] M. Sato and Y. Ando, “*Topological superconductors: a review*,” *Rep. Prog. Phys.* **80**, 076501 (2017) [doi: 10.1088/1361-6633/aa6ac7].
- [292] R. Aguado, “*Majorana quasiparticles in condensed matter*,” *Riv. Nuovo Cimento* **40**, 523–593 (2017) [doi: 10.1393/ncr/i2017-10141-9].
- [293] R. M. Lutchyn, E. P. A. M. Bakkers, L. P. Kouwenhoven, P. Krogstrup, C. M. Marcus, and Y. Oreg, “*Majorana zero modes in superconductor–semiconductor heterostructures*,” *Nat. Rev. Mater.* **3**, 52–68 (2018) [doi: 10.1038/s41578-018-0003-1].
- [294] R. Pawlak, S. Hoffman, J. Klinovaja, D. Loss, and E. Meyer, “*Majorana fermions in magnetic chains*,” *Prog. Part. Nucl. Phys.* **107**, 1–19 (2019) [doi: 10.1016/j.pnpnp.2019.04.004].
- [295] V. Mourik, K. Zuo, S. M. Frolov, S. R. Plissard, E. P. A. M. Bakkers, and L. P. Kouwenhoven, “*Signatures of Majorana Fermions in Hybrid Superconductor-Semiconductor Nanowire Devices*,” *Science* **336**, 1003–1007 (2012) [doi: 10.1126/science.1222360].
- [296] M. T. Deng, C. L. Yu, G. Y. Huang, M. Larsson, P. Caroff, and H. Q. Xu, “*Anomalous Zero-Bias Conductance Peak in a Nb–InSb Nanowire–Nb Hybrid Device*,” *Nano Lett.* **12**, 6414–6419 (2012) [doi: 10.1021/nl303758w].

- [297] A. Das, Y. Ronen, Y. Most, Y. Oreg, M. Heiblum, and H. Shtrikman, “Zero-bias peaks and splitting in an Al–InAs nanowire topological superconductor as a signature of Majorana fermions,” *Nat. Phys.* **8**, 887–895 (2012) [doi: [10.1038/nphys2479](https://doi.org/10.1038/nphys2479)].
- [298] M. T. Deng, S. Vaitiekėnas, E. B. Hansen, J. Danon, M. Leijnse, K. Flensberg, J. Nygård, P. Krogstrup, and C. M. Marcus, “Majorana bound state in a coupled quantum-dot hybrid-nanowire system,” *Science* **354**, 1557–1562 (2016) [doi: [10.1126/science.aaf3961](https://doi.org/10.1126/science.aaf3961)].
- [299] S. M. Albrecht, A. P. Higginbotham, M. Madsen, F. Kuemmeth, T. S. Jespersen, J. Nygård, P. Krogstrup, and C. M. Marcus, “Exponential protection of zero modes in Majorana islands,” *Nature* **531**, 206–209 (2016) [doi: [10.1038/nature17162](https://doi.org/10.1038/nature17162)].
- [300] F. Nichele, A. C. C. Drachmann, A. M. Whiticar, E. C. T. O’Farrell, H. J. Suominen, A. Fornieri, T. Wang, G. C. Gardner, C. Thomas, A. T. Hatke, P. Krogstrup, M. J. Manfra, K. Flensberg, and C. M. Marcus, “Scaling of Majorana Zero-Bias Conductance Peaks,” *Phys. Rev. Lett.* **119**, 136803 (2017) [doi: [10.1103/PhysRevLett.119.136803](https://doi.org/10.1103/PhysRevLett.119.136803)].
- [301] H. Zhang, C.-X. Liu, S. Gazibegovic, D. Xu, J. A. Logan, G. Wang, N. van Loo, J. D. S. Bommer, M. W. A. de Moor, D. Car, R. L. M. O. h. Veld, P. J. van Veldhoven, S. Koelling, M. A. Verheijen, M. Pendharkar, D. J. Pennachio, B. Shojaei, J. S. Lee, C. J. Palmstrøm, E. P. A. M. Bakkers, S. D. Sarma, and L. P. Kouwenhoven, “Quantized Majorana conductance,” *Nature* **556**, 74–79 (2018) [doi: [10.1038/nature26142](https://doi.org/10.1038/nature26142)].
- [302] D. Laroche, D. Bouman, D. J. van Woerkom, A. Proutski, C. Murthy, D. I. Pikulin, C. Nayak, R. J. J. van Gulik, J. Nygård, P. Krogstrup, L. P. Kouwenhoven, and A. Geresdi, “Observation of the 4π -periodic Josephson effect in indium arsenide nanowires,” *Nat. Commun.* **10**, 1–7 (2019) [doi: [10.1038/s41467-018-08161-2](https://doi.org/10.1038/s41467-018-08161-2)].
- [303] A. Fornieri, A. M. Whiticar, F. Setiawan, E. Portolés, A. C. C. Drachmann, A. Keselman, S. Gronin, C. Thomas, T. Wang, R. Kallagher, G. C. Gardner, E. Berg, M. J. Manfra, A. Stern, C. M. Marcus, and F. Nichele, “Evidence of topological superconductivity in planar Josephson junctions,” *Nature* **569**, 89–92 (2019) [doi: [10.1038/s41586-019-1068-8](https://doi.org/10.1038/s41586-019-1068-8)].
- [304] H. Ren, F. Pientka, S. Hart, A. T. Pierce, M. Kosowsky, L. Lunczer, R. Schlereth, B. Scharf, E. M. Hankiewicz, L. W. Molenkamp, B. I. Halperin, and A. Yacoby, “Topological superconductivity in a phase-controlled Josephson junction,” *Nature* **569**, 93–98 (2019) [doi: [10.1038/s41586-019-1148-9](https://doi.org/10.1038/s41586-019-1148-9)].
- [305] M. M. Desjardins, L. C. Contamin, M. R. Delbecq, M. C. Dartiailh, L. E. Bruhat, T. Cubaynes, J. J. Viennot, F. Mallet, S. Rohart, A. Thiaville, A. Cottet, and T. Kontos, “Synthetic spin–orbit interaction for Majorana devices,” *Nat. Mater.* **18**, 1060–1064 (2019) [doi: [10.1038/s41563-019-0457-6](https://doi.org/10.1038/s41563-019-0457-6)].
- [306] S. Manna, P. Wei, Y. Xie, K. T. Law, P. A. Lee, and J. S. Moodera, “Signature of a pair of Majorana zero modes in superconducting gold surface states,” *Proc. Natl. Acad. Sci. U.S.A.* **117**, 8775–8782 (2020) [doi: [10.1073/pnas.1919753117](https://doi.org/10.1073/pnas.1919753117)].

- [307] S. Hart, H. Ren, T. Wagner, P. Leubner, M. Mühlbauer, C. Brüne, H. Buhmann, L. W. Molenkamp, and A. Yacoby, “*Induced superconductivity in the quantum spin Hall edge*,” *Nat. Phys.* **10**, 638–643 (2014) [doi: [10.1038/nphys3036](https://doi.org/10.1038/nphys3036)].
- [308] H.-H. Sun, K.-W. Zhang, L.-H. Hu, C. Li, G.-Y. Wang, H.-Y. Ma, Z.-A. Xu, C.-L. Gao, D.-D. Guan, Y.-Y. Li, C. Liu, D. Qian, Y. Zhou, L. Fu, S.-C. Li, F.-C. Zhang, and J.-F. Jia, “*Majorana Zero Mode Detected with Spin Selective Andreev Reflection in the Vortex of a Topological Superconductor*,” *Phys. Rev. Lett.* **116**, 257003 (2016) [doi: [10.1103/PhysRevLett.116.257003](https://doi.org/10.1103/PhysRevLett.116.257003)].
- [309] J. Wiedenmann, E. Bocquillon, R. S. Deacon, S. Hartinger, O. Herrmann, T. M. Klapwijk, L. Maier, C. Ames, C. Brüne, C. Gould, A. Oiwa, K. Ishibashi, S. Tarucha, H. Buhmann, and L. W. Molenkamp, “ *4π -periodic Josephson supercurrent in HgTe-based topological Josephson junctions*,” *Nat. Commun.* **7**, 1–7 (2016) [doi: [10.1038/ncomms10303](https://doi.org/10.1038/ncomms10303)].
- [310] L. Bours, B. Sothmann, M. Carrega, E. Strambini, E. M. Hankiewicz, L. W. Molenkamp, and F. Giazotto, “*Topological SQUIPT Based on Helical Edge States in Proximity to Superconductors*,” *Phys. Rev. Appl.* **10**, 014027 (2018) [doi: [10.1103/PhysRevApplied.10.014027](https://doi.org/10.1103/PhysRevApplied.10.014027)].
- [311] S. Nadj-Perge, I. K. Drozdov, J. Li, H. Chen, S. Jeon, J. Seo, A. H. MacDonald, B. A. Bernevig, and A. Yazdani, “*Observation of Majorana fermions in ferromagnetic atomic chains on a superconductor*,” *Science* **346**, 602–607 (2014) [doi: [10.1126/science.1259327](https://doi.org/10.1126/science.1259327)].
- [312] M. Ruby, F. Pientka, Y. Peng, F. von Oppen, B. W. Heinrich, and K. J. Franke, “*End States and Subgap Structure in Proximity-Coupled Chains of Magnetic Adatoms*,” *Phys. Rev. Lett.* **115**, 197204 (2015) [doi: [10.1103/PhysRevLett.115.197204](https://doi.org/10.1103/PhysRevLett.115.197204)].
- [313] R. Pawlak, M. Kisiel, J. Klinovaja, T. Meier, S. Kawai, T. Glatzel, D. Loss, and E. Meyer, “*Probing atomic structure and Majorana wavefunctions in mono-atomic Fe chains on superconducting Pb surface*,” *npj Quantum Inf.* **2**, 1–5 (2016) [doi: [10.1038/npjqi.2016.35](https://doi.org/10.1038/npjqi.2016.35)].
- [314] S. Jeon, Y. Xie, J. Li, Z. Wang, B. A. Bernevig, and A. Yazdani, “*Distinguishing a Majorana zero mode using spin-resolved measurements*,” *Science* **358**, 772–776 (2017) [doi: [10.1126/science.aan3670](https://doi.org/10.1126/science.aan3670)].
- [315] G. C. Ménard, S. Guissart, C. Brun, R. T. Leriche, M. Trif, F. Debontridder, D. Demaille, D. Roditchev, P. Simon, and T. Cren, “*Two-dimensional topological superconductivity in Pb/Co/Si(111)*,” *Nat. Commun.* **8**, 1–7 (2017) [doi: [10.1038/s41467-017-02192-x](https://doi.org/10.1038/s41467-017-02192-x)].
- [316] H. Kim, A. Palacio-Morales, T. Posske, L. Rózsa, K. Palotás, L. Szunyogh, M. Thorwart, and R. Wiesendanger, “*Toward tailoring Majorana bound states in artificially constructed magnetic atom chains on elemental superconductors*,” *Sci. Adv.* **4**, eaar5251 (2018) [doi: [10.1126/sciadv.aar5251](https://doi.org/10.1126/sciadv.aar5251)].
- [317] G. C. Ménard, A. Mesaros, C. Brun, F. Debontridder, D. Roditchev, P. Simon, and T. Cren, “*Isolated pairs of Majorana zero modes in a disordered superconducting lead monolayer*,” *Nat. Commun.* **10**, 1–7 (2019) [doi: [10.1038/s41467-019-10397-5](https://doi.org/10.1038/s41467-019-10397-5)].

- [318] G. C. Ménard, C. Brun, R. Leriche, M. Trif, F. Debontridder, D. Demaille, D. Roditchev, P. Simon, and T. Cren, “*Yu-Shiba-Rusinov bound states versus topological edge states in Pb/Si(111)*,” *Eur. Phys. J. Spec. Top.* **227**, 2303–2313 (2019) [doi: [10.1140/epjst/e2018-800056-3](https://doi.org/10.1140/epjst/e2018-800056-3)].
- [319] G. E. Volovik, *The Universe in a Helium Droplet*. Oxford University Press, (2009).
- [320] M. Sato, “*Non-Abelian statistics of axion strings*,” *Phys. Lett. B* **575**, 126–130 (2003) [doi: [10.1016/j.physletb.2003.09.047](https://doi.org/10.1016/j.physletb.2003.09.047)].
- [321] M. Sato, Y. Takahashi, and S. Fujimoto, “*Non-Abelian Topological Order in s-Wave Superfluids of Ultracold Fermionic Atoms*,” *Phys. Rev. Lett.* **103**, 020401 (2009) [doi: [10.1103/PhysRevLett.103.020401](https://doi.org/10.1103/PhysRevLett.103.020401)].
- [322] J. C. Y. Teo and C. L. Kane, “*Majorana Fermions and Non-Abelian Statistics in Three Dimensions*,” *Phys. Rev. Lett.* **104**, 046401 (2010) [doi: [10.1103/PhysRevLett.104.046401](https://doi.org/10.1103/PhysRevLett.104.046401)].
- [323] C. Chan, L. Zhang, T. F. J. Poon, Y.-P. He, Y.-Q. Wang, and X.-J. Liu, “*Generic Theory for Majorana Zero Modes in 2D Superconductors*,” *Phys. Rev. Lett.* **119**, 047001 (2017) [doi: [10.1103/PhysRevLett.119.047001](https://doi.org/10.1103/PhysRevLett.119.047001)].
- [324] L. P. Gor’kov and E. I. Rashba, “*Superconducting 2D System with Lifted Spin Degeneracy: Mixed Singlet-Triplet State*,” *Phys. Rev. Lett.* **87**, 037004 (2001) [doi: [10.1103/PhysRevLett.87.037004](https://doi.org/10.1103/PhysRevLett.87.037004)].
- [325] R. Jackiw and P. Rossi, “*Zero modes of the vortex-fermion system*,” *Nucl. Phys. B* **190**, 681–691 (1981) [doi: [10.1016/0550-3213\(81\)90044-4](https://doi.org/10.1016/0550-3213(81)90044-4)].
- [326] Y. Nishida, L. Santos, and C. Chamon, “*Topological superconductors as nonrelativistic limits of Jackiw-Rossi and Jackiw-Rebbi models*,” *Phys. Rev. B* **82**, 144513 (2010) [doi: [10.1103/PhysRevB.82.144513](https://doi.org/10.1103/PhysRevB.82.144513)].
- [327] M. Sigrist and K. Ueda, “*Phenomenological theory of unconventional superconductivity*,” *Rev. Mod. Phys.* **63**, 239–311 (1991) [doi: [10.1103/RevModPhys.63.239](https://doi.org/10.1103/RevModPhys.63.239)].
- [328] E. Bauer, G. Hilscher, H. Michor, Ch. Paul, E. W. Scheidt, A. Griбанov, Yu. Seropugin, H. Noël, M. Sigrist, and P. Rogl, “*Heavy Fermion Superconductivity and Magnetic Order in Noncentrosymmetric CePt₃Si*,” *Phys. Rev. Lett.* **92**, 027003 (2004) [doi: [10.1103/PhysRevLett.92.027003](https://doi.org/10.1103/PhysRevLett.92.027003)].
- [329] P. A. Frigeri, D. F. Agterberg, A. Koga, and M. Sigrist, “*Superconductivity without Inversion Symmetry: MnSi versus CePt₃Si*,” *Phys. Rev. Lett.* **92**, 097001 (2004) [doi: [10.1103/PhysRevLett.92.097001](https://doi.org/10.1103/PhysRevLett.92.097001)].
- [330] M. Smidman, M. B. Salamon, H. Q. Yuan, and D. F. Agterberg, “*Superconductivity and spin-orbit coupling in non-centrosymmetric materials: a review*,” *Rep. Prog. Phys.* **80**, 036501 (2017) [doi: [10.1088/1361-6633/80/3/036501](https://doi.org/10.1088/1361-6633/80/3/036501)].
- [331] B. Braunecker, G. I. Japaridze, J. Klinovaja, and D. Loss, “*Spin-selective Peierls transition in interacting one-dimensional conductors with spin-orbit interaction*,” *Phys. Rev. B* **82**, 045127 (2010) [doi: [10.1103/PhysRevB.82.045127](https://doi.org/10.1103/PhysRevB.82.045127)].

- [332] J. Shabani, M. Kjaergaard, H. J. Suominen, Y. Kim, F. Nichele, K. Pakrouski, T. Stankevic, R. M. Lutchyn, P. Krogstrup, R. Feidenhans'l, S. Kraemer, C. Nayak, M. Troyer, C. M. Marcus, and C. J. Palmstrøm, “*Two-dimensional epitaxial superconductor-semiconductor heterostructures: A platform for topological superconducting networks*,” *Phys. Rev. B* **93**, 155402 (2016) [doi: 10.1103/PhysRevB.93.155402].
- [333] P. Krogstrup, N. L. B. Ziino, W. Chang, S. M. Albrecht, M. H. Madsen, E. Johnson, J. Nygård, C. M. Marcus, and T. S. Jespersen, “*Epitaxy of semiconductor–superconductor nanowires*,” *Nat. Mater.* **14**, 400–406 (2015) [doi: 10.1038/nmat4176].
- [334] T. Kanne, M. Marnauza, D. Olsteins, D. J. Carrad, J. E. Sestoft, J. de Bruijkere, L. Zeng, E. Johnson, E. Olsson, K. Grove-Rasmussen, and J. Nygård, “*Epitaxial Pb on InAs nanowires*,” arXiv (2020)
- [335] Y. Luh, “*Bound State in Superconductors with Paramagnetic Impurities*,” *Acta Phys. Sin.* **21**, 75–91 (1965) [doi: 10.7498/aps.21.75].
- [336] H. Shiba, “*Classical Spins in Superconductors*,” *Prog. Theor. Phys.* **40**, 435–451 (1968) [doi: 10.1143/PTP.40.435].
- [337] A. I. Rusinov, “*Theory of gapless superconductivity in alloys containing paramagnetic impurities*,” *Sov. Phys. JETP* **29**, 1101 (1969)
- [338] F. Li, T. Nattermann, and V. L. Pokrovsky, “*Vortex Domain Walls in Helical Magnets*,” *Phys. Rev. Lett.* **108**, 107203 (2012) [doi: 10.1103/PhysRevLett.108.107203].
- [339] T. Nattermann and V. L. Pokrovsky, “*Topological Defects in Helical Magnets*,” *J. Exp. Theor. Phys.* **127**, 922–932 (2018) [doi: 10.1134/S106377611811016X].
- [340] M. Uchida, N. Nagaosa, J. P. He, Y. Kaneko, S. Iguchi, Y. Matsui, and Y. Tokura, “*Topological spin textures in the helimagnet FeGe*,” *Phys. Rev. B* **77**, 184402 (2008) [doi: 10.1103/PhysRevB.77.184402].
- [341] P. Milde, D. Köhler, J. Seidel, L. M. Eng, A. Bauer, A. Chacon, J. Kindervater, S. Mühlbauer, C. Pfleiderer, S. Buhrandt, C. Schütte, and A. Rosch, “*Unwinding of a Skyrmion Lattice by Magnetic Monopoles*,” *Science* **340**, 1076–1080 (2013) [doi: 10.1126/science.1234657].
- [342] A. Dussaux, P. Schoenherr, K. Koumpouras, J. Chico, K. Chang, L. Lorenzelli, N. Kanazawa, Y. Tokura, M. Garst, A. Bergman, C. L. Degen, and D. Meier, “*Local dynamics of topological magnetic defects in the itinerant helimagnet FeGe*,” *Nat. Commun.* **7**, 1–9 (2016) [doi: 10.1038/ncomms12430].
- [343] A. Bauer, A. Chacon, M. Wagner, M. Halder, R. Georgii, A. Rosch, C. Pfleiderer, and M. Garst, “*Symmetry breaking, slow relaxation dynamics, and topological defects at the field-induced helix reorientation in MnSi*,” *Phys. Rev. B* **95**, 024429 (2017) [doi: 10.1103/PhysRevB.95.024429].
- [344] P. Schoenherr, J. Müller, L. Köhler, A. Rosch, N. Kanazawa, Y. Tokura, M. Garst, and D. Meier, “*Topological domain walls in helimagnets*,” *Nat. Phys.* **14**, 465–468 (2018) [doi: 10.1038/s41567-018-0056-5].

- [345] S. S. Pershoguba, S. Nakosai, and A. V. Balatsky, “*Skyrmion-induced bound states in a superconductor*,” Phys. Rev. B **94**, 064513 (2016) [doi: [10.1103/PhysRevB.94.064513](https://doi.org/10.1103/PhysRevB.94.064513)].
- [346] G. Yang, P. Stano, J. Klinovaja, and D. Loss, “*Majorana bound states in magnetic skyrmions*,” Phys. Rev. B **93**, 224505 (2016) [doi: [10.1103/PhysRevB.93.224505](https://doi.org/10.1103/PhysRevB.93.224505)].
- [347] S. Rex, I. V. Gornyi, and A. D. Mirlin, “*Majorana bound states in magnetic skyrmions imposed onto a superconductor*,” Phys. Rev. B **100**, 064504 (2019) [doi: [10.1103/PhysRevB.100.064504](https://doi.org/10.1103/PhysRevB.100.064504)].
- [348] M. Garnier, A. Mesaros, and P. Simon, “*Topological superconductivity with orbital effects in magnetic skyrmion based heterostructures*,” arXiv (2019)
- [349] M. Garnier, A. Mesaros, and P. Simon, “*Topological superconductivity with deformable magnetic skyrmions*,” Commun. Phys. **2**, 1–8 (2019) [doi: [10.1038/s42005-019-0226-5](https://doi.org/10.1038/s42005-019-0226-5)].
- [350] D. Steffensen, M. H. Christensen, B. M. Andersen, and P. Kotetes, “*Topological Superconductivity Induced by Magnetic Textures*,” arXiv (2020)
- [351] Y. Tanaka, M. Sato, and N. Nagaosa, “*Symmetry and Topology in Superconductors –Odd-Frequency Pairing and Edge States–*,” J. Phys. Soc. Jpn. **81**, 011013 (2011) [doi: [10.1143/JPSJ.81.011013](https://doi.org/10.1143/JPSJ.81.011013)].
- [352] Y. Ando and L. Fu, “*Topological Crystalline Insulators and Topological Superconductors: From Concepts to Materials*,” Annu. Rev. Condens. Matter Phys. **6**, 361–381 (2015) [doi: [10.1146/annurev-conmatphys-031214-014501](https://doi.org/10.1146/annurev-conmatphys-031214-014501)].
- [353] E. Prada, P. San-Jose, M. W. A. de Moor, A. Geresdi, E. J. H. Lee, J. Klinovaja, D. Loss, J. Nygård, R. Aguado, and L. P. Kouwenhoven, “*From Andreev to Majorana bound states in hybrid superconductor–semiconductor nanowires*,” Nat. Rev. Phys. **2**, 575–594 (2020) [doi: [10.1038/s42254-020-0228-y](https://doi.org/10.1038/s42254-020-0228-y)].
- [354] E. Majorana, “*Teoria simmetrica dell’elettrone e del positrone*,” Nuovo Cim. **14**, 171 (1937) [doi: [10.1007/BF02961314](https://doi.org/10.1007/BF02961314)].
- [355] F. Wilczek, “*Majorana returns*,” Nat. Phys. **5**, 614–618 (2009) [doi: [10.1038/nphys1380](https://doi.org/10.1038/nphys1380)].
- [356] A. P. Schnyder, S. Ryu, A. Furusaki, and A. W. W. Ludwig, “*Classification of topological insulators and superconductors in three spatial dimensions*,” Phys. Rev. B **78**, 195125 (2008) [doi: [10.1103/PhysRevB.78.195125](https://doi.org/10.1103/PhysRevB.78.195125)].
- [357] C. Zhang, S. Tewari, R. M. Lutchyn, and S. Das Sarma, “ *$p_x + ip_y$ Superfluid from s -Wave Interactions of Fermionic Cold Atoms*,” Phys. Rev. Lett. **101**, 160401 (2008) [doi: [10.1103/PhysRevLett.101.160401](https://doi.org/10.1103/PhysRevLett.101.160401)].
- [358] J. C. Y. Teo and T. L. Hughes, “*Existence of Majorana-Fermion Bound States on Disclinations and the Classification of Topological Crystalline Superconductors in Two Dimensions*,” Phys. Rev. Lett. **111**, 047006 (2013) [doi: [10.1103/PhysRevLett.111.047006](https://doi.org/10.1103/PhysRevLett.111.047006)].

- [359] S. Rex, I. V. Gornyi, and A. D. Mirlin, “Majorana modes in emergent-wire phases of helical and cycloidal magnet-superconductor hybrids,” *Phys. Rev. B* **102**, 224501 (2020) [doi: 10.1103/PhysRevB.102.224501].
- [360] K. M. D. Hals, M. Schechter, and M. S. Rudner, “Composite Topological Excitations in Ferromagnet-Superconductor Heterostructures,” *Phys. Rev. Lett.* **117**, 017001 (2016) [doi: 10.1103/PhysRevLett.117.017001].
- [361] L. Schneider, S. Brinker, M. Steinbrecher, J. Hermenau, T. Posske, M. dos Santos Dias, S. Lounis, R. Wiesendanger, and J. Wiebe, “Controlling in-gap end states by linking nonmagnetic atoms and artificially-constructed spin chains on superconductors,” *Nat. Commun.* **11**, 1–6 (2020) [doi: 10.1038/s41467-020-18540-3].
- [362] T. Čadež and P. D. Sacramento, “Zero energy modes in a superconductor with ferromagnetic adatom chains and quantum phase transitions,” *J. Phys.: Condens. Matter* **28**, 495703 (2016) [doi: 10.1088/0953-8984/28/49/495703].
- [363] A. Palacio-Morales, E. Mascot, S. Cocklin, H. Kim, S. Rachel, D. K. Morr, and R. Wiesendanger, “Atomic-scale interface engineering of Majorana edge modes in a 2D magnet-superconductor hybrid system,” *Sci. Adv.* **5**, eaav6600 (2019) [doi: 10.1126/sciadv.aav6600].
- [364] A. E. Böhmer, F. Hardy, L. Wang, T. Wolf, P. Schweiss, and C. Meingast, “Superconductivity-induced re-entrance of the orthorhombic distortion in $Ba_{1-x}K_xFe_2As_2$,” *Nat. Commun.* **6** 2015 [doi: 10.1038/ncomms8911].
- [365] J. Lorenzana, G. Seibold, C. Ortix, and M. Grilli, “Competing Orders in FeAs Layers,” *Phys. Rev. Lett.* **101**, 186402 (2008) [doi: 10.1103/PhysRevLett.101.186402].
- [366] I. Eremin and A. V. Chubukov, “Magnetic degeneracy and hidden metallicity of the spin-density-wave state in ferropnictides,” *Phys. Rev. B* **81**, 024511 (2010) [doi: 10.1103/PhysRevB.81.024511].
- [367] P. M. R. Brydon, J. Schmiedt, and C. Timm, “Microscopically derived Ginzburg-Landau theory for magnetic order in the iron pnictides,” *Phys. Rev. B* **84**, 214510 (2011) [doi: 10.1103/PhysRevB.84.214510].
- [368] G. Giovannetti, C. Ortix, M. Marsman, M. Capone, J. van den Brink, and J. Lorenzana, “Proximity of iron pnictide superconductors to a quantum tricritical point,” *Nat. Commun.* **2**, 1–6 (2011) [doi: 10.1038/ncomms1407].
- [369] X. Wang, J. Kang, and R. M. Fernandes, “Magnetic order without tetragonal-symmetry-breaking in iron arsenides: Microscopic mechanism and spin-wave spectrum,” *Phys. Rev. B* **91**, 024401 (2015) [doi: 10.1103/PhysRevB.91.024401].
- [370] J. Kang, X. Wang, A. V. Chubukov, and R. M. Fernandes, “Interplay between tetragonal magnetic order, stripe magnetism, and superconductivity in iron-based materials,” *Phys. Rev. B* **91**, 121104 (2015) [doi: 10.1103/PhysRevB.91.121104].

- [371] M. H. Christensen, J. Kang, B. M. Andersen, I. Eremin, and R. M. Fernandes, “*Spin reorientation driven by the interplay between spin-orbit coupling and Hund’s rule coupling in iron pnictides*,” Phys. Rev. B **92**, 214509 (2015) [doi: [10.1103/PhysRevB.92.214509](https://doi.org/10.1103/PhysRevB.92.214509)].
- [372] M. H. Christensen, D. D. Scherer, P. Kotetes, and B. M. Andersen, “*Role of multiorbital effects in the magnetic phase diagram of iron pnictides*,” Phys. Rev. B **96**, 014523 (2017) [doi: [10.1103/PhysRevB.96.014523](https://doi.org/10.1103/PhysRevB.96.014523)].
- [373] J. Cano, B. Bradlyn, and M. G. Vergniory, “*Multifold nodal points in magnetic materials*,” APL Mater. **7**, 101125 (2019) [doi: [10.1063/1.5124314](https://doi.org/10.1063/1.5124314)].
- [374] Y. Xu, L. Elcoro, Z.-D. Song, B. J. Wieder, M. G. Vergniory, N. Regnault, Y. Chen, C. Felser, and B. A. Bernevig, “*High-throughput calculations of magnetic topological materials*,” Nature **586**, 702–707 (2020) [doi: [10.1038/s41586-020-2837-0](https://doi.org/10.1038/s41586-020-2837-0)].
- [375] A. Bouhon, G. F. Lange, and R.-J. Slager, “*Topological correspondence between magnetic space group representations*,” arXiv (2020)
- [376] L. Fu, “*Topological Crystalline Insulators*,” Phys. Rev. Lett. **106**, 106802 (2011) [doi: [10.1103/PhysRevLett.106.106802](https://doi.org/10.1103/PhysRevLett.106.106802)].
- [377] T. H. Hsieh, H. Lin, J. Liu, W. Duan, A. Bansil, and L. Fu, “*Topological crystalline insulators in the SnTe material class*,” Nat. Commun. **3**, 1–7 (2012) [doi: [10.1038/ncomms1969](https://doi.org/10.1038/ncomms1969)].
- [378] Y. Tanaka, Z. Ren, T. Sato, K. Nakayama, S. Souma, T. Takahashi, K. Segawa, and Y. Ando, “*Experimental realization of a topological crystalline insulator in SnTe*,” Nat. Phys. **8**, 800–803 (2012) [doi: [10.1038/nphys2442](https://doi.org/10.1038/nphys2442)].
- [379] T. Morimoto and A. Furusaki, “*Topological classification with additional symmetries from Clifford algebras*,” Phys. Rev. B **88**, 125129 (2013) [doi: [10.1103/PhysRevB.88.125129](https://doi.org/10.1103/PhysRevB.88.125129)].
- [380] D. Mendler, P. Kotetes, and G. Schön, “*Magnetic order on a topological insulator surface with warping and proximity-induced superconductivity*,” Phys. Rev. B **91**, 155405 (2015) [doi: [10.1103/PhysRevB.91.155405](https://doi.org/10.1103/PhysRevB.91.155405)].
- [381] J. Kruthoff, J. de Boer, J. van Wezel, C. L. Kane, and R.-J. Slager, “*Topological Classification of Crystalline Insulators through Band Structure Combinatorics*,” Phys. Rev. X **7**, 041069 (2017) [doi: [10.1103/PhysRevX.7.041069](https://doi.org/10.1103/PhysRevX.7.041069)].
- [382] E. J. König and P. Coleman, “*Crystalline-Symmetry-Protected Helical Majorana Modes in the Iron Pnictides*,” Phys. Rev. Lett. **122**, 207001 (2019) [doi: [10.1103/PhysRevLett.122.207001](https://doi.org/10.1103/PhysRevLett.122.207001)].
- [383] J. Zou, Q. Xie, Z. Song, and G. Xu, “*New types of topological superconductors under local magnetic symmetries*,” arXiv (2019)
- [384] R. Ramazashvili, “*Kramers degeneracy in a magnetic field and Zeeman spin-orbit coupling in antiferromagnetic conductors*,” Phys. Rev. B **79**, 184432 (2009) [doi: [10.1103/PhysRevB.79.184432](https://doi.org/10.1103/PhysRevB.79.184432)].

- [385] R. S. K. Mong, A. M. Essin, and J. E. Moore, “*Antiferromagnetic topological insulators*,” *Phys. Rev. B* **81**, 245209 (2010) [doi: 10.1103/PhysRevB.81.245209].
- [386] R.-J. Slager, A. Mesaros, V. Juričić, and J. Zaanen, “*The space group classification of topological band-insulators*,” *Nat. Phys.* **9**, 98–102 (2013) [doi: 10.1038/nphys2513].
- [387] C. Fang, M. J. Gilbert, and B. A. Bernevig, “*Topological insulators with commensurate antiferromagnetism*,” *Phys. Rev. B* **88**, 085406 (2013) [doi: 10.1103/PhysRevB.88.085406].
- [388] Y. Yanase and K. Shiozaki, “ *$M\backslash$ obius topological superconductivity in UPt_3* ,” *Phys. Rev. B* **95**, 224514 (2017) [doi: 10.1103/PhysRevB.95.224514].
- [389] A. Daido, T. Yoshida, and Y. Yanase, “ *\mathbb{Z}_4 Topological Superconductivity in $UCoGe$* ,” *Phys. Rev. Lett.* **122**, 227001 (2019) [doi: 10.1103/PhysRevLett.122.227001].
- [390] S. Raghu, X.-L. Qi, C.-X. Liu, D. J. Scalapino, and S.-C. Zhang, “*Minimal two-band model of the superconducting iron oxypnictides*,” *Phys. Rev. B* **77**, 220503 (2008) [doi: 10.1103/PhysRevB.77.220503].
- [391] M. Daghofer, A. Nicholson, A. Moreo, and E. Dagotto, “*Three orbital model for the iron-based superconductors*,” *Phys. Rev. B* **81**, 014511 (2010) [doi: 10.1103/PhysRevB.81.014511].
- [392] H. Ikeda, R. Arita, and J. Kuneš, “*Phase diagram and gap anisotropy in iron-pnictide superconductors*,” *Phys. Rev. B* **81**, 054502 (2010) [doi: 10.1103/PhysRevB.81.054502].
- [393] S. Graser, A. F. Kemper, T. A. Maier, H.-P. Cheng, P. J. Hirschfeld, and D. J. Scalapino, “*Spin fluctuations and superconductivity in a three-dimensional tight-binding model for $BaFe_2As_2$* ,” *Phys. Rev. B* **81**, 214503 (2010) [doi: 10.1103/PhysRevB.81.214503].
- [394] A. Aperis, P. Kotetes, G. Varelogiannis, and P. M. Oppeneer, “*Small- q phonon-mediated unconventional superconductivity in the iron pnictides*,” *Phys. Rev. B* **83**, 092505 (2011) [doi: 10.1103/PhysRevB.83.092505].
- [395] N. Hao and J. Hu, “*Topological Phases in the Single-Layer $FeSe$* ,” *Phys. Rev. X* **4**, 031053 (2014) [doi: 10.1103/PhysRevX.4.031053].
- [396] C. L. M. Wong, J. Liu, K. T. Law, and P. A. Lee, “*Majorana flat bands and unidirectional Majorana edge states in gapless topological superconductors*,” *Phys. Rev. B* **88**, 060504 (2013) [doi: 10.1103/PhysRevB.88.060504].
- [397] A. Daido and Y. Yanase, “*Majorana flat bands, chiral Majorana edge states, and unidirectional Majorana edge states in noncentrosymmetric superconductors*,” *Phys. Rev. B* **95**, 134507 (2017) [doi: 10.1103/PhysRevB.95.134507].
- [398] M. Biderang, H. Yavari, M.-H. Zare, P. Thalmeier, and A. Akbari, “*Edge currents as a probe of the strongly spin-polarized topological noncentrosymmetric superconductors*,” *Phys. Rev. B* **98**, 014524 (2018) [doi: 10.1103/PhysRevB.98.014524].
- [399] J. Klinovaja, P. Stano, and D. Loss, “*Transition from Fractional to Majorana Fermions in Rashba Nanowires*,” *Phys. Rev. Lett.* **109**, 236801 (2012) [doi: 10.1103/PhysRevLett.109.236801].

- [400] D. Sticlet, L. Seabra, F. Pollmann, and J. Cayssol, “From fractionally charged solitons to Majorana bound states in a one-dimensional interacting model,” *Phys. Rev. B* **89**, 115430 (2014) [doi: 10.1103/PhysRevB.89.115430].
- [401] R. Wakatsuki, M. Ezawa, Y. Tanaka, and N. Nagaosa, “Fermion fractionalization to Majorana fermions in a dimerized Kitaev superconductor,” *Phys. Rev. B* **90**, 014505 (2014) [doi: 10.1103/PhysRevB.90.014505].
- [402] P. Marra and M. Nitta, “Topologically nontrivial Andreev bound states,” *Phys. Rev. B* **100**, 220502 (2019) [doi: 10.1103/PhysRevB.100.220502].
- [403] A. Zazunov, V. S. Shumeiko, E. N. Bratus’, J. Lantz, and G. Wendin, “Andreev Level Qubit,” *Phys. Rev. Lett.* **90**, 087003 (2003) [doi: 10.1103/PhysRevLett.90.087003].
- [404] A. P. Higginbotham, S. M. Albrecht, G. Kiršanskas, W. Chang, F. Kuemmeth, P. Krogstrup, T. S. Jespersen, J. Nygård, K. Flensberg, and C. M. Marcus, “Parity lifetime of bound states in a proximitized semiconductor nanowire,” *Nat. Phys.* **11**, 1017–1021 (2015) [doi: 10.1038/nphys3461].
- [405] I. M. Lifshitz, “Anomalies of Electron Characteristics of a Metal,” *Sov. Phys. JETP* **11**, 1130 (1960)
- [406] G. E. Volovik, “Exotic Lifshitz transitions in topological materials,” *Phys.-Usp.* **61**, 89–98 (2018) [doi: 10.3367/ufne.2017.01.038218].
- [407] S. Tewari and J. D. Sau, “Topological Invariants for Spin-Orbit Coupled Superconductor Nanowires,” *Phys. Rev. Lett.* **109**, 150408 (2012) [doi: 10.1103/PhysRevLett.109.150408].
- [408] D. N. Sheng, Z. Y. Weng, L. Sheng, and F. D. M. Haldane, “Quantum Spin-Hall Effect and Topologically Invariant Chern Numbers,” *Phys. Rev. Lett.* **97**, 036808 (2006) [doi: 10.1103/PhysRevLett.97.036808].
- [409] A. Sakurai, “Comments on Superconductors with Magnetic Impurities,” *Prog. Theor. Phys.* **44**, 1472–1476 (1970) [doi: 10.1143/PTP.44.1472].
- [410] D. Hsieh, Y. Xia, L. Wray, D. Qian, A. Pal, J. H. Dil, J. Osterwalder, F. Meier, G. Bihlmayer, C. L. Kane, Y. S. Hor, R. J. Cava, and M. Z. Hasan, “Observation of Unconventional Quantum Spin Textures in Topological Insulators,” *Science* **323**, 919–922 (2009) [doi: 10.1126/science.1167733].
- [411] L. Fu, C. L. Kane, and E. J. Mele, “Topological Insulators in Three Dimensions,” *Phys. Rev. Lett.* **98**, 106803 (2007) [doi: 10.1103/PhysRevLett.98.106803].
- [412] Z. Ringel, Y. E. Kraus, and A. Stern, “Strong side of weak topological insulators,” *Phys. Rev. B* **86**, 045102 (2012) [doi: 10.1103/PhysRevB.86.045102].
- [413] S. Murakami, “Phase transition between the quantum spin Hall and insulator phases in 3D: emergence of a topological gapless phase,” *New J. Phys.* **9**, 356 (2007) [doi: 10.1088/1367-2630/9/9/356].

- [414] D. V. Chichinadze and A. V. Chubukov, “*Winding numbers of nodal points in Fe-based superconductors*,” Phys. Rev. B **97**, 094501 (2018) [doi: [10.1103/PhysRevB.97.094501](https://doi.org/10.1103/PhysRevB.97.094501)].
- [415] T. Nakayama, T. Shishidou, and D. F. Agterberg, “*Nodal topology in d-wave superconducting monolayer FeSe*,” Phys. Rev. B **98**, 214503 (2018) [doi: [10.1103/PhysRevB.98.214503](https://doi.org/10.1103/PhysRevB.98.214503)].
- [416] A. H. Castro Neto, F. Guinea, N. M. R. Peres, K. S. Novoselov, and A. K. Geim, “*The electronic properties of graphene*,” Rev. Mod. Phys. **81**, 109–162 (2009) [doi: [10.1103/RevModPhys.81.109](https://doi.org/10.1103/RevModPhys.81.109)].
- [417] Y. X. Zhao and Z. D. Wang, “*Topological Classification and Stability of Fermi Surfaces*,” Phys. Rev. Lett. **110**, 240404 (2013) [doi: [10.1103/PhysRevLett.110.240404](https://doi.org/10.1103/PhysRevLett.110.240404)].
- [418] Y. X. Zhao and Z. D. Wang, “*Topological connection between the stability of Fermi surfaces and topological insulators and superconductors*,” Phys. Rev. B **89**, 075111 (2014) [doi: [10.1103/PhysRevB.89.075111](https://doi.org/10.1103/PhysRevB.89.075111)].
- [419] M. Sato, “*Topological odd-parity superconductors*,” Phys. Rev. B **81**, 220504 (2010) [doi: [10.1103/PhysRevB.81.220504](https://doi.org/10.1103/PhysRevB.81.220504)].
- [420] Y. Tanaka, T. Yokoyama, and N. Nagaosa, “*Manipulation of the Majorana Fermion, Andreev Reflection, and Josephson Current on Topological Insulators*,” Phys. Rev. Lett. **103**, 107002 (2009) [doi: [10.1103/PhysRevLett.103.107002](https://doi.org/10.1103/PhysRevLett.103.107002)].
- [421] J. Linder, Y. Tanaka, T. Yokoyama, A. Sudbø, and N. Nagaosa, “*Unconventional Superconductivity on a Topological Insulator*,” Phys. Rev. Lett. **104**, 067001 (2010) [doi: [10.1103/PhysRevLett.104.067001](https://doi.org/10.1103/PhysRevLett.104.067001)].
- [422] J. Röntynen and T. Ojanen, “*Topological Superconductivity and High Chern Numbers in 2D Ferromagnetic Shiba Lattices*,” Phys. Rev. Lett. **114**, 236803 (2015) [doi: [10.1103/PhysRevLett.114.236803](https://doi.org/10.1103/PhysRevLett.114.236803)].
- [423] J. Li, T. Neupert, Z. Wang, A. H. MacDonald, A. Yazdani, and B. A. Bernevig, “*Two-dimensional chiral topological superconductivity in Shiba lattices*,” Nat. Commun. **7**, 1–7 (2016) [doi: [10.1038/ncomms12297](https://doi.org/10.1038/ncomms12297)].
- [424] J. L. Lado and M. Sigrist, “*Two-Dimensional Topological Superconductivity with Antiferromagnetic Insulators*,” Phys. Rev. Lett. **121**, 037002 (2018) [doi: [10.1103/PhysRevLett.121.037002](https://doi.org/10.1103/PhysRevLett.121.037002)].
- [425] X.-L. Qi, T. L. Hughes, and S.-C. Zhang, “*Topological field theory of time-reversal invariant insulators*,” Phys. Rev. B **78**, 195424 (2008) [doi: [10.1103/PhysRevB.78.195424](https://doi.org/10.1103/PhysRevB.78.195424)].
- [426] X.-L. Qi, T. L. Hughes, and S.-C. Zhang, “*Topological invariants for the Fermi surface of a time-reversal-invariant superconductor*,” Phys. Rev. B **81**, 134508 (2010) [doi: [10.1103/PhysRevB.81.134508](https://doi.org/10.1103/PhysRevB.81.134508)].
- [427] J. C. Budich and E. Ardonne, “*Topological invariant for generic one-dimensional time-reversal-symmetric superconductors in class DIII*,” Phys. Rev. B **88**, 134523 (2013) [doi: [10.1103/PhysRevB.88.134523](https://doi.org/10.1103/PhysRevB.88.134523)].

- [428] C. L. M. Wong and K. T. Law, “Majorana Kramers doublets in $d_{x^2-y^2}$ -wave superconductors with Rashba spin-orbit coupling,” *Phys. Rev. B* **86**, 184516 (2012) [doi: 10.1103/PhysRevB.86.184516].
- [429] L. Fu and C. L. Kane, “Time reversal polarization and a Z_2 adiabatic spin pump,” *Phys. Rev. B* **74**, 195312 (2006) [doi: 10.1103/PhysRevB.74.195312].
- [430] B. van Heck, S. Mi, and A. R. Akhmerov, “Single fermion manipulation via superconducting phase differences in multiterminal Josephson junctions,” *Phys. Rev. B* **90**, 155450 (2014) [doi: 10.1103/PhysRevB.90.155450].
- [431] T. Yokoyama and Y. V. Nazarov, “Singularities in the Andreev spectrum of a multiterminal Josephson junction,” *Phys. Rev. B* **92**, 155437 (2015) [doi: 10.1103/PhysRevB.92.155437].
- [432] E. Strambini, S. D’Ambrosio, F. Vischi, F. S. Bergeret, Yu. V. Nazarov, and F. Giazotto, “The ω -SQUIPT as a tool to phase-engineer Josephson topological materials,” *Nat. Nanotechnol.* **11**, 1055–1059 (2016) [doi: 10.1038/nnano.2016.157].
- [433] R.-P. Riwar, M. Houzet, J. S. Meyer, and Y. V. Nazarov, “Multi-terminal Josephson junctions as topological matter,” *Nat. Commun.* **7**, 1–5 (2016) [doi: 10.1038/ncomms11167].
- [434] E. Eriksson, R.-P. Riwar, M. Houzet, J. S. Meyer, and Y. V. Nazarov, “Topological transconductance quantization in a four-terminal Josephson junction,” *Phys. Rev. B* **95**, 075417 (2017) [doi: 10.1103/PhysRevB.95.075417].
- [435] J. S. Meyer and M. Houzet, “Nontrivial Chern Numbers in Three-Terminal Josephson Junctions,” *Phys. Rev. Lett.* **119**, 136807 (2017) [doi: 10.1103/PhysRevLett.119.136807].
- [436] H.-Y. Xie, M. G. Vavilov, and A. Levchenko, “Topological Andreev bands in three-terminal Josephson junctions,” *Phys. Rev. B* **96**, 161406 (2017) [doi: 10.1103/PhysRevB.96.161406].
- [437] M. Houzet and J. S. Meyer, “Majorana-Weyl crossings in topological multiterminal junctions,” *Phys. Rev. B* **100**, 014521 (2019) [doi: 10.1103/PhysRevB.100.014521].
- [438] H.-Y. Xie and A. Levchenko, “Topological supercurrents interaction and fluctuations in the multiterminal Josephson effect,” *Phys. Rev. B* **99**, 094519 (2019) [doi: 10.1103/PhysRevB.99.094519].
- [439] P. Kotetes, M. T. Mercaldo, and M. Cuoco, “Synthetic Weyl Points and Chiral Anomaly in Majorana Devices with Nonstandard Andreev-Bound-State Spectra,” *Phys. Rev. Lett.* **123**, 126802 (2019) [doi: 10.1103/PhysRevLett.123.126802].
- [440] M. T. Mercaldo, P. Kotetes, and M. Cuoco, “Magnetolectrically tunable Andreev bound state spectra and spin polarization in p -wave Josephson junctions,” *Phys. Rev. B* **100**, 104519 (2019) [doi: 10.1103/PhysRevB.100.104519].
- [441] L. Peralta Gavensky, G. Usaj, and C. A. Balseiro, “Topological phase diagram of a three-terminal Josephson junction: From the conventional to the Majorana regime,” *Phys. Rev. B* **100**, 014514 (2019) [doi: 10.1103/PhysRevB.100.014514].

- [442] K. Sakurai, M. T. Mercaldo, S. Kobayashi, A. Yamakage, S. Ikegaya, T. Habe, P. Kotetes, M. Cuoco, and Y. Asano, “*Nodal Andreev spectra in multi-Majorana three-terminal Josephson junctions*,” *Phys. Rev. B* **101**, 174506 (2020) [doi: [10.1103/PhysRevB.101.174506](https://doi.org/10.1103/PhysRevB.101.174506)].
- [443] J. S. Meyer and M. Houzet, “*Conductance quantization in topological Josephson trijunctions*,” ArXiv (2019)
- [444] H. Weisbrich, R. L. Klees, G. Rastelli, and W. Belzig, “*Second Chern Number and Non-Abelian Berry Phase in Topological Superconducting Systems*,” arXiv (2020)
- [445] R. L. Klees, J. C. Cuevas, W. Belzig, and G. Rastelli, “*Many-body Quantum Geometry in Superconductor-Quantum Dot Chains*,” arXiv (2020)
- [446] N. Pankratova, H. Lee, R. Kuzmin, K. Wickramasinghe, W. Mayer, J. Yuan, M. G. Vavilov, J. Shabani, and V. E. Manucharyan, “*Multiterminal Josephson Effect*,” *Phys. Rev. X* **10**, 031051 (2020) [doi: [10.1103/PhysRevX.10.031051](https://doi.org/10.1103/PhysRevX.10.031051)].
- [447] A. A. Burkov, “*Weyl Metals*,” *Annu. Rev. Condens. Matter Phys.* **9**, 359–378 (2018) [doi: [10.1146/annurev-conmatphys-033117-054129](https://doi.org/10.1146/annurev-conmatphys-033117-054129)].
- [448] C. Fang, H. Weng, X. Dai, and Z. Fang, “*Topological nodal line semimetals**,” *Chin. Phys. B* **25**, 117106 (2016) [doi: [10.1088/1674-1056/25/11/117106](https://doi.org/10.1088/1674-1056/25/11/117106)].
- [449] K. T. Law, P. A. Lee, and T. K. Ng, “*Majorana Fermion Induced Resonant Andreev Reflection*,” *Phys. Rev. Lett.* **103**, 237001 (2009) [doi: [10.1103/PhysRevLett.103.237001](https://doi.org/10.1103/PhysRevLett.103.237001)].
- [450] J. D. Sau, S. Tewari, R. M. Lutchyn, T. D. Stanescu, and S. Das Sarma, “*Non-Abelian quantum order in spin-orbit-coupled semiconductors: Search for topological Majorana particles in solid-state systems*,” *Phys. Rev. B* **82**, 214509 (2010) [doi: [10.1103/PhysRevB.82.214509](https://doi.org/10.1103/PhysRevB.82.214509)].
- [451] K. Flensberg, “*Tunneling characteristics of a chain of Majorana bound states*,” *Phys. Rev. B* **82**, 180516 (2010) [doi: [10.1103/PhysRevB.82.180516](https://doi.org/10.1103/PhysRevB.82.180516)].
- [452] J. J. He, T. K. Ng, P. A. Lee, and K. T. Law, “*Selective Equal-Spin Andreev Reflections Induced by Majorana Fermions*,” *Phys. Rev. Lett.* **112**, 037001 (2014) [doi: [10.1103/PhysRevLett.112.037001](https://doi.org/10.1103/PhysRevLett.112.037001)].
- [453] P. Kotetes, D. Mendler, A. Heimes, and G. Schön, “*Majorana fermion fingerprints in spin-polarised scanning tunnelling microscopy*,” *Physica E* **74**, 614–624 (2015) [doi: [10.1016/j.physe.2015.08.032](https://doi.org/10.1016/j.physe.2015.08.032)].
- [454] D. Sticlet, C. Bena, and P. Simon, “*Spin and Majorana Polarization in Topological Superconducting Wires*,” *Phys. Rev. Lett.* **108**, 096802 (2012) [doi: [10.1103/PhysRevLett.108.096802](https://doi.org/10.1103/PhysRevLett.108.096802)].
- [455] T. Mizushima, M. Sato, and K. Machida, “*Symmetry Protected Topological Order and Spin Susceptibility in Superfluid $^3\text{He-B}$* ,” *Phys. Rev. Lett.* **109**, 165301 (2012) [doi: [10.1103/PhysRevLett.109.165301](https://doi.org/10.1103/PhysRevLett.109.165301)].

- [456] Z. Wang, X.-L. Qi, and S.-C. Zhang, “*Topological field theory and thermal responses of interacting topological superconductors*,” Phys. Rev. B **84**, 014527 (2011) [doi: [10.1103/PhysRevB.84.014527](https://doi.org/10.1103/PhysRevB.84.014527)].
- [457] S. Ryu, J. E. Moore, and A. W. W. Ludwig, “*Electromagnetic and gravitational responses and anomalies in topological insulators and superconductors*,” Phys. Rev. B **85**, 045104 (2012) [doi: [10.1103/PhysRevB.85.045104](https://doi.org/10.1103/PhysRevB.85.045104)].
- [458] A. Furusaki, N. Nagaosa, K. Nomura, S. Ryu, and T. Takayanagi, “*Electromagnetic and thermal responses in topological matter: Topological terms, quantum anomalies and D-branes*,” C. R. Phys. **14**, 871–883 (2013) [doi: [10.1016/j.crhy.2013.03.002](https://doi.org/10.1016/j.crhy.2013.03.002)].
- [459] D. Bulmash, P. Hosur, S.-C. Zhang, and X.-L. Qi, “*Unified Topological Response Theory For Gapped and Gapless Free Fermions*,” Phys. Rev. X **5**, 021018 (2015) [doi: [10.1103/PhysRevX.5.021018](https://doi.org/10.1103/PhysRevX.5.021018)].
- [460] Y. Imai, K. Wakabayashi, and M. Sigrist, “*Thermal Hall conductivity in the spin-triplet superconductor with broken time-reversal symmetry*,” Phys. Rev. B **95**, 024516 (2017) [doi: [10.1103/PhysRevB.95.024516](https://doi.org/10.1103/PhysRevB.95.024516)].
- [461] S. M. Young and C. L. Kane, “*Dirac Semimetals in Two Dimensions*,” Phys. Rev. Lett. **115**, 126803 (2015) [doi: [10.1103/PhysRevLett.115.126803](https://doi.org/10.1103/PhysRevLett.115.126803)].
- [462] Y. X. Zhao and A. P. Schnyder, “*Nonsymmorphic symmetry-required band crossings in topological semimetals*,” Phys. Rev. B **94**, 195109 (2016) [doi: [10.1103/PhysRevB.94.195109](https://doi.org/10.1103/PhysRevB.94.195109)].
- [463] C. Fang, Y. Chen, H.-Y. Kee, and L. Fu, “*Topological nodal line semimetals with and without spin-orbital coupling*,” Phys. Rev. B **92**, 081201 (2015) [doi: [10.1103/PhysRevB.92.081201](https://doi.org/10.1103/PhysRevB.92.081201)].
- [464] B.-J. Yang, T. A. Bojesen, T. Morimoto, and A. Furusaki, “*Topological semimetals protected by off-centered symmetries in nonsymmorphic crystals*,” Phys. Rev. B **95**, 075135 (2017) [doi: [10.1103/PhysRevB.95.075135](https://doi.org/10.1103/PhysRevB.95.075135)].
- [465] J. Zhang, Y.-H. Chan, C.-K. Chiu, M. G. Vergniory, L. M. Schoop, and A. P. Schnyder, “*Topological band crossings in hexagonal materials*,” Phys. Rev. Mater. **2**, 074201 (2018) [doi: [10.1103/PhysRevMaterials.2.074201](https://doi.org/10.1103/PhysRevMaterials.2.074201)].
- [466] M. Malard, P. E. de Brito, S. Östlund, and H. Johannesson, “*Movable but not removable band degeneracies in a symmorphic crystal*,” Phys. Rev. B **98**, 165127 (2018) [doi: [10.1103/PhysRevB.98.165127](https://doi.org/10.1103/PhysRevB.98.165127)].

“👍, 🗨️, 🗨️?”

– Brian M. Andersen

